TABLE OF CONTENTS

	Page	
NOTATION	vi	1/A4
SUMMARY	1	1/A10
CHAPTER 1. INTRODUCTION	2	1/A11
CHAPTER 2. DERIVATION OF BASIC METHOD FOR COMPUTING C_N AND C_m CHARACTERISTICS	6	1/B1
2.1 Bodies of Revolution	6	1/B1
2.2 Bodies of Circular and Noncircular Cross Section Alone and With Lifting Surfaces	11	1/B6
2.3 Empirical Input Values	14	1/B9
2.3.1 Crossflow drag coefficient	14	1/B9
2.3.2 Crossflow drag proportionality factor	17	1/B12
2.4 Formulas and Values of $(C_n/C_{n_o})_{SB}$ and $(C_n/C_{n_o})_{Newt}$ for Various Cross Sections	18	1/B13
2.4.1 Formulas of $(C_n/C_{n_o})_{SB}$	18	1/B13
2.4.2 Formulas of $(C_n/C_{n_o})_{Newt}$	19	1/B14
2.4.3 Values of $(C_n/C_{n_o})_{SB}$ and $(C_n/C_{n_o})_{Newt}$	20	1/C1
2.5 Relative Influence of Crossflow Terms	21	1/C2
CHAPTER 3. METHOD APPLIED TO BODIES OF REVOLUTION	23	1/C4
3.1 Cone-Cylinder and Ogive-Cylinder Bodies at $M_\infty = 2.9$	23	1/C4
3.2 Ogive-Cylinder Bodies at $M_\infty = 0.6$ to 2.0	24	1/C5
3.3 Predicted Effect of Change in Crossflow Reynolds Number from Subcritical to Supercritical	26	1/C7
CHAPTER 4. METHOD APPLIED TO BODIES OF ELLIPTIC CROSS SECTION	28	1/C9
4.1 Bodies Studied and Tests at $M_\infty = 0.6$ to 2.0	28	1/C9
4.2 Equations Used to Compute C_N and C_m for Each Body	29	1/C9
4.2.1 Equations for bodies with constant a/b cross sections (bodies B_1 and B_2)	31	1/C12
4.2.2 Equations for body with variable a/b cross sections (body B_3)	31	1/C12

Page

4.3 Comparison of Computed With Measured Normal-Force and Normal-Force-Center Characteristics 33 1/C14

4.3.1 Bodies with constant a/b cross sections (bodies B_1 and B_2) . . . 33 1/C14

4.3.2 Body with variable a/b cross sections (body B_3) 33 1/C14

CHAPTER 5. METHOD APPLIED TO BODY-WING AND BODY-WING-TAIL CONFIGURATIONS 35 1/D2

5.1 Configurations Studied and Tests at M_∞ = 0.6 to 2.0 . . . . . 35 1/D2

5.2 Methodology Used to Compute C_N and C_m 36 1/D3

5.3 Comparison of Computed with Measured Normal-Force and Normal-Force-Center Characteristics 39 1/D6

5.3.1 Body-wing configurations 39 1/D6

5.3.2 Body-wing-tail configurations 41 1/D8

CHAPTER 6. VISUAL OBSERVATION OF FLOWS OVER MODELS 43 1/D10

6.1 Models Considered 44 1/D11

6.2 Vapor-Screen and Oil-Flow Techniques 45 1/D12

6.2.1 Vapor-screen technique 45 1/D12

6.2.2 Oil-flow technique 46 1/D13

6.3 Photographs Obtained from Vapor-Screen and Oil-Flow Techniques . . . 47 1/D14

6.3.1 Photographs from vapor-screen technique 47 1/D14

6.3.2 Photographs from oil-flow technique 49 1/E2

CHAPTER 7. EXPERIMENTAL SIDE FORCES ON MODELS AT $\beta = 0°$ . . . 52 1/E5

7.1 Bodies Alone 52 1/E5

7.1.1 Effects of nose fineness ratio and Mach number 52 1/E5

7.1.2 Effect of nose-tip rounding 54 1/E7

7.1.3 Effect of afterbody side strakes 54 1/E7

7.1.4 Effect of elliptic cross section 54 1/E7

7.2 Body-Wing and Body-Wing-Tail Configurations 55 1/E8

7.2.1 Effects of adding a wing and a wing plus tail to a body 55 1/E8

7.2.2 Effects of wing aspect ratio and taper ratio 55 1/E8

CHAPTER 8. CONCLUDING REMARKS 56 1/E9

	Page	
APPENDIX A – DERIVATION OF $(C_n/C_{n_o})_{Newt}$ FOR WINGED-CIRCULAR AND WINGED-ELLIPTIC CROSS SECTIONS	59	1/E12
Winged-Circular Cross Section with Wing Planform Perpendicular to Crossflow Velocity	59	1/E12
Winged-Elliptic Cross Section with Semimajor Axis and Wing Planform Perpendicular to Crossflow Velocity	60	1/E13
Winged-Elliptic Cross Section with Semiminor Axis and Wing Planform Perpendicular to Crossflow Velocity	62	1/F1
APPENDIX B – DERIVATION OF $(C_n/C_{n_o})_{Newt}$ FOR WINGED-SQUARE CROSS SECTIONS WITH ROUNDED CORNERS	64	1/F3
APPENDIX C – FORMULAS TO COMPUTE GEOMETRIC PARAMETERS FOR TANGENT OGIVES	67	1/F6
REFERENCES	68	1/F7
FIGURES	75	1/F14

NOTATION

A	body cross-sectional area
A_b	body base area (at $x = \ell$)
A_p	planform area
A_r	reference area (taken as A_b for the comparisons of computed with experimental results)
A_s	surface wetted area
A_w	exposed wing planform area (2 panels)
a	speed of sound
a,b	semimajor and semiminor axes of elliptic cross section
C_A	axial-force coefficient, $\frac{F_a}{q_\infty A_r}$
C_{d_n}	crossflow drag coefficient of circular cylinder section, $\frac{F_n}{q_n(\Delta\ell_{cy})d_{cy}}$
C_D	drag coefficient, $\frac{\text{drag}}{q_\infty A_r}$
C_L	lift coefficient, $\frac{\text{lift}}{q_\infty A_r}$
C_m	pitching-moment coefficient about station at x_m from nose, $\frac{\text{pitching moment}}{q_\infty A_r X}$
C_N	normal-force coefficient, $\frac{F_n}{q_\infty A_r}$
C_n	local normal-force coefficient per unit length
C_p	pressure coefficient, $\frac{p - p_\infty}{q_\infty}$
C_Y	side-force coefficient, $\frac{F_y}{q_\infty A_r}$
d	body cross-section diameter
f	cross force per unit length along body length
f_p	potential cross force per unit length along body length
f_v	viscous cross force per unit length along body length

F_a, F_n, F_y	axial, normal, and side force
k	corner rounding for body cross section, $\frac{r}{w}$
K_1, K_2	longitudinal and transverse apparent mass coefficients
ℓ	body length
ℓ_A	body aftersection length
ℓ_N	body nose length
M_n	Mach number component normal to body axis, $M_\infty \sin \alpha$
M_∞	free-stream Mach number
p	pressure
p_∞	free-stream static pressure
q_n	dynamic pressure component normal to body axis, $q_\infty \sin^2 \alpha$
q_∞	free-stream dynamic pressure, $\frac{1}{2} \rho V_\infty^2$
r	body cross-section radius or corner radius
r_a	arc radius of ogive
S	displacement of crossflow
s	semispan
t	time
Re	free-stream Reynolds number, $\frac{\rho V_\infty X}{\mu}$
Re_n	Reynolds number component normal to body axis, $Re \frac{d}{X} \sin \alpha$
V	body volume
V_n	velocity component normal to body axis, $V_\infty \sin \alpha$
V_∞	free-stream velocity
w	body width

X	reference length (generally taken as d for the comparisons of computed with experimental results)
x	axial distance from body nose
x_{ac}	axial distance from body nose to aerodynamic normal-force center (center of pressure)
x_c	axial distance from body nose to centroid of body planform area
x_m	axial distance from body nose to pitching-moment reference center
x_{sf}	axial distance from body nose to aerodynamic side-force center
α	angle of attack
β	angle of sideslip
ϵ	wing planform semiapex angle
η	crossflow drag proportionality factor (ratio of crossflow drag for a finite-length cylinder to that for an infinite-length cylinder)
μ	viscosity coefficient of air
ρ	density of air
ϕ	angle of roll about body longitudinal axis

Subscripts

b	body base
cy	cylinder
$Newt$	Newtonian theory
$nose$	body nose
o	equivalent circular body or cross section
SB	slender-body theory
$stag$	stagnation

Item 830-D NAS 1.12:474

OCT 26 1977

NASA TECHNICAL REPORT

NASA TR R-474

COMPLETED
ORIGINAL

NASA TR R-474

PREDICTION OF STATIC AERODYNAMIC CHARACTERISTICS FOR SLENDER BODIES ALONE AND WITH LIFTING SURFACES TO VERY HIGH ANGLES OF ATTACK

Leland Howard Jorgensen

Ames Research Center
Moffett Field, Calif. 94035

NATIONAL AERONAUTICS AND SPACE ADMINISTRATION · WASHINGTON, D. C. · SEPTEMBER 1977

1. Report No.	2. Government Accession No.	3. Recipient's Catalog No.
NASA TR R-474		

4. Title and Subtitle	5. Report Date
PREDICTION OF STATIC AERODYNAMIC CHARACTERISTICS FOR SLENDER BODIES ALONE AND WITH LIFTING SURFACES TO VERY HIGH ANGLES OF ATTACK*	September 1977
	6. Performing Organization Code
7. Author(s)	8. Performing Organization Report No.
Leland Howard Jorgensen	A-6968
	10. Work Unit No.
9. Performing Organization Name and Address	505-06-97
Ames Research Center Moffett Field, California 94035	11. Contract or Grant No.
	13. Type of Report and Period Covered
12. Sponsoring Agency Name and Address	Technical Report
National Aeronautics and Space Administration Washington, D. C. 20546	14. Sponsoring Agency Code

15. Supplementary Notes

*Formerly issued as NASA TM X-73,123 with limited distribution. Reissued for unlimited distribution.

16. Abstract

An engineering-type method is presented for computing normal-force and pitching-moment coefficients for slender bodies of circular and noncircular cross section alone and with lifting surfaces. In this method, a semi-empirical term representing viscous-separation crossflow is added to a term representing potential-theory crossflow.

For many bodies of revolution, computed aerodynamic characteristics are shown to agree with measured results for investigated free-stream Mach numbers from 0.6 to 2.9. The angles of attack extend from 0° to 180° for $M_\infty = 2.9$ and from 0° to 60° for $M_\infty = 0.6$ to 2.0.

For several bodies of elliptic cross section, measured results are also predicted reasonably well over the investigated Mach number range from 0.6 to 2.0 and at angles of attack from 0° to 60°. As for the bodies of revolution, the predictions are best for supersonic Mach numbers.

For body-wing and body-wing-tail configurations with wings of aspect ratios 3 and 4, measured normal-force coefficients and centers are predicted reasonably well at the upper test Mach number of 2.0. However, with a decrease in Mach number to $M_\infty = 0.6$, the agreement for C_N rapidly deteriorates, although the normal-force centers remain in close agreement.

Vapor-screen and oil-flow pictures are shown for many body, body-wing, and body-wing-tail configurations. When separation and vortex patterns are asymmetric, undesirable side forces are measured for the models even at zero sideslip angle. Generally, the side-force coefficients decrease or vanish with the following: increase in Mach number, decrease in nose fineness ratio, change from sharp to blunt nose, and flattening of body cross section (particularly the body nose).

17. Key Words (Suggested by Author(s))		18. Distribution Statement
High angle of attack	Aerodynamic theory	Unlimited
Noncircular bodies	Vapor-screen technique	
Bodies of revolution	Vortex flow	
Wing-body configurations	Oil-flow technique	STAR Category – 02
Wing-body-tail configurations		

19. Security Classif. (of this report)	20. Security Classif. (of this page)	21. No. of Pages	22. Price*
Unclassified	Unclassified	243	$7.50

*For sale by the National Technical Information Service, Springfield, Virginia 22161

To the memory of H. Julian Allen,

a giant in aerodynamic research.

Born: 1 April 1910

Died: 29 January 1977

PREDICTION OF STATIC AERODYNAMIC CHARACTERISTICS FOR SLENDER BODIES ALONE AND WITH LIFTING SURFACES TO VERY HIGH ANGLES OF ATTACK*

Leland Howard Jorgensen

Ames Research Center

SUMMARY

An engineering-type method is presented for computing normal-force and pitching-moment coefficients for slender bodies of circular and noncircular cross section alone and with lifting surfaces. In this method, a semiempirical term representing viscous-separation crossflow is added to a term representing potential-theory crossflow. In computing C_N and C_m for bodies alone, slender-body theory is used for the term representing the potential crossflow. For bodies with thin wings and tails, the linearized potential method of Nielsen, Kaattari, and Pitts, modified for high angles of attack, is used.

For many bodies of revolution, computed aerodynamic characteristics are shown to agree with measured results for investigated free-stream Mach numbers from 0.6 to 2.9. The angles of attack extend from 0° to 180° for $M_\infty = 2.9$ and from 0° to 60° for $M_\infty = 0.6$ to 2.0.

For several bodies of elliptic cross section, measured results are also predicted reasonably well over the investigated Mach number range from 0.6 to 2.0 and at angles of attack from 0° to 60°. As for the bodies of revolution, the predictions are best for supersonic Mach numbers.

For body-wing and body-wing-tail configurations with wings of aspect ratios 3 and 4, measured normal-force coefficients and centers are predicted reasonably well at the upper test Mach number of 2.0. However, with a decrease in Mach number to $M_\infty = 0.6$, the agreement for C_N rapidly deteriorates, although the normal-force centers remain in close agreement.

For $M_\infty = 0.6$, 0.9, and 2.0 and angles of attack of 10°, 20°, 30°, 40°, and 50°, vapor-screen and oil-flow pictures are shown for many body, body-wing, and body-wing-tail configurations. When separation and vortex patterns are asymmetric, undesirable side forces are measured for the models even at zero sideslip angle.

These side forces can be significantly affected by changes in Mach number, nose fineness ratio, nose bluntness, and body cross section. Generally, the side-force coefficients decrease or vanish with the following: increase in Mach number, decrease in nose fineness ratio, change from sharp to blunt nose, and flattening of body cross section (particularly the body nose). Additions of afterbody strakes, wings, or wings plus tail produce much smaller or no appreciable effects.

---

*Formerly issued as NASA TM X-73,123 with limited distribution. Reissued for unlimited distribution.

CHAPTER 1

INTRODUCTION

Over the last several years, high angle-of-attack aerodynamics has increased in importance because of the demand for greater maneuverability of space shuttle vehicles, missiles, and military aircraft (both manned and remotely piloted). Until recently there has been a general lack of analytical methods and aerodynamic data suitable for use in the preliminary design of most advanced configurations for flight to high angles of attack over a wide range of Mach and Reynolds numbers. There has been, however, considerable research leading to the development of methods for predicting the static aerodynamic characteristics of simple shapes, primarily slender bodies of revolution.

Prior to the work of Allen in 1949 (ref. 1), most analytical procedures for computing the aerodynamic characteristics of bodies were based on potential-flow theory, and their usefulness was limited to very low angles of attack. Allen proposed a method for predicting the static longitudinal forces and moments for bodies of revolution inclined to angles of attack considerably higher than those for which theories based only on potential-flow concepts are known to apply. In this method, a crossflow lift attributed to viscous-flow separation is added to the lift predicted by potential theory. This method has been used quite successfully to compute the aerodynamic coefficients of inclined bodies (e.g., refs. 1–6), although most data available for study until 1961 were for bodies at angles of attack below about 20°, and the formulas were initially written to apply only over about this angle-of-attack range.

In 1961, Allen's concept was adapted by Jorgensen and Treon (ref. 7) for computing the normal-force, axial-force, and pitching-moment coefficients for a rocket booster throughout the angle-of-attack range from 0° to 180°. Reasonable agreement of theory with experiment was obtained for a test model of the rocket booster over the Mach number range from 0.6 to 4. The Allen concept was further applied by Saffell, Howard, and Brooks (ref. 8) in 1971 in a computer-programmed method for predicting the static longitudinal aerodynamic characteristics of low aspect-ratio missiles operating at angles up to 180°.

In 1958, a method for computing the aerodynamic characteristics for bodies of noncircular cross section was proposed by Jorgensen (ref. 6). In this method, normal-force and pitching-moment coefficients (C_{N_o} and C_{m_o}) are computed by Allen's formulas for the

equivalent body of revolution which has the same axial distribution of cross-sectional area as the noncircular body. Then the values of C_N and C_m for the noncircular body are computed from C_N/C_{N_o} and C_m/C_{m_o} ratios determined from apparent mass coefficients (i.e., from slender-body theory). Good agreement of theory with experiment (ref. 6) was obtained by this procedure for bodies of elliptic cross section at the conditions investigated (a/b = 1 to 2, $\phi = 0°$ and $90°$, M_∞ = 2 to 4, and $\alpha = 0°$ to $20°$).

Early in 1973, the Allen concept was again applied by Jorgensen (ref. 9) to further develop an engineering-type procedure for computing normal-force, axial-force, and pitching-moment coefficients for slender bodies of circular and noncircular cross sections at $\alpha = 0°$ to $180°$. The C_N and C_m formulas were written, however, for a body whose cross-sectional shape remains constant over the body length, but the cross-sectional area, of course, is allowed to vary.

In 1973, Jorgensen (refs. 10 and 11) rewrote the C_N and C_m expressions to apply for the general case of a slender body alone or with lifting surfaces where the cross-sectional shape, as well as the cross-sectional area, is allowed to vary along the body length. For the special case of winged-elliptic cones, simplified expressions for C_N and C_m were also presented. Good agreement between predicted and experimental results was shown. However, experimental results available for comparison with the method were limited to simple elliptic bodies and winged-elliptic cones at angles of attack less than about $20°$ and Mach numbers only from 2 to 4. Thus, it was concluded that additional comparisons for these and more diverse configurations were needed at higher angles of attack and lower Mach numbers to determine validity limits for the method.

In 1972-73 there was a great need to enlarge the relatively small data base for bodies alone and in combination with wings and tails at subsonic, transonic, and supersonic Mach numbers. This need still exists today, but it has been alleviated significantly by some recent introductory investigations into this high α field (e.g., refs. 12–21). Most studies have been initiated primarily for application to missile aerodynamics. Two recent studies, however, have been more aircraft oriented in that they have been directed toward the determination of experimental aerodynamic characteristics for slender bodies with thin wings (ref. 20) and with wings and a tail (ref. 21). There is still need for study and analysis of much of this recently obtained data both for slender bodies alone and for bodies with wings at very high

angles of attack. As previously mentioned, the Jorgensen method should be further compared with experiment. Also, there is an urgent need for continued study of unwanted side forces and yawing moments which have been shown to develop for models at high α values with $\beta = 0°$. These unwanted side forces and yawing moments, which probably lead to undesirable stall/spin characteristics, have been measured on noses alone, bodies alone, bodies with wings, and bodies with wings and a tail (e.g., refs. 12–21).

In view of the foregoing, the present study was initiated to accomplish the following objectives:

1. Review and extend the derivation of Jorgensen's engineering-type method (refs. 9–11) for computing the normal-force and pitching-moment characteristics of slender circular and noncircular bodies alone and with thin lifting surfaces.

2. Assess the method for predicting the aerodynamic characteristics of missile-like bodies of revolution.

3. Assess the method for predicting the aerodynamic characteristics of bodies of elliptic cross section.

4. Assess the method for predicting the aerodynamic characteristics of bodies with thin wings alone and in combination with a tail.

5. Present and discuss visual observations of the vortex flow fields over models of bodies alone and in combination with wings.

6. Present and discuss data pertaining to the origin and alleviation of undesirable side forces and yawing moments associated with high α flight at $\beta = 0°$.

In connection with objectives (5) and (6), the present study is limited in scope to an experimental study of the vortex flow fields and side forces associated with bodies and body-wing combinations. It is firmly believed that a larger experimental foundation must be acquired at this time to aid in the further development of flow-field modeling techniques that can be applied with confidence in preliminary design studies. This is not to say that important semiempirical modeling techniques have not already been studied. Most of these techniques have been based on an impulsive flow analogy and applied to slender bodies of revolution. In this analogy, it is assumed that the crossflow plane is swept uniformly down the length of an inclined body at the rate $V_\infty \cos \alpha$. Then there is an analogy made between the leeward flow field and the developing wake behind an impulsively started cylinder in

crossflow. This analogy was initially suggested by Allen and Perkins (ref. 2) and applied by Kelly (ref. 22).

The impulsive flow analogy probably has been used most elegantly in recent studies by Wardlaw (refs. 23 and 24). In one of his latest studies (ref. 24), he simulated the viscous crossflow plane by superimposing a large number of point vortices on the potential solution for flow about a cylinder. For some pointed-nose bodies, he has shown qualitative agreement with experimental observations, but even the latest Wardlaw method still must be considered to be in an early exploratory phase. Others have used the impulsive-flow analogy and attempted to model the crossflow field (e.g., refs. 25–32).

Attempts also have been made to solve the crossflow field problem with the Navier-Stokes equations (refs. 33 and 34), but these studies have been applied only to bodies at supersonic speeds and moderate to low angles of attack. Computer times appear to become prohibitive for most practical cases, and turbulence modeling is not yet demonstrated.

Because of many deficiencies in the understanding of the physical flow fields around bodies and wings at very high angles of attack, further experimental investigation is required before much reliability can be realized from further analytic modeling.

CHAPTER 2

DERIVATION OF BASIC METHOD FOR COMPUTING C_N AND C_m CHARACTERISTICS

Here we first review the derivation of some basic equations for computing the normal-force and pitching-moment coefficients, C_N and C_m, for slender bodies of revolution to very high angles of attack (section 2.1). Then we extend the derivation to obtain more general C_N and C_m equations that can be used for slender bodies of circular and noncircular cross section alone and with thin lifting surfaces (section 2.2). Necessary empirical input values of crossflow drag coefficient for circular cylinders are presented in section 2.3, and theoretical formulas to obtain input local normal-force coefficients for noncircular configurations are presented in section 2.4. Finally, in section 2.5, we briefly discuss the relative influence of derived potential-flow and viscous crossflow terms used in the basic equations to compute both C_N and C_m as a function of angle of attack.

2.1 Bodies of Revolution

In 1949, H. J. Allen (ref. 1) proposed a heuristic concept for predicting the static longitudinal forces and moments for bodies of revolution inclined to angles of attack considerably higher than those for which theories based only on potential-flow concepts are known to apply. In this concept, a crossflow lift attributed to viscous crossflow separation is added to the crossflow lift predicted by potential-flow theory. For the potential-flow lift, Allen used the slender-body equation derived in 1923 by Max Munk for airship hulls (ref. 35).

From the momentum consideration, Munk (ref. 35) showed that, for slender (high-fineness-ratio) bodies, the potential-flow cross force per unit length f_p at any station along the body is given by

$$f_p = (K_2 - K_1) q_\infty \sin 2\alpha \frac{dA}{dx} \tag{2.1}$$

where A is the cross-sectional area of the body at any axial distance x from the nose apex; α is the angle of attack; and K_2 and K_1 are, respectively, the transverse and longitudinal apparent mass coefficients for the body. From calculations of K_2 and K_1 made initially by H. Lamb (ref. 36) for ellipsoids of various fineness ratios, Munk (ref. 35) has shown that

$K_2 - K_1$ is approximately unity for high fineness ratios. It has been customary to assume a value of unity for the factor $K_2 - K_1$, and it is assumed in this formulation.

G. N. Ward (ref. 37) has shown that the section cross force f_p at small angles of attack acts at an angle midway between the normal to the axis of revolution of the body and the normal to the free-stream velocity (i.e., at an angle $\alpha/2$). With this consideration, equation (2.1) is multiplied by $\cos(\alpha/2)$ to determine the normal-force distribution. At high α, the potential lift becomes small in comparison with the viscous crossflow lift, and it is of little practical consequence whether this low α multiplier [$\cos(\alpha/2)$] is retained or replaced with unity.

Now consider the derivation of the crossflow lift attributed to viscous crossflow separation. Allen (ref. 1), for a body of revolution of high fineness ratio, first treated each circular cross section as an element of an infinitely long circular cylinder of the same cross-sectional area. With this assumption, the local cross force per unit length due to viscosity is given by

$$f_v = 2rC_{d_n}\frac{\rho V_n^2}{2} \tag{2.2}$$

where r is the body radius at any station x from the nose apex; V_n is the velocity normal to the longitudinal axis; ρ is the mass density; and C_{d_n} is the steady-state crossflow (or normal) drag coefficient based on q_n, diameter, and unit length at station x. C_{d_n} is a function of both the Mach number and Reynolds number components normal to the cylinder longitudinal axis. Hence, for a body at angle of attack, C_{d_n} is a function of

$$M_n = \frac{V_n}{a} = M_\infty \sin\alpha \tag{2.3}$$

and

$$Re_n = Re \sin\alpha \tag{2.4}$$

where

$$V_n = V_\infty \sin\alpha \tag{2.5}$$

Here M_∞, Re, and V_∞ are free-stream values, respectively, of Mach number, Reynolds number, and velocity; the speed of sound is denoted by a.

For this study, C_{d_n} is taken as the steady-state crossflow drag coefficient for a circular cylinder. Other researchers (e.g., refs. 22–32) have assumed that the development of the crossflow with distance along an inclined body of uniform diameter is analogous to the development with time of the flow on a cylinder impulsively set in motion from rest. In this analogy, it is assumed that the crossflow plane is swept uniformly down the length of an inclined body at the rate $V_\infty \cos \alpha$. When this analogy is assumed, the value of C_{d_n} starts from zero (at zero time), then increases to a maximum value about 25 percent higher than the steady-state value, then decreases to the steady-state value for laminar flow (see, e.g., sketch (a) from ref. 27). For turbulent flow, experiments conducted by Sarpkaya (ref. 27) indicate that the steady-state condition is reached almost at the start of the motion. Thus, for turbulent flow, both the steady-state assumption and the impulsive-flow assumption give the same result. However, for laminar flow there is a difference, but this difference is not studied in this report.

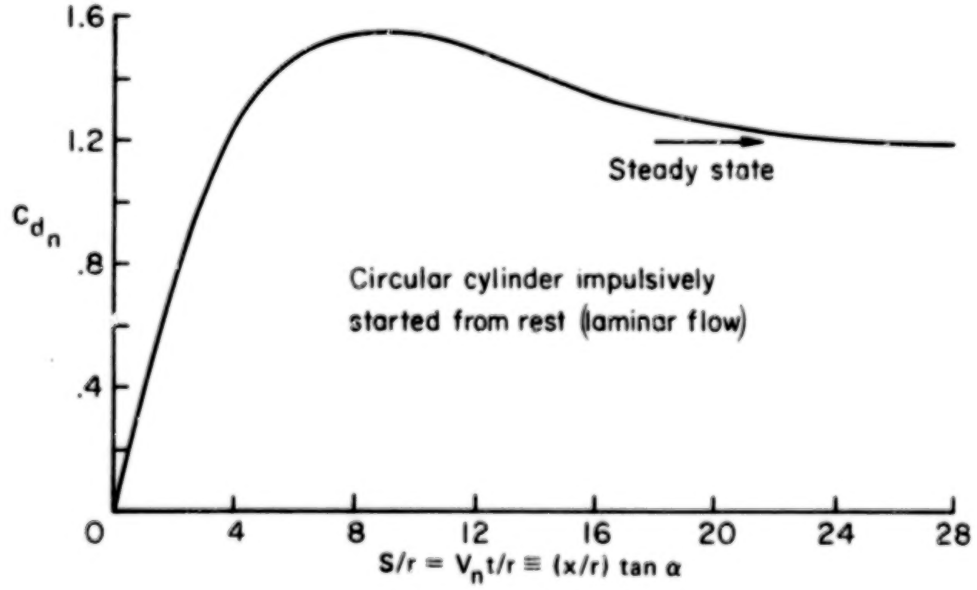

Sketch (a)

Because of spillage flow around the ends of a finite length cylinder, the value of C_{d_n} is less than that for an infinitely long (truly two-dimensional) cylinder in the same free stream. Equation (2.2) should be multiplied by a proportionality factor η, which is the ratio of C_{d_n} for a finite length cylinder to that for an infinite length cylinder. This factor η, which approaches unity as the cylinder length to diameter approaches infinity, is given from experimental results (discussed later). In the practical use of η, it is assumed that the ℓ/d of

the cylinder is the same as that for the body of revolution being considered. It is also assumed that the net-force effect of the front and rear end flows is approximately the same for both configurations. Thus, equation (2.2) is modified to give

$$f_v = 2\eta r C_{d_n} q_\infty \sin^2 \alpha \tag{2.6}$$

where

$$q_\infty = \frac{1}{2}\rho V_\infty^2 = \frac{1}{2}\rho V_n^2 \frac{1}{\sin^2 \alpha} = \frac{q_n}{\sin^2 \alpha} \tag{2.7}$$

Following Allen (ref. 1), the potential-flow solution of Munk and the viscous crossflow solution are combined to determine the cross-force distribution along the body of revolution. With the potential cross force per unit length acting at $\alpha/2$ from the normal to the free-stream direction and the viscous cross force per unit length acting normal to the longitudinal axis, the total cross force per unit length normal to the longitudinal axis is given by

$$f = f_p \cos \frac{\alpha}{2} + f_v \tag{2.8}$$

or

$$\frac{f}{q_\infty} = \sin 2\alpha \cos \frac{\alpha}{2} \frac{dA}{dx} + 2\eta C_{d_n} (\sin^2 \alpha) r \tag{2.9}$$

From equation (2.9), the equations for the normal-force and pitching-moment coefficients for bodies of revolution can be easily derived. With the normal force given by $F_n = \int_0^\ell f \, dx$ and the normal-force coefficient defined by $C_N = (F_n/q_\infty A_r)$, we obtain

$$C_N = \frac{\sin 2\alpha \cos (\alpha/2)}{A_r} \int_0^\ell \frac{dA}{dx} dx + \frac{2\eta C_{d_n} \sin^2 \alpha}{A_r} \int_0^\ell r \, dx \tag{2.10}$$

Likewise, with the pitching-moment coefficient defined by

$$C_m = \frac{\text{pitching moment}}{q_\infty A_r X} = \frac{\int_0^\ell f(x_m - x)dx}{q_\infty A_r X},$$

we obtain

$$C_m = \frac{\sin 2\alpha \cos (\alpha/2)}{A_r X} \int_0^\ell \frac{dA}{dx} (x_m - x)dx + \frac{2\eta C_{d_n} \sin^2 \alpha}{A_r X} \int_0^\ell r(x_m - x)dx \tag{2.11}$$

where A_r is the reference area; X is the reference length; ℓ is the body length; and x_m is the axial distance from the nose to the pitching-moment reference center.

General integrated expressions for bodies of revolution at $\alpha = 0°$ to $180°$ can be obtained from equations (2.10) and (2.11). For the sign convention in sketch (b), Jorgensen (ref. 9) has written the following equations for the normal-force and pitching-moment coefficients:

$$C_N = \frac{A_b}{A_r} \sin 2\alpha' \cos \frac{\alpha'}{2} + \eta C_{d_n} \frac{A_p}{A_r} \sin^2 \alpha' \; ; \quad 0° \leq \alpha \leq 180° \tag{2.12}$$

$$C_m = \left[\frac{V - A_b(\ell - x_m)}{A_r X}\right] \sin 2\alpha' \cos \frac{\alpha'}{2} + \eta C_{d_n} \frac{A_p}{A_r} \left(\frac{x_m - x_c}{X}\right) \sin^2 \alpha' \; ;$$

$$0° \leq \alpha \leq 90° \tag{2.13}$$

and

$$C_m = -\left(\frac{V - A_b x_m}{A_r X}\right) \sin 2\alpha' \cos \frac{\alpha'}{2} + \eta C_{d_n} \frac{A_p}{A_r} \left(\frac{x_m - x_c}{X}\right) \sin^2 \alpha' \; ;$$

$$90° \leq \alpha \leq 180° \tag{2.14}$$

where A_b is the body base area; A_p is the planform area; V is the body volume; x_c is the distance from the nose apex to the centroid of planform area; and $\alpha' = \alpha$ for $0° \leq \alpha \leq 90°$ and $\alpha' = 180° - \alpha$ for $90° \leq \alpha \leq 180°$.

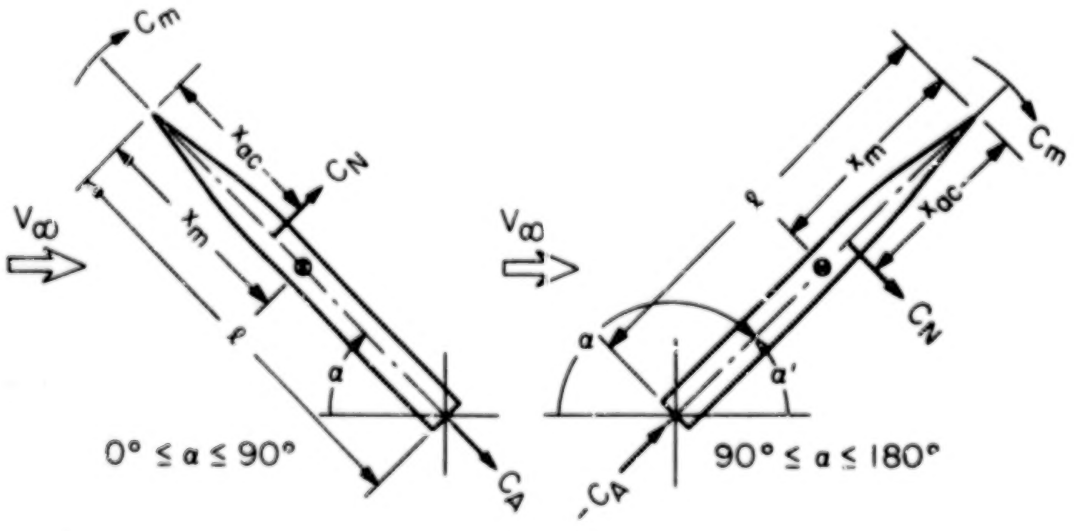

Sketch (b)

The axial distance from the nose apex to the aerodynamic force center is then given by

$$x_{ac} = \left(\frac{x_m}{X} - \frac{C_m}{C_N}\right) X \tag{2.15}$$

When lift and drag coefficients are desired, they may be obtained at all α values from the conversion expressions:

$$C_L = C_N \cos \alpha - C_A \sin \alpha \tag{2.16}$$

$$C_D = C_N \sin \alpha + C_A \cos \alpha \tag{2.17}$$

Generally, it can be shown that for values of α well removed from $\alpha = 0°$ and $180°$ precise prediction of C_A is not necessary to obtain reasonably accurate values of C_L and C_D.

Jorgensen (ref. 9) has suggested that, for rough engineering estimates, the axial-force coefficients for slender bodies can be approximated by

$$C_A \approx C_{A_{\alpha=0°}} \cos^2 \alpha \; ; \quad 0° \leqslant \alpha \leqslant 90° \tag{2.18}$$

and

$$C_A \approx C_{A_{\alpha=180°}} \cos^2 \alpha \; ; \quad 90° \leqslant \alpha \leqslant 180° \tag{2.19}$$

Here $\cos^2 \alpha$ is merely the ratio of the dynamic pressure in the axial direction to the dynamic pressure in the free-stream direction. A more precise method is also outlined in reference 9, along with procedures for determining $C_{A_{\alpha=0°}}$ and $C_{A_{\alpha=180°}}$ for often used conical and tangent ogive noses and flat bases.

2.2 Bodies of Circular and Noncircular Cross Section Alone and With Lifting Surfaces

For the general case of a body alone or with lifting surfaces where the cross-sectional shape can vary along the body length, procedures similar to those used for a body of revolution are assumed. Both the potential and viscous separation crossflow terms in equations (2.10) and (2.11) for C_N and C_m are generalized further.

The potential crossflow term is generalized by multiplying the value inside the integral by the ratio $(C_n/C_{n_o})_{SB}$ – the ratio of the local normal-force coefficient per unit length C_n for the desired cross-sectional shape to the similar coefficient C_{n_o} for the equivalent circular

shape having the same cross-sectional area. The necessary ratios can be determined from apparent mass coefficients (slender-body theory) for many cross-sectional shapes. In 1958, this procedure was first shown (ref. 6) to have merit in predicting experimental C_N and C_m results for slender bodies of various cross sections at supersonic speeds and angles of attack up to about 20°. However, because of very limited experimental data, further evaluation was not possible at that time.

The viscous crossflow terms in equations (2.10) and (2.11) are further generalized by multiplying the values within the integrals by $(C_n/C_{n_o})_{Newt}$. Here the local ratio of C_n to C_{n_o} at each x station is assumed to be given by Newtonian impact theory. C_{d_n} remains as the crossflow drag coefficient for the equivalent circular cylinder section.

With equations (2.10) and (2.11) generalized as discussed, and for positive dA/dx values,

$$C_N = \frac{\sin 2\alpha \cos(\alpha/2)}{A_r} \int_0^{\ell} \left(\frac{C_n}{C_{n_o}}\right)_{SB} \frac{dA}{dx}\, dx + \frac{2\eta C_{d_n} \sin^2 \alpha}{A_r} \int_0^{\ell} \left(\frac{C_n}{C_{n_o}}\right)_{Newt} r\, dx \tag{2.20}$$

and

$$C_m = \frac{\sin 2\alpha \cos(\alpha/2)}{A_r X} \int_0^{\ell} \left(\frac{C_n}{C_{n_o}}\right)_{SB} \frac{dA}{dx}\, (x_m - x)dx + \frac{2\eta C_{d_n} \sin^2 \alpha}{A_r X} \int_0^{\ell} \left(\frac{C_n}{C_{n_o}}\right)_{Newt} r(x_m - x)dx \tag{2.21}$$

In equations (2.20) and (2.21), the first terms (from slender-body theory) are not applicable as written for winged-body sections where the dA/dx values are zero or negative, and procedures similar to those suggested in reference 38 probably should be used. Further adaptation of this method for use with body-wing and body-wing-tail configurations is considered in chapter 5.

In the second term of equations (2.20) and (2.21), there is some experimental justification for formulating the ratio (C_n/C_{n_o}) from Newtonian theory and multiplying it by the available experimental or theoretical crossflow drag coefficient for the equivalent circular cross section C_{d_n}. For subcritical crossflow Mach and Reynolds numbers, Jorgensen

(ref. 11) has shown that C_n/C_{n_o} values from Newtonian theory agree reasonably well (but somewhat fortuitously) with those from two-dimensional tests (refs. 39–43) of elliptic cross sections and square cross sections with rounded corners. Jorgensen's comparisons are shown in table 1. Good agreement also can be expected at high supersonic and hypersonic crossflow Mach numbers where Newtonian theory by definition should be most applicable. The most doubtful regimes include the transonic crossflow Mach number regime and the supercritical Reynolds number regime. (These regimes are discussed further for circular cross sections in the following section.)

Where reliable experimental crossflow drag data exist for a desired noncircular cross section, these data, of course, can be used. Then the values of C_{d_n} for the particular cross sections can be substituted in equations (2.20) and (2.21) in lieu of the product $C_{d_n}(C_n/C_{n_o})_{Newt}$, where C_{d_n} as now written is for a circular cross section only. Of course, if the shape of the noncircular cross section varies along the body length, values of C_{d_n} must be substituted within the integral in the second term of equations (2.20) and (2.21), and a great deal of empirical input data may be necessary for some configurations.

TABLE 1.– C_{d_n} AND C_n/C_{n_o} VALUES FOR TWO-DIMENSIONAL CYLINDERS OF VARIOUS CROSS SECTIONS AT $\alpha = 90°$ AS COMPUTED BY NEWTONIAN THEORIES AND MEASURED AT SUBCRITICAL MACH AND REYNOLDS NUMBERS

CROSS SECTION	NEWTONIAN THEORY		MOD. NEWT. THEORY FOR $C_{p_{stag}} = 1.8$		MEASURED		
	C_{d_n}	C_n/C_{n_o}	C_{d_n}	C_n/C_{n_o}	C_{d_n}	C_n/C_{n_o}	REF.
● ○	1.33	1.00	1.20	1.00	1.20	1.00	39
● ⬭ a/b = 2	0.94	0.50	0.85	0.50	0.70	0.41	40,41
a/b = 4	0.59	0.22	0.53	0.22	0.35	0.15	40
● ⬭ a/b = 2	1.65	1.75	1.49	1.75	1.60	1.89	41,42
● r = kw, k = 0.0	2.00	1.33	1.80	1.33	2.05	1.51	40
k = 0.02	1.97	1.33	1.78	1.33	2.00	1.48	41
k = 0.08	1.89	1.26	1.70	1.26	1.65	1.22	43
k = 0.24	1.68	1.14	1.51	1.14	1.12	0.85	43
k = 0.50	1.33	1.00	1.20	1.00	1.20	1.00	39

NOTE: ALL C_{d_n}'s IN TABLE ARE BASED ON WIDTH OF CROSS SECTION, NOT EQUIVALENT d.

2.3 Empirical Input Values

2.3.1 *Crossflow drag coefficient*– To compute C_N and C_m for the equations derived in the previous section, values of crossflow drag coefficient C_{d_n} are needed for an "infinite length" or truly two-dimensional circular cylinder placed normal to an airstream. As previously mentioned, C_{d_n} is a function of both the Mach number and Reynolds number components normal to the cylinder longitudinal axis, and hence for a configuration at angle of attack it is a function of $M_n = M_\infty \sin \alpha$ and $Re_n = Re \sin \alpha$. In these simple relations, introduced previously as equations (2.3) and (2.4), M_n is commonly called the crossflow Mach number and Re_n, the crossflow Reynolds number. For circular cylinders, necessary "state-of-the-knowledge" plots have been prepared for the variation of C_{d_n} with M_n and Re_n (figs. 1-3).

Figure 1 shows the variation of C_{d_n} with M_n over the M_n range from 0 to 8. It was prepared from the data of references 44 through 49 and from data obtained recently by John M. Macha in the Ames 2- by 2-Foot Transonic Wind Tunnel. Also shown for reference are the theoretical variations predicted from Newtonian and modified Newtonian theories. Because of the close agreement of the Newtonian values with experiment at the higher Mach numbers, it is not surprising that computer programs utilizing Newtonian theories have been used successfully to predict space-shuttle-booster results in wind tunnels at hypersonic Mach numbers (see, e.g., ref. 50). Except for the transonic range, where data are very limited, the variation of C_{d_n} with M_n is well documented in figure 1.

In the transonic range, the black symbols in figure 1 represent values of C_{d_n} obtained recently from pressure-distribution tests of circular cylinders of various diameters (1.9 to 5.1 cm) at crossflow Reynolds numbers from about 1.3×10^5 to 4.9×10^5. Many values of C_{d_n} were initially computed from the extensive pressure distributions measured by Macha on the cylinders in the Ames 2- by 2-Foot Transonic Wind Tunnel. Because there was a general increase in C_{d_n} with decrease in cylinder diameter d (but not Re_n) for M_n values from about 0.9 to 1.2, plots of C_{d_n} vs. d were constructed, and values of C_{d_n} were obtained by extrapolating the curves to $d = 0$. The black symbols in figure 1 represent these extrapolated values of C_{d_n}, values that should come closest to representing data for no interference between the models and the wind tunnel. These data agree well with the rocket

flight-test results obtained in 1953 by Welsh (ref. 49), but these or similar-sized models should be tested further in a larger transonic wind tunnel.

As shown in figure 1, there is a critical crossflow Reynolds number effect that can drastically lower the values of C_{d_n} at M_n below about 0.5. For M_n less than about 0.5, if the crossflow Reynolds number Re_n exceeds the critical value of about 2×10^5, the value of C_{d_n} decreases considerably. This variation is shown in greater detail in figures 2 and 3.

Figure 2 gives the variation of C_{d_n} with Re_n for M_n less than about 0.4. It has been well documented over the last 60 years (e.g., refs. 39, 43, 45, 51) that $C_{d_n} \cong 1.2$ for laminar boundary-layer flow and separation just before the critical Reynolds number of about $Re_n = 2\times10^5$. At about $Re_n = 5\times10^5$ there is evidence (e.g., refs. 52-54) of laminar boundary-layer flow around the front of the cylinder to an angular position of about 80° or 90°, where the flow separates, undergoes transition, and reattaches at an angular position of about 110° to form a laminar separation bubble. Then the turbulent flow separates at some position downstream (an angular location of about 130°). With a further increase in Reynolds number into the supercritical regime, the bubble decreases in size until the transition to turbulent flow moves upstream of the location of laminar separation, and the bubble disappears (ref. 54). From the low C_{d_n} value between about 0.15 and 0.30, C_{d_n} increases gradually, at least for an increase in Re_n up to about 5×10^6. The supercritical Reynolds number regime has only been investigated recently in any detail (refs. 43 and 52-54), and there is still considerable uncertainty in the magnitude and trend of C_{d_n} with Re_n and M_n. The shading in figure 2 indicates the approximate spread or uncertainty in C_{d_n} based on known data.

Jones, Cincotta, and Walker (ref. 54) probably have made the most detailed study of circular cylinders in supercritical flow. With the use of freon gas to obtain high Re_n, they have shown that there is an effect of M_n on the variation of C_{d_n} with Re_n. Figure 3 (taken from ref. 54) summarizes their C_{d_n} results for $M_n = 0.25$ to 0.50. The reader is referred to reference 54 for their interpretation of these C_{d_n} results based on pressure-distribution and visual-flow studies.

For noncircular bodies, as mentioned in section 2.2, experimental values of C_{d_n} for noncircular instead of circular cross sections can be used with slight modification to equations (2.20) and (2.21). These data are generally not available for crossflow Mach numbers

above critical. However, some data are available for subcritical crossflow Mach numbers, and these data should be used if the crossflow Reynolds number Re_n exceeds the critical value (the Re_n where C_{d_n} drops rather drastically with a slight increase in Re_n). In table 2 some

TABLE 2.– REFERENCES FROM WHICH EXPERIMENTAL VALUES OF C_{d_n} VS Re_n CAN BE OBTAINED FOR VARIOUS CROSS SECTIONS AND FLOW DIRECTIONS

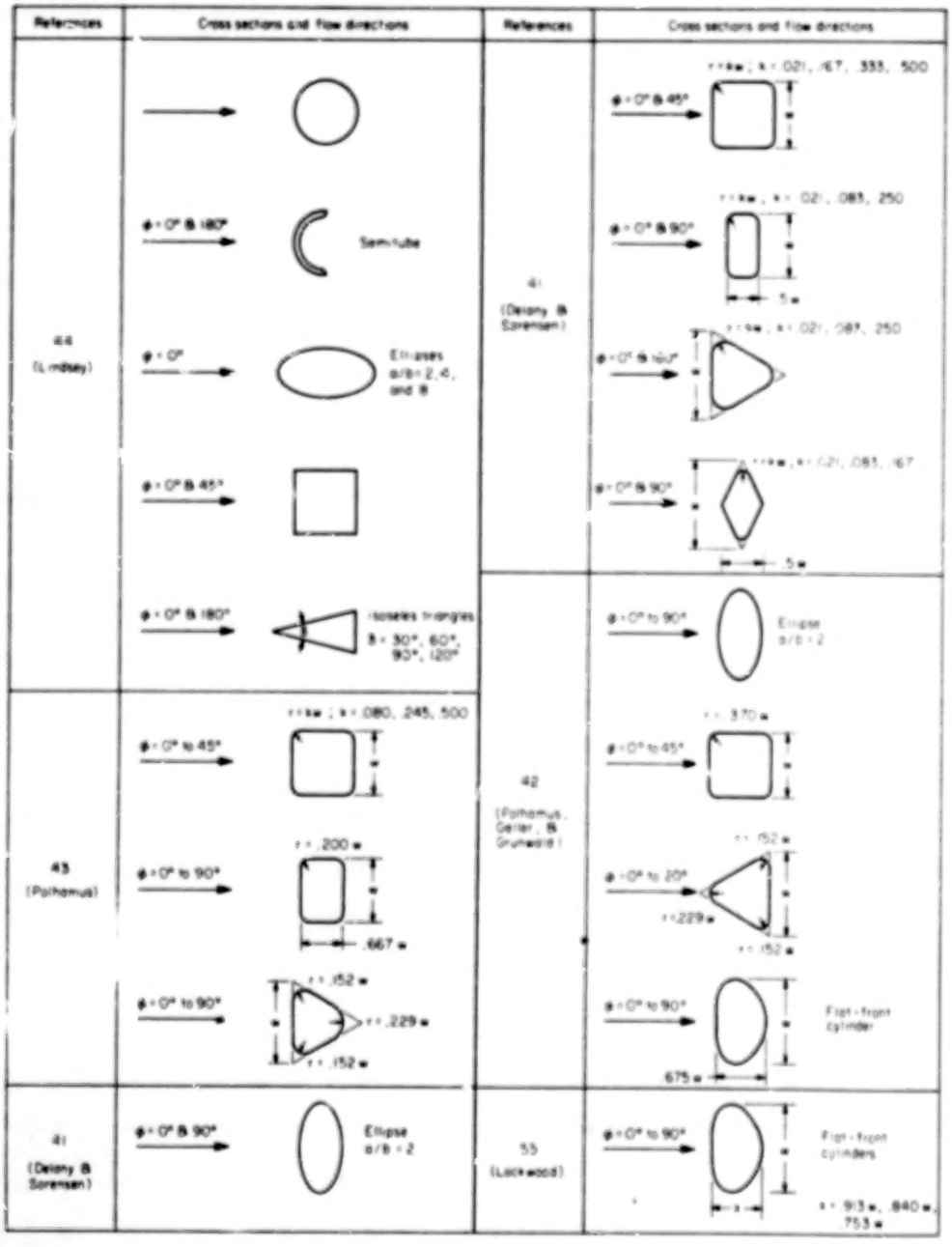

references are listed from which experimental values of C_{d_n} versus Re_n can be obtained for various cross sections and flow directions. It should be noted that most experimental values of C_{d_n} are based on cross-sectional width w and must be multiplied by w/d, where d is the diameter of the equivalent circular cross section.

2.3.2 *Crossflow drag proportionality factor*– In the equations used to compute C_N and C_m, η is the crossflow drag proportionality factor, that is, the ratio of the crossflow drag coefficient for a finite-length cylinder to that for an infinite-length cylinder. Cylinder drag coefficients from which values of η can be determined have been measured (to the author's knowledge) only at very low subsonic Mach numbers (refs. 56 and 57).

Values of η for circular cylinders at very low crossflow Mach numbers (from ref. 56) are plotted as a function of length/diameter ratio in figure 4. Values of η for flat plates are also plotted, but as a function of plate length/width ratio. The values for the flat plates are only slightly less than those for the circular cylinders. Thus, it is likely that figure 4 can be used to estimate values of η for many cross sections varying from circular to flat. However, these values may be acceptable only for very low crossflow Mach numbers.

An indication of the variation of η with crossflow Mach number M_n can be obtained by computing values of η from high-α C_N data (ref. 16) for slender bodies of revolution. From equation (2.12),

$$\eta C_{d_n} = \frac{C_N - \sin 2\alpha \cos(\alpha/2)\,(A_b/A_r)}{(A_p/A_r)\sin^2\alpha} \tag{2.22}$$

For two bodies of fineness ratio 10 and 12 (sketched in fig. 5), the variation of ηC_{d_n} with M_n (for M_n = 0.4 to 1.6) has been computed from equation (2.22) with the use of C_N data for values of α from about 45° to 60°. As shown in figure 5, the results for the two bodies agree closely. Now with the variation of C_{d_n} with M_n in figure 1 and the variation of ηC_{d_n} with M_n in figure 5, the variation of η with M_n has been computed and the results plotted in figure 6. (The circular symbols denote the computed values over the M_n range from 0.4 to 1.6; the square and diamond symbols represent values of η for very low crossflow Mach numbers obtained from fig. 4)

For most supersonic and hypersonic values of M_n, η probably can be assumed to be unity, an assumption indicated as being essentially correct from past investigations (e.g.,

refs. 3, 6, 7, and 9). The greatest uncertainty appears to be within the transonic M_n range, and here further research is desirable. In this study, however, figures 5 and 6 are used in lieu of better information.

2.4 Formulas and Values of $(C_n/C_{n_o})_{SB}$ and $(C_n/C_{n_o})_{Newt}$ for Various Cross Sections

To use equations (2.20) and (2.21) for computing C_N and C_m, ratios of the section normal-force coefficients (C_n) to those for the equivalent circular sections (C_{n_o}) must be determined. The ratios $(C_n/C_{n_o})_{SB}$ from slender-body theory are used in the first term of each equation, and the ratios $(C_n/C_{n_o})_{Newt}$ from Newtonian theory are used in the second term.

Formulas of $(C_n/C_{n_o})_{SB}$ and $(C_n/C_{n_o})_{Newt}$ are now presented for some of the more general cross sections encountered in missile and aircraft aerodynamics. Then, for several sample cross sections, values of $(C_n/C_{n_o})_{SB}$ and $(C_n/C_{n_o})_{Newt}$ are plotted and compared.

2.4.1 *Formulas of* $(C_n/C_{n_o})_{SB}$ – From slender-body theory (e.g., refs. 58–61), the ratio of C_n for a winged-body cross section to that for the equivalent (same area) circular-body cross section can be determined for many cross-sectional shapes. In ref. 11, $(C_n/C_{n_o})_{SB}$ expressions are determined for winged-circular and winged-elliptic cross sections (see sketches (c), (d), and (e)).

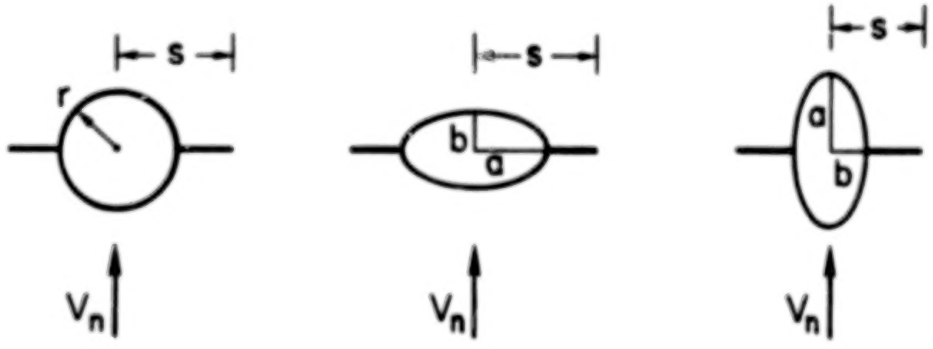

(c) (d) (e)

Sketches (c), (d), and (e)

For a winged-circular cross section with the wing planform perpendicular to the cross-flow velocity V_n (sketch (c)),

$$\left(\frac{C_n}{C_{n_o}}\right)_{SB} = \frac{s^2}{r^2} + \frac{r^2}{s^2} - 1 \tag{2.23}$$

For a winged-elliptic cross section with the semimajor axis a and wing planform perpendicular to the crossflow velocity V_n (sketch (d)),

$$\left(\frac{C_n}{C_{n_O}}\right)_{SB} = \frac{1}{ab}\,(k_1^2 + a^2) \tag{2.24}$$

where

$$k_1 = \sigma_1 - \frac{(a+b)^2}{4\sigma_1}$$

$$\sigma_1 = \frac{1}{2}\left(s + \sqrt{s^2 + b^2 - a^2}\right)$$

For a winged-elliptic cross section with the semiminor axis b and wing planform perpendicular to the crossflow velocity V_n (sketch (e)),

$$\left(\frac{C_n}{C_{n_O}}\right)_{SB} = \frac{1}{ab}\,(k_2^2 + b^2) \tag{2.25}$$

where

$$k_2 = \sigma_2 - \frac{(a+b)^2}{4\sigma_2}$$

$$\sigma_2 = \frac{1}{2}\left(s + \sqrt{s^2 + a^2 - b^2}\right)$$

For an elliptic cross section without a wing (e.g., ref. 37),

$$\left(\frac{C_n}{C_{n_O}}\right)_{SB} = \frac{a}{b}\cos^2\phi + \frac{b}{a}\sin^2\phi \tag{2.26}$$

where ϕ is the angle of roll about the body longitudinal axis, being 0° with the semimajor axis a perpendicular to the crossflow velocity and 90° with the semiminor axis b perpendicular to the crossflow velocity (see sketches (d) and (e)).

2.4.2 *Formulas of* $(C_n/C_{n_O})_{Newt}$ – From Newtonian impact theory, $(C_n/C_{n_O})_{Newt}$ expressions also have been derived for winged-circular and winged-elliptic cross sections (see appendix A).

For a winged-circular cross section with the wing planform perpendicular to the crossflow velocity V_n (sketch (c)), we obtain, from equation (A10),

$$\left(\frac{C_n}{C_{n_o}}\right)_{Newt} = \frac{3}{2}\left(\frac{s}{r} - \frac{1}{3}\right) \tag{2.27}$$

For a winged-elliptic cross section with the semimajor axis a and wing planform perpendicular to the crossflow velocity V_n (sketch (d)), we obtain, from equation (A16),

$$\left(\frac{C_n}{C_{n_o}}\right)_{Newt} = \frac{3}{2}\sqrt{\frac{a}{b}}\left\{\frac{-b^2/a^2}{[1-(b^2/a^2)]^{3/2}}\log\left[\frac{a}{b}\left(1+\sqrt{1-\frac{b^2}{a^2}}\right)\right]+\frac{1}{1-(b^2/a^2)}+\frac{s}{a}-1\right\} \tag{2.28}$$

For a winged-elliptic cross section with the semiminor axis b and wing planform perpendicular to the crossflow velocity V_n (sketch (e)), we obtain, from equation (A21),

$$\left(\frac{C_n}{C_{n_o}}\right)_{Newt} = \frac{3}{2}\sqrt{\frac{b}{a}}\left\{\frac{a^2/b^2}{[(a^2/b^2)-1]^{3/2}}\tan^{-1}\left(\sqrt{\frac{a^2}{b^2}-1}\right)-\frac{1}{(a^2/b^2)-1}+\frac{s}{b}-1\right\} \tag{2.29}$$

From Newtonian impact theory, an expression for $(C_n/C_{n_o})_{Newt}$ also has been derived for winged-square cross sections with rounded corners (sketch (f)). From equation (B15),

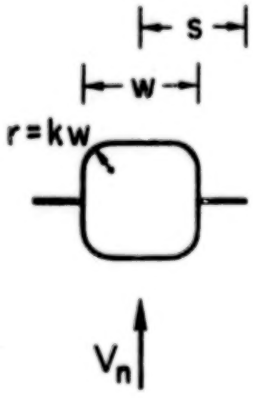

$$\left(\frac{C_n}{C_{n_o}}\right)_{Newt} = \frac{3}{2}\left(\frac{s}{w} - \frac{k}{3}\right)\sqrt{\frac{\pi}{1-(4-\pi)k^2}}\,; \quad 0 \leqslant k \leqslant 0.5 \tag{2.30}$$

where the equivalent diameter (from eq. (B12)) is

$$d = 2w\sqrt{\frac{1-(4-\pi)k^2}{\pi}} \tag{2.31}$$

Sketch (f)

2.4.3 *Values of* $(C_n/C_{n_o})_{SB}$ *and* $(C_n/C_{n_o})_{Newt}$ – From equations (2.23) through (2.29), values of $(C_n/C_{n_o})_{SB}$ and $(C_n/C_{n_o})_{Newt}$ were computed for circular and elliptic cross sections alone and with wings. The results are plotted and compared in figures 7 through 10.

In figure 7, the variation of (C_n/C_{n_o}) with axis ratio a/b is given for an elliptic cross section without wings. As previously noted in reference 9, values of (C_n/C_{n_o}) from

slender-body theory are reasonably close to those from Newtonian theory for many a/b values of interest.

In figure 8, the variation of (C_n/C_{n_o}) with the ratio of wing semispan s to body radius r is given for a winged-circular cross section. For $s/r < 2$, the values from both theories are reasonably close, but with further increase in s/r, the values of $(C_n/C_{n_o})_{SB}$ greatly exceed those of $(C_n/C_{n_o})_{Newt}$.

In figure 9, values of (C_n/C_{n_o}) are presented for a winged-elliptic cross section with the semimajor axis a perpendicular to the crossflow velocity V_n. For the axis ratios of $a/b = 2$ and 3, the figure gives the variation of (C_n/C_{n_o}) with the ratio of semispan s to semimajor axis a. As either a/b or s/a increases, the disagreement between the results from the theories increases.

In figure 10, values of (C_n/C_{n_o}) are presented for a winged-elliptic cross section with the semiminor axis b perpendicular to the crossflow velocity V_n. For axis ratios of $a/b = 2$ and 3, the variation of (C_n/C_{n_o}) with s/b is given. There is closer agreement between the values computed from the two theories for this cross-sectional arrangement than for the arrangement where the semimajor axis and wing are perpendicular to V_n.

Table 3, taken from reference 9, shows the variation of $(C_n/C_{n_o})_{Newt}$ with corner rounding k for square cross sections. The values of C_n/C_{n_o} computed from slender-body theory are reasonably close to those computed from Newtonian theory (eq. (2.30)).

TABLE 3.-- C_n/C_{n_o} FROM NEWTONIAN THEORY FOR SQUARE CROSS SECTIONS WITH ROUNDED CORNERS

k	0	0.05	0.1	0.2	0.3	0.4	0.5
C_n/C_{n_o}	1.33	1.29	1.25	1.17	1.11	1.05	1.00

Corresponding values from slender-body theory vary from 1.19 at $k = 0$ (no corner radius) to 1.00 at $k = 0.5$ (completely circular cross section).

2.5 Relative Influence of Crossflow Terms

It is interesting to examine briefly the relative influence of the potential and viscous crossflow terms in the equations for C_N and C_m. For demonstration, Jorgensen (ref. 9)

compared the magnitudes of the terms for an ogive-cylinder body of fineness ratio 11 ($\ell_N/d = 5$) at $\alpha = 0°$ to 180° and $M_\infty = 2.9$. The computed values (by eqs. (2.12) to (2.14)) are presented in figure 11. For this body, the viscous crossflow term contributes most of the normal force at high values of α and, of course, all of the normal force at $\alpha = 90°$. Although the slender-body potential term contributes relatively little to C_N at high α, it has a significant influence on C_m.

The results in figure 11 are indicative of those computed for most slender bodies (ref. 9). However, as shown in chapter 5, the relative contributions of the crossflow terms can be modified considerably with the addition of thin lifting surfaces (wings and tails) to a body.

CHAPTER 3

METHOD APPLIED TO BODIES OF REVOLUTION

In recent years, there has been increased interest in the basic aerodynamics of slender bodies of revolution because of emphasis on achieving more maneuverability from missiles. Some designs that use thrust-vector control systems are being considered for missile flight at angles of attack ranging from 0° to 180° (e.g., refs. 13, 15, and 62). We will now assess the prediction method of chapter 2 by comparing predicted with measured longitudinal aerodynamic coefficients for various bodies of revolution.

3.1 Cone-Cylinder and Ogive-Cylinder Bodies at $M_\infty = 2.9$

We will compare predicted longitudinal aerodynamic coefficients with those measured by Jernell (ref. 63) for a series of three cone-cylinder and four ogive-cylinder bodies at $\alpha = -5°$ to 180°. The free-stream Mach number is about 2.9 (Jernell quotes 2.86), and the Reynolds number based on body diameter is about 1.25×10^5. The bodies with various nose and aftersection fineness ratios were tested in the NASA-Langley Unitary Plan Wind Tunnel.

Figure 12 shows the seven bodies considered along with values of the geometric parameters required to compute the aerodynamic characteristics. For the cone-cylinder bodies (numbers 1-3), all of the geometric parameters are easily computed, but for the bodies with tangent ogive noses (numbers 4-7) the required values of A_p/d^2, V/d^3, x_c/d, and A_s/d^2 are not so easily obtained. Some convenient formulas (from ref. 9) for computing these parameters for tangent ogives are given in appendix C.

Equations (2.12) to (2.15), (2.18), and (2.19), along with the procedure outlined in chapter 2, have been used to compute the variation of C_N, C_A, C_m and x_{ac}/ℓ with α for the seven bodies considered. The values of $C_{A_{\alpha=0°}}$ and $C_{A_{\alpha=180°}}$ used in equations (2.18) and (2.19) were computed in reference 9 with the assumption of turbulent boundary-layer flow. (Jernell (ref. 63) states that "boundary-layer transition was effected" by artificial trips throughout the α range.) The values include the contributions of fore pressure, base pressure, and the turbulent skin friction. The reader who wishes to make similar calculations is referred to reference 9. No attempt was made to estimate effects of wind-tunnel support interference.

In figures 13 to 16, computed values of C_N, C_A, and C_m as a function of α are compared with the experimental results for the seven bodies. Generally, there is close agreement of the computed with the measured results, especially in the variation of C_N and C_m with α. As expected, because of the approximation formulas used to predict C_A with α, the poorest agreement is between the predicted and measured values of C_A.

It is satisfying to find that effects of afterbody fineness ratio, nose fineness ratio, and nose shape on C_N and C_m are predicted so well. Generally the magnitudes of C_N and C_m increase with an increase in fineness ratio, just as the computed results predict. Figure 13 shows the effect of afterbody fineness ratio for cone-cylinder bodies, all with fineness-ratio-3 conical noses. Likewise, figure 14 shows the effect of afterbody fineness ratio for ogive-cylinder bodies, all with fineness-ratio-5 ogival noses. Figure 15 shows the effect of nose fineness ratio for ogive-cylinder bodies, and figure 16 shows the minor effect of change in nose shape from conical to ogival for a given nose fineness ratio of 3.

In figure 17, computed positions of aerodynamic normal-force center (symbols) are compared with measured positions (lines from ref. 63) for the seven bodies at $M_\infty = 2.9$. The positions, x_{ac}/ℓ, are measured from the nose tip of each body in terms of the body length. As for the C_N and C_m results, the agreement of the computed with the measured values is reasonably close, especially for α near 90°. Note that symbols are used to denote computed values because only lines are given in reference 63 to denote the measured results.

To assess the analytical method, plots of C_m versus α may be omitted if plots of both C_N and x_{ac} versus α are included. Hence, for conciseness, plots of C_m versus α are omitted in the remainder of this study. Because precise prediction of C_A versus α is beyond the scope of this study, plots of C_A versus α are also omitted.

3.2 Ogive-Cylinder Bodies at $M_\infty = 0.6$ to 2.0

As shown in the previous section, the analytical method predicts the aerodynamic coefficients reasonably well for various cone-cylinder and ogive-cylinder bodies at a supersonic Mach number of 2.9. We will now assess the method of predicting the C_N and x_{ac} results for four ogive-cylinder bodies at $\alpha = 0°$ to 60° throughout the Mach number range from 0.6 to 2.0 ($M_\infty = 0.6$, 0.9, 1.2, and 2.0).

Sketches of the four bodies considered are shown in figure 18. Bodies N_2C_1 and N_7C_1 were previously tested by Jorgensen and Nelson (ref. 16) in the NASA-Ames 6- by 6-Foot Wind Tunnel. Recently, these same bodies were retested in the same tunnel at $M_\infty = 0.6$. They were also retested at $M_\infty = 0.6$, 0.9, 1.2, and 2.0 with cylindrical extensions attached to the aftersections. Cylinder C_2, two diameters long, was attached to body N_2C_1 to form body $N_2C_1C_2$, and cylinder C_3, four diameters long, was attached to body N_7C_1 to form body $N_7C_1C_3$. Thus, the bodies include nose fineness ratios of 2.5 and 3.5 (noses N_7 and N_2), aftersection fineness ratios of 7, 9, and 11 (aftersections C_1, C_1C_2, and C_1C_3), and overall fineness ratios of 9.5 (N_7C_1), 10.5 (N_2C_1), 12.5 ($N_2C_1C_2$), and 13.5 ($N_7C_1C_3$).

In figures 19-22, computed values of C_N and $(\ell - x_{ac})/d$ as a function of α are compared with the measured results for the four bodies. The aerodynamic normal-force center, $(\ell - x_{ac})/d$, is measured forward on each body from its base in terms of its body diameter. For bodies N_2C_1 and N_7C_1 (figs. 19 and 20, respectively), the results for all Mach numbers are compared on the same plots, and one can observe, at a given value of α, the variation of C_N and $(\ell - x_{ac})/d$ with M_∞. For the longer bodies, $N_2C_1C_2$ (fig. 21) and $N_7C_1C_3$ (fig. 22), the results for each Mach number are compared on a separate plot. With these separate plots, there is less confusion in comparing predicted with measured values of $(\ell - x_{ac})/d$.

Generally, the variation of C_N with α is predicted closely for each body throughout the α and M_∞ ranges considered. At the lowest Mach number, $M_\infty = 0.6$, the C_N values previously measured (ref. 16) for the shortest body, N_7C_1, are believed to be erroneous (fig. 20). The values from the retest agree closely with the predicted results.

The aerodynamic normal-force centers are predicted best for the supersonic Mach numbers. Generally, for the subsonic Mach numbers, the predicted aerodynamic centers are more rearward on the bodies than the measured centers. For all Mach numbers and low values of α, the agreement of the predicted with the measured positions probably should be better than shown. The force and moment balance located inside each body was chosen to measure the large normal forces and pitching moments expected over the high α range. Thus, the accuracy of the experimental aerodynamic centers (determined from C_m/C_N) at the low values of α is somewhat less than at the high values, and there is more scatter in the data.

In this study, we have concentrated primarily on predicting the static aerodynamic characteristics for bodies at high angles of attack. For bodies at low angles of attack, more theoretically exact prediction methods have been proposed. For example, for angles of attack less than about 20°, Perkins and Jorgensen (ref. 4) have shown that the agreement of theory with experiment at supersonic Mach numbers can be improved by replacing slender-body potential theory (e.g., the first term in eq. (2.10)) with Van Dyke's hybrid theory (ref. 64) or Tsien's linearized theory (ref. 65). They also suggest the use of an empirical modification to the viscous crossflow theory (e.g., the second term in eq. (2.10)). In this modification, an experimentally determined correlation curve for the distribution of the crossflow drag coefficient along the body length is used when there is laminar crossflow. It is questionable whether the extra computation needed in these more detailed methods is warranted for most engineering studies. However, if an accurate loading distribution over a body length is desired, a more detailed method should be considered (ref. 4).

3.3 Predicted Effect of Change in Crossflow Reynolds Number from Subcritical to Supercritical

At present there is a general lack of aerodynamic data for which predicted results can be compared for bodies of revolution at supercritical crossflow Reynolds numbers and subcritical crossflow Mach numbers. Jorgensen (ref. 9), however, has computed results which demonstrate what might be expected for a slender body of revolution. The body chosen for study consists of a tangent ogive nose of fineness ratio 5 with a cylindrical after-section of fineness ratio 6 (body 7 in fig. 12).

For free-stream (and crossflow) Mach numbers less than about 0.4, the variation of C_N and x_{ac}/ℓ with α has been computed for free-stream Reynolds numbers of 10^5, 10^6, and 10^7, and the curves are shown in figure 23. There is a significant effect of Reynolds number on both C_N and x_{ac}/ℓ throughout most of the α range. These curves, of course, reflect the strong influence of crossflow Reynolds number Re_n on crossflow drag coefficient C_{d_n} for two-dimensional circular cylinders (see fig. 2).

As shown in figure 2, C_{d_n} for a circular cylinder drops considerably as Re_n increases from 10^5 (subcritical) to 10^6 (supercritical), and then there is a gradual rise as Re_n increases from 10^6 to 10^7 (in the supercritical range). There is much more uncertainty in the magnitude

of C_{d_n} at supercritical Re_n (such as 10^6 and 10^7) than at subcritical Re_n (values less than about 2×10^5), and the shading in figure 2 indicates the uncertainty because of scatter in known data.

In figure 23, the shaded bands in the C_N and x_{ac}/ℓ curves for $Re = 10^6$ reflect the uncertainty in these curves resulting from the scatter in the C_{d_n} data shown in figure 2. It is clearly evident, however, that this uncertainty in the curves is relatively small compared with the large effect of change in Reynolds number.

Figure 23(b) shows the ratio of C_N for the body at $Re = 10^6$ and 10^7 to C_N for the body at the subcritical Re of 10^5. With this figure the effect of Re can be studied throughout the α range: for example, at α near 90°, the body at $Re = 10^6$ develops only about 25 percent of the C_N developed at $Re = 10^5$, but at $\alpha < 10°$, 100 percent of the C_N is developed. Similar study of the movement of x_{ac}/ℓ with change in Re can be made with the use of figures 23(c) and (d).

Although no experimental data are available with which to compare these predicted effects for bodies of revolution, there are limited data for an early version of a noncircular space-shuttle body (ref. 66). Jorgensen (ref. 9) predicted some experimental trends (ref. 66) showing the decrease in C_N with α that results from an increase in crossflow Reynolds number from subcritical to supercritical.

CHAPTER 4

METHOD APPLIED TO BODIES OF ELLIPTIC CROSS SECTION

In this chapter, we compare predicted with measured normal-force and normal-force-center characteristics for three bodies of elliptic cross section at $\alpha = 0°$ to 60° and $M_\infty = 0.6$ to 2.0. First, however, we introduce the bodies considered, review the experimental test conditions, and present the equations used to compute C_N and C_m for each body.

4.1 Bodies Studied and Tests at $M_\infty = 0.6$ to 2.0

Figure 24(a) shows the three bodies of elliptic cross section considered here. Planform views of the bodies as they were oriented (in five different configurations) for the tests are shown in figure 24(b). All of the bodies were tested previously and the results presented in a data report (ref. 18).

The basic circular body B_1 consists of a circular-arc tangent-ogive nose of fineness ratio 3 followed by a cylindrical aftersection of fineness ratio 7. Bodies B_2 and B_3 have elliptic cross sections, and they have the same length and axial distribution of cross-sectional area as B_1. Hence the fineness ratio of $\ell/d = 10$ for B_1 is also the equivalent fineness ratio for B_2 and B_3, and all bodies have equal volumes. For B_2, the ratio of the semimajor to the semiminor cross-sectional axis ($a/b = 2$) is held constant along the body length. Bodies B_1 and B_2 were investigated in 1958 (ref. 6) only for $\alpha = 0°$ to 20° and $M_\infty = 2$ to 4. Body B_3 (new to the investigation in ref. 18) consists of the same nose shape as B_2 but has an afterbody section of variable a/b over four body diameters in length and a constant $a/b = 2$ over the rear three body diameters (see fig. 24(a)). Photographs of B_3 in figure 25 enable one to establish a clearer mental image of this more complex body.

Six-component aerodynamic force and moment coefficients were measured in the study of reference 18 for these bodies in the Ames 6- by 6-Foot Wind Tunnel. However, in this chapter, only the variation of C_N and $(\ell - x_{ac})/d$ with α is considered.

All bodies were tested at $M_\infty = 0.6$, 0.9, 1.2, 1.5, and 2.0 and $\alpha = 0°$ to 58°. For the data used here, the Reynolds numbers, based on base diameter, are 6.5×10^5 at $M_\infty = 0.6$ and 0.9 and 3.8×10^5 at $M_\infty = 1.2$, 1.5, and 2.0. The elliptic bodies were tested at $\phi = 0°$ (flattest side of nose pitching against the flow) and 90° (see fig. 24(b)).

4.2 Equations Used to Compute C_N and C_m for Each Body

For the general case of a slender body in which the cross-sectional shape varies along the length, the normal-force and pitching-moment coefficients can be computed from equations (2.20) and (2.21):

$$C_N = \frac{\sin 2\alpha \cos(\alpha/2)}{A_r} \int_0^{\ell} \left(\frac{C_n}{C_{n_o}}\right)_{SB} \frac{dA}{dx}\, dx + \frac{2\eta C_{d_n} \sin^2 \alpha}{A_r} \int_0^{\ell} \left(\frac{C_n}{C_{n_o}}\right)_{Newt} r\, dx \tag{4.1}$$

and

$$C_m = \frac{\sin 2\alpha \cos(\alpha/2)}{A_r X} \int_0^{\ell} \left(\frac{C_n}{C_{n_o}}\right)_{SB} \frac{dA}{dx} (x_m - x)dx + \frac{2\eta C_{d_n} \sin^2 \alpha}{A_r X} \int_0^{\ell} \left(\frac{C_n}{C_{n_o}}\right)_{Newt} r(x_m - x)dx \tag{4.2}$$

The axial distance from the body base to the normal-force center (see sketch (g)) is then given in terms of the body diameter by

$$\frac{(\ell - x_{ac})}{d} = \frac{C_m}{C_N} + \frac{(\ell - x_m)}{d} \tag{4.3}$$

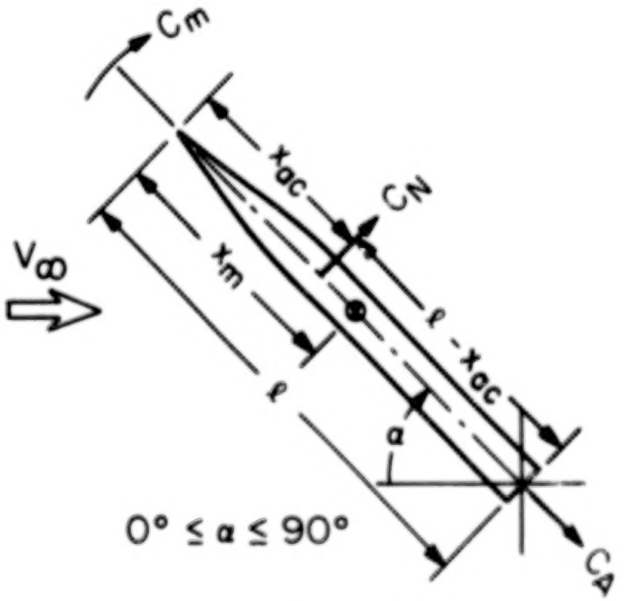

Sketch (g)

As previously discussed, $(C_n/C_{n_o})_{SB}$ in equations (4.1) and (4.2) is the ratio of the local normal-force coefficient for the noncircular cross section to that for the equivalent (same area) circular cross section as determined from slender-body theory. The similar ratio $(C_n/C_{n_o})_{Newt}$ is determined from Newtonian impact theory. From equation (2.26),

$$\left(\frac{C_n}{C_{n_o}}\right)_{SB} = \frac{a}{b}\cos^2\phi + \frac{b}{a}\sin^2\phi \tag{4.4}$$

where ϕ is the angle of roll about the body longitudinal axis, being 0° with the semimajor axis a perpendicular to the crossflow velocity and 90° with the semiminor axis b perpendicular to the crossflow velocity (see sketches (h) and (i)).

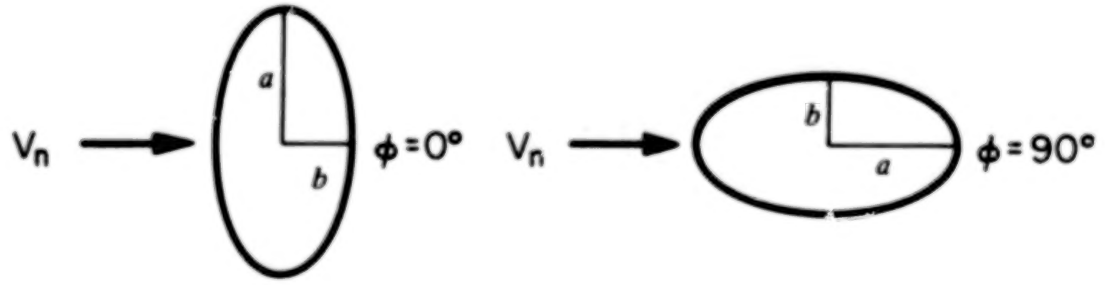

(h) (i)

Sketches (h) and (i)

From Newtonian theory, for the semimajor axis a perpendicular to the crossflow velocity V_n, equation (2.28) reduces to

$$\left(\frac{C_n}{C_{n_o}}\right)_{Newt} = \frac{3}{2}\sqrt{\frac{a}{b}}\left\{\frac{-b^2/a^2}{(1-(b^2/a^2)^{3/2}}\log\left[\frac{a}{b}\left(1+\sqrt{1-\frac{b^2}{a^2}}\right)\right]+\frac{1}{1-(b^2/a^2)}\right\} \tag{4.5}$$

For the semiminor axis b perpendicular to the crossflow velocity V_n, equation (2.29) reduces to

$$\left(\frac{C_n}{C_{n_o}}\right)_{Newt} = \frac{3}{2}\sqrt{\frac{b}{a}}\left\{\frac{a^2/b^2}{[(a^2/b^2)-1]^{3/2}}\tan^{-1}\left(\sqrt{\frac{a^2}{b^2}-1}\right)-\frac{1}{(a^2/b^2)-1}\right\} \tag{4.6}$$

For the bodies of this investigation, equations (4.1) and (4.2) can be simplified by integration. The simplified equations, which were used to compute C_N and C_m values for

each body, are presented next. In all the C_N and C_m equations, empirical input values of η and C_{d_n} from chapter 2 are used.

4.2.1 *Equations for bodies with constant a/b cross sections (bodies B_1 and B_2)*– Both bodies B_1 and B_2 have cross sections of constant a/b over the body length. For this condition, equations (4.1) and (4.2) reduce to

$$C_N = \left(\frac{A_b}{A_r} \sin 2\alpha \cos \frac{\alpha}{2}\right)\left(\frac{C_N}{C_{N_o}}\right)_{SB} + \left(\eta C_{d_n} \frac{A_p}{A_r} \sin^2 \alpha\right)\left(\frac{C_N}{C_{N_o}}\right)_{Newt} \tag{4.7}$$

and

$$C_m = \left[\frac{V - A_b(\ell - x_m)}{A_r X}\right]\left(\sin 2\alpha \cos \frac{\alpha}{2}\right)\left(\frac{C_m}{C_{m_o}}\right)_{SB} + \left[\eta C_{d_n} \frac{A_p}{A_r}\left(\frac{x_m - x_c}{X}\right) \sin^2 \alpha\right]\left(\frac{C_m}{C_{m_o}}\right)_{Newt} \tag{4.8}$$

where

$$\left(\frac{C_N}{C_{N_o}}\right)_{SB} = \left(\frac{C_m}{C_{m_o}}\right)_{SB} = \left(\frac{C_n}{C_{n_o}}\right)_{SB}$$

$$\left(\frac{C_N}{C_{N_o}}\right)_{Newt} = \left(\frac{C_m}{C_{m_o}}\right)_{Newt} = \left(\frac{C_n}{C_{n_o}}\right)_{Newt}$$

4.2.2 *Equations for body with variable a/b cross sections (body B_3)*– Body 3 has a midsection length of variable a/b, but the equivalent body of revolution is B_1 for which $dA/dx = 0$ rearward of the nose-cylinder junction. Thus, equations (4.1) and (4.2) reduce to

$$C_N = \left(\frac{A_b}{A_r} \sin 2\alpha \cos \frac{\alpha}{2}\right)\left(\frac{C_N}{C_{N_o}}\right)_{SB_{nose}} + \frac{2\eta C_{d_n} \sin^2 \alpha}{A_r} \int_0^{\ell} \left(\frac{C_n}{C_{n_o}}\right)_{Newt} r \, dx \tag{4.9}$$

and

$$C_m = \left[\frac{V - A_b(\ell - x_m)}{A_r X}\right]_{nose} \left(\sin 2\alpha \cos \frac{\alpha}{2}\right)\left(\frac{C_m}{C_{m_o}}\right)_{SB_{nose}}$$

$$+ \frac{2\eta C_{d_n} \sin^2 \alpha}{A_r X} \int_o^{\ell} \left(\frac{C_n}{C_{n_o}}\right)_{Newt} r(x_m - x)dx \qquad (4.10)$$

where

$$\left(\frac{C_N}{C_{N_o}}\right)_{SB_{nose}} = \left(\frac{C_m}{C_{m_o}}\right)_{SB_{nose}} = \left(\frac{C_n}{C_{n_o}}\right)_{SB_{nose}}$$

and $A_{b_{nose}} = A_b$. Also, for the bodies studied,

$$\left[\frac{V - A_b(\ell - x_m)}{A_r X}\right]_{nose} = \left[\frac{V - A_b(\ell - x_m)}{A_r X}\right]$$

Some potential or inviscid normal force can be expected intuitively to be carried over past the nose shoulder of body B_3, even though the approximate slender-body term gives zero normal force over the aftersection. For body B_3 at $\phi = 90°$ (fig. 24(b)), the span increases with length past the nose shoulder, and it might seem reasonable to compute the slender-body terms for C_N and C_m based on the maximum span (or base) geometry. For this estimation,

$$C_N = \left(\frac{A_b}{A_r} \sin 2\alpha \cos \frac{\alpha}{2}\right)\left(\frac{C_N}{C_{N_o}}\right)_{SB_b} + \frac{2\eta C_{d_n} \sin^2 \alpha}{A_r} \int_o^{\ell} \left(\frac{C_n}{C_{n_o}}\right)_{Newt} r\, dx \qquad (4.11)$$

and

$$C_m = \left[\frac{V - A_b(\ell - x_m)}{A_r X}\right]\left(\sin 2\alpha \cos \frac{\alpha}{2}\right)\left(\frac{C_m}{C_{m_o}}\right)_{SB_b}$$

$$+ \frac{2\eta C_{d_n} \sin^2 \alpha}{A_r X} \int_o^{\ell} \left(\frac{C_n}{C_{n_o}}\right)_{Newt} r(x_m - x)dx \qquad (4.12)$$

where

$$\left(\frac{C_N}{C_{N_o}}\right)_{SB_b} = \left(\frac{C_m}{C_{m_o}}\right)_{SB_b} = \left(\frac{C_n}{C_{n_o}}\right)_{SB_b}$$

4.3 Comparison of Computed With Measured Normal-Force and Normal-Force-Center Characteristics

In figures 26 through 28, computed values of C_N and $(\ell - x_{ac})/d$ versus α are compared with measured values (from ref. 18) for the bodies studied. The comparisons are made for the bodies at $\alpha = 0°$ to 60° and free-stream Mach numbers of 0.6, 0.9, 1.2, 1.5, and 2.0.

4.3.1 *Bodies with constant a/b cross sections (bodies B_1 and B_2)*– Generally, there is reasonably good agreement in figure 26 of the computed with the measured results for bodies B_1 and B_2 (bodies of constant a/b along the length). The agreement is, however, better at the supersonic Mach numbers than at the subsonic. These comparisons, along with previous successful comparisons in chapter 3, tend to validate the prediction method as a useful tool in body aerodynamic studies, at least for bodies with circular and elliptic cross sections of constant a/b.

4.3.2 *Body with variable a/b cross sections (body B_3)*– As for bodies B_1 and B_2, the predicted characteristics for body B_3 (with variable a/b) agree reasonably well with the measured results (fig. 27). However, the prediction of C_N generally is not as close as for bodies B_1 and B_2. The prediction of $(\ell - x_{ac})/d$ at high α is remarkably close, especially at supersonic Mach numbers. This close prediction of $(\ell - x_{ac})/d$, however, might be somewhat fortuitous since the prediction of C_N is not nearly as close.

The prediction of C_N with α is least accurate for body B_3 oriented at $\phi = 90°$. Generally, for this case, C_N is underpredicted at the lower values of α throughout the M_∞ range. At the subsonic values of M_∞, C_N is underpredicted over the entire α range studied.

Note that these predictions were made with equations (4.9) and (4.10), which do not account for any potential or inviscid lift rearward of the nose section. Intuitively and analytically (ref. 64), some inviscid normal force can be expected to be generated rearward of the nose. This is especially true for body B_3 at $\phi = 90°$ because the span increases with length past the nose, and it might seem reasonable to estimate the slender-body

potential-flow terms for C_N and C_m based on the maximum span (see eqs. (4.11) and (4.12)). When the maximum span estimate is used, the prediction of C_N with α improves somewhat (see fig. 28). However, the prediction of $(\ell - x_{ac})/d$ with α deteriorates, since the predicted values of $(\ell - x_{ac})/d$ move well forward of the measured values (fig. 28).

CHAPTER 5

METHOD APPLIED TO BODY-WING AND BODY-WING-TAIL CONFIGURATIONS

In this chapter, we compare predicted with measured normal-force and normal-force-center characteristics for three body-wing configurations and three body-wing-tail configurations at $\alpha = 0°$ to $60°$ and $M_\infty = 0.6$ to 2.0. First, however, we introduce the configuration models tested, review the experimental test conditions, and present the methodology used to compute C_N and C_m for each model.

5.1 Configurations Studied and Tests at $M_\infty = 0.6$ to 2.0

Many body-wing and body-wing-tail model combinations have been tested, and the data are reported in references 20 and 21. Planform views of the model components tested in the many model combinations are shown in figure 29. These components include a basic circular body B_1, an elliptic body B_2 with $a/b = 2$, five flat-plate wings (W_1 to W_5), and a combination horizontal and vertical tail T. The bodies B_1 and B_2 are two of the bodies considered in chapter 4 (see fig. 24(a)). All the wings were designed to have the same planform area ($16\ d^2$) if the wings extended into the body B_1 to the axial centerline. Based on the phantom wing chord at the body centerline, the taper ratios for wings W_1, W_2, and W_3 were 0, 0.25, and 0.50, respectively (fig. 29(a)). They were also 0.25 for W_4 and W_5 (fig. 29(b)). Wings W_1, W_2, and W_3 (fig. 29(a)) had an aspect ratio of about 4; wings W_4, W_2, and W_5 (fig. 29(b)) has aspect ratios of about 5, 4, and 3, respectively. Pertinent planform dimensions of the exposed parts of the wings are given in tables in figure 29. The tail dimensions are given in figure 29(a).

The tests (refs. 20 and 21) were conducted in the Ames 6- by 6-Foot Wind Tunnel at $\alpha = 0°$ to $58°$ and $M_\infty =$ 0.6 to 2.0. The Reynolds number, based on body diameter d, was about 4×10^5.

Results from these tests (refs. 20 and 21) showed that changing wing taper ratio from 0 to 0.5 changed the aerodynamic characteristics very little. Also, changing wing aspect ratio from 3 to 5 changed the aerodynamic characteristics very little. Thus, to achieve more conciseness in the present investigation, only three body-wing configurations and three body-wing-tail configurations were considered.

Planform views of the configurations studied in the present investigation are shown in figure 30: the basic circular body B_1 with wings of aspect ratio 3 and 4 (W_5 and W_2, respectively) and the elliptic body B_2 with the wing of aspect ratio 3 (W_5). These configurations (B_1W_5, B_1W_2, and B_2W_5) were also investigated with the tail T attached (configurations B_1W_5T, B_1W_2T, and B_2W_5T).

5.2 Methodology Used to Compute C_N and C_m

From equations (2.20) and (2.21), we obtain

$$C_N = \frac{\sin 2\alpha \cos(\alpha/2)}{A_r} \int_0^{\ell} \left(\frac{C_n}{C_{n_o}}\right)_{SB} \frac{dA}{dx}\, dx + \frac{2\eta C_{d_n} \sin^2 \alpha}{A_r} \int_0^{\ell} \left(\frac{C_n}{C_{n_o}}\right)_{Newt} r\, dx \tag{5.1}$$

and

$$C_m = \frac{\sin 2\alpha \cos(\alpha/2)}{A_r X} \int_0^{\ell} \left(\frac{C_n}{C_{n_o}}\right)_{SB} \frac{dA}{dx} (x_m - x)dx + \frac{2\eta C_{d_n} \sin^2 \alpha}{A_r X} \int_0^{\ell} \left(\frac{C_n}{C_{n_o}}\right)_{Newt} r(x_m - x)dx \tag{5.2}$$

The first terms represent the C_N and C_m values from slender-body potential-flow theory; the second terms represent the values from the viscous crossflow method modified by Newtonian theory. The first terms are not applicable, as written, for body-wing sections where the body dA/dx values are zero or negative. Also, for body-wing and body-wing-tail configurations, more comprehensive methods from potential theory are available.

For this study, the first-term (potential-flow) contributions to C_N and C_m were computed from the linear method presented in NACA Report 1307 (ref. 38). This method, referred to as the N-K-P method (for Nielsen, Kaattari, and Pitts), is restricted to bodies of circular cross section with wings and tails that do not have swept-forward leading edges or swept-back trailing edges. It is further restricted to small angles of attack and small angles of

wing and tail incidence in which the forces are linear with angle. To obtain the wing-body interference, certain factors are defined that are the ratios of the lift on the components in combination to the lift on the wing alone. These ratios are obtained primarily by slender-body theory, but the wing lift is obtained by linear potential theory. Wing-tail interference is treated by assuming one completely rolled-up vortex per wing panel and evaluating the tail load by strip theory.

To combine the N-K-P method with the crossflow method, the N-K-P potential terms must be multiplied by a correction factor $(\sin 2\alpha)/2\alpha$ to produce a more correct type of nonlinear behavior to these terms and to eliminate the potential contribution as $\alpha \to 90°$. With this modification,

$$C_N = (C_N)_{N\text{-}K\text{-}P} \frac{\sin 2\alpha}{2\alpha} + \frac{2\eta C_{d_n} \sin^2 \alpha}{A_r} \int_o^{\ell} \left(\frac{C_n}{C_{n_o}}\right)_{Newt} r \, dx \qquad (5.3)$$

and

$$C_m = (C_m)_{N\text{-}K\text{-}P} \frac{\sin 2\alpha}{2\alpha} + \frac{2\eta C_{d_n} \sin^2 \alpha}{A_r X} \int_o^{\ell} \left(\frac{C_n}{C_{n_o}}\right)_{Newt} r(x_m - x) dx \qquad (5.4)$$

Since the N-K-P method is restricted to bodies of circular cross section with wings and tails, a further assumption must be made to estimate potential theory values of C_N and C_m for noncircular bodies with wings and tails. The local widths of the noncircular body in planform are replaced by the local diameters of a circular body, thus keeping the overall wing and tail spans constant (see sketch (j)). The crossflow method, of course, requires no such assumption for noncircular bodies.

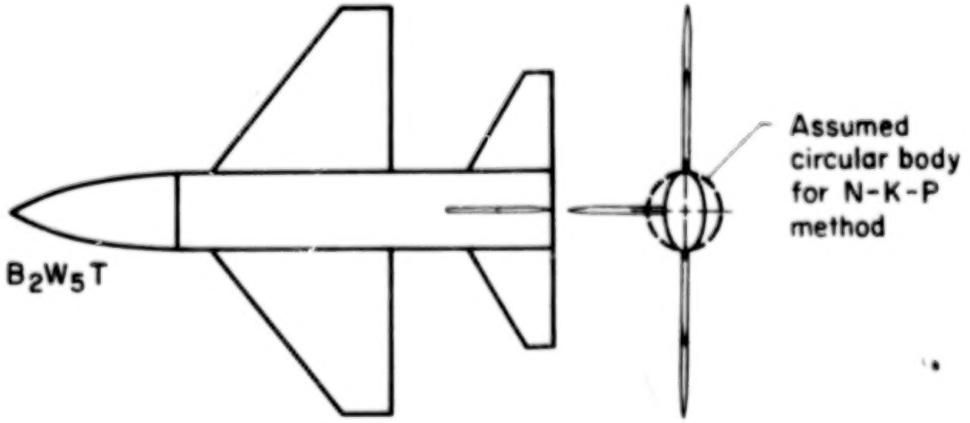

Sketch (j)

For the way in which the crossflow method is formulated in chapter 2, values of crossflow drag coefficient C_{d_n} for a circular cylinder are used. As shown in figure 1, there is considerable variation of C_{d_n} with crossflow Mach number M_n for values of M_n from about 0.4 to 3. Also, for M_n less than about 0.5, there is considerable change in C_{d_n} as the crossflow Reynolds number Re_n exceeds the critical value of about 2×10^5 (figs. 2 and 3). These variations of C_{d_n} with M_n and Re_n may be expected for near-circular bodies, but surely not for very flat bodies or winged bodies. From the data available, values of C_{d_n} for flat bodies and plates do not appear to change nearly as appreciably with M_n and Re_n over the ranges shown in figures 1 and 2 (see, e.g., refs. 41, 66, and 67). Thus, for the body-wing configurations, it is likely that a constant value of C_{d_n} will give closer agreement of theory with experiment, especially at α where M_n is near or in the transonic regime.

For flat-faced, two-dimensional configurations, reasonable values of crossflow drag coefficient can be computed from Newtonian or modified Newtonian theory (see, e.g., table 1 and ref. 66). For circular cylinders at low subsonic and hypersonic M_n, values of C_{d_n} computed from Newtonian or modified Newtonian theory also agree reasonably well with experiment (see fig. 1). In this study, modified Newtonian theory is used to compute the circular-cylinder C_{d_n} value that is substituted into equations (5.3) and (5.4).

From modified Newtonian theory,

$$C_{d_n} = \frac{2}{3} C_{p_{stag}}$$

$$= 1.2 \text{ for } C_{p_{stag}} = 1.8$$

For $M_n >$ about 4, $C_{p_{stag}} \approx 1.8$ from perfect-gas relations (e.g., ref. 68). In this study for wing-body and wing-body-tail configurations, it is assumed that $C_{d_n} = 1.2$ for all values of M_n (and hence, M_∞).

The axial distance from the body base to the normal-force center is given (in body diameters) by

$$\frac{\ell - x_{ac}}{d} = \frac{C_m}{C_N} + \frac{(\ell - x_m)}{d} \tag{5.5}$$

In this study, we present normal-force centers instead of C_m values.

The entire method has been computer programmed for Ames Research Center by Nielsen Engineering & Research, Inc., Mountain View, Calif. The program is similar to those given in reference 69, and it combines essential parts of the N-K-P and crossflow programs in reference 69. It is written in Fortran IV for the CDC 6600 or 7600 machines. No tapes, drums, or disks other than the standard input/output units are required. The running time for a typical case is less than 1 sec.

5.3 Comparison of Computed With Measured Normal-Force and Normal-Force-Center Characteristics

In figures 31 through 36, computed values of C_N and $(\ell - x_{ac})/d$ versus α are compared with measured values (refs. 20 and 21) for some of the body-wing and body-wing-tail configurations studied. As for the bodies alone, the normal-force coefficients are based on body cross-sectional area at the body base. Of course they can be easily converted to the more often used exposed wing planform area by dividing by A_w/A_b, where $A_w/A_b = 15.92$ for the bodies with W_5 and 16.49 for the bodies with W_2. The comparisons are made for the configurations at $\alpha = 0°$ to about 60°. For configuration B_1W_5, $M_\infty = 0.6, 0.9, 1.5$, and 2.0 (fig. 31). For the other configurations (B_1W_2, B_2W_5, $B_1W_5T_1$, $B_1W_2T_1$, and B_2W_5T), $M_\infty = 0.6$ and 2.0.

5.3.1 *Body-wing configurations*– Let us first look at the results in figure 31 for the circular body B_1 with the aspect ratio 3 wing W_5. At $M_\infty = 0.6$ (fig. 31(a)), the measured C_N values are predicted closely by the modified N-K-P potential method only for α up to about 10° or 15°. Then this potential-flow method overpredicts C_N for most of the higher α range considered. With even the potential-flow method overpredicting C_N, the combination of the potential-flow and crossflow methods greatly overpredicts C_N. It is to be expected, however, that at α near 90° the combination method should predict C_N reasonably well, since C_N is given entirely by the crossflow method (modified Newtonian impact theory) at $\alpha = 90°$. Despite the difficulty in predicting C_N over most of the high α range, the positions of the normal-force center are predicted closely by the combination method.

With increase in Mach number to $M_\infty = 0.9$, the comparisons of computed with measured results are not significantly improved (fig. 31(b)). In fact, the normal-force centers are not predicted as closely as at $M_\infty = 0.6$. Not until the free-stream Mach numbers become

supersonic do the modified N-K-P and combination methods give reasonable estimates of C_N. At $M_\infty = 1.5$, the measured C_N results are only underpredicted a small amount by the modified N-K-P method for α up to about 30° or 40° (fig. 31(c)). At $M_\infty = 2.0$, the C_N results are predicted best by the combination method throughout the α range studied, although the experimental results are still overpredicted by this method (fig. 31(d)). It appears that the combination method should improve in its ability to predict C_N as M_∞ increases throughout the supersonic range.

With increase in wing aspect ratio from 3 to 4 (configuration B_1W_5 to B_1W_2), the comparisons generally are not changed significantly. As shown in figure 32(a), for $M_\infty = 0.6$ the modified N-K-P and combination methods still overpredict C_N significantly at high α. In fact, the overprediction for B_1W_2 is greater than for B_1W_5 (compare figs. 31(a) and 32(a)). As for the lower-aspect-ratio configuration, the C_N results are predicted best by the combination method as the Mach number is increased to $M_\infty = 2.0$ (fig. 32(b)).

When the body cross section is changed from circular to elliptical with the same aspect-ratio-3 wing (configuration B_1W_5 to B_2W_5), the C_N results for $M_\infty = 0.6$ are predicted closely (possibly fortuitously) by the modified N-K-P method (fig. 33(a)). As before, when the Mach number is increased to $M_\infty = 2.0$, the combination method still gives the best C_N prediction throughout the α range (fig. 33(b)).

The break or significant deviation from linearity in the C_N curve with increasing angle of attack at the subsonic Mach numbers makes it extremely difficult to formulate a rational method for predicting C_N throughout the high α range. This break is attributed to flow separation over the wing upper surface. For wings of generally lower aspect ratio and higher leading edge sweep than those studied here, the break has been attributed to vortex breakdown near the wing trailing edge of vortices shed from the leading edge. Vortex breakdown or bursting has been studied rather extensively by Wentz and Kohlman (ref. 70) for thin delta and modified delta wings with sweep angles from 45° to 85° at low speed. They have observed that as α increases the position of vortex bursting of the trailing vortices moves upstream toward the trailing edge and crosses the trailing edge at a specific α. Above this α, a loss of lift occurs on the wing due to vortex bursting, and the effect becomes progressively larger as α increases. Mendenhall and Nielsen (ref. 71) have more recently collected data from several investigators for the α value at which vortex bursting occurs at the trailing edge

of delta wings tested at low speeds. They were unable to correlate the data and suggested that the factors which control vortex bursting were not reproduced or controlled between the various sets of test data. The wings used in the present investigation were generally swept less than those studied by Wentz and Kohlman (ref. 70) and Mendenhall and Nielsen (ref. 71). However, a 45° delta wing similar to that of W_1 (fig. 29(a)) was investigated by Wentz and Kohlman (ref. 70). For this wing they failed to observe vortices, but they, of course, measured a loss in C_L with increase in α over a particular value (near 20°). Despite the interesting research thus far, it seems that further research into the factors that control vortex bursting and flow separation is needed. The C_N versus α data presented here indicate that this is especially desirable for subsonic Mach numbers. Some initial exploratory flow-field pictures from recent vapor-screen and oil-flow tests are presented in chapter 6.

5.3.2 *Body-wing-tail configurations*– Now consider the results for the same body-wing combinations but with the tail added (figs. 34-36). Generally, the comparisons of computed with measured results indicate similar trends as for the body-wing configurations. At $M_\infty = 0.6$ and for the circular body B_1, the C_N results over most of the investigated α range are underpredicted, even by the modified N-K-P method (figs. 34(a) and 35(a)). With change to the elliptic body, however, the C_N results (for $B_2 W_S T$) are closely predicted up to α near 50° (fig. 36(a)). At $M_\infty = 2.0$, the C_N results are predicted best by the combination method (modified N-K-P plus crossflow), although as for the body-wing configurations the measured results are still overpredicted (fig. 36(b)).

With the addition of the tail, there is generally more movement of the aerodynamic center ($\ell - x_{ac}/d$) with α at $M_\infty = 0.6$ (compare, e.g., results for $B_1 W_S$ and $B_1 W_S T$ in figs. 31(a) and 34(a)). This movement, which takes place at α from about 10° to 40°, is only partially predicted by the combination method. It may be attributed to forebody and wing wake flow over the tail. Further investigation of the forebody and wing wake flow over the tail appears to be desirable.

From the comparisons presented, it seems obvious that the methodology presented here represents only an initial step into the complex problem of predicting the aerodynamic characteristics of body-wing and body-wing-tail configurations to very high angles of attack. The reader interested in this field may wish to study several other initial approaches such as those of Mendenhall and Nielsen (ref. 71) and Axelson (ref. 72). One should also include the

Polhamus suction analogy for wings (ref. 73) and some of its various adaptations and extensions (e.g., refs. 71, 74, and 75). Much additional research is necessary in the high α field, and this research initially should include visual observations of the flow fields. In chapter 6, we will show some of the photographs obtained from an exploratory visual study of the flow over bodies alone, bodies with a wing, and bodies with a wing and a tail.

CHAPTER 6

VISUAL OBSERVATION OF FLOWS OVER MODELS

It is a well-established fact that as the angle of attack (or incidence) of a model is increased above about 5° or 10° some flow separates from the upper surface, and vortices and/or regions of flow separation are formed. The basic vortex phenomena are easily described by referring to a body of revolution (see sketch (k)). At low to moderate angles of attack, two vortices are shed from the pointed body, and the vortex formation is symmetrical (e.g., refs. 2, 5, 6, 13, 25, and 27). With further increase in angle of attack, the vortex formation may become somewhat asymmetrical. At some higher angle of attack, the feeding vortex sheets tear, and three or more vortices may appear (depending on the model geometry and free-stream flow conditions as well as angle of attack). Both symmetric and asymmetric vortex formations are illustrated in sketch (k). Although generally illuminating

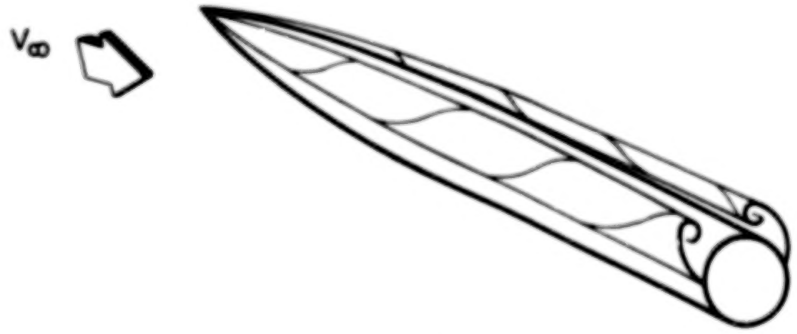

Symmetric vortex formation

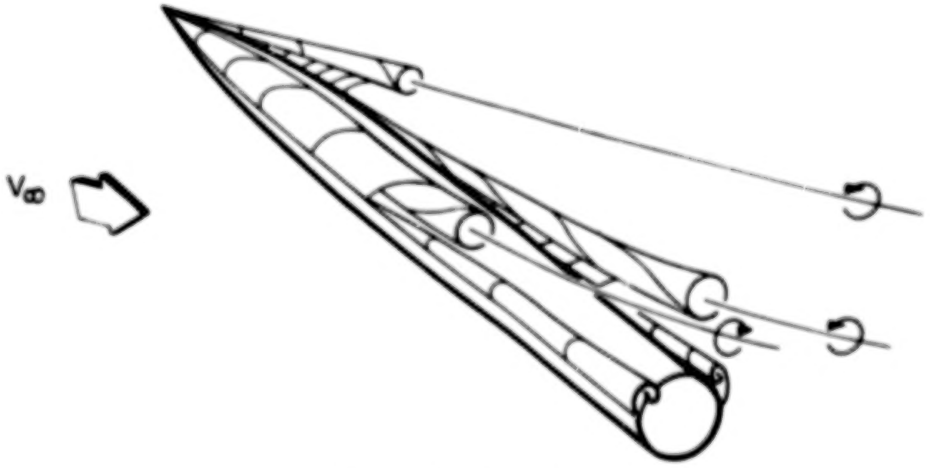

Asymmetric vortex formation and breakaway

Sketch (k)

in concept, the illustrations in sketch (k) are somewhat simplistic, and further observations of vortex formations over many bodies alone and with wings and tails at various free-stream flow conditions are desirable.

For observing the vortex formations over many models, the "vapor-screen technique" (e.g., refs. 2, 6, 76, and 77) is very useful and much less time-consuming than the more detailed pressure-probe-survey techniques (e.g., refs. 5 and 25). In this study, we have used the vapor-screen technique to observe the vortex formations over many of the same model configurations considered in chapters 3 through 5. In addition, we have added several ogival noses of different fineness ratio that attach to the body and body-wing-tail combinations previously described. To observe surface flow and especially flow separation positions, the "oil-flow technique" (e.g., refs. 6, 17, and 76) also has been used for many of the same configurations.

In this chapter, photographs are presented that show the flows over the various bodies alone and in combination with a wing and a wing plus tail at $\alpha = 10°$ to $50°$. The free-stream Mach numbers are 0.6, 0.9, and 2.0, and the Reynolds number is about 4.3×10^5 based on body diameter. Before presenting the photographs, we will specify which models are considered and briefly review the vapor-screen and oil-flow techniques used for the tests in the Ames 6- by 6-Foot Wind Tunnel.

6.1 Models Considered

As in the previous chapters, the models considered are identified according to body B, nose N, cylinder C, cylinder strake S, wing W, and tail T. For the bodies of elliptic cross section (fig. 24), the roll orientation ϕ is also specified. The configurations investigated and the figures in this report where the configuration dimensions are given are listed as follows:

Configuration	Figure
$B_1 = N_1C_1$	24, 37
N_2C_1	37
N_3C_1	37
N_4C_1	37
N_3C_1S	37

Configuration	Figure
$B_2 \quad \phi = 0°$	24
$B_2 \quad \phi = 90°$	24
$B_3 \quad \phi = 0°$	24
$B_3 \quad \phi = 90°$	24
$B_1 W_5 = N_1 C_1 W_5$	29
$B_1 W_2 = N_1 C_1 W_2$	29
$B_1 W_2 T = N_1 C_1 W_2 T$	29
$N_3 C_1 W_2$	29,37
$N_3 C_1 W_2 T$	29,37

Plan-view sketches of these configurations are shown in figure 38.

Figure 37, which has not been presented before, shows a series of circular-arc tangent ogive noses that attach to the circular cylinder C_1. Noses N_1, N_2, and N_3 have fineness ratios of 3, 3.5, and 5, respectively. Nose N_4 is formed by rounding the tip of a fineness-ratio-3.5 ogive (such as N_2) to give a resulting fineness ratio of 3.

The thin wings and tail shown in figure 29 also attach to the cylinder C_1, so many combinations of nose, cylinder, wing, and tail are possible. For this report only some representative combinations are considered.

6.2 Vapor-Screen and Oil-Flow Techniques

6.2.1 *Vapor-screen technique*– In the vapor-screen technique, the wind tunnel is run with moist air. In fact, water is added to the airstream as needed.

For supersonic Mach numbers, as the moist air expands through the supersonic nozzle into the test section it cools, and the moisture condenses to form a fog. This fog is illuminated by a sheet of bright light produced by high-intensity mercury-vapor lamps and projected through the tunnel window(s) and across the stream. This sheet of light appears as a uniformly lighted screen of fog particles in the absence of a disturbance. However, with a model in the stream the uniform distribution of fog particles is disturbed, and the model disturbance affects the light scattered by the water particles. Wakes and vortices typically appear as dark "holes" in the screen.

For very high subsonic ($M_\infty = 0.9$) and transonic Mach numbers, similar dark regions may appear at the vortex locations, but for lower subsonic flows ($M_\infty = 0.6$) light (condensation) regions often appear at the vortex locations. There are, in fact, cases where a light area will appear above a left wing panel and a dark area above the right panel, and both areas will indicate separated regions and/or vortex flow. The physics may not always be simply explained, but the reader interested in more detail is referred to the treatise of McGregor (ref. 77).

Figure 39(a) shows a schematic drawing of the vapor-screen apparatus for the Ames 6- by 6-Foot Wind Tunnel. Two light-source boxes and various camera locations are indicated. In this study, two light boxes were used for observations at $M_\infty = 0.6$, but only one was required for necessary illumination at $M_\infty = 0.9$ and 2.0. Each box contains six 900-W mercury-vapor lamps (BH-6) and mirrors to reflect the light through collimating slits. The light boxes (shown in fig. 39(b)) connect to a common shaft that passes over the tunnel, and the boxes can be pivoted in tandem and moved so that the light screen can cut the model longitudinal axis at the desired positions. A Honeywell-Pentax spot light meter was focused on the vapor screen and moved with the light box shown in figure 39(b) to aid in maintaining consistent illumination for the photography.

For the present investigation, a Hasselblad 70-mm still camera (model 500 EL/7) was mounted on the sting support rearward of the model base (fig. 39(c)). The camera was enclosed in a protective housing. The 16-mm gun camera shown mounted above the Hasselblad in figure 39(c) was not used for this study. All models were painted black to minimize light reflection and to improve the quality of the photographs. The Hasselblad camera had a 50-mm f4 (wide-angle) lens, and TRI-X (400 ASA) film was used.

6.2.2 *Oil-flow technique*– Flow patterns on the model surfaces at angles of attack were visualized through use of the oil-flow technique. In this technique, the models were covered with a mixture of oil and titanium dioxide (TiO_2) and then run wet in the wind tunnel. The formula for the mixture was 5 teaspoons of SAE 30 oil and 5 teaspoons of TiO_2, with about 3 drops of oleic acid added as an anticoagulant. To provide good contrast of the mixture with the models, all models were first painted a flat black. Photographs of the oil-flow patterns on the models were taken during each run with Hasselblad cameras

focused through a side window and a special small window at the top of the test section of the Ames 6- by 6-Foot Wind Tunnel.

6.3 Photographs Obtained from Vapor-Screen and Oil-Flow Techniques

6.3.1 *Photographs from vapor-screen technique*– Photographs taken with the vapor-screen technique for the models at $M_\infty = 0.6$, 0.9, and 2.0 are shown in figures 40 to 54. Figure 40, presented as a prelude to the other figures, identifies some of the various items that appear in the other figures: the light sheet, light shadow, model support, model base, vortex regions, vortex feeding sheets, and local shocks. The two photographs in figure 40 are for body N_3C_1 at $\alpha \approx 30°$ and $M_\infty = 2.0$. Light sheets are shown at the base of the nose (station 1) and at a more aft cylinder position (station 2). In the remaining vapor-screen photographs (figs. 41-54), a photograph of the flow field at the body base (station 3) is also included. The positions of the three flow-field stations are indicated on a model sketch in each figure. A model shadow similar to that shown in figure 40 usually does not appear on the photographs for $M_\infty = 0.6$. As previously mentioned, at $M_\infty = 0.6$, two light-source boxes were used in tandem, and light came from both sides of the wind tunnel.

For a body of revolution ($B_1 = N_1C_1$) at $M_\infty = 0.6$ (fig. 41(a)), the simplistic flow model of the two rather tightly rolled-up vortices shown in sketch (k) is not evident, even at $\alpha < 30°$. Rather there appear to be separation regions from both sides of the body that seem to almost coalesce along the lee side but do not roll up. In fact, two narrow separation sheets very close together appear to trail back from the nose over the body length. With an increase in α to about 40°, the separation regions from the nose appear more like the usual vortex regions. However, these vortex regions are very light in color in contrast to the dark regions at lower α, and these vortex regions become asymmetric as they trail back over the body. Also, more than two regions develop.

With increase in Mach number to $M_\infty = 0.9$ and 2.0 (figs. 41(b) and (c)), the more traditional vortex formations appear, where there are two rather symmetric vortices (dark holes in the vapor sheet) shed from the body. Along both sides of the body, separation sheets "feed" the vortices, and, of course, the vortices grow with movement from the nose to the base of the body. At $M_\infty = 2.0$, local shocks from the vortex regions appear (fig. 41(c)).

From observation of figures 41 to 43, the effect of increasing nose fineness ratio from 3 (nose N_1) to 5 (nose N_3) can be studied. Generally, with an increase in nose fineness ratio, the vortex formation becomes asymmetric at a lower α. Compare, for example, photographs for N_1C_1 at $\alpha \approx 30°$ (fig. 41) with those for N_3C_1 at $\alpha \approx 30°$ (fig. 43). For all of these bodies, as for the remaining models to be discussed, vortex asymmetry is the worst at the lowest Mach number investigated ($M_\infty = 0.6$). Asymmetric flow separation and vortex asymmetry are accompanied by undesirable side forces (considered in chapter 7).

When the tip of a fineness-ratio-3.5 nose (N_2) was rounded to make a fineness-ratio-3 nose (N_4), a strange vortex pattern developed at $M_\infty = 0.6$ for the body N_4C_1 at $\alpha \approx 40°$ and 50°. This pattern (fig. 44(a)) consists of two very symmetric vortices from the nose located above two separation regions stacked one on top of the other (at station 2). The entire unusual pattern appears to be symmetric even up to $\alpha \approx 50°$. However, at the higher Mach numbers ($M_\infty = 0.9$ and 2.0), the patterns are again similar to those for N_2C_1 (compare, e.g., figs. 42 and 44).

When strakes were attached to the side of the cylinder C_1 of body N_3C_1, the vortex patterns became more symmetrical for α up to about 30° (compare figs. 43 and 45). However, at about 40° and above, there was no effect. Apparently, the asymmetric pattern, originating with the fineness-ratio-5 nose, could not be influenced by the strakes back on the cylinder. Note that the hand of the asymmetry of the vortices can be either left or right, and occasionally the pattern will switch even while it is being observed during a test run.

When the body cross section was changed from circular (body B_1) to elliptic (body B_2 with $a/b = 2$), the vortex patterns became more symmetric with the body oriented at $\phi = 0°$ (flattest side toward the flow). This can be seen by comparison of figures 41 and 46. However, when the elliptic body B_2 was rolled to $\phi = 90°$, the vortex patterns became more asymmetric (see fig. 47).

From tests of body B_3, the body of elliptic cross section with variable a/b, the vortex symmetry was influenced mostly by the nose. As shown in figure 48, when B_3 was oriented at $\phi = 0°$ (flattest side of nose toward the flow), the vortex patterns were essentially symmetric at all test conditions. However, when B_3 was rolled to $\phi = 90°$ (thinnest side of nose toward the flow), the patterns became quite asymmetric at many test conditions (see fig. 49).

When wing W_5 of aspect ratio 3 was attached to body B_1, the body vortex growth over the wings was retarded, but extensive regions of flow separation above the wing appeared (fig. 50). These regions were especially large and diffuse for $M_\infty = 0.6$ and 0.9 (figs. 50(a) and (b)). For $M_\infty = 2.0$, distinct vortices formed, originating at the forward wing-body juncture at the leading edge, on the wing upper surface, and at the wing tips. Thus, at the base of the body there were a pair of vortices from the nose, a pair from the wing-body juncture, a pair from the wing leading edge, and a pair from the wing tips (see fig. 50(c)).

In contrast with the flow at $M_\infty = 2.0$, the flow at $M_\infty = 0.6$ is very diffuse, and there is the possibility that the phenomenon of vortex bursting or breakdown (e.g., refs. 70 and 71) has taken place at the higher angles of attack. This phenomenon (mentioned in chapter 5) might be indicated in some of the vapor-screen pictures by the light-colored diffuse vortex regions. Such regions can be observed at $M_\infty = 0.6$ for both bodies alone and with wings, especially at the higher angles of attack. The phenomenon of vortex bursting might help explain the fact (demonstrated in previous chapters) that the C_N characteristics for the bodies alone and with wings and tail are generally predicted best at the supersonic Mach numbers. The prediction methods, of course, do not account for this phenomenon.

When wing W_2 of aspect ratio 4 was attached to body B_1, similar flow patterns were obtained as with wing W_5 of aspect ratio 3. This can be confirmed by comparing the photographs in figures 50 and 51. Note, however, that the vortices shed from the wing tips of $B_1 W_2$ at $M_\infty = 2.0$ lie outside the photograph frames.

With the addition of the tail T to configuration $B_1 W_2$, there were no appreciable changes in the flow patterns (see photographs in figs. 51 and 52).

When wing W_2 was attached to body $N_3 C_1$, the nose-cylinder configuration that produced the greatest asymmetry at $M_\infty = 0.6$ and 0.9, the vortex asymmetry from the fineness-ratio-5 ogival nose still persisted (compare figs. 43 and 53). This asymmetry also persisted when tail T was attached to the configuration (see fig. 54).

6.3.2 *Photographs from oil-flow technique*– To obtain visual indications of the flow over the surface of the models, the oil-flow technique was used. Photographs from this technique support those from the vapor-screen technique in that flow-separation positions are quite clearly defined. As illustrated in a schematic of a body crossflow plane (sketch (l)),

oil ridges form near separation regions, and flow symmetry or asymmetry can be correlated with results from the vapor-screen technique.

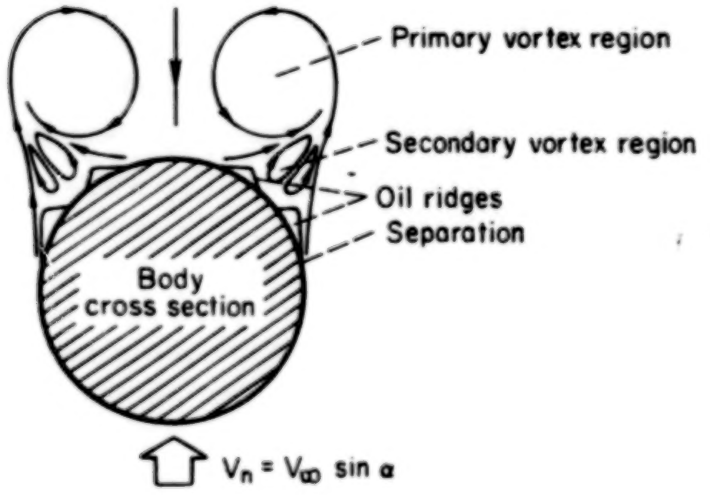

Sketch (l)

Photographs taken with the oil-flow technique for some selected models at $M_\infty = 0.6$, 0.9, and 2.0 are shown in figures 55 to 65. Both planform and side views are shown at the specified angles of attack. To avoid a tunnel support at the top of the test section, the planform views were taken with the camera somewhat off center, so the model planforms are not completely symmetrical. For convenience in comparing the oil-flow and vapor-screen photographs, the figures for each technique are indexed as follows:

Configuration	Oil-flow figures	Vapor-screen figures
$B_1 = N_1C_1$	55	41
N_2C_1	56	42
N_3C_1	57	43
N_4C_1	58	44
N_3C_1S	59	45
$B_2 \quad \phi = 0°$	60	46
$B_2 \quad \phi = 90°$	61	47

Configuration	Oil-flow figures	Vapor-screen figures
$B_3 \quad \phi = 0°$	62	48
$B_3 \quad \phi = 90°$	63	49
$B_1 W_2 T = N_1 C_1 W_2 T$	64	52
$N_3 C_1 W_2 T$	65	54

The reader, of course, can make detailed observations of the comparable oil-flow and vapor-screen photographs for configurations of particular interest. Generally, when there is asymmetric flow separation from a model surface (indicated by the oil flow), there is also asymmetric arrangement of the vortices in the flow field (indicated by the vapor screen). Again, note that the hand of the asymmetry can be either left or right. Thus, because the oil-flow and vapor-screen photographs were not taken simultaneously, it is possible to observe a left-hand separation asymmetry and a right-hand vortex asymmetry or vice versa. The observer also should be aware that some local flow disturbances in the oil flow result from joints and wax-filled screw holes in the bodies.

CHAPTER 7

EXPERIMENTAL SIDE FORCES ON MODELS AT $\beta = 0°$

When models are pitched to high angles of attack, side forces can occur on the models even at zero sideslip angle (e.g., refs. 12-21, 78, and 79). These side forces generally occur at angles of attack between about 20° to 60° and in the subsonic-transonic Mach number range. They result from asymmetric flow separation and vortex flow over the leeward side of the models as shown in the photographs presented in chapter 6.

As noted in a recent paper by Keener, Chapman, and Kruse (ref. 78), some aircraft have been lost due to uncontrolled flight at high angles of attack, and some of the loss in controllability might have originated from undesirable side forces and yawing moments attributed to flow separation and vortex asymmetry. Research on this phenomenon recently has increased considerably because the flight envelopes of modern aircraft and missiles are being extended into the higher angle-of-attack range.

We will now present and discuss some side-force data obtained recently (refs. 16, 18-21) in the Ames 6- by 6-Foot Wind Tunnel for most of the model configurations considered in previous chapters (especially chapter 6) and shown in figure 38. For the bodies alone, we will discuss the effects of nose-fineness ratio, Mach number, nose-tip rounding, afterbody side strakes, and elliptic cross section. Then we will consider the effect of adding a wing and a wing plus tail to a body.

7.1 Bodies Alone

7.1.1 *Effects of nose fineness ratio and Mach number*– In figure 66, the effect of nose fineness ratio ℓ_N/d on side-force coefficient C_Y and center position $(\ell - x_{sf})/d$ for ogive-cylinder bodies of revolution is shown. Both C_Y and $(\ell - x_{sf})/d$, measured from the body base, are plotted as a function of angle of attack α for α up to 60°. Plots are presented for $M_\infty = 0.6$, 0.9, and 1.2. The models were tested at Mach numbers up to $M_\infty = 2$, but there were no side forces above about $M_\infty = 1.2$. The magnitudes of the side forces decrease with increasing Mach number.

It is readily apparent from figure 66 that the largest side forces were obtained with the fineness-ratio-5 nose N_3 attached to the cylinder afterbody C_1 (of fineness ratio 7). With decrease in nose fineness ratio, the side forces decrease, and they almost disappear over most of

the α range for the body with the fineness-ratio-3 nose. For body N_3C_1 (with the fineness-ratio-5 nose) at $M_\infty = 0.6$, it has been shown that the maximum value of side force can become about 40 percent of the normal force (ref. 16). Keener et al. (ref. 78) have recently shown that the maximum value of C_Y increases even more (to the order of C_N or greater) as the Mach number is decreased from 0.6 to 0.25. There is no question that the side-force coefficients increase with decrease in Mach number and/or increase in nose fineness ratio. Wardlaw and Morrison (ref. 79) also support these conclusions from their recent correlations of collected data.

Note that the side-force centers seem to start well back on the cylinder; then as α increases above about 25°, they move forward onto the nose (see, e.g., fig. 66(a)). At some much higher α (say about 45° to 55°) they then tend to move back onto the cylinder. Note also that for N_3C_1, the body with the largest side forces, the maximum values of C_Y are located well forward on the body.

The side forces can be studied in conjunction with the vapor-screen photographs shown in chapter 6. In figure 67, the data for N_3C_1 at $M_\infty = 0.6$ and 0.9 are plotted along with the vapor-screen photographs (from figs. 43(a) and (b)) taken at $\alpha = 10°$, 20°, 30°, 40°, and 50°. The vapor-screen photographs shown in figure 67 were taken at a crossplane station 3.5 diameters forward of the model base. It is obvious that when the vortices become asymmetric (between $\alpha = 20°$ and 30°) the side forces develop. So long as the vortices remain steadily asymmetric, the side forces remain. Of course, as shown in chapter 6, an asymmetric vortex system results from asymmetric flow separation from the body surface. There is obviously a need to analytically model the instability process that leads to asymmetric separation, asymmetric vortices, and undesirable side forces.

In lieu of a theoretical method for computing the angle of attack for onset of side force, experimental procedures must be used. Keener et al. (ref. 78) have found that the onset angles can be roughly correlated with nose fineness ratio (or semiapex angle) as families of curves of constant afterbody. They have found that the angle of onset of side force for a given body is essentially invariant with Mach number, and, for a nose with no afterbody, the onset angle is given approximately by two times the semiapex angle. The general effect of increasing afterbody length is to decrease the angle of onset; that is, the longer the afterbody the smaller the angle at which a side force is first encountered. A

somewhat similar finding is reported by Wardlaw and Morrison (ref. 79). They also have produced (ref. 79) a rough correlation of data for the angle of attack at which the maximum side force is observed. It tends to decrease with increasing Mach number and body fineness ratio.

Keener et al. (ref. 78) also have made a rough correlation of data for the "upper-limit" angle of attack at which the static side force disappears and the wake flow becomes essentially oscillatory like a Karman vortex street from a two-dimensional cylinder. This upper-limit α also tends to decrease with increasing Mach number, varying from about a maximum of 80° at $M_\infty = 0.25$ to a minimum of 50° at $M_\infty = 0.9$.

7.1.2 *Effect of nose-tip rounding*– When the tip of a fineness-ratio-3.5 nose (N_2) was rounded to make a fineness-ratio-3 nose (N_4), the side forces at $M_\infty = 0.6$ and 0.9 almost disappeared. This is shown in figure 68 where C_Y and its center position are plotted against α for bodies N_1C_1, N_2C_1, and N_4C_1. As discussed in chapter 6, this nose rounding brought more symmetry to the flow field. The round-nosed body N_4C_1, however, appears to be no better than the sharp-nosed body N_1C_1 of the same fineness ratio ($\ell_N/d = 3$).

7.1.3 *Effect of afterbody side strakes*– When strakes were attached to the sides of the cylinder C_1 of body N_3C_1 ($\ell_N/d = 5$), the side forces were not significantly changed. As shown in figure 69, the variation of C_Y with α was changed somewhat, but the maximum values of C_Y were about the same.

7.1.4 *Effect of elliptic cross section*– The effect of elliptic cross section and roll angle on side-force coefficient and position is shown in figure 70. Results are compared for body B_1 (a circular body of $\ell/d = 10$) and body B_2 (the equivalent elliptic body of constant $a/b = 2$) at $M_\infty = 0.6$ and 0.9. With the elliptic body B_2 oriented at $\phi = 0°$ (flat side pitching against the free-stream flow), the side-force coefficients are very small and close to those for B_1. However, when B_2 is rolled to $\phi = 90°$, the side-force coefficients increase considerably. According to reference 18, C_Y becomes more than twice C_N at $\alpha = 50°$ for B_2 at $\phi = 90°$ and $M_\infty = 0.6$. As shown in chapter 6, the separation and vortex patterns were very symmetric for B_2 at $\phi = 0°$, but they became very asymmetric for B_2 at $\phi = 90°$.

From tests of body B_3, the body of elliptic cross section with variable a/b, it was found that the wake flow-field asymmetry and side forces were influenced mostly by the nose. As shown in figure 71, when B_3 was oriented at $\phi = 0°$ (flattest side of nose pitching

against the free-stream flow), the side-force coefficients were very small and close to those for B_1 (the equivalent body of revolution). However, when B_3 was rolled to $\phi = 90°$, undesirable side forces developed, and, as shown in chapter 6, the vortex flow was quite asymmetric (fig. 49).

As for the bodies of revolution, the maximum values of side-force coefficient decreased as the free-stream Mach number increased. At $M_\infty = 1.5$ there were essentially no side forces measured on any of the elliptic bodies, even for the worst roll orientation (ref. 18).

7.2 Body-Wing and Body-Wing-Tail Configurations

7.2.1 *Effects of adding a wing and a wing plus tail to a body*– In figure 72, the effects on side-force coefficient and side-force position of adding a wing and a wing plus tail to a body are shown. The body N_3C_1, which has a fineness-ratio-5 nose, produced the largest side forces for the bodies of revolution tested. As shown in figure 72, these side forces and their positions remain about the same with the thin wing W_2 of aspect ratio 4 attached or even with the tail T added. (Dimensions for the wing and tail are given in fig. 29 and for the body in fig. 37.)

From these comparisons it can be concluded that the most important influence comes from the body nose. As mentioned in chapter 6, the vortex asymmetry that appeared from the fineness-ratio-5 nose, when tested with only the afterbody cylinder C_1, still persisted when the wing and the wing plus tail were attached (see e.g., figs. 43, 53, and 54).

7.2.2 *Effects of wing aspect ratio and taper ratio*– For thin wings of about equal planform area (fig. 29) but with aspect ratios of 3, 4, and 5, there was essentially no effect of aspect ratio on the measured side forces for the body-wing models tested (ref. 20). Likewise, a change in taper ratio from 0 to about 0.5 resulted in no appreciable side-force effect (ref. 20). The results were also unchanged when the tail T (fig. 29) was attached to the wing-body models (ref. 21).

CHAPTER 8

CONCLUDING REMARKS

A review and an extension of an engineering-type method have been presented for computing the normal-force and pitching-moment coefficients for slender bodies of circular and noncircular cross section alone and with lifting surfaces. In this method, a semiempirical term representing viscous separation crossflow is added to a term representing potential-theory crossflow. In the generalized equations written for C_N and C_m, ratios are required of the local normal-force coefficient per unit length for the cross section of interest to that for the equivalent (same area) circular cross section. These ratios are given both from slender-body and Newtonian theories. Formulas and numerical values of these ratios are included here for winged-elliptic and winged-square cross sections, the square cross sections having rounded corners if desired.

In computing normal-force and pitching-moment coefficients for the bodies alone, slender-body theory was used for the term representing potential crossflow. In computations for the bodies with thin wings and a tail, the linearized potential-flow method of Nielsen, Kaattari, and Pitts was used, modified for high angles of attack.

For many bodies of revolution, computed aerodynamic characteristics were found to agree well with measured results for investigated free-stream Mach numbers from 0.6 to 2.9. The angles of attack ranged from about 0° to 180° for $M_\infty = 2.9$ and from about 0° to 60° for $M_\infty = 0.6$ to 2.0. Agreement of predicted with measured results was best at supersonic Mach numbers.

For several bodies of elliptic cross section, measured results were also predicted reasonably well over the investigated Mach number range from 0.6 to 2.0 and at $\alpha = 0°$ to 60°. As for the bodies of revolution, the predictions were best for supersonic Mach numbers. The predictions were better for a body in which the cross-sectional shape (a/b) remained constant over the length than for a body in which it varied. Although the prediction technique probably can be improved with further research, it is felt that the predictions are sufficiently accurate for most preliminary design studies.

For body-wing and body-wing-tail configurations with wings of aspect ratio 3 and 4, measured normal-force coefficients and normal-force centers were predicted reasonably well at the upper test Mach number of 2.0. However, with a decrease in Mach number to

$M_\infty = 0.6$, the agreement for C_N rapidly deteriorated, although the normal-force centers remained in good agreement. At the subsonic Mach numbers ($M_\infty = 0.6$ and 0.9) and angles of attack above 10° or 20°, the measured results were even overpredicted somewhat by just the potential-flow term of the combination method.

From vapor-screen and oil-flow studies, it was observed that the flow was completely separated over the wings at the subsonic Mach numbers for $\alpha >$ about 20°. There was some evidence of vortex bursting or breakdown for some of the models (including bodies alone) at subsonic Mach numbers. At $M_\infty = 2$, however, discrete vortices from the bodies and wings were observed at the base of the models.

For many body, body-wing, and body-wing-tail configurations, vapor-screen and oil-flow photographs were obtained for $M_\infty = 0.6$, 0.9, and 2.0 and $\alpha = 10°, 20°, 30°, 40°$, and 50°. It has been observed that, when the separation and vortex patterns were asymmetric, undesirable side forces could be measured on the models even at zero sideslip angle. These side forces generally originated when the angle of attack exceeded about 20°.

For bodies alone, the side forces can be significantly affected by changes in Mach number, nose-fineness ratio, nose bluntness, and elliptic cross section. The side-force coefficients decrease with increase in Mach number through the subsonic-transonic range and disappear with increase in Mach number into the supersonic range.

From tests (at $0.6 \leqslant M_\infty \leqslant 2.0$) of tangent-ogive noses connected to a circular cylinder of fineness ratio 7, it has been found that the side-force coefficients increase from about zero for a fineness-ratio-3 nose to a maximum of about 40 percent of the normal-force coefficient for a fineness-ratio-5 nose. Other researchers have reported even more increases in C_Y (of the order of C_N or greater) as the Mach number is decreased from 0.6 to 0.25.

Nose-tip rounding significantly decreased the side-force coefficients for a circular body with a sharp-nosed ogive of fineness ratio 3.5. However, the beneficial decrease was no greater than that obtained by merely using a sharp-nosed ogive nose of the same fineness ratio (fineness ratio 3) as that for the resulting blunted nose.

When strakes were attached to the sides of the afterbody cylinder of an ogive-cylinder model with an undesirable fineness-ratio-5 nose, the side forces were not significantly changed. Thus, the influence of the nose was dramatized.

Changes in cross section from circular to elliptic for an ogive-cylinder body (of fineness-ratio-3 nose and fineness-ratio-7 afterbody) produced some interesting effects on side-force coefficient. At all test Mach numbers (0.6 to 2.0) and angles of attack (0° to 60°), the side-force coefficients were generally small or negligible for the circular body and the generated elliptic bodies at $\phi = 0°$ (flat side pitching against the stream crossflow). With the elliptic bodies at $\phi = 90°$, however, some values of side-force coefficient became as large as twice the values of normal-force coefficient at the same high angles of attack. From the standpoint of reducing undesirable side forces at high angles of attack, it was always found best to have the flattest side of the elliptic-body nose pitching against the stream crossflow, even when a/b was not constant over the body length.

Undesirable side forces measured for body-wing and body-wing-tail models were generally about the same as those measured for the bodies alone. As for the bodies alone, the side forces developed at subsonic Mach numbers for $\alpha >$ about 20°. Also, as for the bodies alone, the side forces and yawing moments increased with increase in nose fineness ratio. Fineness ratios greater than 3 produced the largest side forces. No effects of wing aspect ratio or taper ratio were observed. From these comparisons, it can be concluded that the most important influence comes from the body nose.

Ames Research Center

National Aeronautics and Space Administration

Moffett Field, California 94035, March 18, 1977

APPENDIX A

DERIVATION OF $(C_n/C_{n_o})_{Newt}$ FOR WINGED-CIRCULAR AND WINGED-ELLIPTIC CROSS SECTIONS

Winged-Circular Cross Section with Wing Planform Perpendicular to Crossflow Velocity

For blunt configurations of the type shown in sketch (m), it is assumed that each elemental particle of fluid strikes the configuration at velocity V_n and thereupon loses its normal component of momentum. This leads to the well-known Newtonian expression for the pressure coefficient:

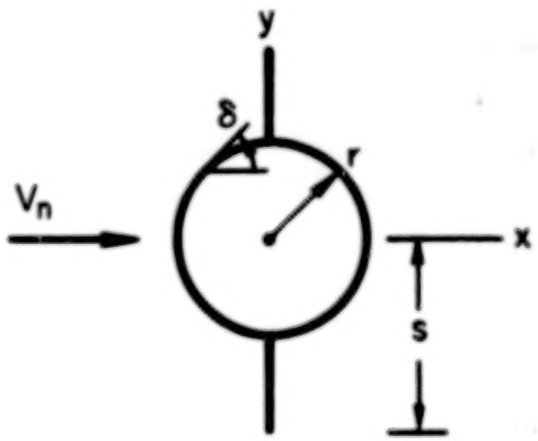

Sketch (m)

$$C_p = 2 \sin^2 \delta \qquad \text{(A1)}$$

where δ is the local angle that a tangent to a forward-facing surface makes with the free-stream direction (sketch(m)). In Newtonian flow, the pressure coefficients over the rearward face are assumed to be zero. The total section crossflow drag coefficient (based on body diameter, $d = 2r$) is then given by

$$C_d = \frac{2}{d} \int_0^s C_p \, dy$$

$$= \frac{2}{d} \int_0^r C_{p_{body}} \, dy + \frac{2}{d} \int_r^s C_{p_{wing}} \, dy \qquad \text{(A2)}$$

For a circular section, as shown in sketch (m),

$$x^2 + y^2 = r^2 \qquad \text{(A3)}$$

$$\tan \delta = \frac{dy}{dx} = -\frac{x}{y} = -\sqrt{\frac{r^2}{y^2} - 1} \qquad \text{(A4)}$$

$$\sin^2 \delta = \frac{\tan^2 \delta}{1 + \tan^2 \delta} = 1 - \frac{y^2}{r^2} \tag{A5}$$

Equations (A1) and (A5) are substituted into equation (A2) to give

$$C_d = \frac{1}{r} \int_0^r 2 \left(1 - \frac{y^2}{r^2}\right) dy + \frac{1}{r} \int_r^s 2 \, dy \tag{A6}$$

since

$$C_{p_{wing}} = 2 \sin^2 \delta = 2 \tag{A7}$$

From integration of equation (A6), we obtain

$$C_d = \frac{4}{3} + 2 \left(\frac{s}{r} - 1\right) = 2 \left(\frac{s}{r} - \frac{1}{3}\right) \tag{A8}$$

where, for the equivalent circular section,

$$C_{d_n} = \frac{4}{3} \tag{A9}$$

Thus, the ratio of the normal-force coefficient per unit length for the winged-circular section to that for the equivalent circular section is given by

$$\left(\frac{C_n}{C_{n_o}}\right)_{Newt} = \left(\frac{C_d}{C_{d_n}}\right)_{Newt} = \frac{3}{2} \left(\frac{s}{r} - \frac{1}{3}\right) \tag{A10}$$

Winged-Elliptic Cross Section with Semimajor Axis and Wing Planform Perpendicular to Crossflow Velocity

For a winged-elliptic cross section where the semimajor axis a and the wing planform are perpendicular to the crossflow velocity V_n (see sketch (n)), the same procedure is followed in the derivation of $(C_n/C_{n_o})_{Newt}$ as introduced for the winged-circular cross section. Both the basic equations, (A1) and (A2), are used again.

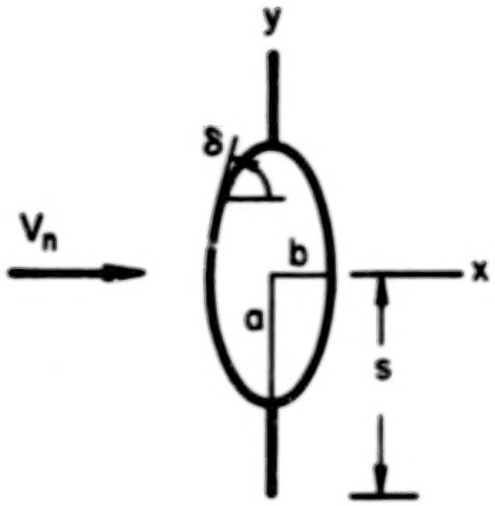

Sketch (n)

For an elliptic body, as shown in sketch (n)

$$\frac{x^2}{b^2} + \frac{y^2}{a^2} = 1 \tag{A11}$$

$$\tan \delta = \frac{dy}{dx} = -\frac{a^2}{b^2}\left(\frac{x}{y}\right) = -\frac{a}{b}\sqrt{\frac{a^2}{y^2} - 1} \tag{A12}$$

and

$$\sin^2 \delta = \frac{\tan^2 \delta}{1 + \tan^2 \delta} = \frac{a^2 - y^2}{a^2 - y^2[1 - (b^2/a^2)]} \tag{A13}$$

With equation (A13) combined with equations (A1), (A2), and (A7), we obtain the section crossflow drag coefficient:

$$C_d = \frac{4}{d}\int_0^a \frac{a^2 - y^2}{a^2 - y^2[1 - (b^2/a^2)]}\,dy + \frac{4}{d}\int_a^s dy \tag{A14}$$

where d is the diameter of the equivalent circular body and is given by

$$d = 2\sqrt{ab} \tag{A15}$$

Also, as for the winged-circular cross section, the crossflow drag coefficient for the equivalent circular cross section is given by $C_{d_n} = 4/3$.

Thus, by integrating equation (A14), substituting $2\sqrt{ab}$ for d, and dividing the result by 4/3, we obtain

$$\left(\frac{C_n}{C_{n_o}}\right)_{Newt} = \frac{3}{2}\sqrt{\frac{a}{b}}\left\{\frac{-b^2/a^2}{[1 - (b^2/a^2)]^{3/2}}\log\left[\frac{a}{b}\left(1 + \sqrt{1 - \frac{b^2}{a^2}}\right)\right] + \frac{1}{1 - (b^2/a^2)} + \frac{s}{a} - 1\right\} \tag{A16}$$

since

$$\left(\frac{C_n}{C_{n_o}}\right)_{Newt} = \left(\frac{C_d}{C_{d_n}}\right)_{Newt}$$

Winged-Elliptic Cross Section with Semiminor Axis and Wing Planform Perpendicular to Crossflow Velocity

For a winged-elliptic cross section where the semiminor axis b and the wing planform are perpendicular to the crossflow velocity V_n (sketch (o)), the same procedure is followed as for the previous configurations.

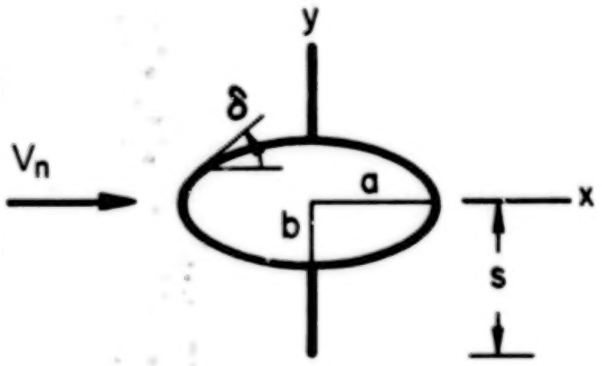

Sketch (o)

For an elliptic body as shown in sketch (o),

$$\frac{x^2}{a^2} + \frac{y^2}{b^2} = 1 \tag{A17}$$

$$\tan \delta = \frac{dy}{dx} = -\frac{b^2}{a^2}\left(\frac{x}{y}\right) = -\frac{b}{a}\sqrt{\frac{b^2}{y^2} - 1} \tag{A18}$$

and

$$\sin^2 \delta = \frac{\tan^2 \delta}{1 + \tan^2 \delta} = \frac{b^2 - y^2}{b^2 - y^2[1 - (a^2/b^2)]} \tag{A19}$$

With equation (A19) combined with equations (A1), (A2), and (A7), we obtain

$$C_d = \frac{4}{d}\int_o^b \frac{b^2 - y^2}{b^2 - y^2[1 - (a^2/b^2)]}\, dy + \frac{4}{d}\int_o^s dy \tag{A20}$$

where $d = 2\sqrt{ab}$ is the diameter of the equivalent circular cross section. As before, the crossflow drag coefficient for the equivalent circular cross section is given by $C_{d_n} = 4/3$.

Thus, by integrating equation (A20), substituting $2\sqrt{ab}$ for d, and dividing the result by 4/3, we obtain

$$\left(\frac{C_n}{C_{n_O}}\right)_{Newt} = \frac{3}{2}\sqrt{\frac{b}{a}}\left\{\frac{a^2/b^2}{[(a^2/b^2)-1]^{3/2}}\tan^{-1}\left(\sqrt{\frac{a^2}{b^2}-1}\right) - \frac{1}{(a^2/b^2)-1} + \frac{s}{b} - 1\right\} \quad \text{(A21)}$$

since

$$\left(\frac{C_n}{C_{n_O}}\right)_{Newt} = \left(\frac{C_d}{C_{d_n}}\right)_{Newt}$$

APPENDIX B

DERIVATION OF $(C_n/C_{n_o})_{Newt}$ FOR WINGED-SQUARE CROSS SECTIONS WITH ROUNDED CORNERS

For winged-square cross sections with rounded corners (sketch (p)), the pressure coefficient over the front face is given by

$$C_p = 2 \sin^2 \delta \qquad \text{(B1)}$$

where δ is the local angle that a tangent to a forward-facing surface makes with the free-stream direction. In Newtonian flow, the pressure coefficients over the rearward face are assumed to be zero. The total section drag coefficient (based on width w) is then given by

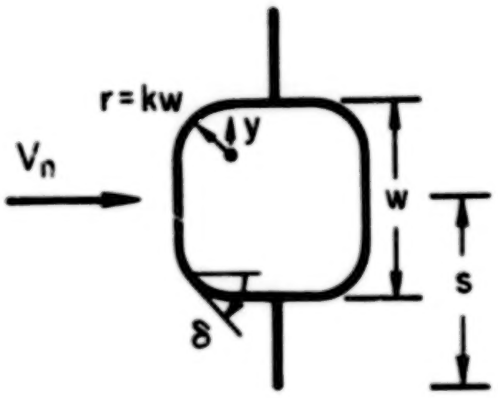

Sketch (p)

$$\begin{aligned} C_d &= \frac{2}{w}\int_o^s C_p \, dy \\ &= \frac{2}{w}\int_o^{w/2} C_{p_{body}} \, dy + \frac{2}{w}\int_{w/2}^s C_{p_{wing}} \, dy \\ &= \frac{2}{w}\int_o^{(w/2)-r} C_{p_{flat}} \, dy + \frac{2}{w}\int_o^r C_{p_{corner}} \, dy + \frac{2}{w}\int_{w/2}^s C_{p_{wing}} \, dy \end{aligned} \qquad \text{(B2)}$$

For a rounded corner, as shown in sketch (p),

$$x^2 + y^2 = r^2 \qquad \text{(B3)}$$

$$\tan \delta = \frac{dy}{dx} = -\frac{x}{y} = -\sqrt{\frac{r^2}{y^2} - 1} \qquad \text{(B4)}$$

and

$$\sin^2 \delta = \frac{\tan^2 \delta}{1 + \tan^2 \delta} = 1 - \frac{y^2}{r^2} \qquad \text{(B5)}$$

The pressure coefficient for the rounded corner, obtained by substituting equation (B5) into (B1), is

$$C_{p_{corner}} = 2\left(1 - \frac{y^2}{r^2}\right) \tag{B6}$$

The pressure coefficients for the front flat portion of the body and for the wing are given by

$$C_p = 2 \sin^2 \delta = 2 \tag{B7}$$

since $\delta = 90°$.

Thus, with equations (B6) and (B7) substituted into equation (B2), we write

$$C_d = \frac{4}{w}\int_0^{(w/2)-r} dy + \frac{4}{w}\int_0^{r}\left(1 - \frac{y^2}{r^2}\right) dy + \frac{4}{w}\int_{w/2}^{s} dy \tag{B8}$$

From integration of equation (B8), we obtain

$$C_d = \frac{4}{w}\left(s - \frac{r}{3}\right) = 4\left(\frac{s}{w} - \frac{k}{3}\right) \tag{B9}$$

Now, to obtain $(C_n/C_{n_o})_{Newt}$, it is necessary to find the diameter d of the equivalent circular cross section which has the same area as the cross section studied. The area of the equivalent circular cross section is, of course,

$$A = \frac{\pi}{4} d^2 \tag{B10}$$

and the area of the cross section studied is

$$A = w^2[1 - k^2(4 - \pi)] \tag{B11}$$

By equating equations (B10) and (B11), we obtain the equivalent diameter

$$d = 2w\sqrt{\frac{1 - (4 - \pi)k^2}{\pi}} \tag{B12}$$

With C_d from equation (B9) based on d instead of w,

$$C_d = 4\left(\frac{s}{w} - \frac{k}{3}\right)\frac{w}{d} \tag{B13}$$

where, for the equivalent circular section,

$$C_{d_n} = \frac{4}{3} \tag{B14}$$

Thus, from equations (B12), (B13), and (B14), we obtain

$$\left(\frac{C_n}{C_{n_o}}\right)_{Newt} = \left(\frac{C_d}{C_{d_n}}\right)_{Newt} = \frac{3}{2}\left(\frac{s}{w} - \frac{k}{3}\right)\sqrt{\frac{\pi}{1 - (4 - \pi)k^2}}\ ; \tag{B15}$$

$$0 \leq k \leq 0.5$$

APPENDIX C

FORMULAS TO COMPUTE GEOMETRIC PARAMETERS FOR TANGENT OGIVES

To compute the aerodynamic characteristics of bodies of revolution having tangent ogive nose shapes, various geometric parameters must be obtained. To compute C_N and C_m, the planform area A_p is required; to compute C_m, it is also necessary to obtain volume V and distance x_c from the nose vertex to the centroid of planform area. To compute skin-friction drag, the wetted surface area A_s is needed.

For an ogival nose of length ℓ_N and diameter d (see sketch (q)) the following useful formulas have been derived (ref. 9):

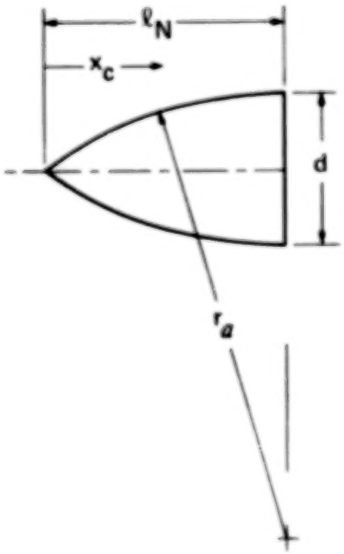

Sketch (q)

$$\frac{A_p}{d^2} = \frac{\ell_N}{d}\sqrt{R^2 - \left(\frac{\ell_N}{d}\right)^2} + R^2 \sin^{-1}\left(\frac{\ell_N/d}{R}\right) - 2\left(\frac{\ell_N}{d}\right)\left(R - \frac{1}{2}\right) \tag{C1}$$

$$\frac{V}{d^3} = \pi\left[\frac{2}{3}\left(\frac{\ell_N}{d}\right)^3 - \frac{A_p}{d^2}\left(R - \frac{1}{2}\right)\right] \tag{C2}$$

$$\frac{x_c}{d} = \frac{\ell_N}{d} - \frac{(2/3)\left\{R^3 - [R^2 - (\ell_N/d)^2]^{3/2}\right\} - (\ell_N/d)^2\,[R - (1/2)]}{A_p/d^2} \tag{C3}$$

and

$$\frac{A_s}{d^2} = 2\pi R\left[\left(R - \frac{1}{2}\right)\sin^{-1}\left(\frac{-\ell_N/d}{R}\right) + \frac{\ell_N}{d}\right] \tag{C4}$$

where R is the ratio of the ogival arc radius r_a to base diameter d and

$$R = \frac{r_a}{d} = \left(\frac{\ell_N}{d}\right)^2 + \frac{1}{4} \tag{C5}$$

REFERENCES

1. Allen, H. Julian: Estimation of the Forces and Moments Acting on Inclined Bodies of Revolution of High Fineness Ratio. NACA RM A9126, 1949.
2. Allen, H. Julian; and Perkins, Edward W.: A Study of Effects of Viscosity on Flow Over Slender Inclined Bodies of Revolution. NACA Rep. 1048, 1951.
3. Perkins, Edward M.; and Kuehn, Donald M.: Comparison of the Experimental and Theoretical Distributions of Lift on a Slender Inclined Body of Revolution at M = 2. NACA TN 3715, 1956.
4. Perkins, Edward W.; and Jorgensen, Leland, H.: Comparison of Experimental and Theoretical Normal-Force Distributions (Including Reynolds Number Effects) on an Ogive-Cylinder Body at Mach Number 1.98. NACA TN 3716, 1956.
5. Jorgensen, Leland H.; and Perkins, Edward W.: Investigation of Some Wake Vortex Characteristics of an Inclined Ogive-Cylinder Body at Mach Number 2. NACA Rep. 1371, 1958.
6. Jorgensen, Leland H.: Inclined Bodies of Various Cross Sections at Supersonic Speeds. NASA MEMO 10-3-58A, 1958.
7. Jorgensen, Leland H.; and Treon, Stuart L.: Measured and Estimated Aerodynamic Characteristics for a Model of a Rocket Booster at Mach Numbers From 0.6 to 4 and at Angles of Attack From 0° to 180°. NASA TM X-580, 1961.
8. Saffell, Bernard F., Jr.; Howard, Millard L.; and Brooks, Eugene N., Jr.: Method for Predicting the Static Aerodynamic Characteristics of Typical Missile Configurations for Angles of Attack to 180 Degrees. Rep. 3645, Naval Ship Research and Development Center, March 1971.
9. Jorgensen, Leland H.: Prediction of Static Aerodynamic Characteristics for Space-Shuttle-Like and Other Bodies at Angles of Attack From 0° to 180°. NASA TN D-6996, 1973.
10. Jorgensen, Leland H.: Estimation of Aerodynamics for Slender Bodies Alone and With Lifting Surfaces at α's From 0° to 90°. AIAA J., vol. 11, no. 3, March 1973, pp. 409-412.

11. Jorgensen, Leland H.: A Method for Estimating Static Aerodynamic Characteristics for Slender Bodies of Circular and Noncircular Cross Section Alone and With Lifting Surfaces at Angles of Attack from 0° to 90°. NASA TN D-7228, 1973.

12. Pick, George S.: Side Forces on Ogive-Cylinder Bodies at High Angles of Attack in Transonic Flow. J. Spacecraft & Rockets, vol. 9, no. 6, June 1972, pp. 389-390.

13. Clark, William H.; Peoples, John R.; and Briggs, M. Michael: Occurrence and Inhibition of Large Yawing Moments During High Incidence Flight of Slender Missile Configurations. AIAA Paper 72-968, 1972.

14. Coe, Paul L., Jr.; Chambers, Joseph R.; and Letko, William: Asymmetric Lateral-Directional Characteristics of Pointed Bodies of Revolution at High Angles of Attack. NASA TN D-7095, 1972.

15. Fleeman, E. L.; and Nelson, R. C.: Aerodynamic Forces and Moments on a Slender Body With a Jet Plume for Angles of Attack Up to 180 Degrees. AIAA Paper 74-110, 1974.

16. Jorgensen, Leland H.; and Nelson, Edgar R.: Experimental Aerodynamic Characteristics for a Cylindrical Body of Revolution With Various Noses at Angles of Attack From 0° to 58° and Mach Numbers From 0.6 to 2.0. NASA TM X-3128, 1974.

17. Keener, Earl R.; and Chapman, Gary T.: Onset of Aerodynamic Side Forces at Zero Sideslip on Symmetric Forebodies at High Angles of Attack. AIAA Paper 74-770, 1974.

18. Jorgensen, Leland H.; and Nelson, Edgar R.: Experimental Aerodynamic Characteristics for Bodies of Elliptic Cross Section at Angles of Attack From 0° to 58° and Mach Numbers From 0.6 to 2.0. NASA TM X-3129, 1975.

19. Jorgensen, Leland H.; and Nelson, Edgar R.: Experimental Aerodynamic Characteristics for a Cylindrical Body of Revolution With Side Strakes and Various Noses at Angles of Attack from 0° to 58° and Mach Numbers From 0.6 to 2.0. NASA TM X-3130, 1975.

20. Jorgensen, Leland H.; and Howell, Michael H.: Experimental Aerodynamic Characteristics for Slender Bodies With Thin Wings at Angles of Attack From 0° to 58° and Mach Numbers from 0.6 to 2.0. NASA TM X-3309, 1976.

21. Jorgensen, Leland H.; and Nelson, Edgar R.: Experimental Aerodynamic Characteristics for Slender Bodies with Thin Wings and Tail at Angles of Attack From 0° to 58° and Mach Numbers from 0.6 to 2.0. NASA TM X-3310, 1976.

22. Kelly, H. R.: The Estimation of Normal Force, Drag, and Pitching Moment Coefficients for Blunt Based Bodies of Revolution at Large Angles of Attack. J. Aeronaut. Sci., vol. 21, no. 8, Aug. 1954, pp. 549-555.

23. Wardlaw, Andrew B., Jr.: Prediction of Yawing Force at High Angle of Attack. AIAA J., vol. 12, no. 8, Aug. 1974, pp. 1142-1144.

24. Wardlaw, Andrew B., Jr.: Multivortex Model of Asymmetric Shedding on Slender Bodies at High Angle of Attack. AIAA Paper 75-123, 1975.

25. Thomson, K. D.; and Morrison, D. F.: The Spacing, Position, and Strength of Vortices in the Wake of Slender Cylindrical Bodies at Large Incidence. J. Fluid Mech., vol. 50, pt. 4, 1971, pp. 751-783.

26. Thomson, K. D.: The Estimation of Viscous Normal Force, Pitching Moment, Side Force and Yawing Moment on Bodies of Revolution at Incidences Up to 90°. Australian Weapons Research Est. WRE-Rep. 782, 1972.

27. Sarpkaya, T.: Separated Flow About Lifting Bodies and Impulsive Flow About Cylinders. AIAA J., vol. 4, no. 3, 1966, pp. 414-420.

28. Bryson, A. E.: Symmetric Vortex Separation on Circular Cylinders and Cones. J. Appl. Mech., vol. 26, Dec. 1959, pp. 643-648.

29. Schindel, L. H.: Effects of Vortex Separation on the Lift Distribution on Bodies of Elliptic Cross Section. J. Aircraft, vol. 6, no. 6, June 1969, pp. 537-542.

30. Angelucci, S. B.: A Multivortex Method for Axisymmetric Bodies at Angle of Attack. J. Aircraft, vol. 8, no. 12, Dec. 1971, pp. 959-966.

31. Marshall, J. F.; and Deffenbaugh, F. D.: Separated Flow Over Bodies of Revolution Using an Unsteady Discrete-Vorticity Cross Wake. NASA CR-2414, 1974.

32. Fidler, J. E.; and Bateman, M. C.: Asymmetric Vortex Effects on Missile Configurations. AIAA Paper 75-209, 1975.

33. Walitt, L.; and Trulio, J. G.: A Numerical Method for Computing Three-Dimensional Viscous Supersonic Flow Field About Slender Bodies. NASA CR-1963, 1971.

34. Lubard, S. C.; and Helliwell, W. S.: Calculation of the Flow on a Cone at High Angle of Attack. AIAA Paper 73-636, 1973.

35. Munk, Max M.: The Aerodynamic Forces on Airship Hulls. NACA Rep. 184, 1923.

36. Lamb, Horace: The Inertia Coefficients of an Ellipsoid Moving in Fluid. British Advisory Committee for Aeronautics, R&M 623, Oct. 1918.

37. Ward, G. N.: Supersonic Flow Past Slender Pointed Bodies. Quar. J. Mech. & Appl. Math., vol. 2, pt. I, March 1949, pp. 75-97.

38. Pitts, William C.; Nielsen, Jack N.; and Kaattari, George E.: Lift and Center of Pressure of Wing-Body-Tail Combinations at Subsonic, Transonic, and Supersonic Speeds. NACA Rep. 1307, 1957.

39. Wieselberger, C.: New Data on the Laws of Fluid Resistance. NACA TN 84, 1922.

40. Lindsey, W. F.: Drag of Cylinders of Simple Shapes. NACA Rep. 619, 1938.

41. Delany, Noel K.; and Sorensen, Norman E.: Low-Speed Drag of Cylinders of Various Shapes. NACA TN 3038, 1953.

42. Polhamus, Edward C.; Geller, Edward W.; and Grunwald, Kalman J.: Pressure and Force Characteristics of Noncircular Cylinders as Affected by Reynolds Number With a Method Included for Determining the Potential Flow About Arbitrary Shapes. NASA TR R-46, 1959.

43. Polhamus, Edward C.: Effect of Flow Incidence and Reynolds Number on Low-Speed Aerodynamic Characteristics of Several Noncircular Cylinders With Applications to Directional Stability and Spinning. NASA TR R-29, 1959.

44. Lindsey, W. F.: Drag of Cylinders of Simple Shapes NACA Rep. 619, 1938.

45. Stack, John: Compressibility Effects in Aeronautical Engineering. NACA ACR, 1941.

46. Gowen, Forrest E.; and Perkins, Edward W.: Drag of Circular Cylinders for a Wide Range of Reynolds Numbers and Mach Numbers. NACA TN 2960, 1953.

47. Walter, L. W.; and Lange, A. H.: Surface Temperature and Pressure Distributions on a Circular Cylinder in Supersonic Cross-Flow. NAVORD Rep. 2854 (Aeroballistic Res. Rep. 180), U. S. Naval Ord. Lab., White Oak, Md., June 5, 1953.

48. Penland, Jim A.: Aerodynamic Characteristics of a Circular Cylinder at Mach Number 6.86 and Angles of Attack up to 90°. NACA TN 3861, 1957.

49. Welsh, Clement J.: The Drag of Finite-Length Cylinders Determined from Flight Tests at High Reynolds Numbers for a Mach Number Range From 0.5 to 1.3. NACA TN 2941. 1953.

50. Hamilton, Richard K.: Correlation of Space Shuttle Applicable Experimental Hypersonic Aerodynamic Characteristics With Theory. NASA TM X-2272, 1971, pp. 455-492.

51. Relf, E. F.: Discussion of the Results of Measurements of the Resistance of Wires, with Some Additional Tests on the Resistance of Wires of Small Diameter. R&M 102, British A.C.A., 1914.

52. Roshko, Anatol: Experiments on the Flow Past a Circular Cylinder at Very High Reynolds Numbers. J. Fluid Mech., vol. 10, pt. 3, May 1961, pp. 345-356.

53. Schmidt, Louis V.: Fluctuating Force Measurements Upon a Circular Cylinder at Reynolds Numbers Up to 5×10^6. NASA TM X-57,779, 1966.

54. Jones, George W., Jr.; Cincotta, Joseph J.; and Walker, Robert W.: Aerodynamic Forces on a Stationary and Oscillating Circular Cylinder at High Reynolds Numbers. NASA TR R-300, 1969.

55. Lockwood, Vernard E.: Effects of Reynolds Number and Flow Incidence on the Force Characteristics of a Family of Flat-Front Cylinders. NASA TN D-3932, 1967.

56. Goldstein, Sydney: Modern Developments in Fluid Dynamics. Oxford, The Clarendon Press, vol. 2, sec. 195, 1938, pp. 439-440.

57. McKinney, Linwood W.: Effects of Fineness Ratio and Reynolds Number on the Low-Speed Crosswind Drag Characteristics of Circular and Modified-Square Cylinders. NASA TN D-540, 1960.

58. Bryson, Arthur E., Jr.: Stability Derivatives for a Slender Missile With Application to a Wing-Body-Vertical-Tail Configuration. J. Aeronaut. Sci., vol. 20, no. 5, May 1953, pp. 297-308.

59. Bryson, Arthur E., Jr.: Evaluation of the Inertia Coefficients of the Cross Section of a Slender Body. J. Aeronaut. Sci., vol. 21, no. 6, June 1954, pp. 424-427.

60. Bryson, Arthur E., Jr.: The Aerodynamic Forces on a Slender Low (or High) Wing, Circular Body, Vertical Tail Configuration. J. Aeronaut. Sci., vol. 21, no. 8, Aug. 1954, pp. 574-575.

61. Nielsen, Jack N.: Missile Aerodynamics. New York, McGraw-Hill Book Company, Inc., 1960.

62. Nelson, R. C.; and Fleeman, E. L.: High Angle-of-Attack Aerodynamics on a Slender Body with a Jet Plume. J. Spacecraft & Rockets, vol. 12, no. 1, Jan. 1975, pp. 12-16.

63. Jernell, Lloyd S.: Aerodynamic Characteristics of Bodies of Revolution at Mach Numbers From 1.50 to 2.86 and Angles of Attack to 180°. NASA TM X-1658, 1968.

64. Van Dyke, Milton D.: First- and Second-Order Theory of Supersonic Flow Past Bodies of Revolution. J. Aeronaut. Sci., vol. 18, no. 3, Mar. 1951, pp. 161-178.

65. Tsien, Hsue-Shen: Supersonic Flow Over an Inclined Body of Revolution. J. Aeronaut. Sci., vol. 5, no. 12, Oct. 1938, pp. 480-483.

66. Jorgensen, Leland H.; and Brownson, Jack J.: Effects of Reynolds Number and Body Corner Radius on Aerodynamic Characteristics of a Space Shuttle-Type Vehicle at Subsonic Mach Numbers. NASA TN D-6615, 1972.

67. Hoerner, Sighard F.: Fluid-Dynamic Drag. Published by the author, 2 King Lane, Greenbriar, Brick Town, New Jersey 08723, 1965.

68. Ames Research Staff: Equations, Tables, and Charts for Compressible Flow. NACA Rep. 1135, 1953.

69. Mendenhall, Michael R.; Goodwin, Frederick K.; Dillenius, Marnix F. E.; and Kline, David M.: Computer Programs for Calculating the Static Longitudinal Aerodynamic Characteristics of Wing-Body-Tail Configurations. NASA CR-2474, 1975.

70. Wentz, W. H., Jr.; and Kohlman, D. L.: Wind Tunnel Investigations of Vortex Breakdown on Slender Sharp-Edged Wings. NASA CR-98737, 1968.

71. Mendenhall, Michael R.; and Nielsen, Jack N.: Effect of Symmetrical Vortex Shedding on the Longitudinal Aerodynamic Characteristics of Wing-Body-Tail Combinations. NASA CR-2473, 1975.

72. Axelson, John A.: Estimation of Transonic Aircraft Aerodynamics to High Angles of Attack. AIAA Paper 75-996, 1975.

73. Polhamus, E. C.: Prediction of Vortex-Lift Characteristics by a Leading-Edge Suction Analogy. J. Aircraft, vol. 8, no. 4, April 1971, pp. 193-199.

74. Bradley, R. G.; Smith, C. W.; and Bhateley, I. C.: Vortex-Lift Prediction for Complex Wing Planforms. J. Aircraft, vol. 10, no. 6, June 1973, pp. 379-381.

75. Lamar, J. E.: Extension of the Leading Edge Suction Analogy to Wings With Separated Flow Around the Side Edges at Subsonic Speeds. NASA TR R-428, 1974.

76. Jorgensen, Leland H.: Elliptic Cones Alone and With Wings at Supersonic Speeds. NACA TN 4045, 1957 or NACA Rep. 1376, 1958.

77. McGregor, I.: The Vapor-Screen Method of Flow Visualization. J. Fluid Mech., vol. 11, pt. 4, 1961, pp. 481-511.

78. Keener, E. R.; Chapman, G. T.; and Kruse, R. L.: Effects of Mach Number and Afterbody Length on Onset of Asymmetric Forces on Bodies at Zero Sideslip and High Angles of Attack. AIAA Paper 76-66, 1976.

79. Wardlaw, Andrew B., Jr.; and Morrison, Alfred M.: Induced Side Forces on Bodies of Revolution at High Angle of Attack. Naval Surface Weapons Center, White Oak, Md., NSWC/WOL/TR 75-176, 1975.

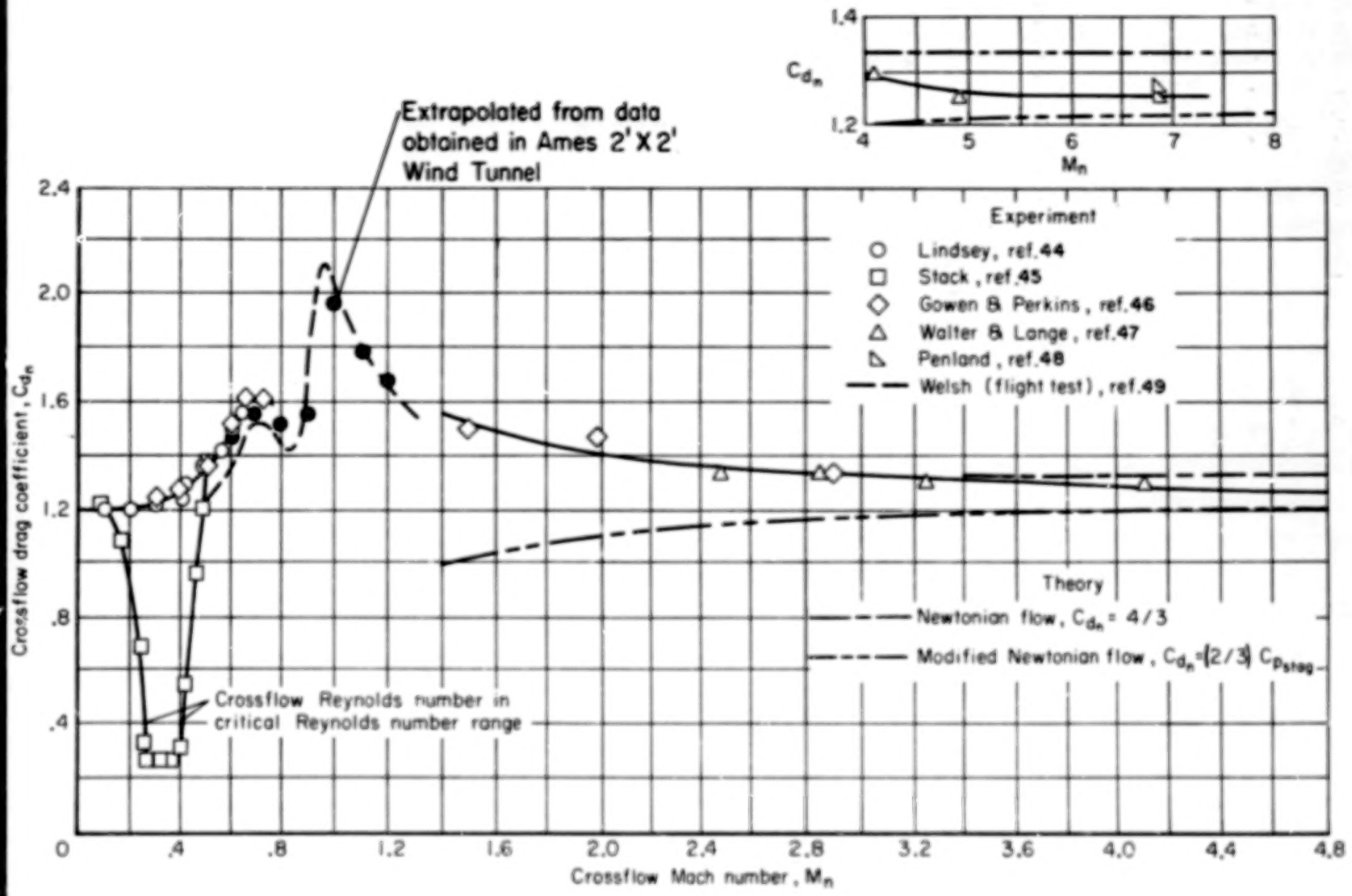

Figure 1.– Variation of crossflow drag coefficient with crossflow Mach number for circular cylinders.

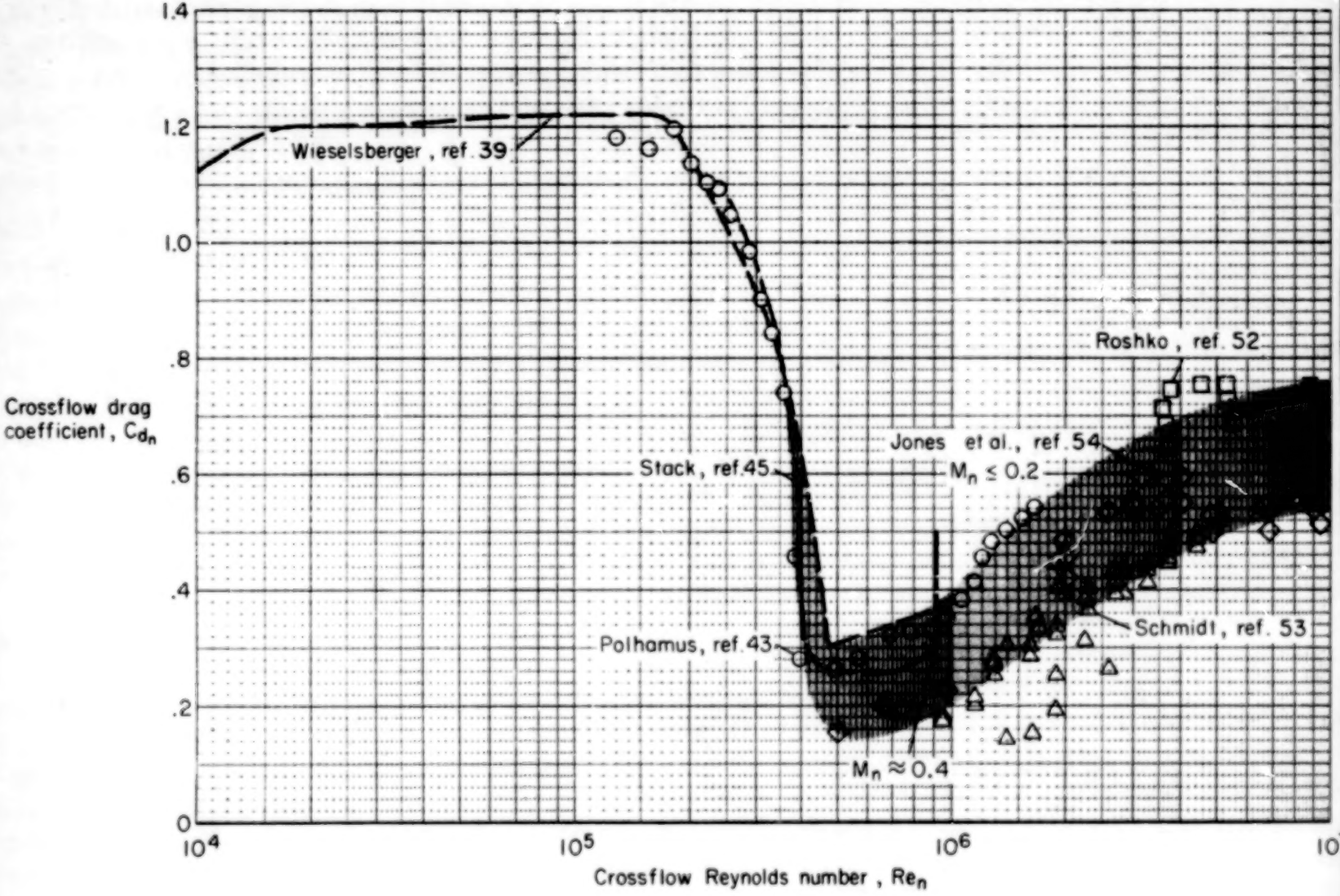

Figure 2.– Variation of crossflow drag coefficient with crossflow Reynolds number for circular cylinders at subcritical crossflow Mach numbers ($M_n \leq 0.4$).

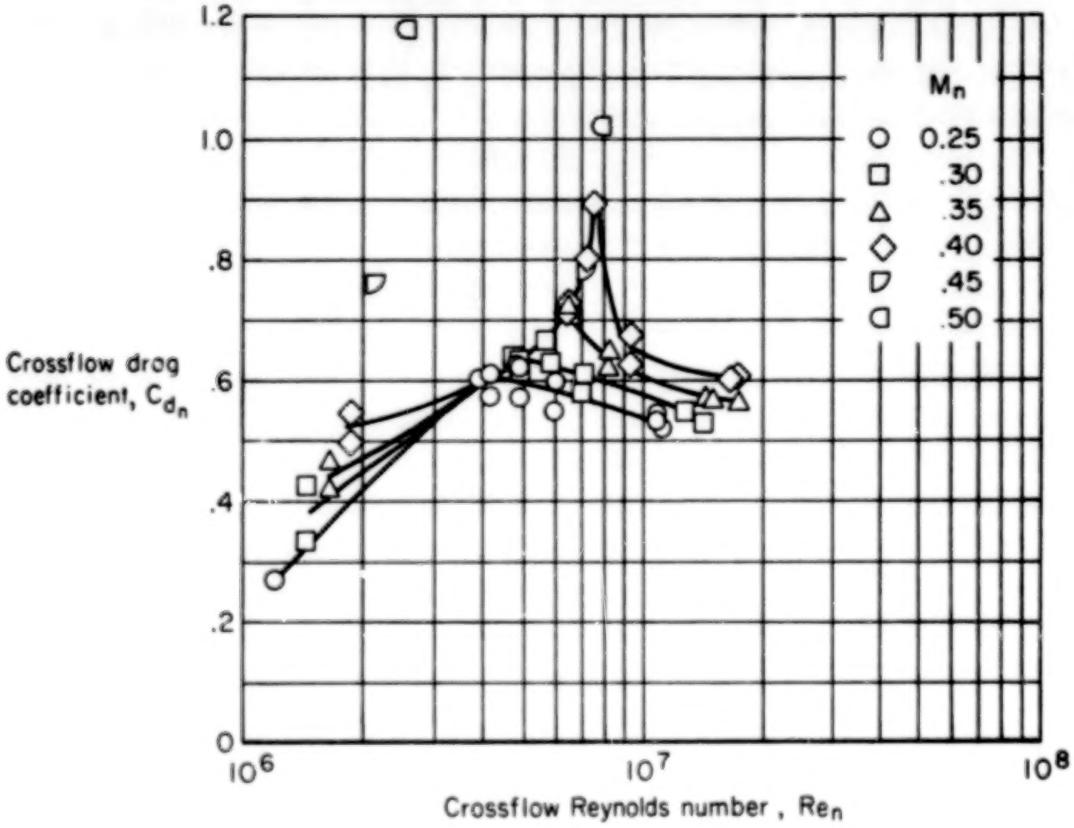

Figure 3.– Variation of crossflow drag coefficient with crossflow Reynolds number for circular cylinders at supercritical Reynolds numbers and at crossflow Mach numbers from 0.25 to 0.50 (from ref. 54).

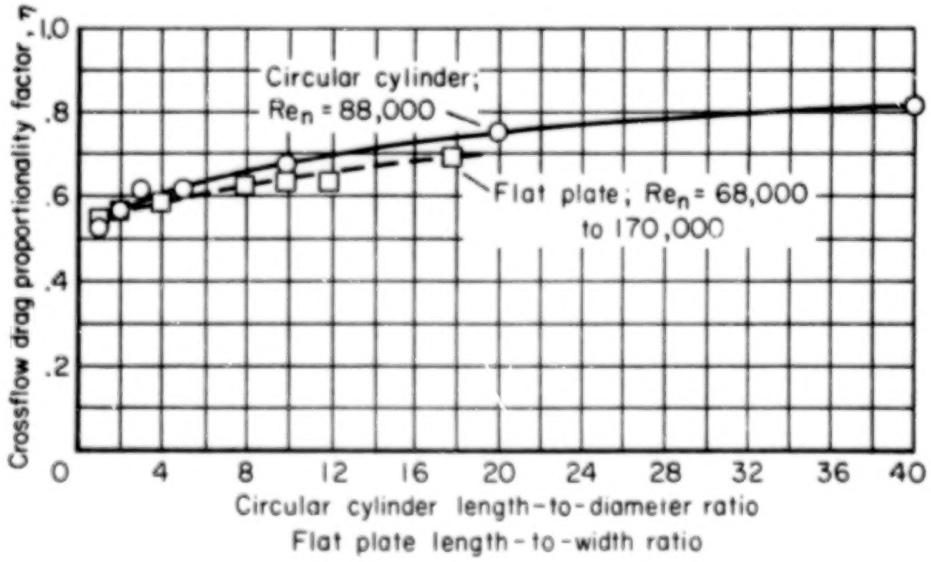

Figure 4.– Ratio of crossflow drag coefficient for a finite-length cylinder (or flat plate) to that for an infinite-length cylinder (or flat plate) (from ref. 56).

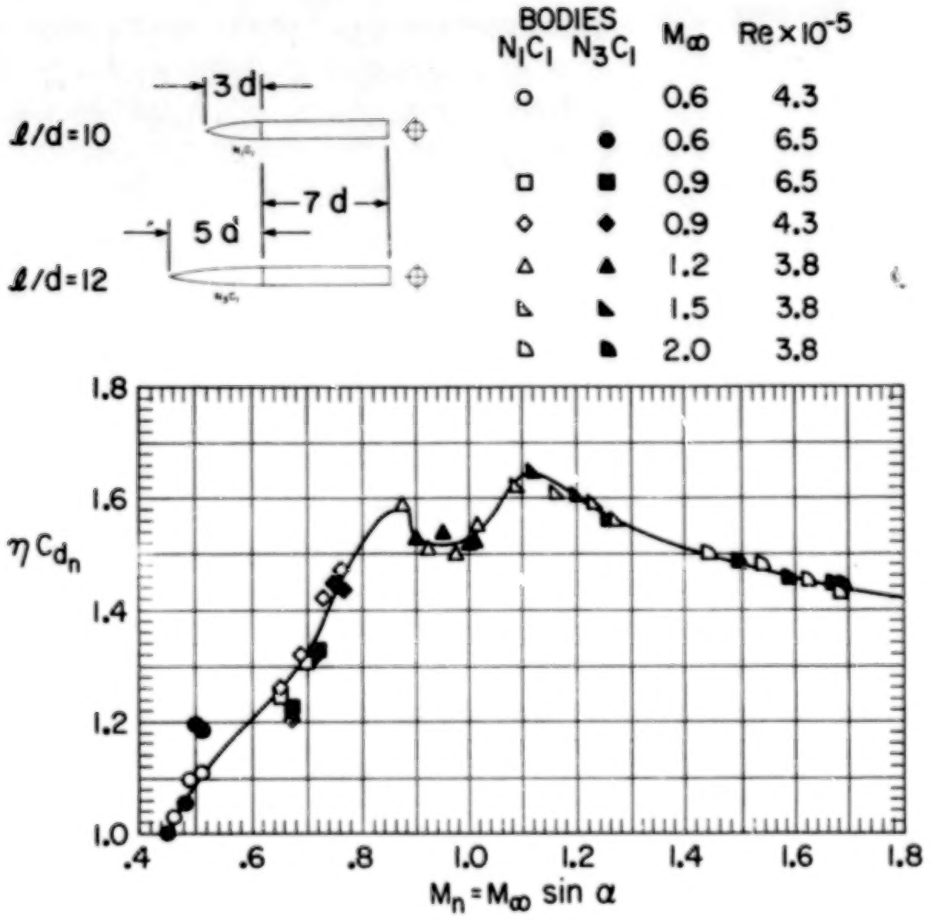

Figure 5.– Variation of $\eta\ C_{d_n}$ with M_n (crossflow Mach number) computed from experimental C_N data (ref. 16) for bodies of revolution at high α ($45° < \alpha < 60°$).

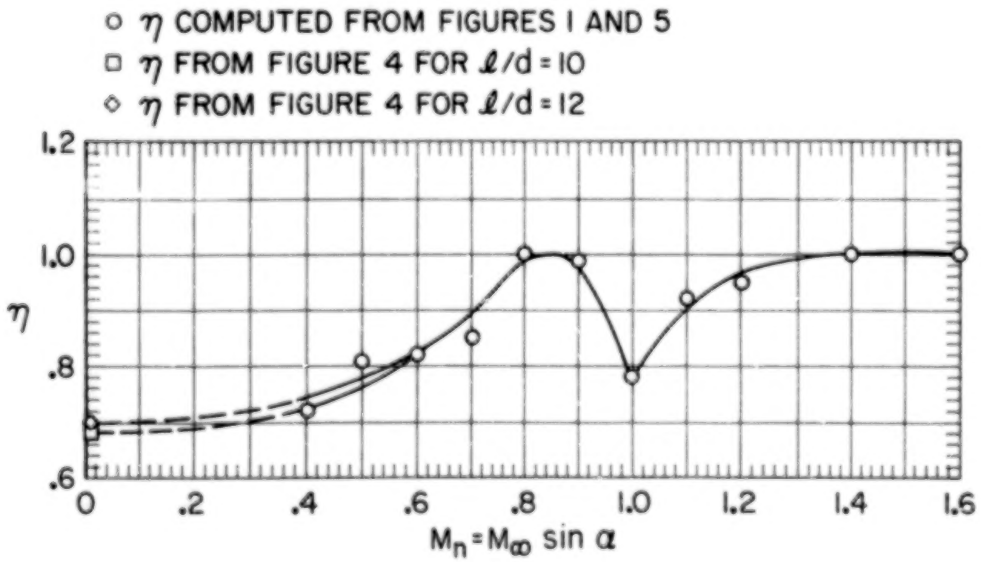

Figure 6.– Variation of η with M_n, obtained from experimental results in figures 1, 4, and 5.

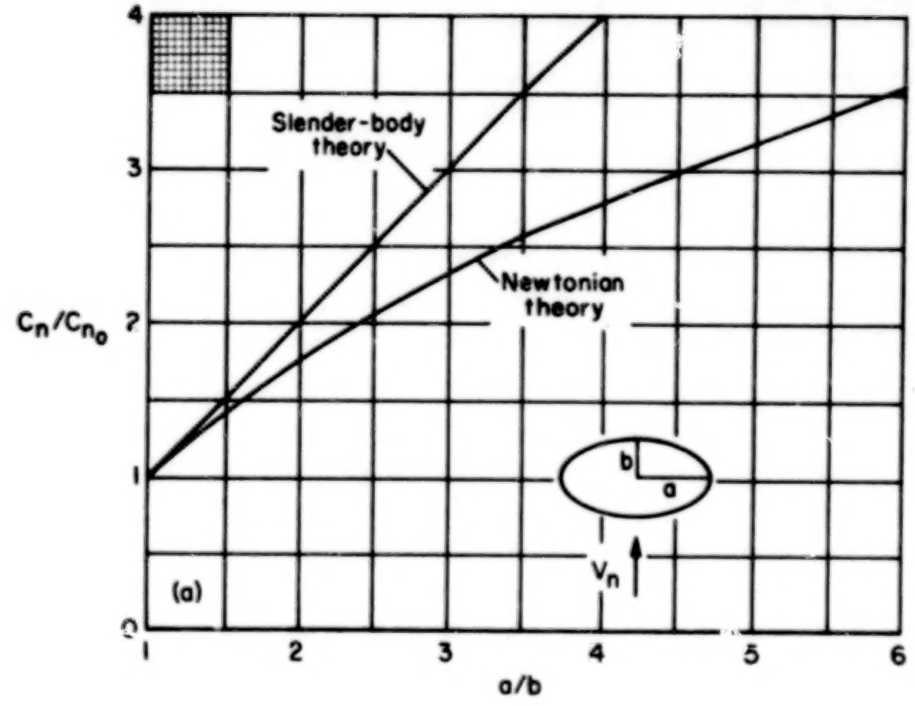

(a) Semimajor axis a perpendicular to crossflow velocity V_n.

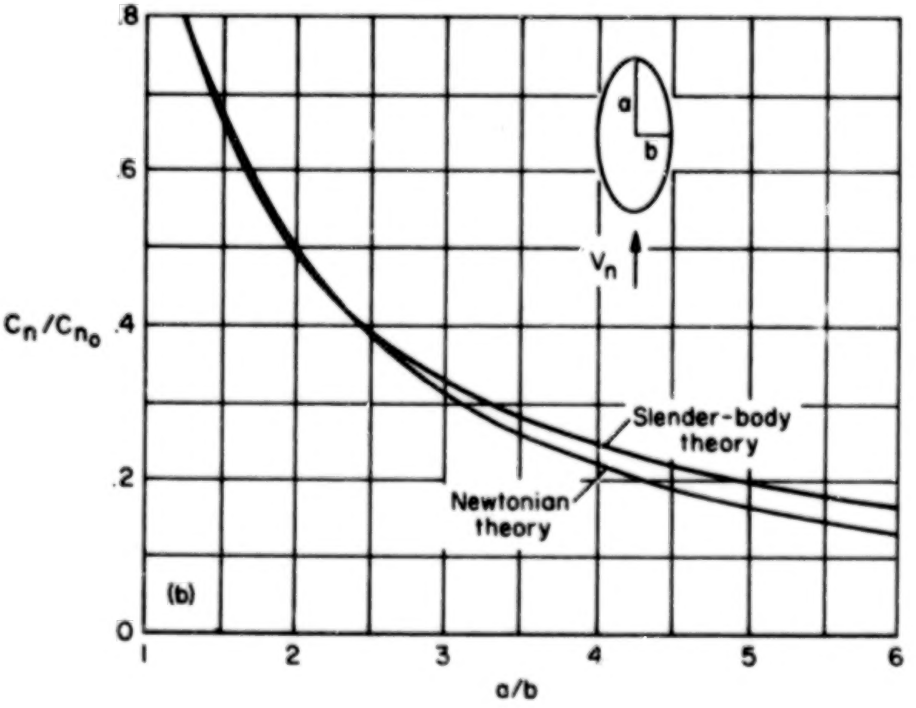

(b) Semiminor axis b perpendicular to crossflow velocity V_n.

Figure 7.– Ratio of local normal-force coefficient for an elliptic cross section to that for the equivalent circular cross section.

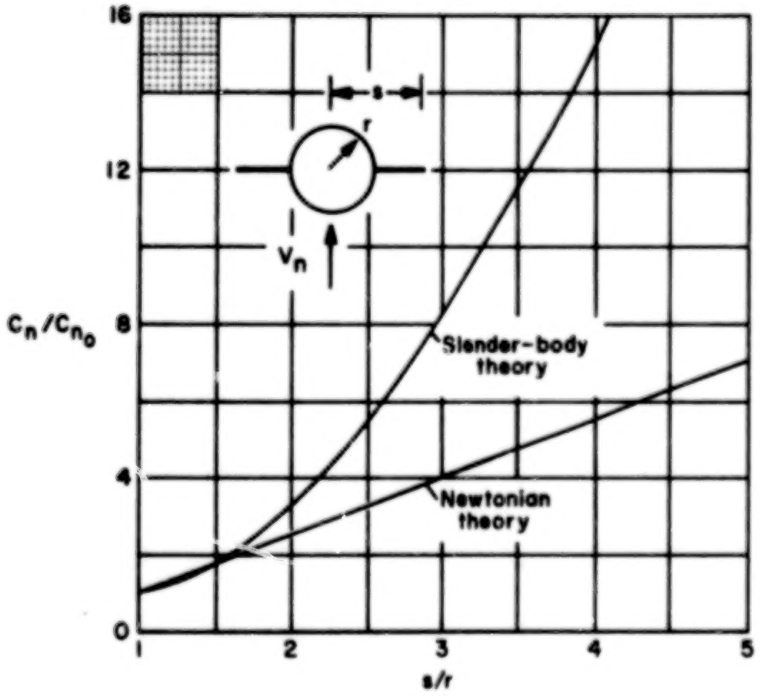

Figure 8.– Ratio of local normal-force coefficient for a winged-circular cross section to that for the equivalent circular cross section.

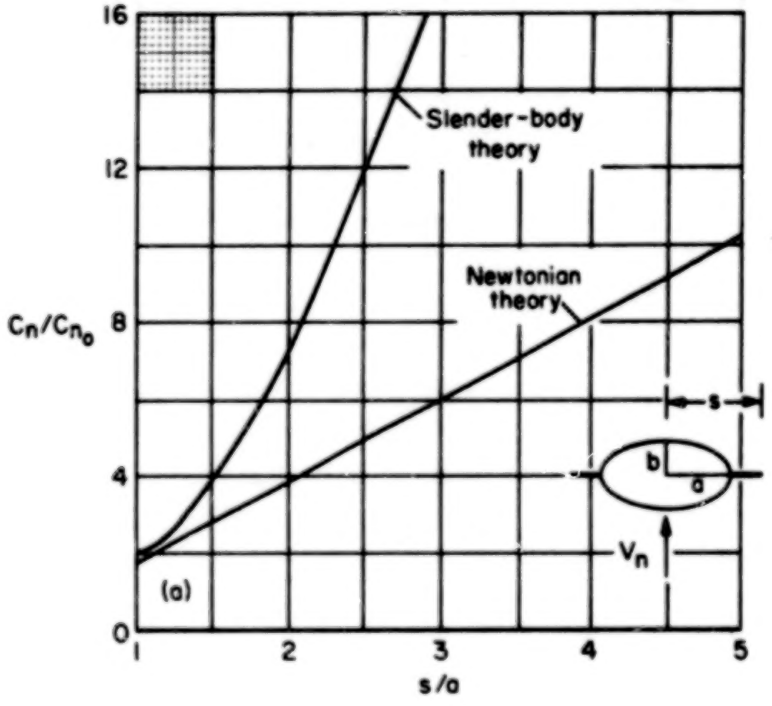

(a) $a/b = 2$

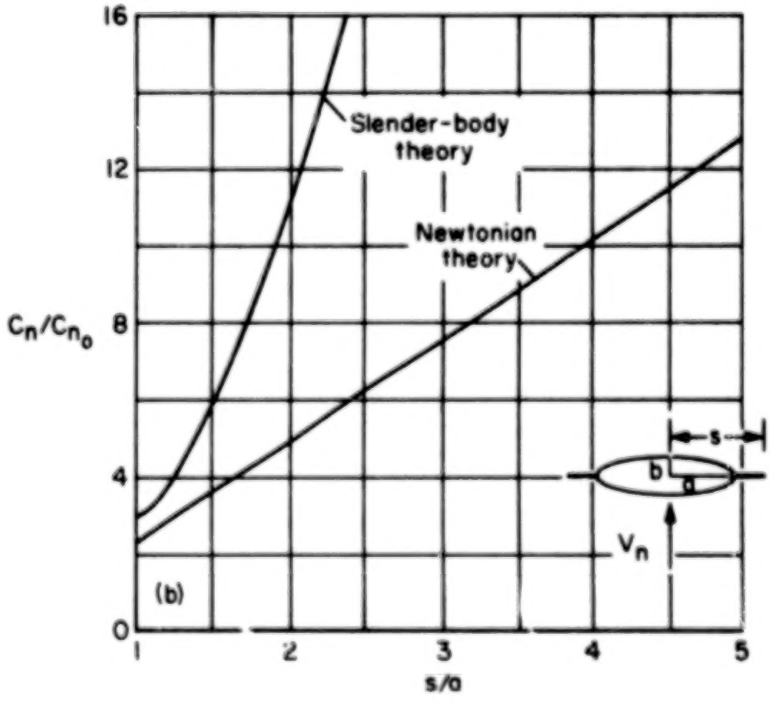

(b) $a/b = 3$

Figure 9.– Ratio of local normal-force coefficient for a winged-elliptic cross section to that for the equivalent circular cross section; semimajor axis a perpendicular to crossflow velocity V_n.

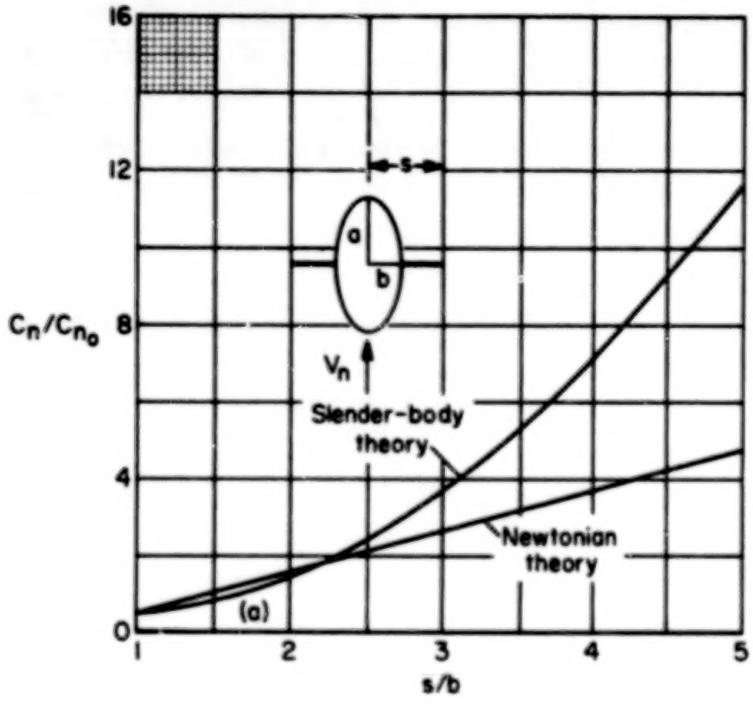

(a) $a/b = 2$

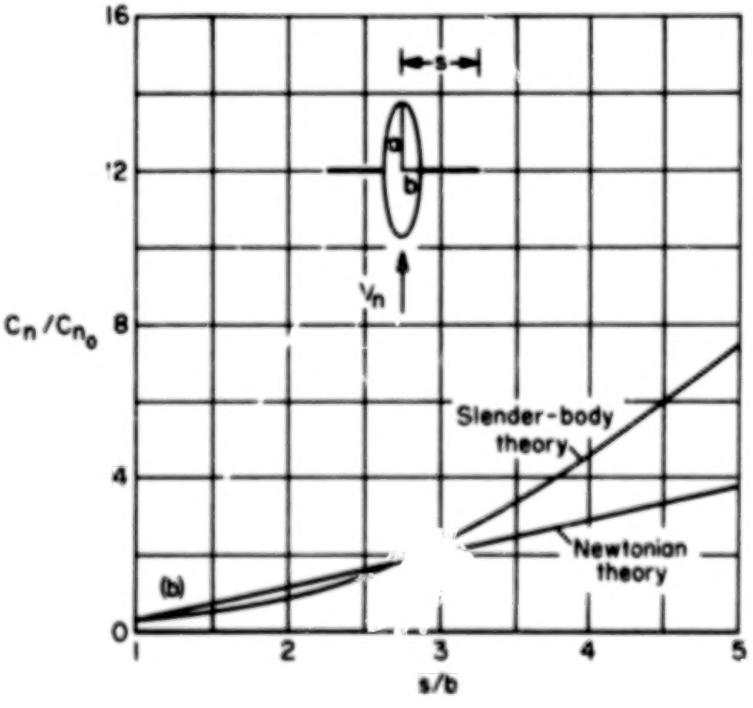

(b) $a/b = 3$

Figure 10.– Ratio of local normal-force coefficient for a winged-elliptic cross section to that for the equivalent circular cross section; semiminor axis b perpendicular to crossflow velocity V_n.

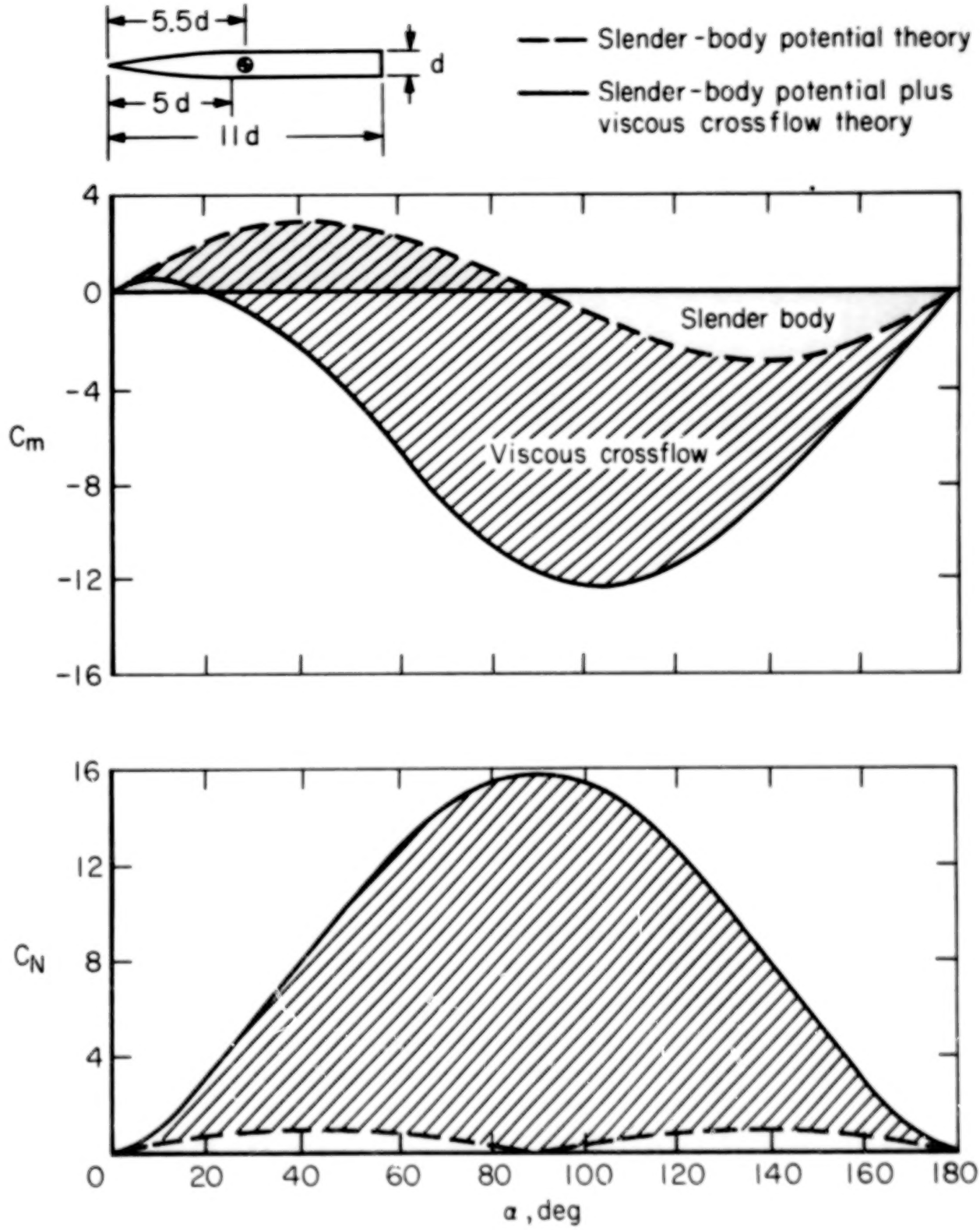

Figure 11.– Computed components of normal-force and pitching-moment coefficients for an ogive-cylinder body at $\alpha = 0°$ to 180° and $M_\infty = 2.9$ (from ref. 9).

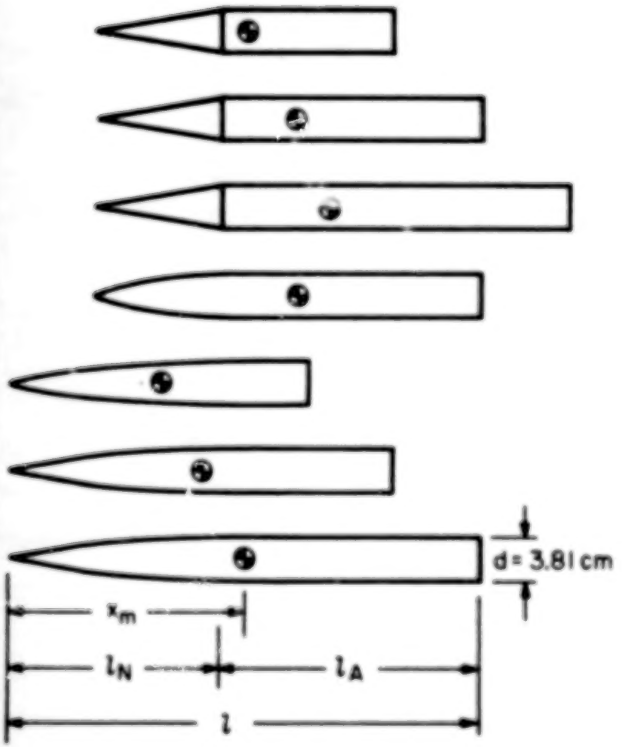

Body no.	$\frac{l}{d}$	$\frac{l_N}{d}$	$\frac{l_A}{d}$	$\frac{x_m}{d}$	$\frac{A_p}{d^2}$	$\frac{V}{d^3}$	$\frac{x_c}{d}$	$\frac{A_s}{d^2}$	Nose shape
1	7	3	4	3.5	5.500	3.925	4.183	17.34	Cone
2	9	3	6	4.5	7.500	5.495	5.200	23.62	Cone
3	11	3	8	5.5	9.500	7.065	6.211	29.91	Cone
4	9	3	6	4.5	8.011	5.977	4.963	25.24	Ogive
5	7	5	2	3.5	5.340	3.671	4.200	16.82	Ogive
6	9	5	4	4.5	7.340	5.241	5.234	23.10	Ogive
7	11	5	6	5.5	9.340	6.811	6.255	29.38	Ogive

Figure 12.– Bodies for which the aerodynamic characteristics were measured in reference 63 and computed in the present study for $M_\infty = 2.9$.

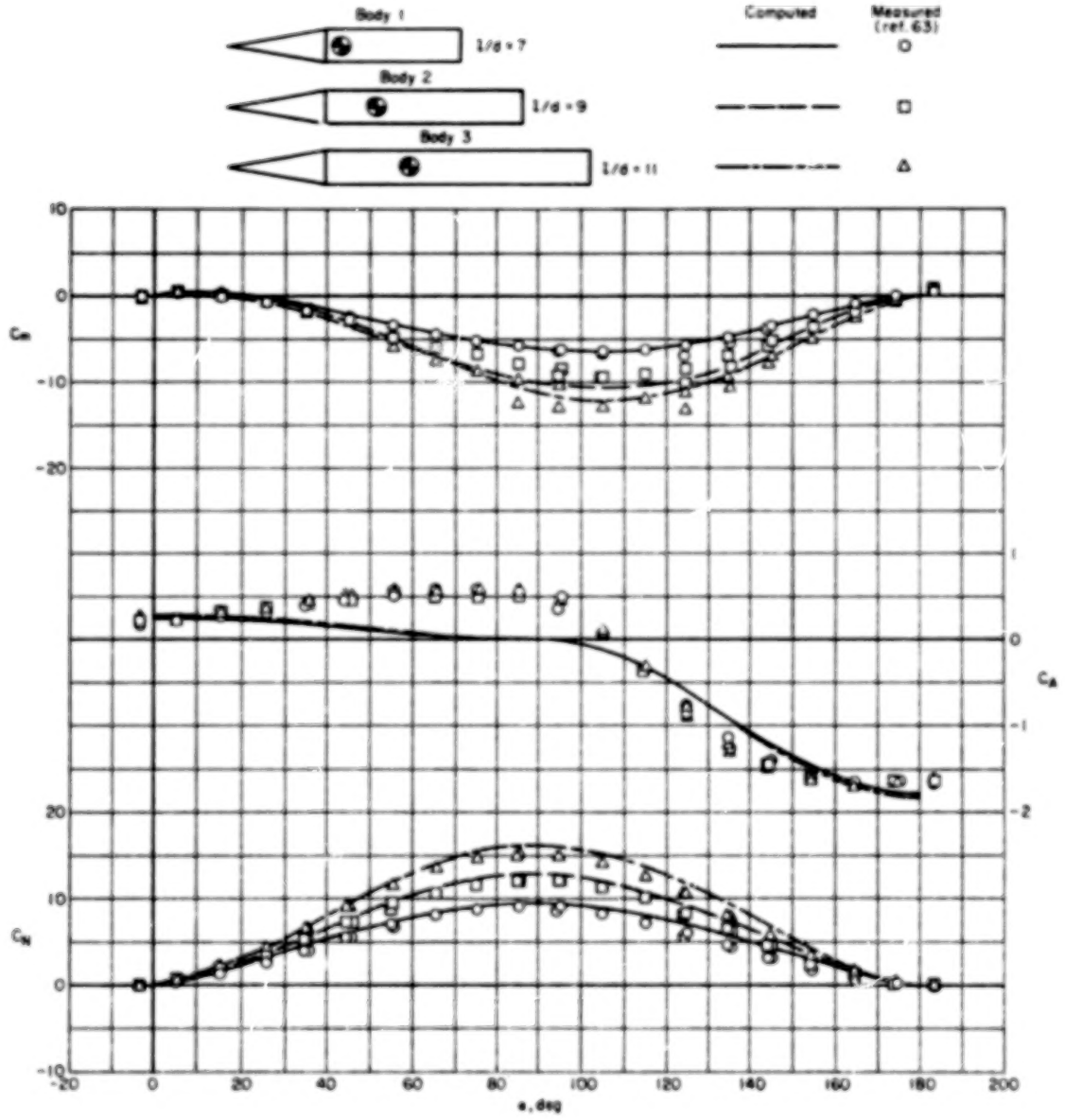

Figure 13.– Comparison of computed with measured aerodynamic characteristics for cylindrical bodies with conical noses of fineness ratio 3; $M_\infty = 2.9$.

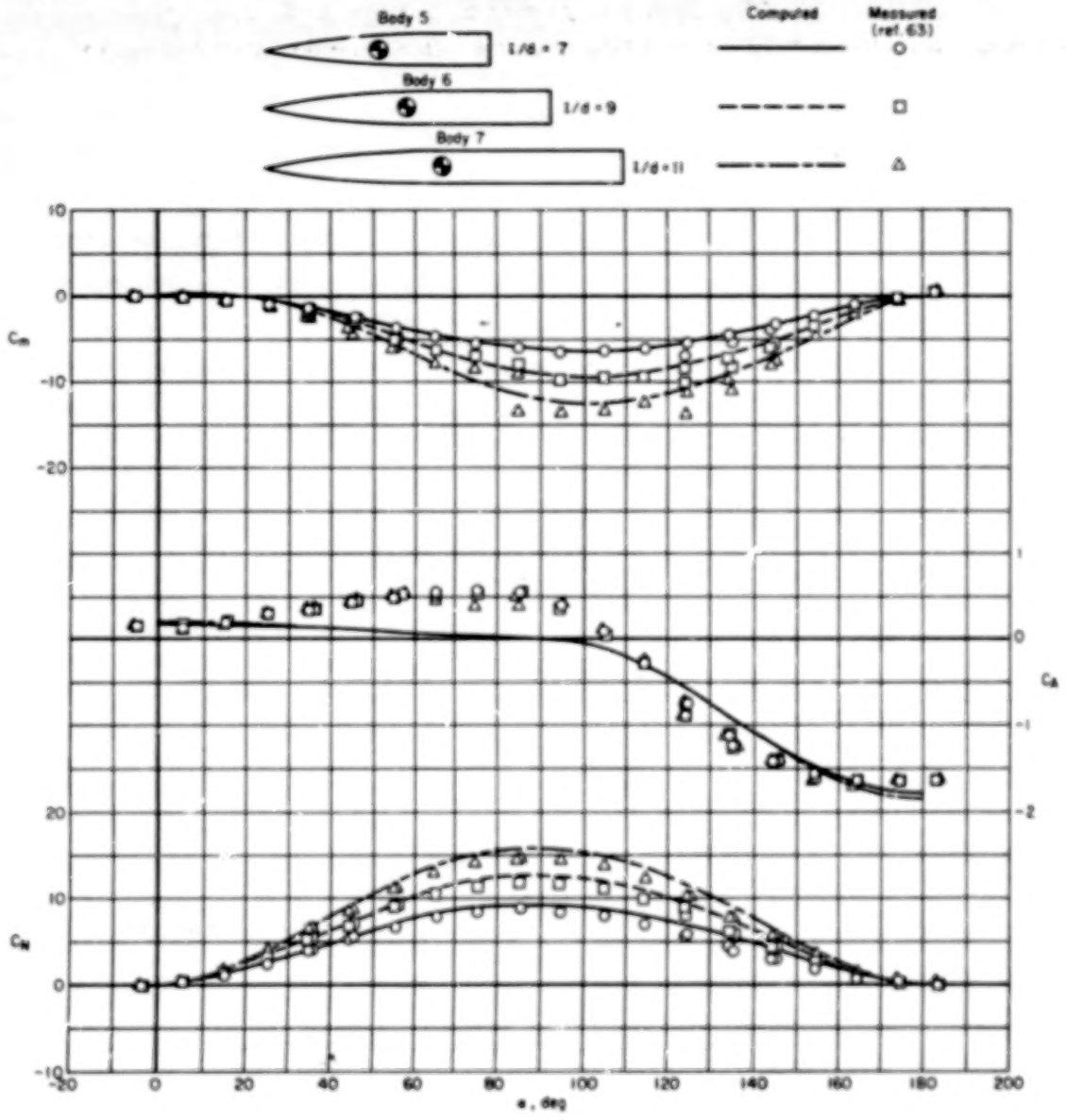

Figure 14.– Comparison of computed with measured aerodynamic characteristics for cylindrical bodies with ogival noses of fineness ratio 5; $M_\infty = 2.9$.

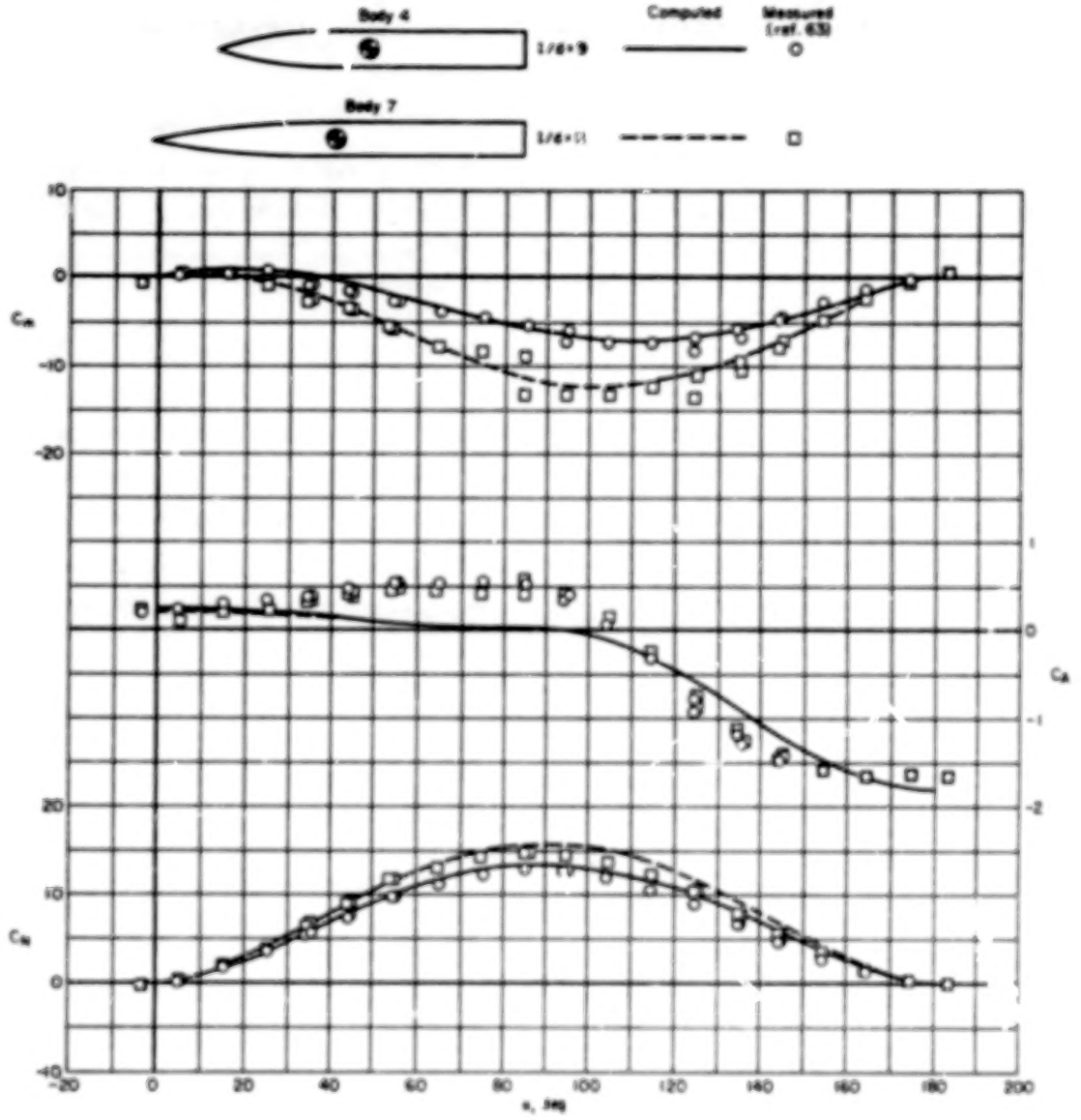

Figure 15.– Comparison of computed with measured aerodynamic characteristics for cylindrical bodies with ogival noses of fineness ratios 3 and 5; $M_\infty = 2.9$.

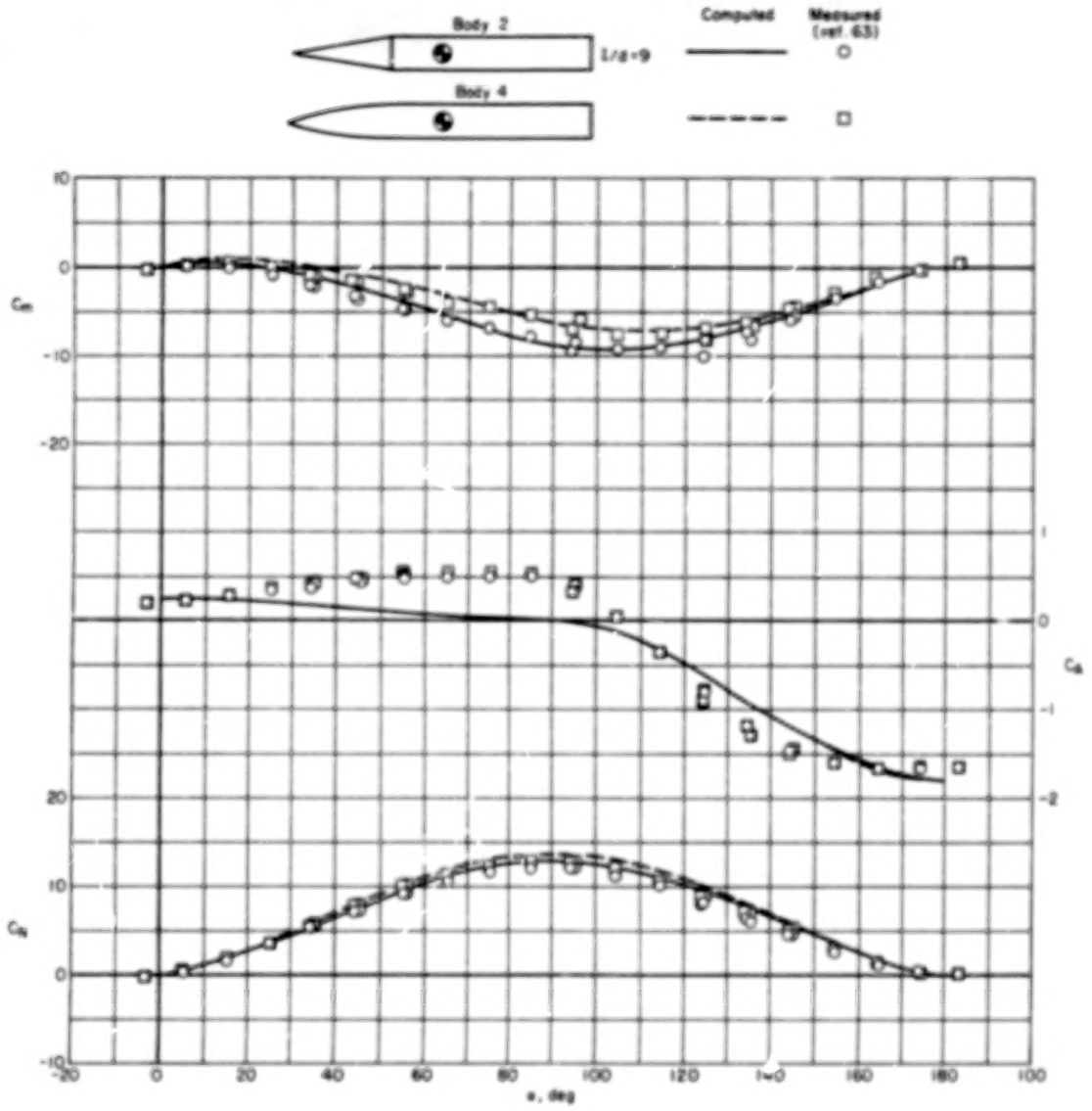

Figure 16.– Comparison of computed with measured aerodynamic characteristics for cylindrical bodies with conical and ogival noses of fineness ratio 3; $M_{\infty} = 2.9$.

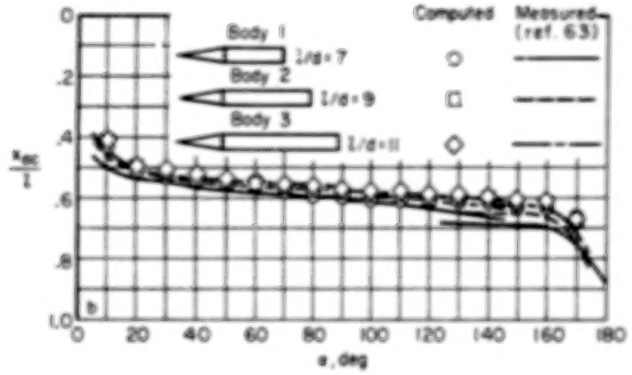

(a) Cylindrical bodies with conical noses of fineness ratio 3.

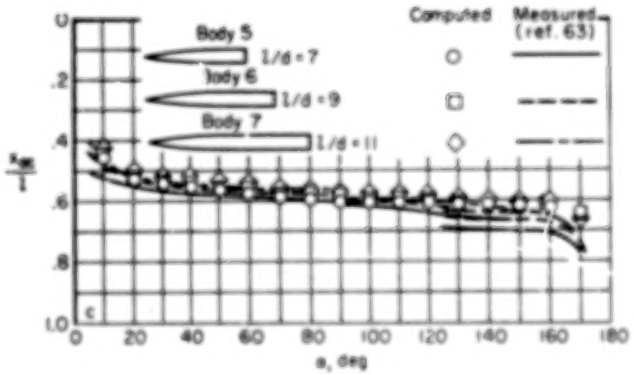

(b) Cylindrical bodies with ogival noses of fineness ratio 5.

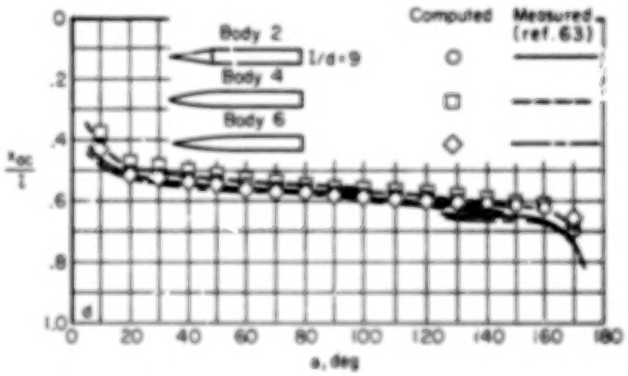

(c) Cylindrical bodies with conical and ogival noses, overall fineness ratio 9.

Figure 17.– Comparison of computed with measured aerodynamic force centers for cylindrical bodies with conical and ogival noses; $M_\infty = 2.9$.

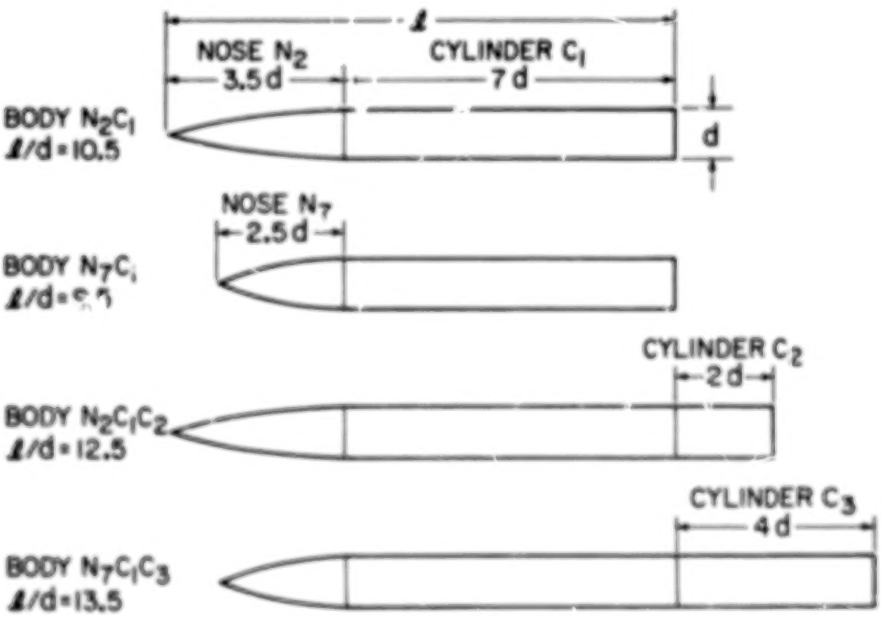

Figure 18.– Ogive-cylinder bodies for which the aerodynamic characteristics have been computed and measured for $0.6 \leq M_\infty \leq 2.0$.

TABLE OF CONTENTS

	Page	
NOTATION	vi	1/A4
SUMMARY	1	1/A10
CHAPTER 1. INTRODUCTION	2	1/A11
CHAPTER 2. DERIVATION OF BASIC METHOD FOR COMPUTING C_N AND C_m CHARACTERISTICS	6	1/B1
2.1 Bodies of Revolution	6	1/B1
2.2 Bodies of Circular and Noncircular Cross Section Alone and With Lifting Surfaces	11	1/B6
2.3 Empirical Input Values	14	1/B9
2.3.1 Crossflow drag coefficient	14	1/B9
2.3.2 Crossflow drag proportionality factor	17	1/B12
2.4 Formulas and Values of $(C_n/C_{n_o})_{SB}$ and $(C_n/C_{n_o})_{Newt}$ for Various Cross Sections	18	1/B13
2.4.1 Formulas of $(C_n/C_{n_o})_{SB}$	18	1/B13
2.4.2 Formulas of $(C_n/C_{n_o})_{Newt}$	19	1/B14
2.4.3 Values of $(C_n/C_{n_o})_{SB}$ and $(C_n/C_{n_o})_{Newt}$	20	1/C1
2.5 Relative Influence of Crossflow Terms	21	1/C2
CHAPTER 3. METHOD APPLIED TO BODIES OF REVOLUTION	23	1/C4
3.1 Cone-Cylinder and Ogive-Cylinder Bodies at $M_\infty = 2.9$	23	1/C4
3.2 Ogive-Cylinder Bodies at $M_\infty = 0.6$ to 2.0	24	1/C5
3.3 Predicted Effect of Change in Crossflow Reynolds Number from Subcritical to Supercritical	26	1/C7
CHAPTER 4. METHOD APPLIED TO BODIES OF ELLIPTIC CROSS SECTION	28	1/C9
4.1 Bodies Studied and Tests at $M_\infty = 0.6$ to 2.0	28	1/C9
4.2 Equations Used to Compute C_N and C_m for Each Body	29	1/C9
4.2.1 Equations for bodies with constant a/b cross sections (bodies B_1 and B_2)	31	1/C12
4.2.2 Equations for body with variable a/b cross sections (body B_3)	31	1/C12

Page

4.3 Comparison of Computed With Measured Normal-Force and Normal-Force-Center Characteristics 33 1/C14

4.3.1 Bodies with constant a/b cross sections (bodies B_1 and B_2) . . . 33 1/C14

4.3.2 Body with variable a/b cross sections (body B_3) 33 1/C14

CHAPTER 5. METHOD APPLIED TO BODY-WING AND BODY-WING-TAIL CONFIGURATIONS 35 1/D2

5.1 Configurations Studied and Tests at M_∞ = 0.6 to 2.0 . . . . . 35 1/D2

5.2 Methodology Used to Compute C_N and C_m 36 1/D3

5.3 Comparison of Computed with Measured Normal-Force and Normal-Force-Center Characteristics 39 1/D6

5.3.1 Body-wing configurations 39 1/D6

5.3.2 Body-wing-tail configurations 41 1/D8

CHAPTER 6. VISUAL OBSERVATION OF FLOWS OVER MODELS 43 1/D10

6.1 Models Considered 44 1/D11

6.2 Vapor-Screen and Oil-Flow Techniques 45 1/D12

6.2.1 Vapor-screen technique 45 1/D12

6.2.2 Oil-flow technique 46 1/D13

6.3 Photographs Obtained from Vapor-Screen and Oil-Flow Techniques . . . 47 1/D14

6.3.1 Photographs from vapor-screen technique 47 1/D14

6.3.2 Photographs from oil-flow technique 49 1/E2

CHAPTER 7. EXPERIMENTAL SIDE FORCES ON MODELS AT $\beta = 0°$ . . . 52 1/E5

7.1 Bodies Alone 52 1/E5

7.1.1 Effects of nose fineness ratio and Mach number 52 1/E5

7.1.2 Effect of nose-tip rounding 54 1/E7

7.1.3 Effect of afterbody side strakes 54 1/E7

7.1.4 Effect of elliptic cross section 54 1/E7

7.2 Body-Wing and Body-Wing-Tail Configurations 55 1/E8

7.2.1 Effects of adding a wing and a wing plus tail to a body 55 1/E8

7.2.2 Effects of wing aspect ratio and taper ratio 55 1/E8

CHAPTER 8. CONCLUDING REMARKS 56 1/E9

	Page	
APPENDIX A – DERIVATION OF $(C_n/C_{n_o})_{Newt}$ FOR WINGED-CIRCULAR AND WINGED-ELLIPTIC CROSS SECTIONS	59	1/E12
Winged-Circular Cross Section with Wing Planform Perpendicular to Crossflow Velocity	59	1/E12
Winged-Elliptic Cross Section with Semimajor Axis and Wing Planform Perpendicular to Crossflow Velocity	60	1/E13
Winged-Elliptic Cross Section with Semiminor Axis and Wing Planform Perpendicular to Crossflow Velocity	62	1/F1
APPENDIX B – DERIVATION OF $(C_n/C_{n_o})_{Newt}$ FOR WINGED-SQUARE CROSS SECTIONS WITH ROUNDED CORNERS	64	1/F3
APPENDIX C – FORMULAS TO COMPUTE GEOMETRIC PARAMETERS FOR TANGENT OGIVES	67	1/F6
REFERENCES	68	1/F7
FIGURES	75	1/F14

NOTATION

A	body cross-sectional area
A_b	body base area (at $x = \ell$)
A_p	planform area
A_r	reference area (taken as A_b for the comparisons of computed with experimental results)
A_s	surface wetted area
A_w	exposed wing planform area (2 panels)
a	speed of sound
a,b	semimajor and semiminor axes of elliptic cross section
C_A	axial-force coefficient, $\frac{F_a}{q_\infty A_r}$
C_{d_n}	crossflow drag coefficient of circular cylinder section, $\frac{F_n}{q_n(\Delta\ell_{cy})d_{cy}}$
C_D	drag coefficient, $\frac{\text{drag}}{q_\infty A_r}$
C_L	lift coefficient, $\frac{\text{lift}}{q_\infty A_r}$
C_m	pitching-moment coefficient about station at x_m from nose, $\frac{\text{pitching moment}}{q_\infty A_r X}$
C_N	normal-force coefficient, $\frac{F_n}{q_\infty A_r}$
C_n	local normal-force coefficient per unit length
C_p	pressure coefficient, $\frac{p - p_\infty}{q_\infty}$
C_Y	side-force coefficient, $\frac{F_y}{q_\infty A_r}$
d	body cross-section diameter
f	cross force per unit length along body length
f_p	potential cross force per unit length along body length
f_v	viscous cross force per unit length along body length

F_a, F_n, F_y	axial, normal, and side force
k	corner rounding for body cross section, $\frac{r}{w}$
K_1, K_2	longitudinal and transverse apparent mass coefficients
ℓ	body length
ℓ_A	body aftersection length
ℓ_N	body nose length
M_n	Mach number component normal to body axis, $M_\infty \sin \alpha$
M_∞	free-stream Mach number
p	pressure
p_∞	free-stream static pressure
q_n	dynamic pressure component normal to body axis, $q_\infty \sin^2 \alpha$
q_∞	free-stream dynamic pressure, $\frac{1}{2} \rho V_\infty^2$
r	body cross-section radius or corner radius
r_a	arc radius of ogive
S	displacement of crossflow
s	semispan
t	time
Re	free-stream Reynolds number, $\frac{\rho V_\infty X}{\mu}$
Re_n	Reynolds number component normal to body axis, $Re \frac{d}{X} \sin \alpha$
V	body volume
V_n	velocity component normal to body axis, $V_\infty \sin \alpha$
V_∞	free-stream velocity
w	body width

X	reference length (generally taken as d for the comparisons of computed with experimental results)
x	axial distance from body nose
x_{ac}	axial distance from body nose to aerodynamic normal-force center (center of pressure)
x_c	axial distance from body nose to centroid of body planform area
x_m	axial distance from body nose to pitching-moment reference center
x_{sf}	axial distance from body nose to aerodynamic side-force center
α	angle of attack
β	angle of sideslip
ϵ	wing planform semiapex angle
η	crossflow drag proportionality factor (ratio of crossflow drag for a finite-length cylinder to that for an infinite-length cylinder)
μ	viscosity coefficient of air
ρ	density of air
ϕ	angle of roll about body longitudinal axis

Subscripts

b	body base
cy	cylinder
$Newt$	Newtonian theory
$nose$	body nose
o	equivalent circular body or cross section
SB	slender-body theory
$stag$	stagnation

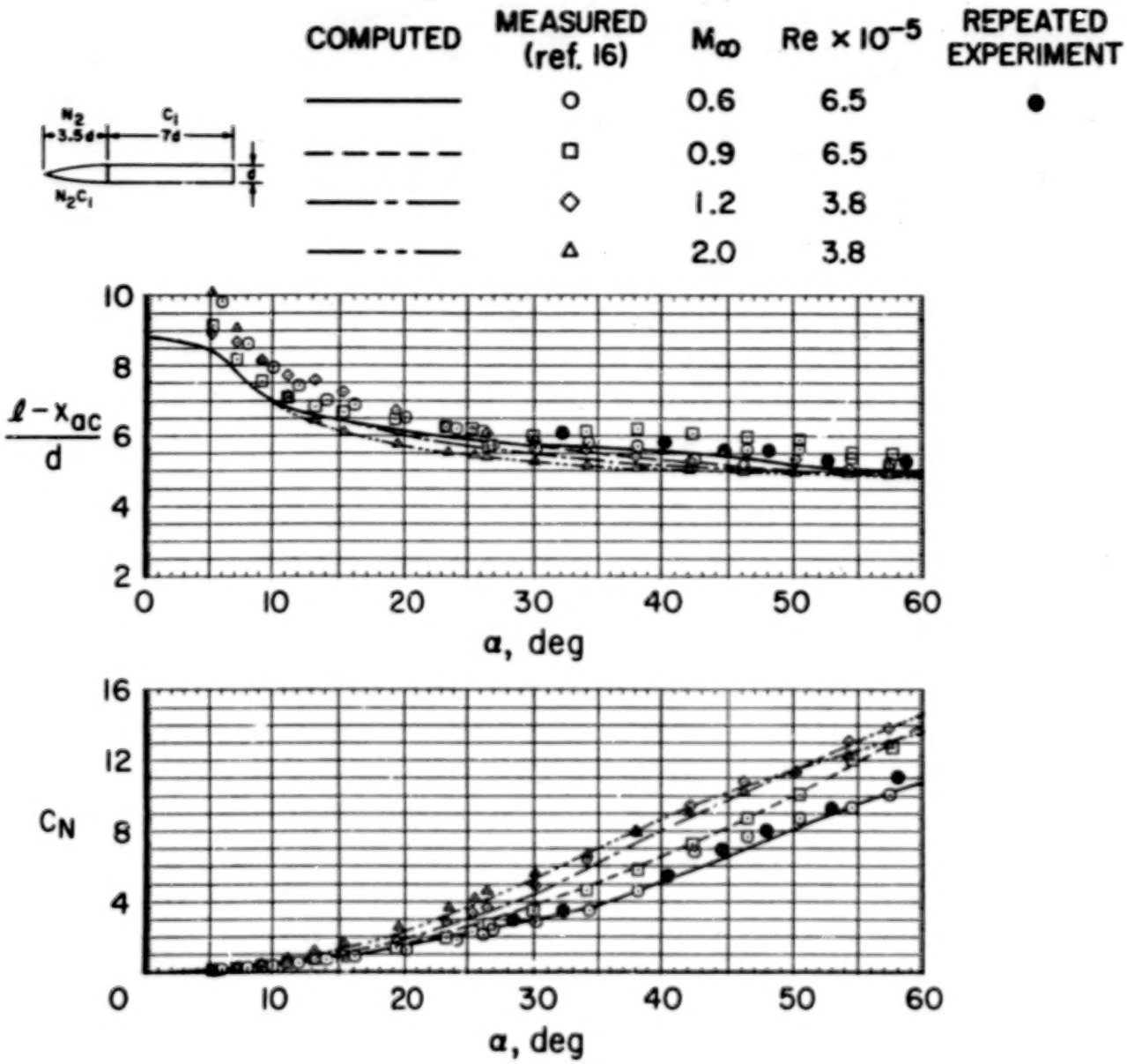

Figure 19.– Effect of Mach number on comparison of computed with measured aerodynamic characteristics for body N_2C_1; $0.6 \leq M_\infty \leq 2.0$.

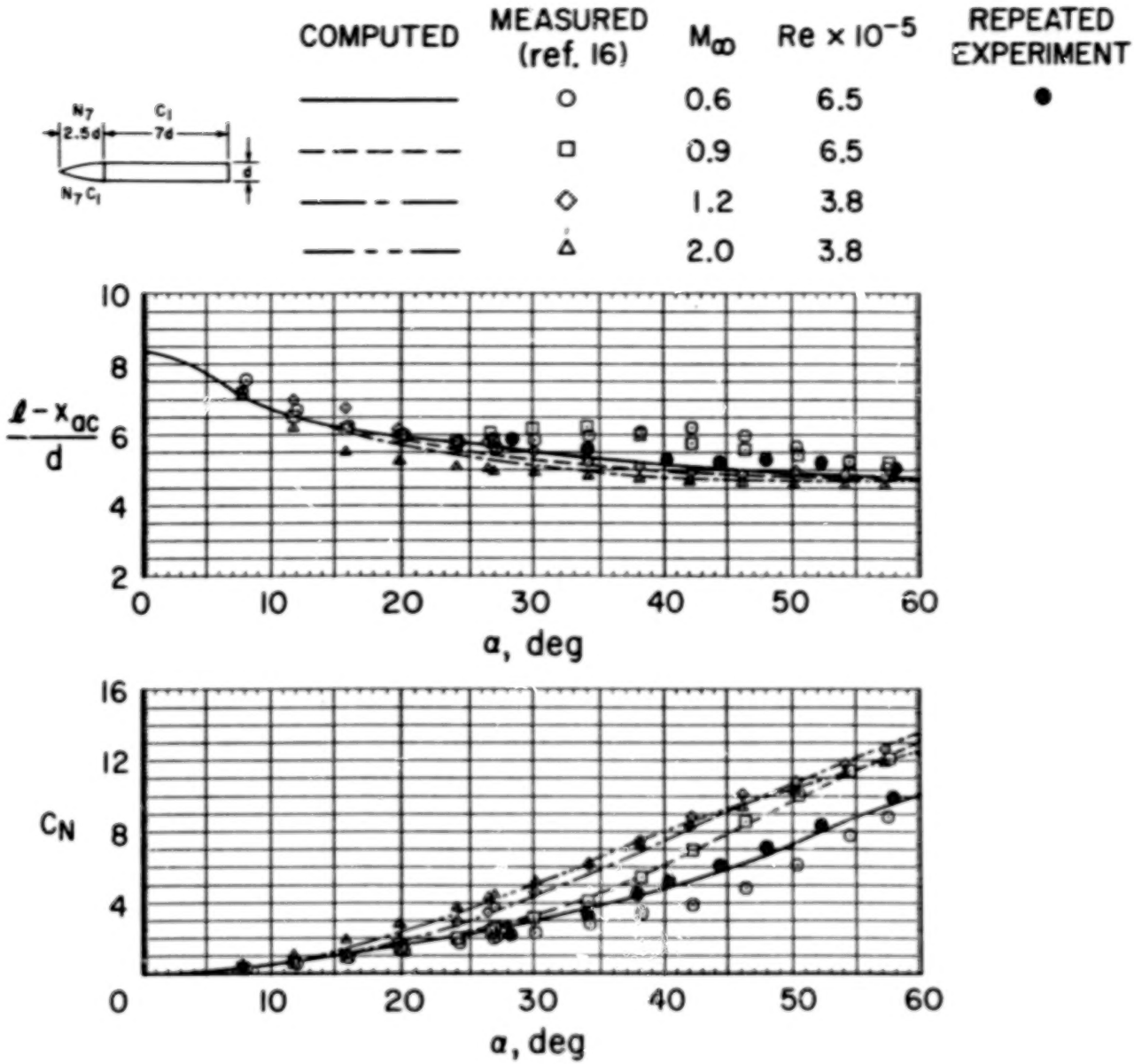

Figure 20.– Effect of Mach number on comparison of computed with measured aerodynamic characteristics for body N_7C_1 ; $0.6 \leqslant M_\infty \leqslant 2.0$.

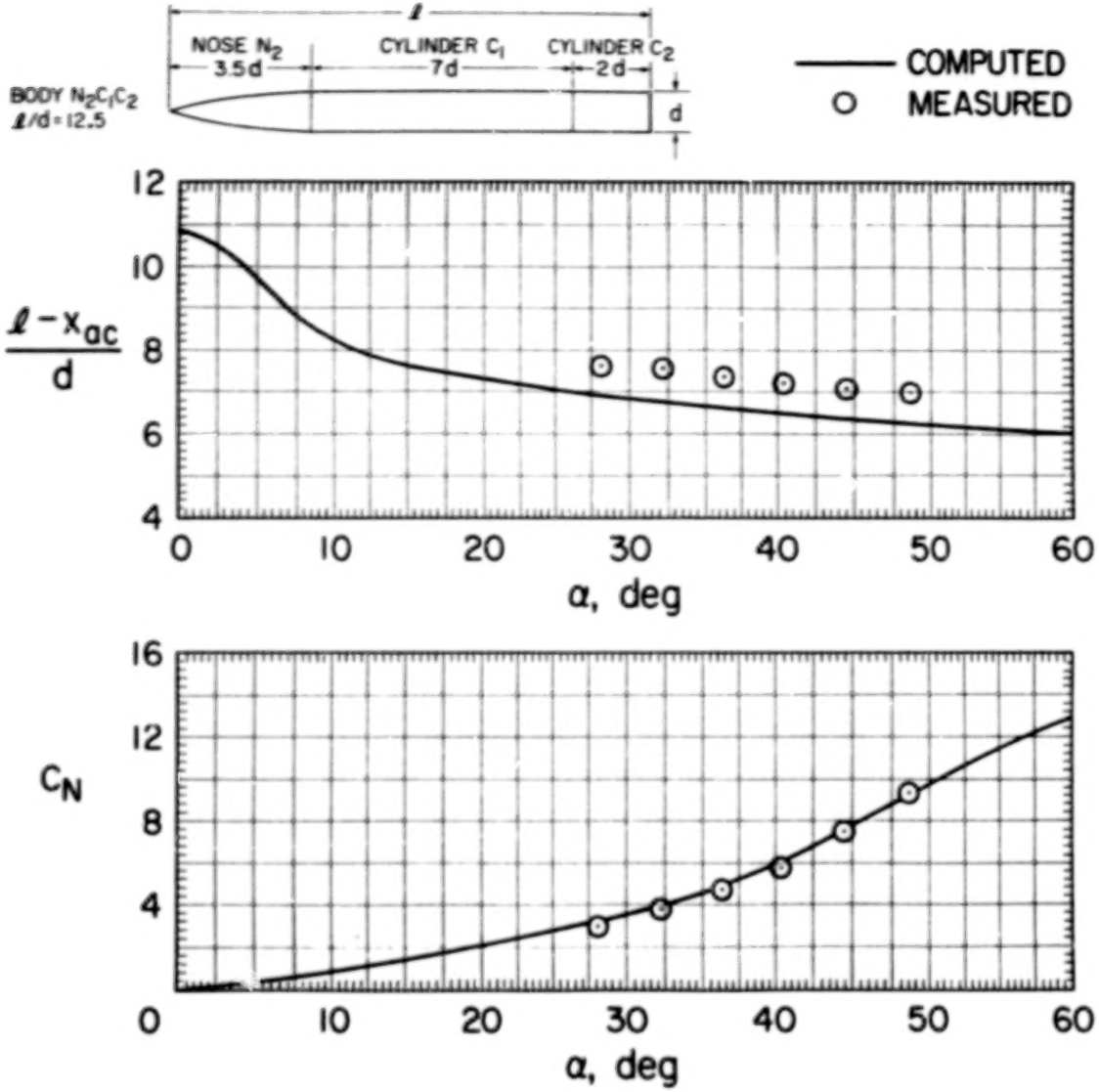

(a) $M_\infty = 0.6$

Figure 21.– Effect of Mach number on comparison of computed with measured aerodynamic characteristics for body $N_2C_1C_2$; $0.6 \leq M_\infty \leq 2.0$, Re = 4.3×10^5.

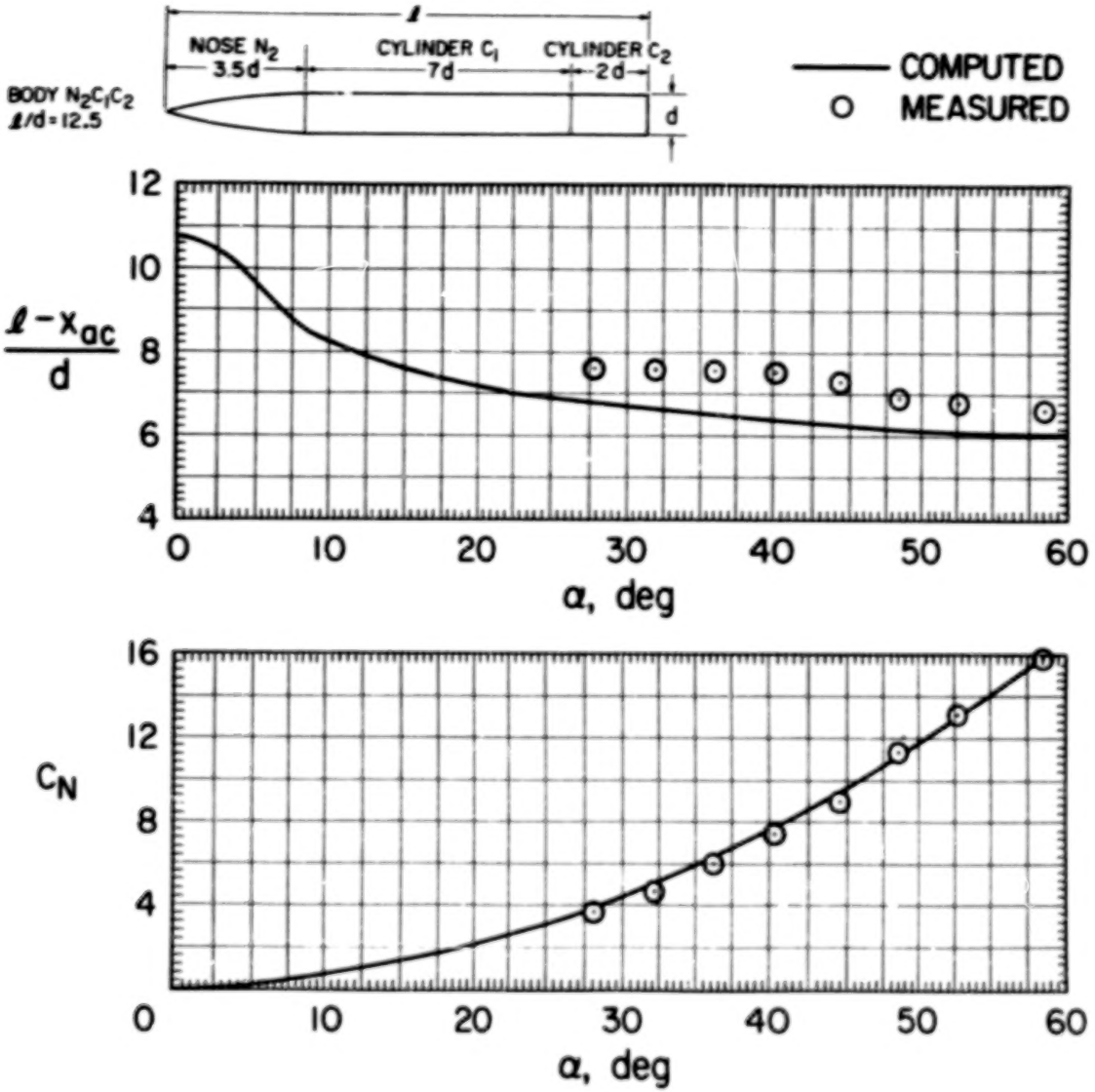

(b) $M_\infty = 0.9$

Figure 21.– Continued.

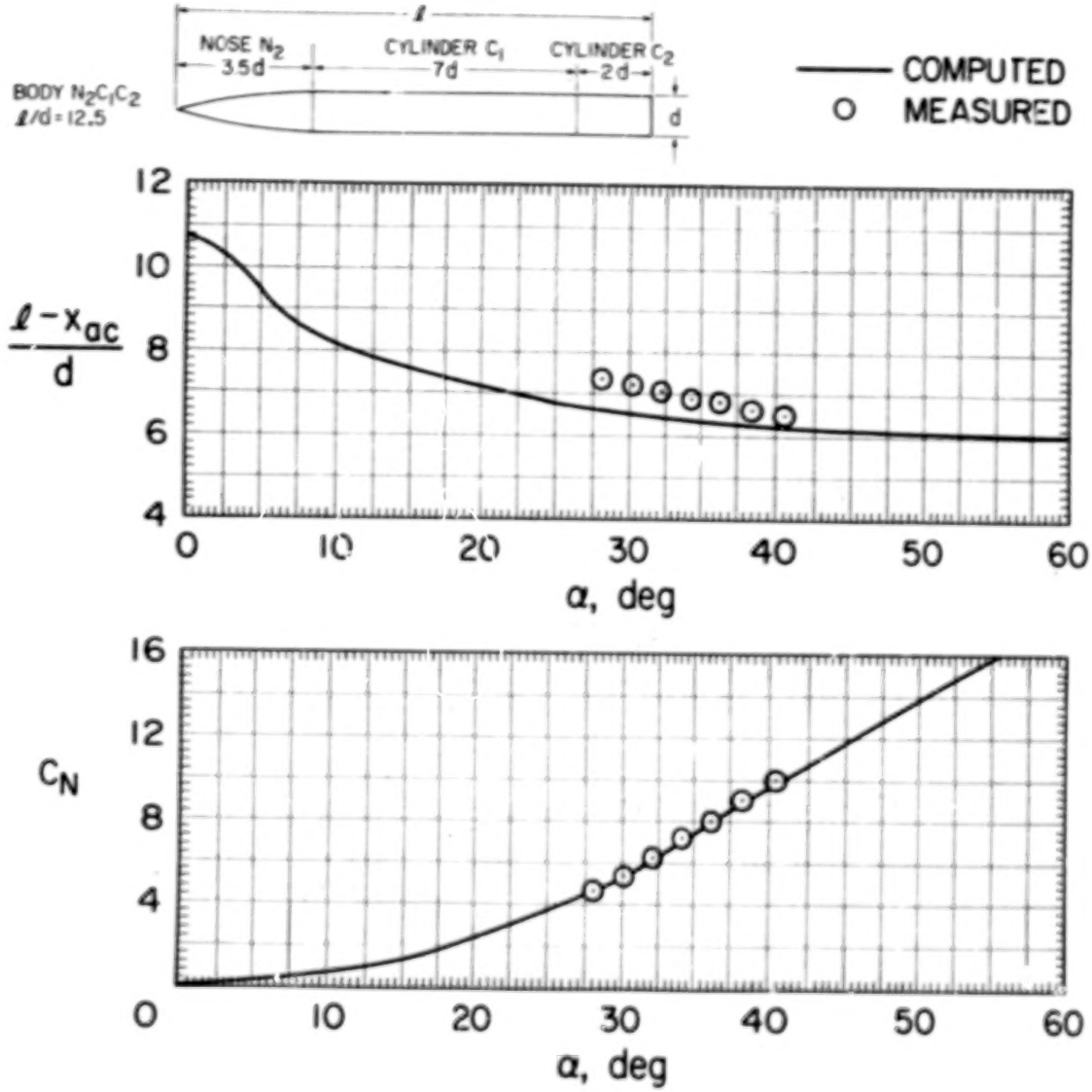

(c) $M_\infty = 1.2$

Figure 21.– Continued.

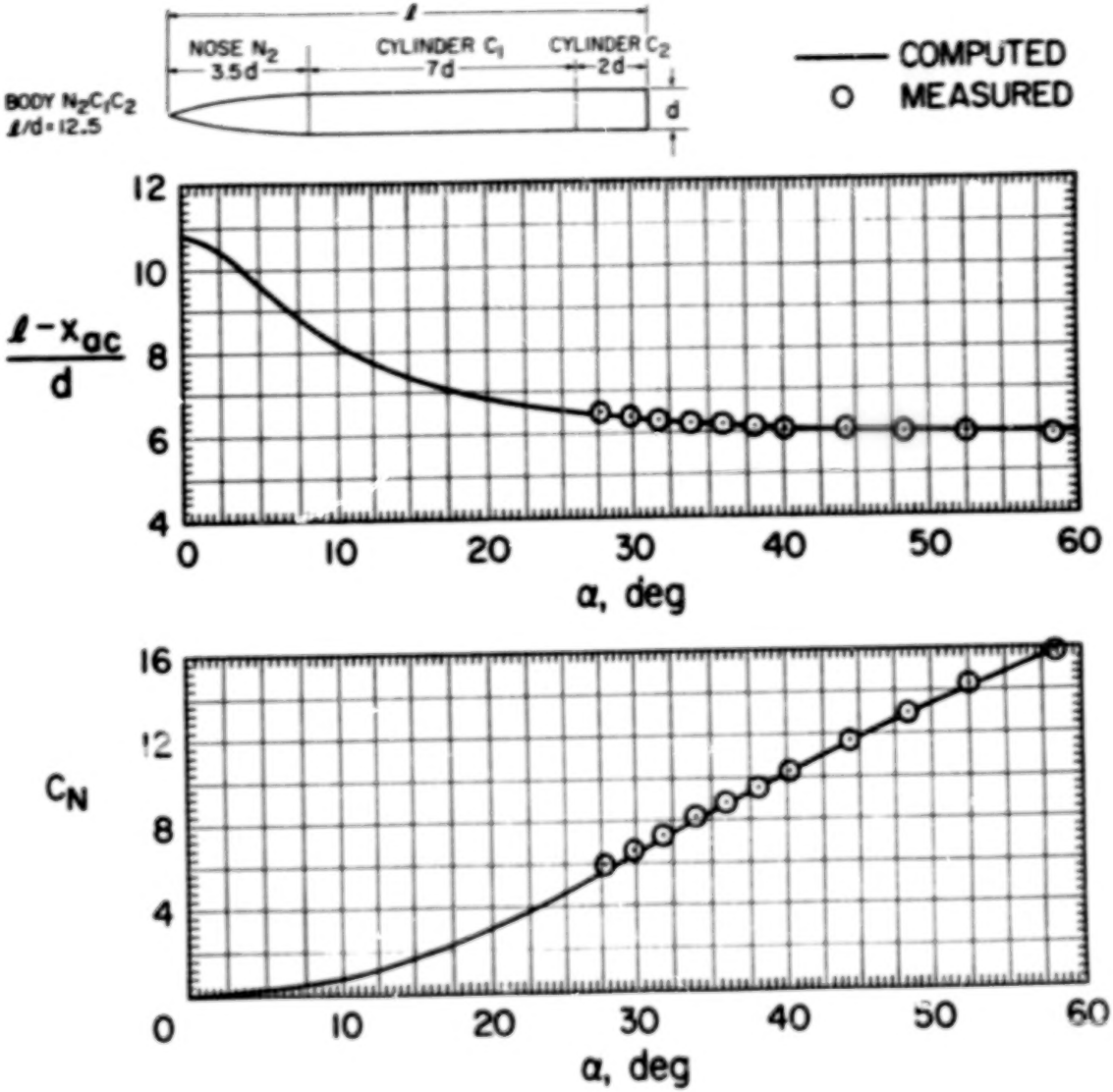

(d) $M_\infty = 2.0$

Figure 21.– Concluded.

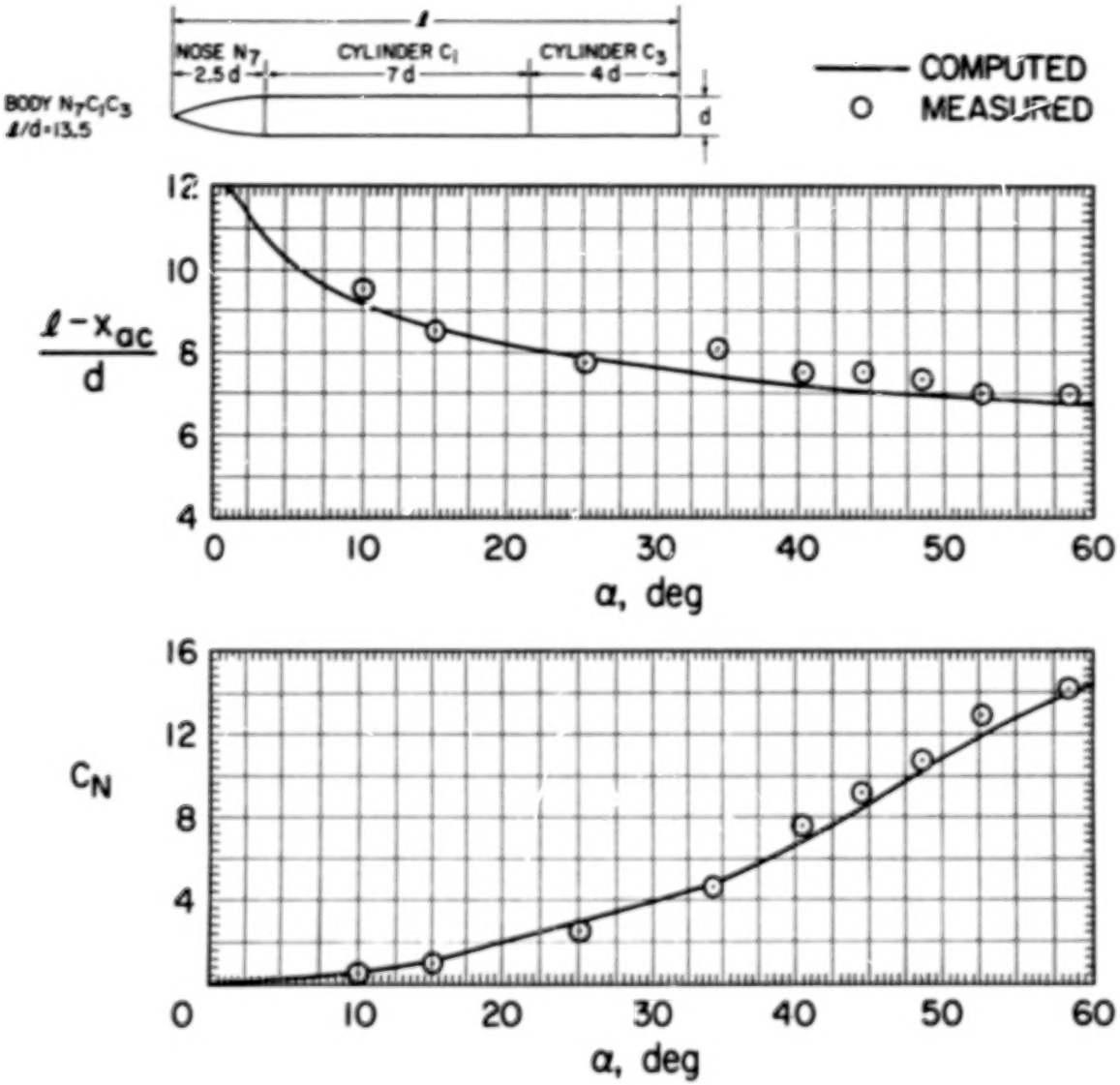

(a) $M_\infty = 0.6$

Figure 22.– Effect of Mach number on comparison of computed with measured aerodynamic characteristics for body $N_7C_1C_3$; $0.6 \leq M_\infty \leq 2.0$, Re = 4.3×10^5.

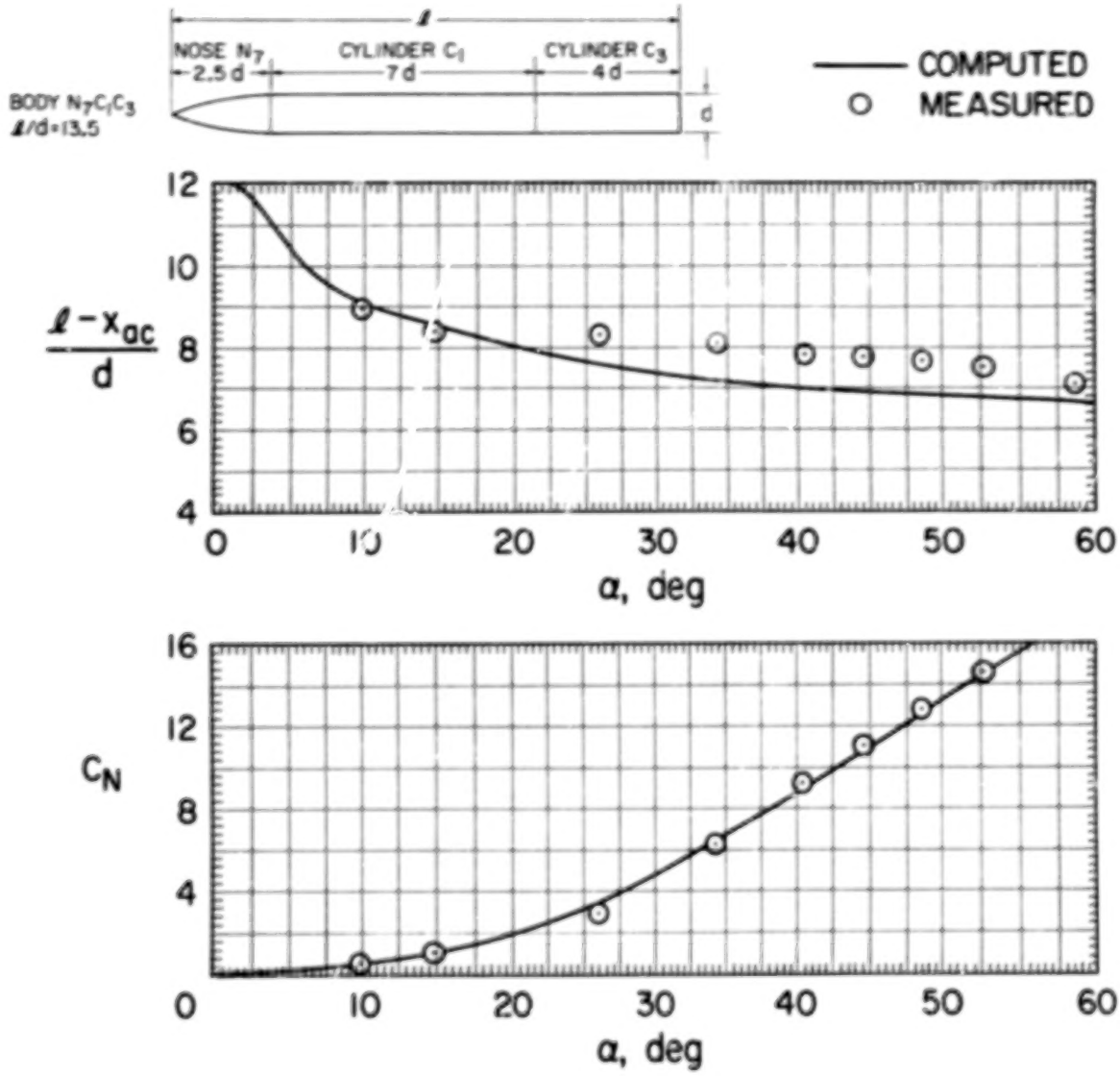

(b) $M_\infty = 0.9$

Figure 22.– Continued.

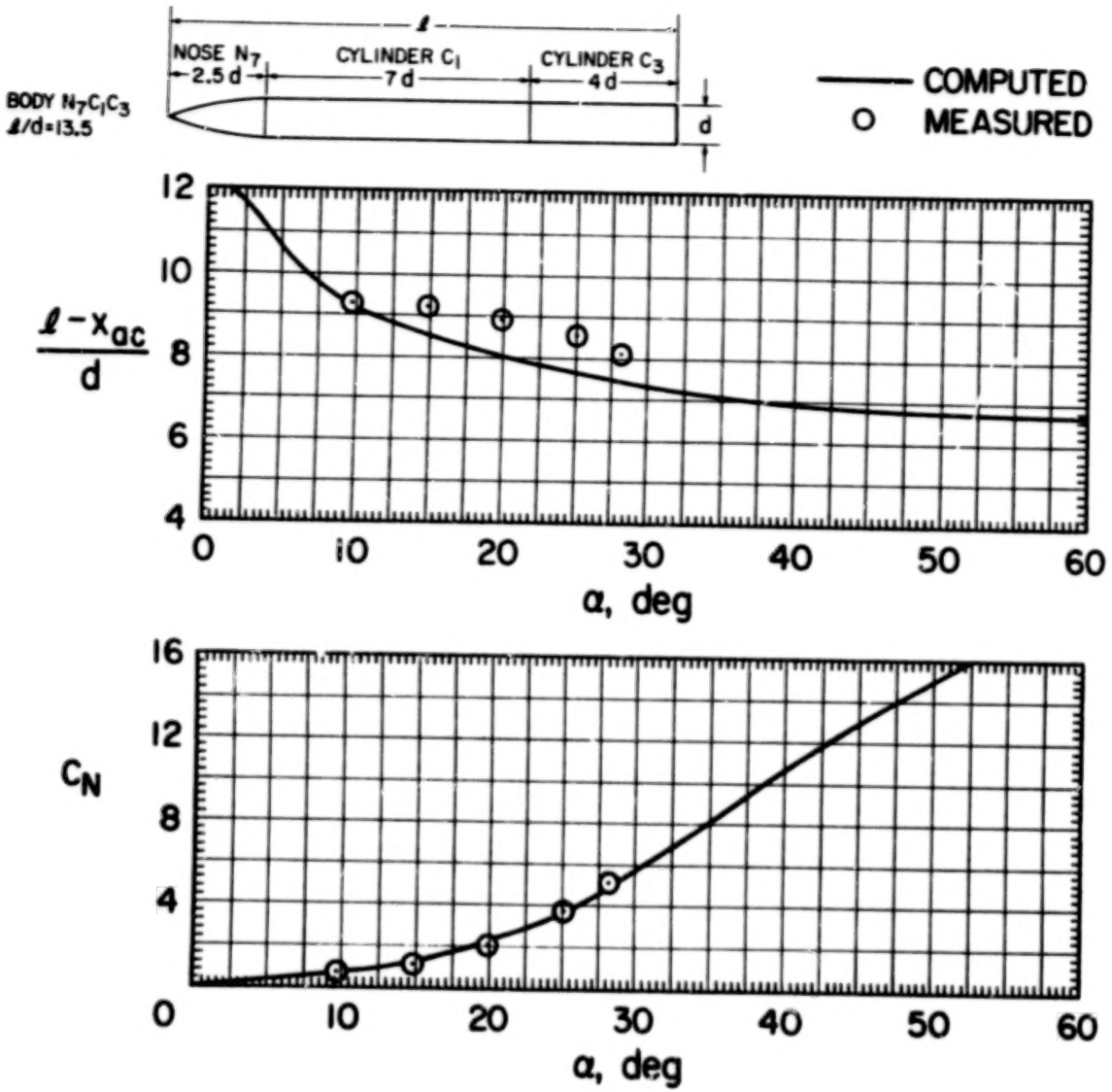

(c) $M_\infty = 1.2$

Figure 22.– Continued.

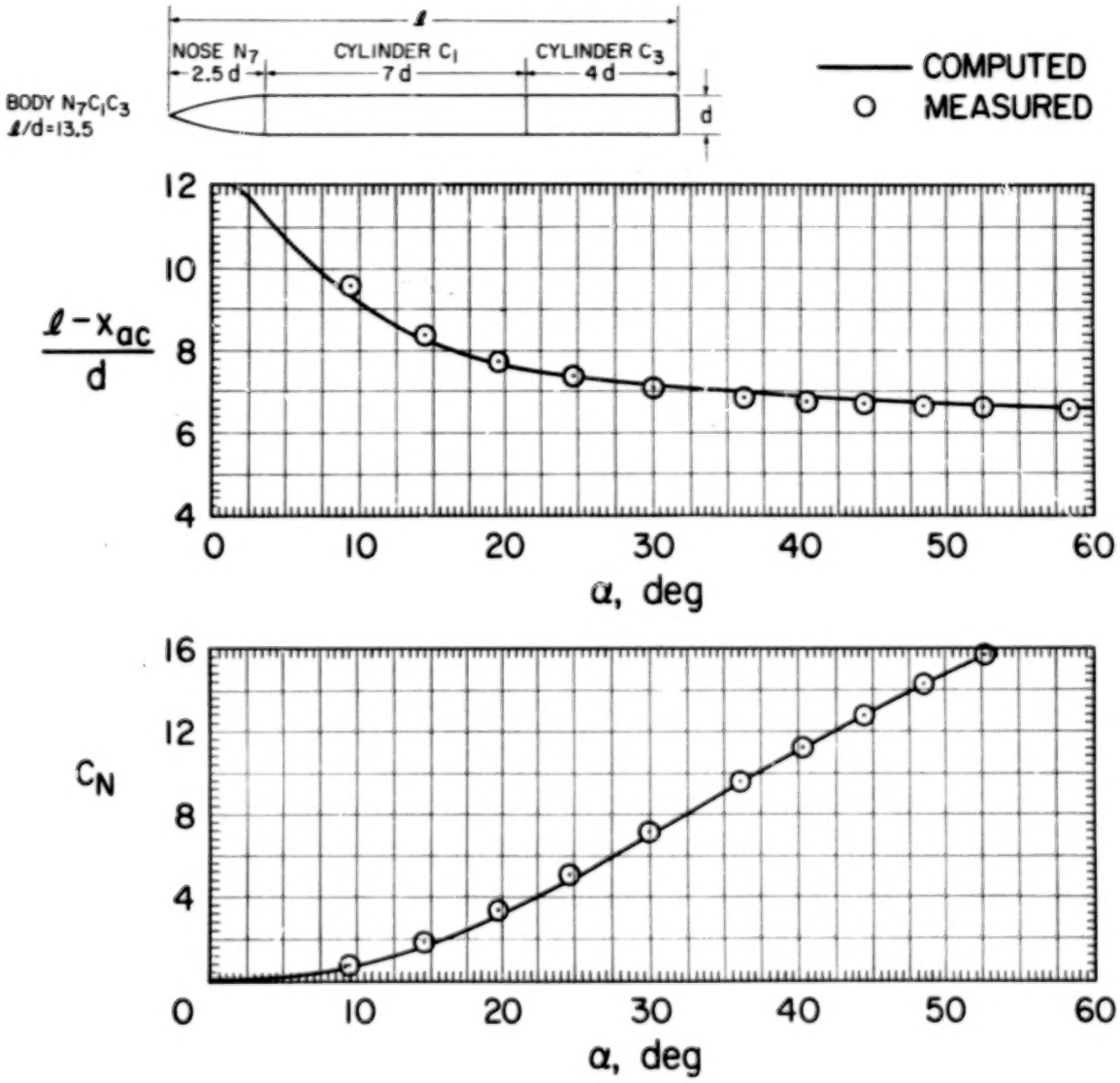

(d) $M_\infty = 2.0$

Figure 22.– Concluded.

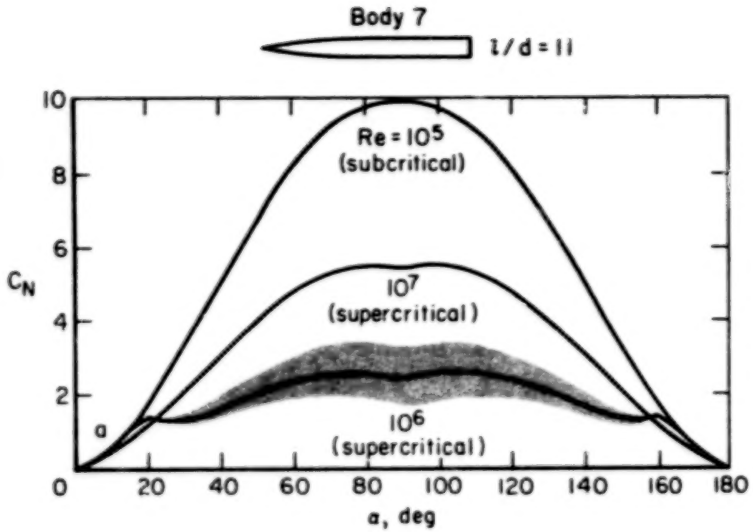

(a) Normal force coefficients.

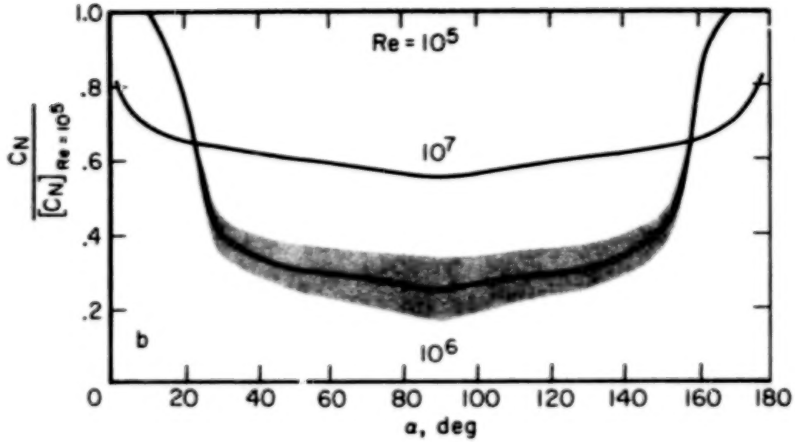

(b) Ratios of normal force coefficients.

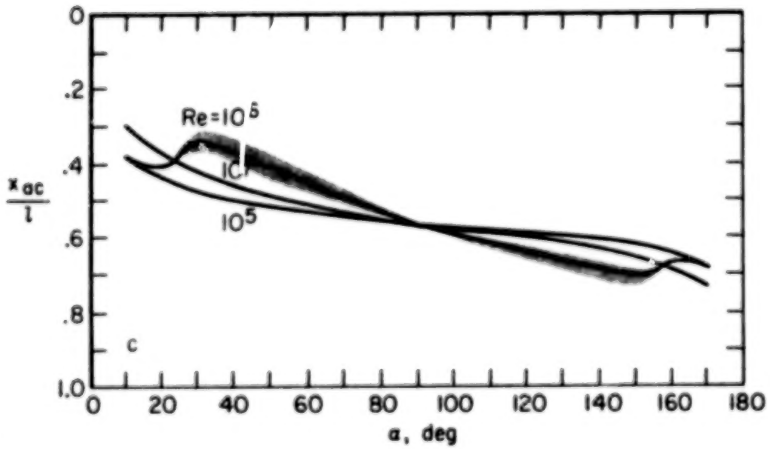

(c) Aerodynamic force centers.

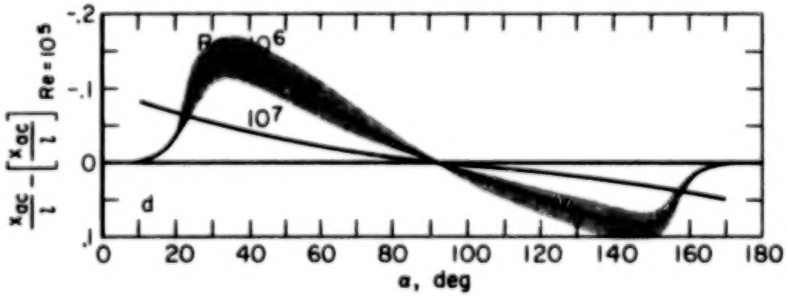

(d) Differences between aerodynamic force centers.

Figure 23.– Effect of supercritical Reynolds numbers on the computed aerodynamic characteristics of an ogive-cylinder body at subcritical crossflow Mach numbers ($M_N \lesssim 0.4$).

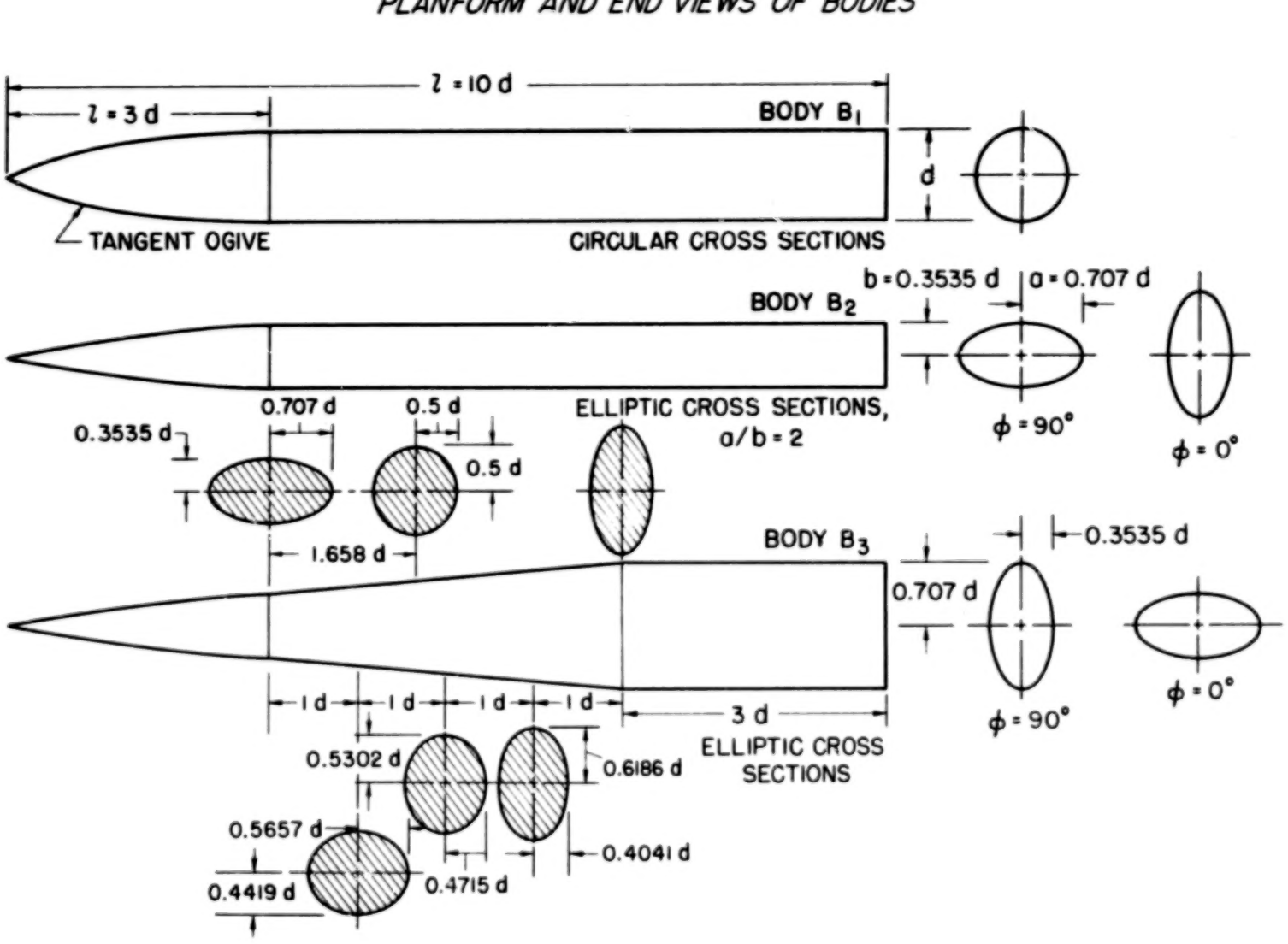

(a) Model dimensions with $d = 6.6$ cm (2.6 in.)

Figure 24.– Bodies of elliptic cross section for which the aerodynamic characteristics were measured in reference 18 and computed in this study.

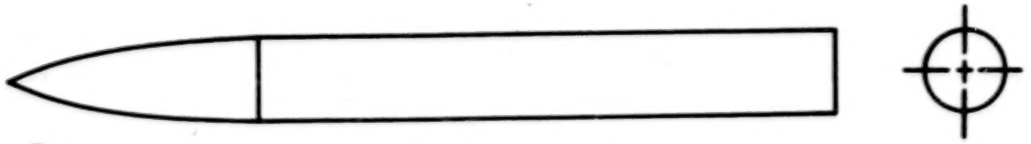

B_1

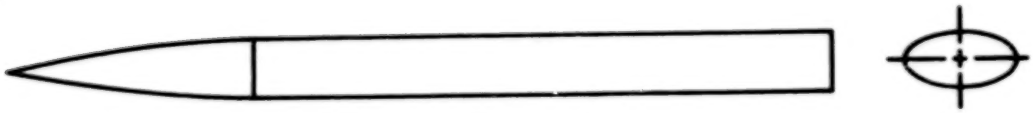

$B_2\ \phi = 90°$

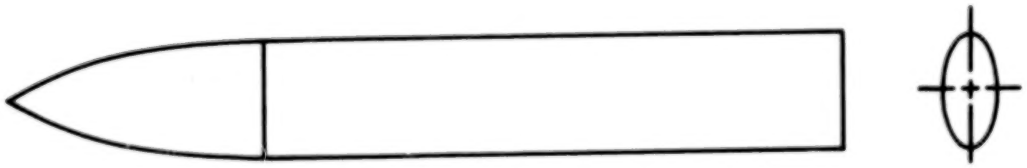

$B_2\ \phi = 0°$

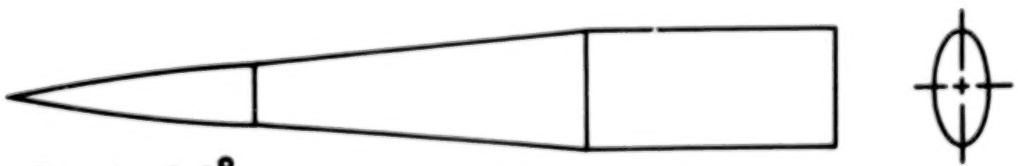

$B_3\ \phi = 90°$

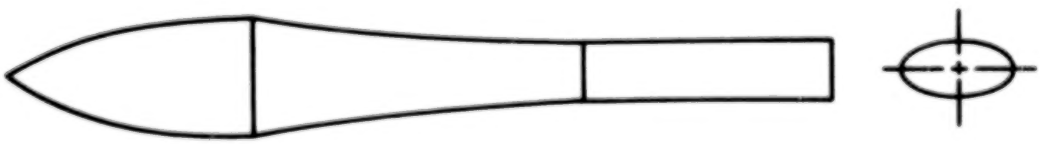

$B_3\ \phi = 0°$

(b) Planform views of configurations studied.

Figure 24.– Concluded.

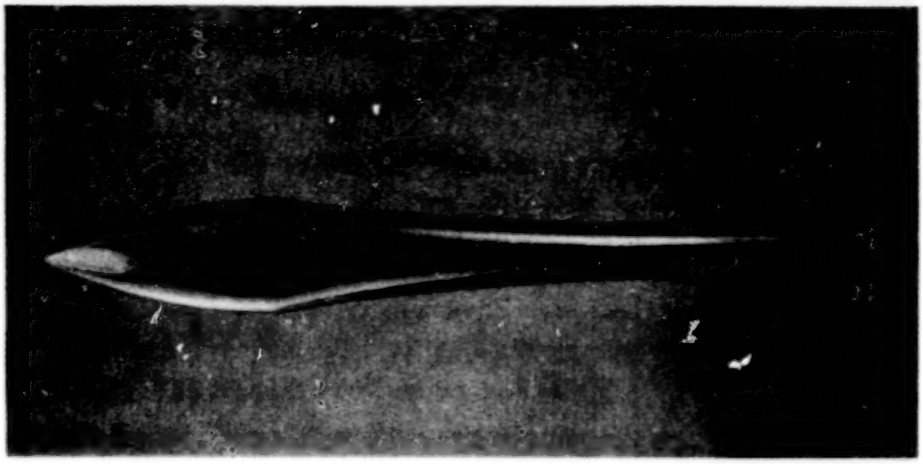

(a) Planform view at $\phi = 0°$.

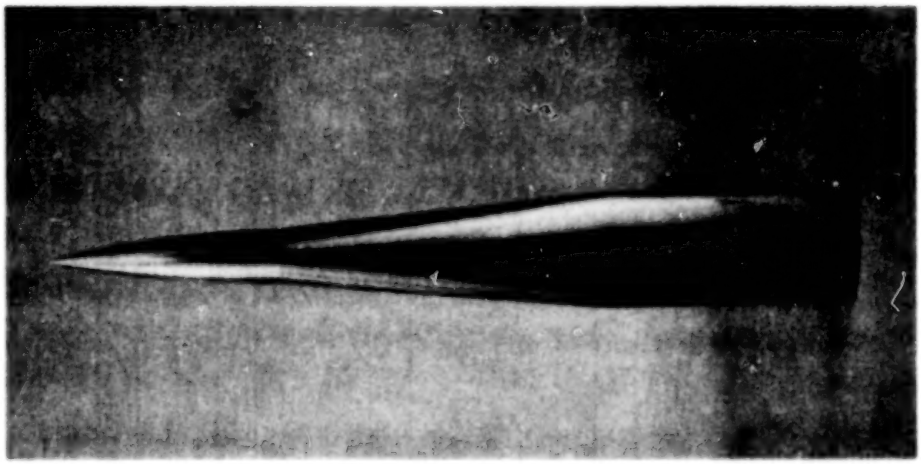

(b) Planform view at $\phi = 90°$.

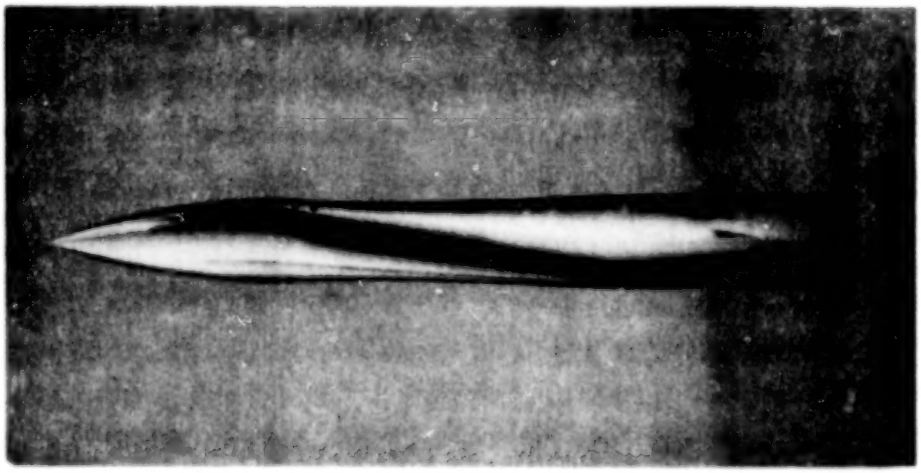

(c) Three-quarter view.

Figure 25.– Photographs of aluminum body B_3.

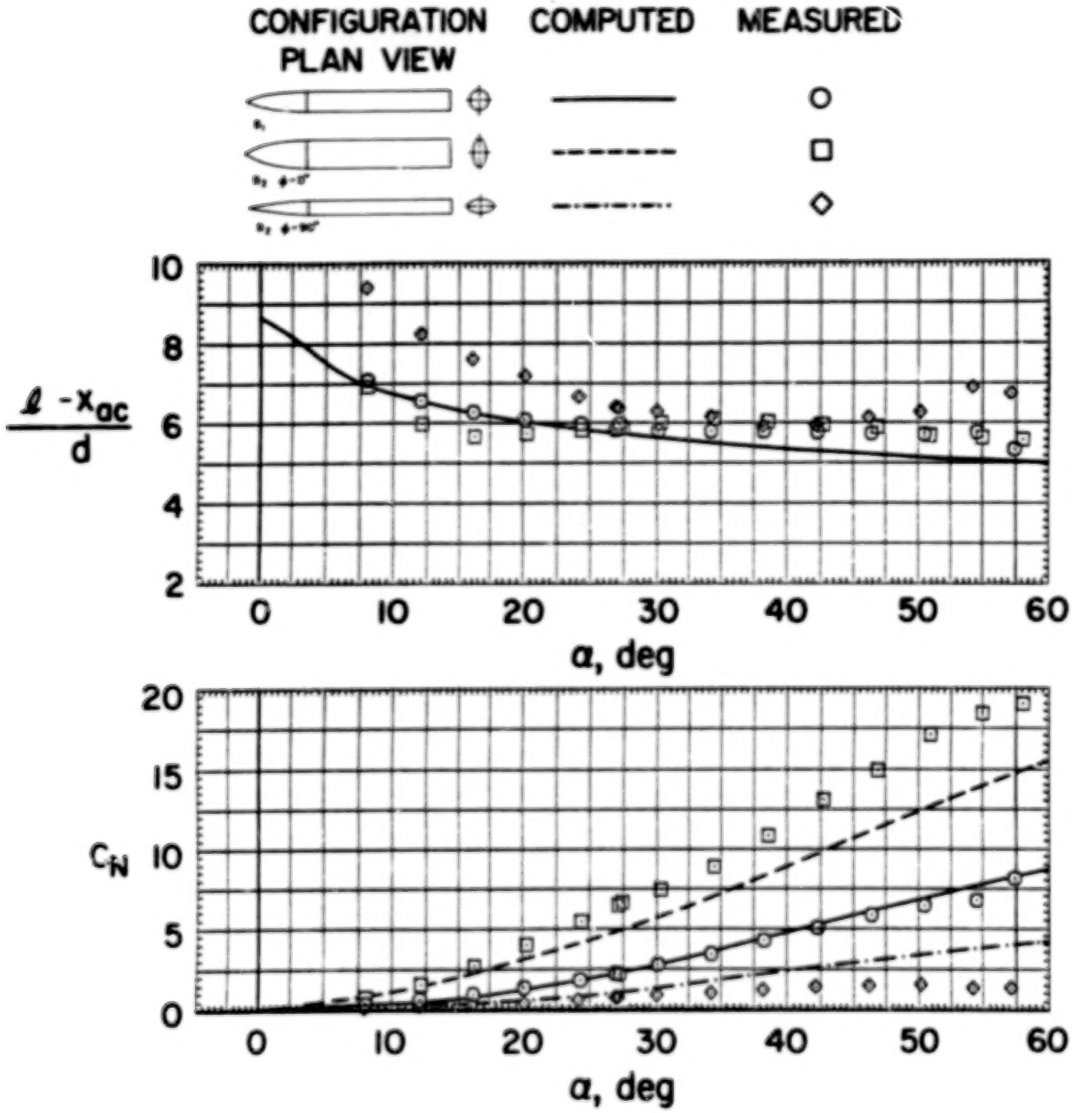

(a) $M_\infty = 0.6$, Re = 6.5×10^5.

Figure 26.– Comparison of computed with measured aerodynamic characteristics for bodies B_1 and B_2; $0.6 \leq M_\infty \leq 2.0$.

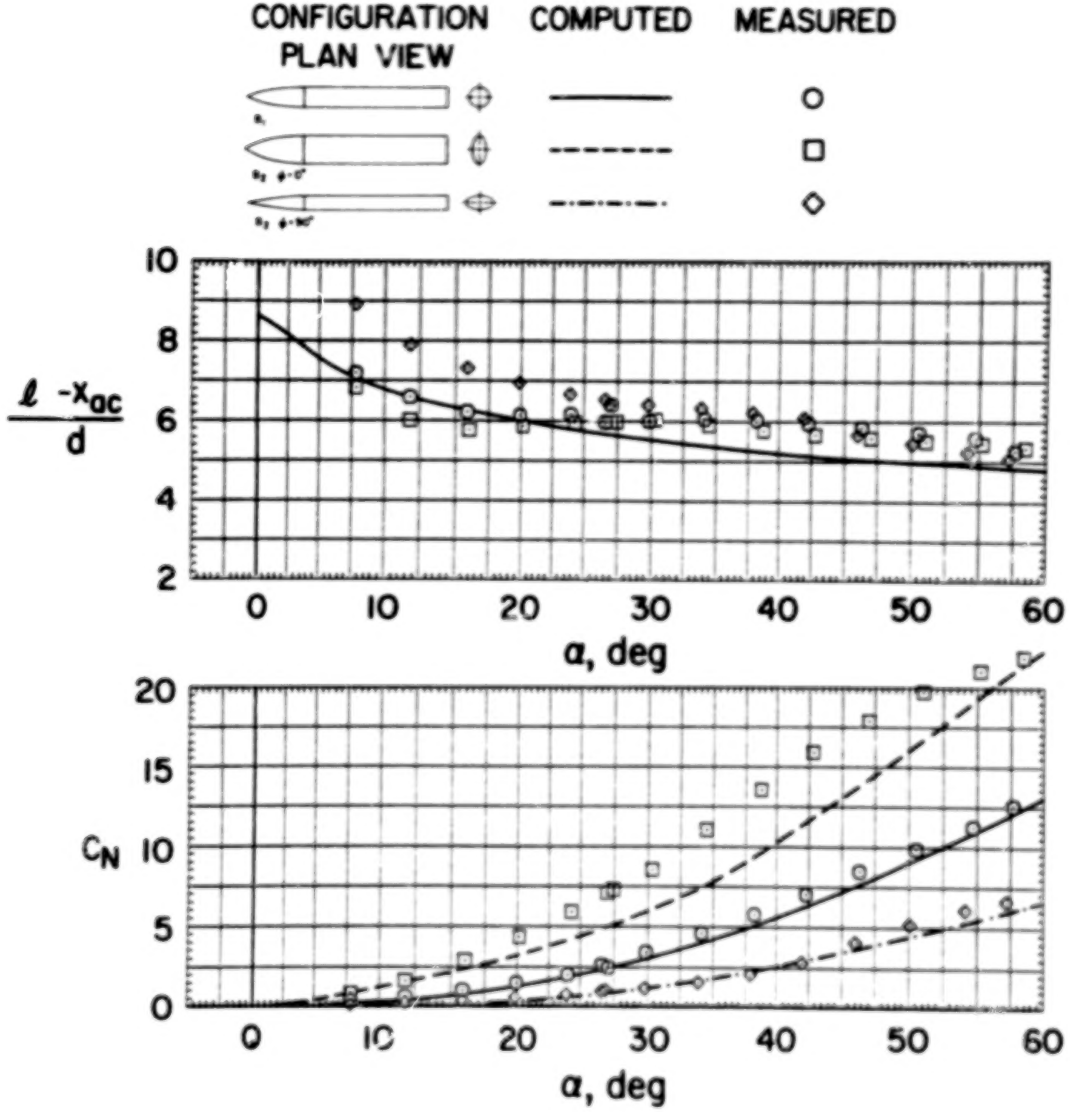

(b) $M_\infty = 0.9$, Re = 6.5×10^5.

Figure 26.– Continued.

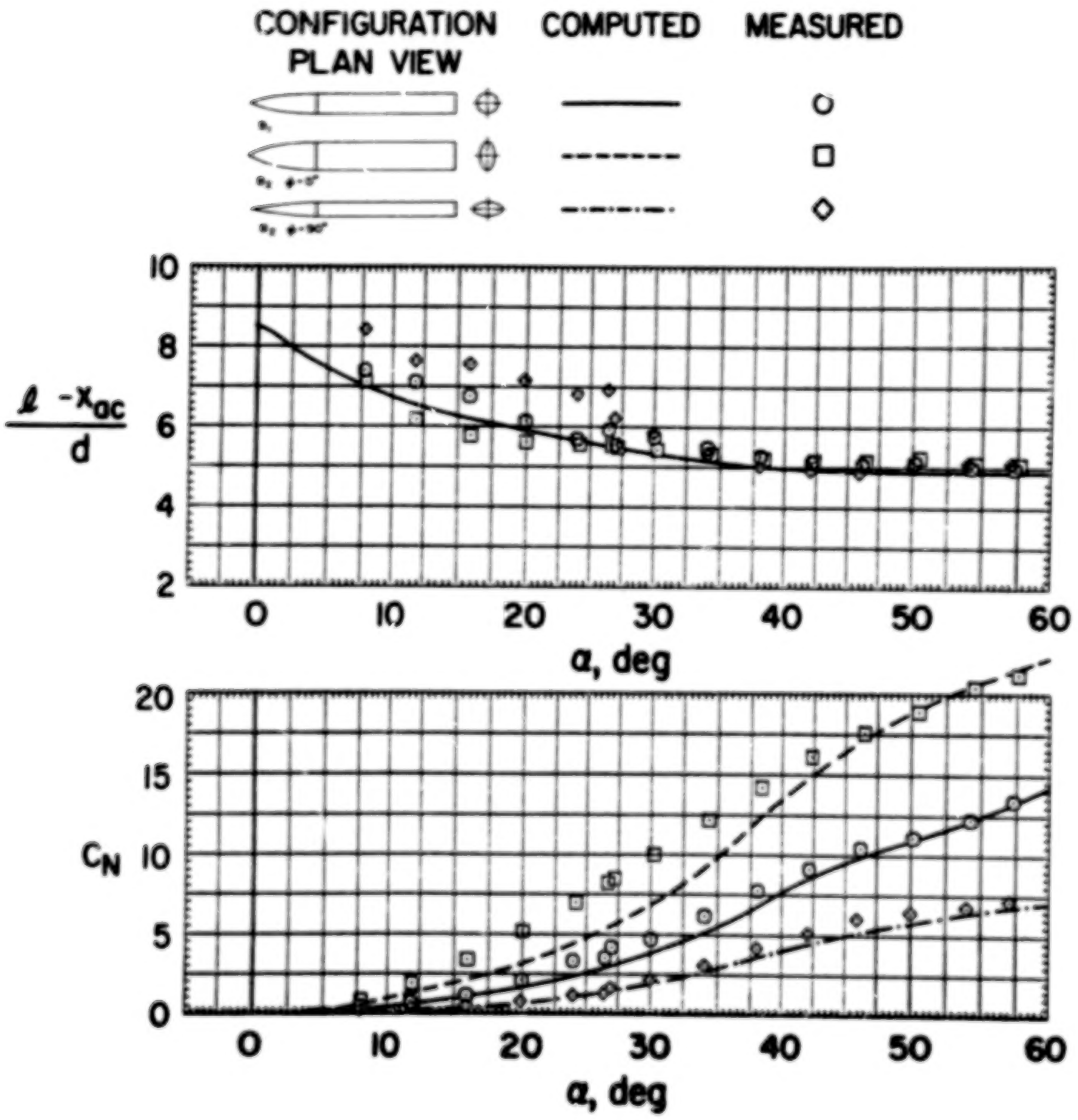

(c) $M_\infty = 1.2$, $Re = 3.8 \times 10^5$.

Figure 26.– Continued.

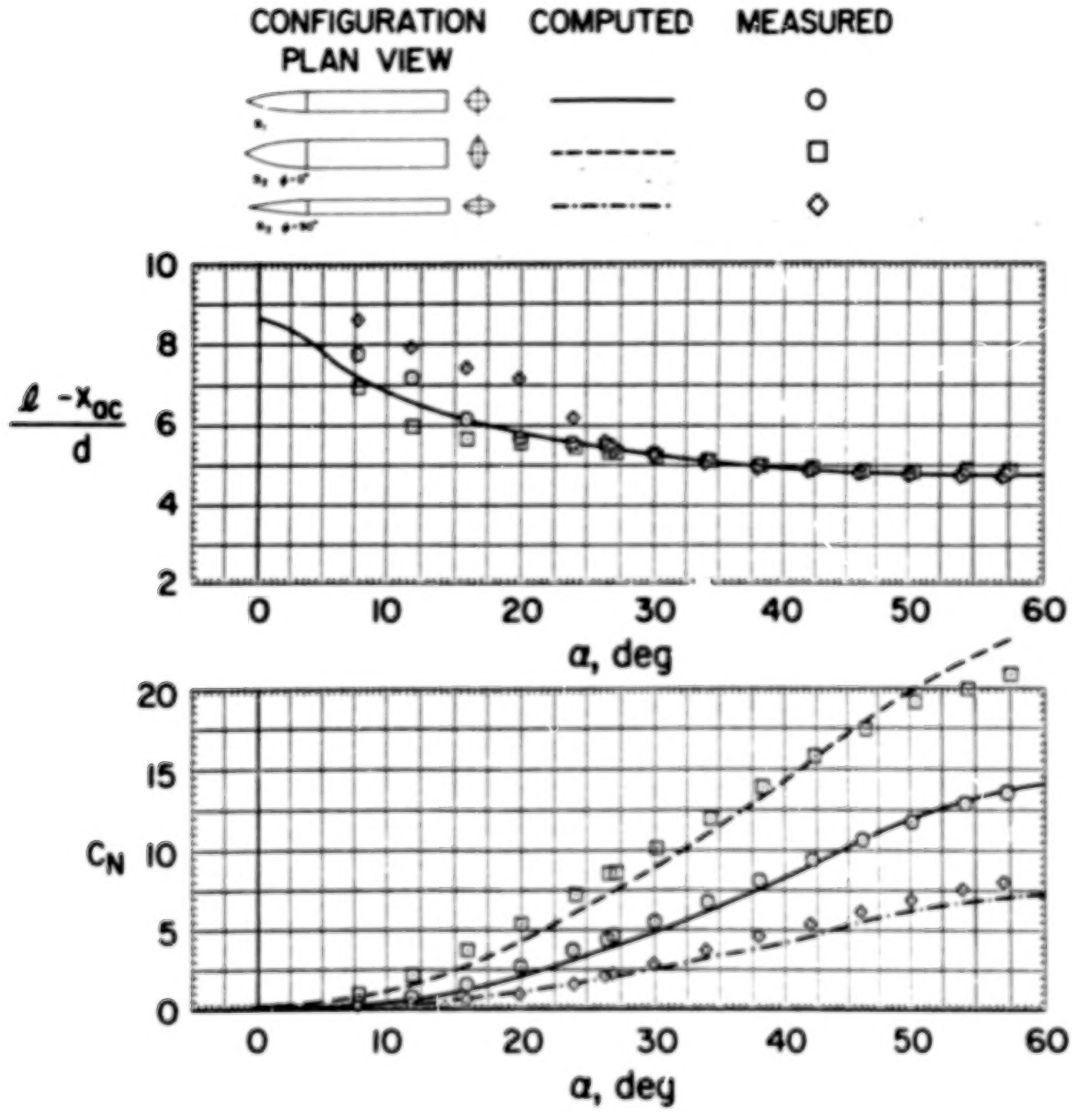

(d) $M_\infty = 1.5$, Re = 3.8×10^5.

Figure 26.– Continued.

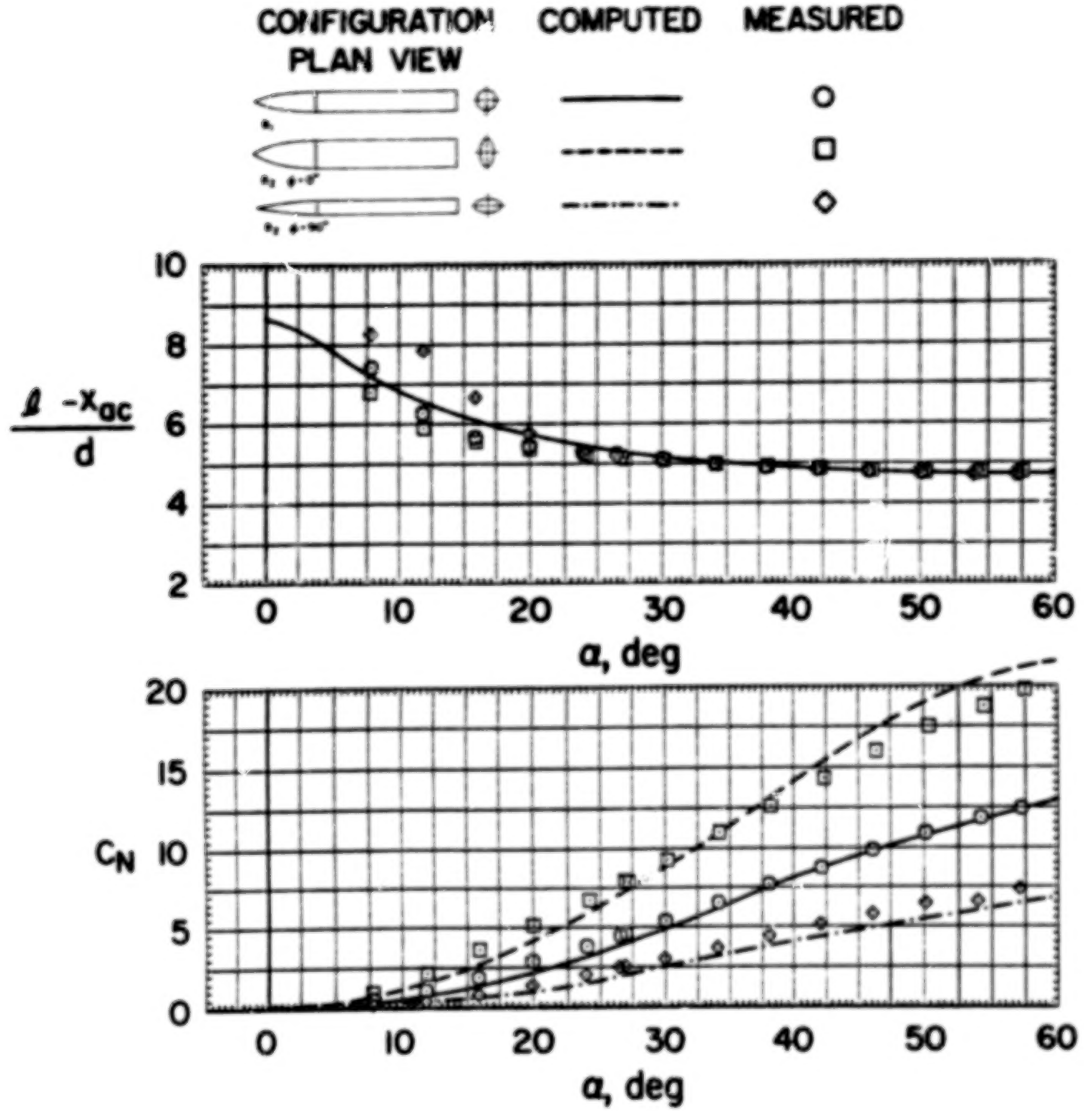

(e) $M_\infty = 2.0$, Re = 3.8×10^5.

Figure 26.– Concluded.

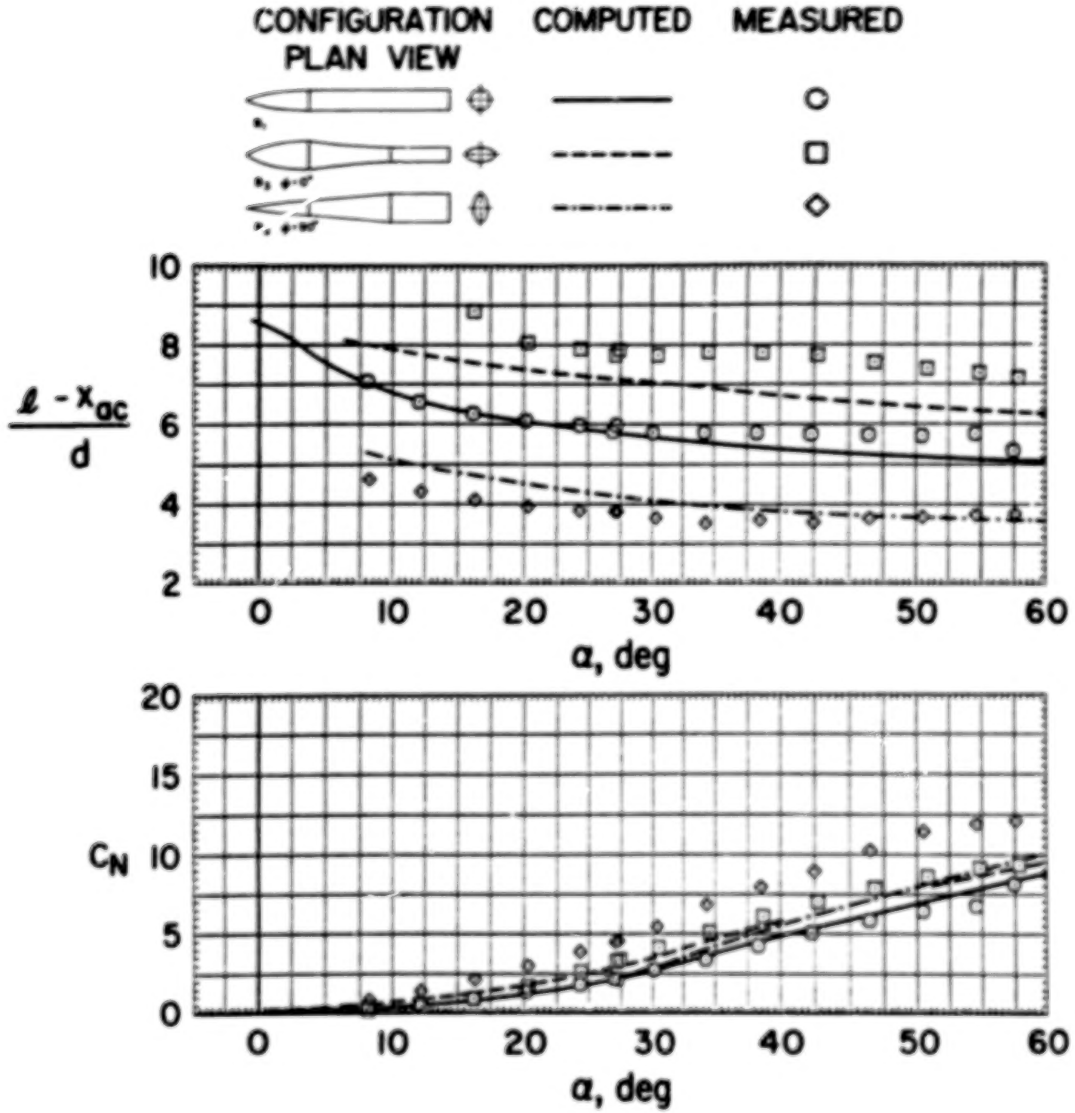

(a) $M_\infty = 0.6$, Re = 6.5×10^5.

Figure 27.– Comparison of computed with measured aerodynamic characteristics for bodies B_1 and B_3; $0.6 \leq M_\infty < 2.0$.

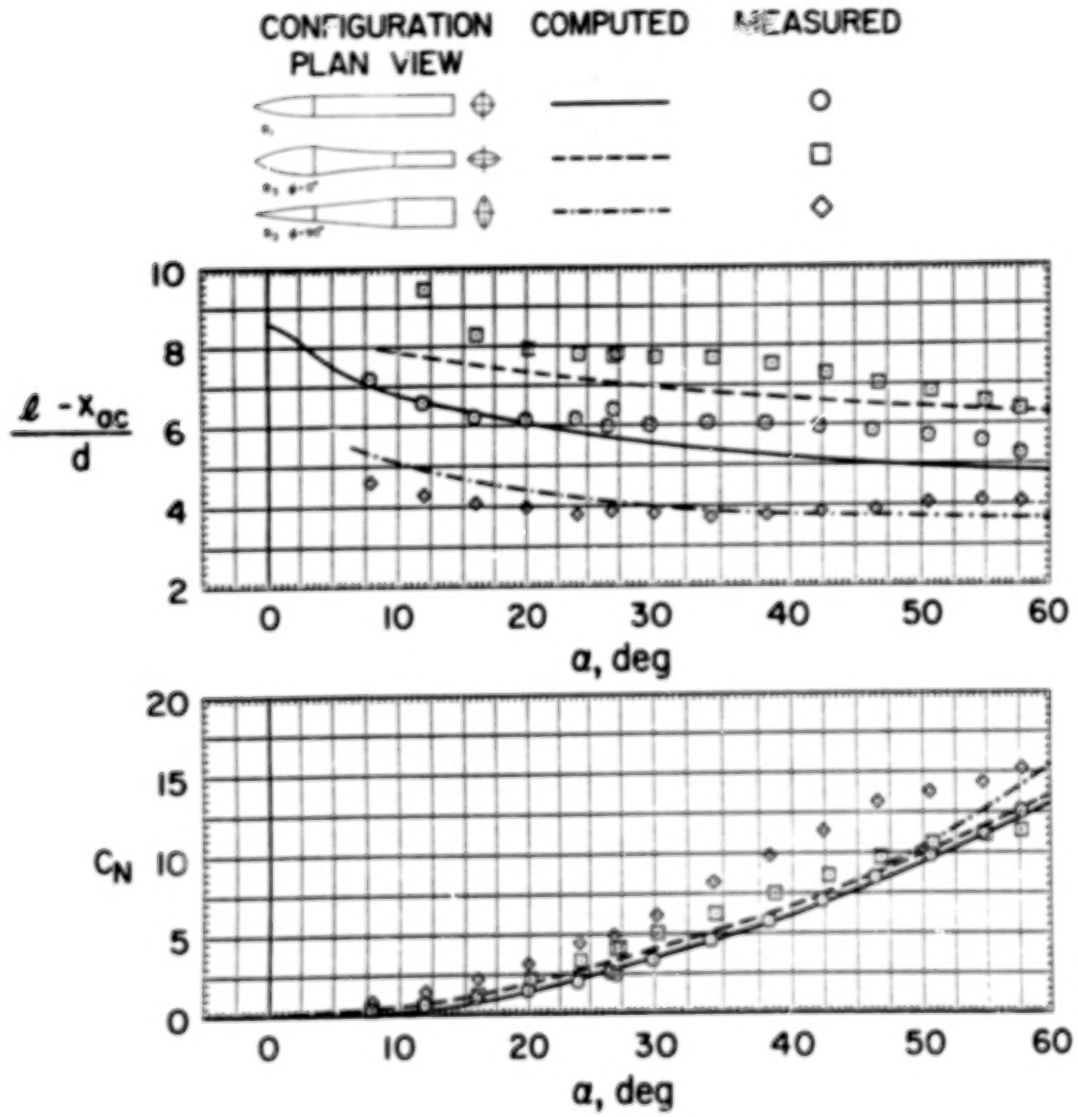

(b) $M_\infty = 0.9$, $Re = 6.5 \times 10^5$.

Figure 27.– Continued.

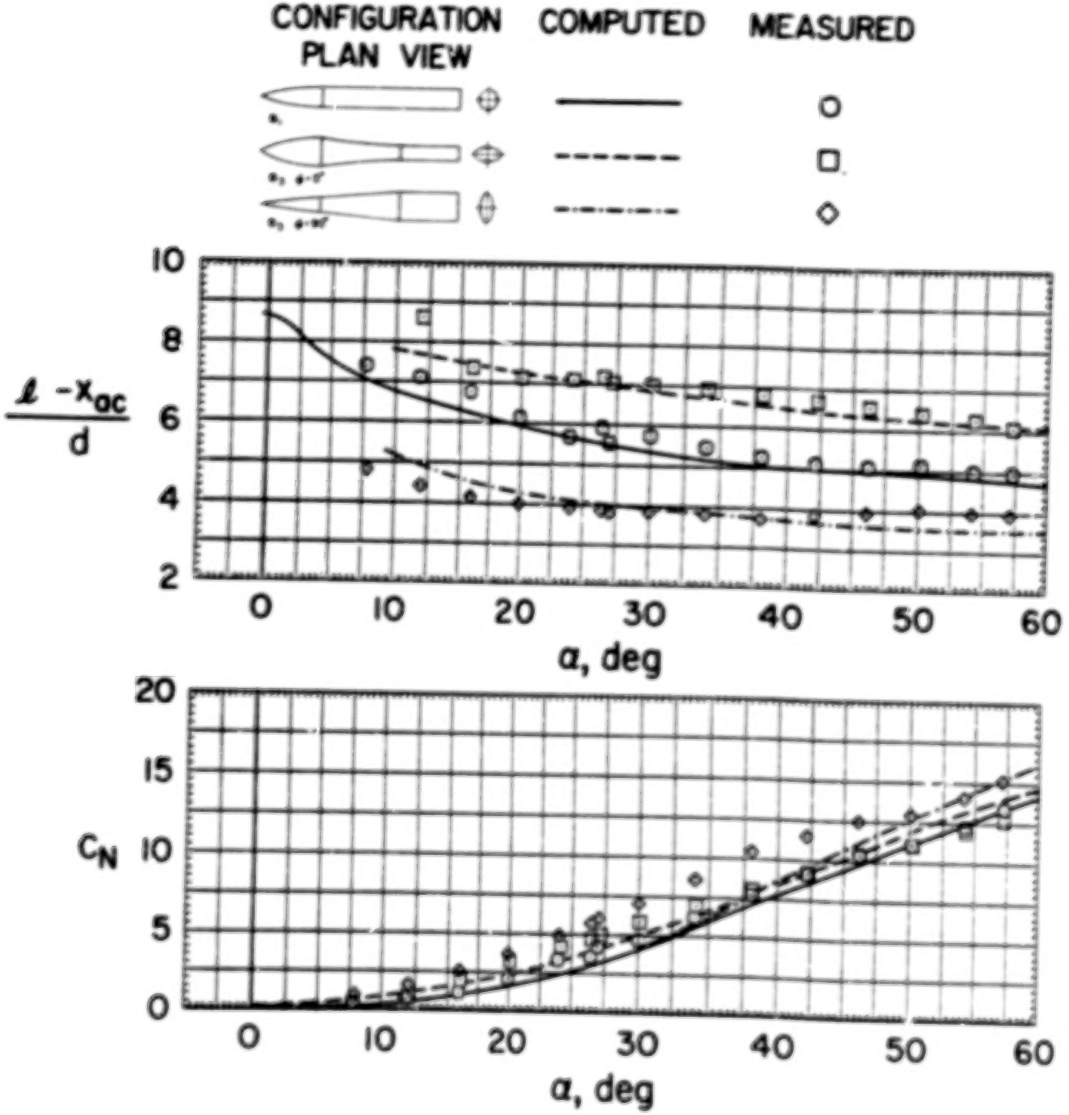

(c) $M_\infty = 1.2$, Re = 3.8×10^5.

Figure 27.– Continued.

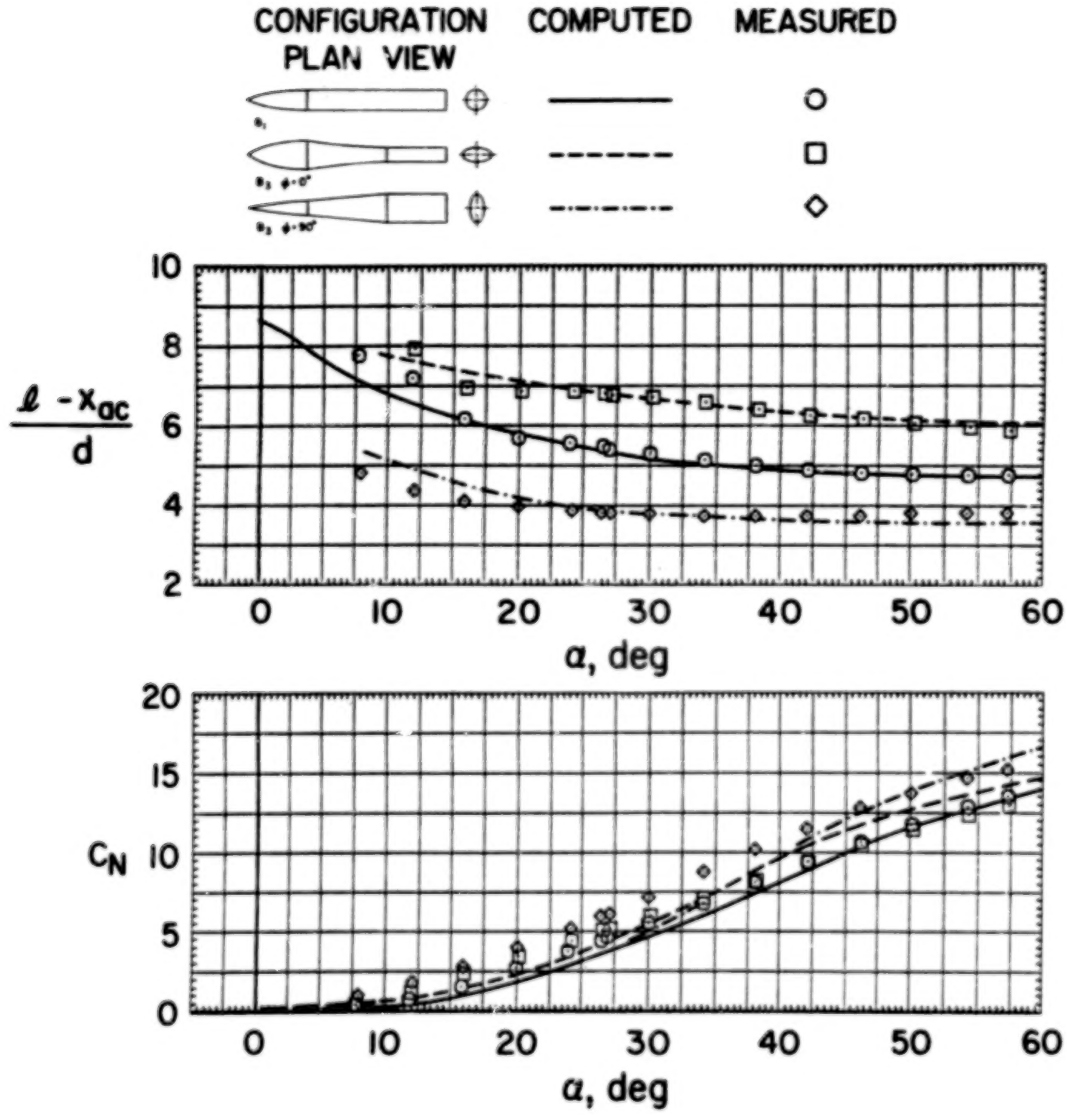

(d) $M_\infty = 1.5$, Re = 3.8×10^5.

Figure 27.– Continued.

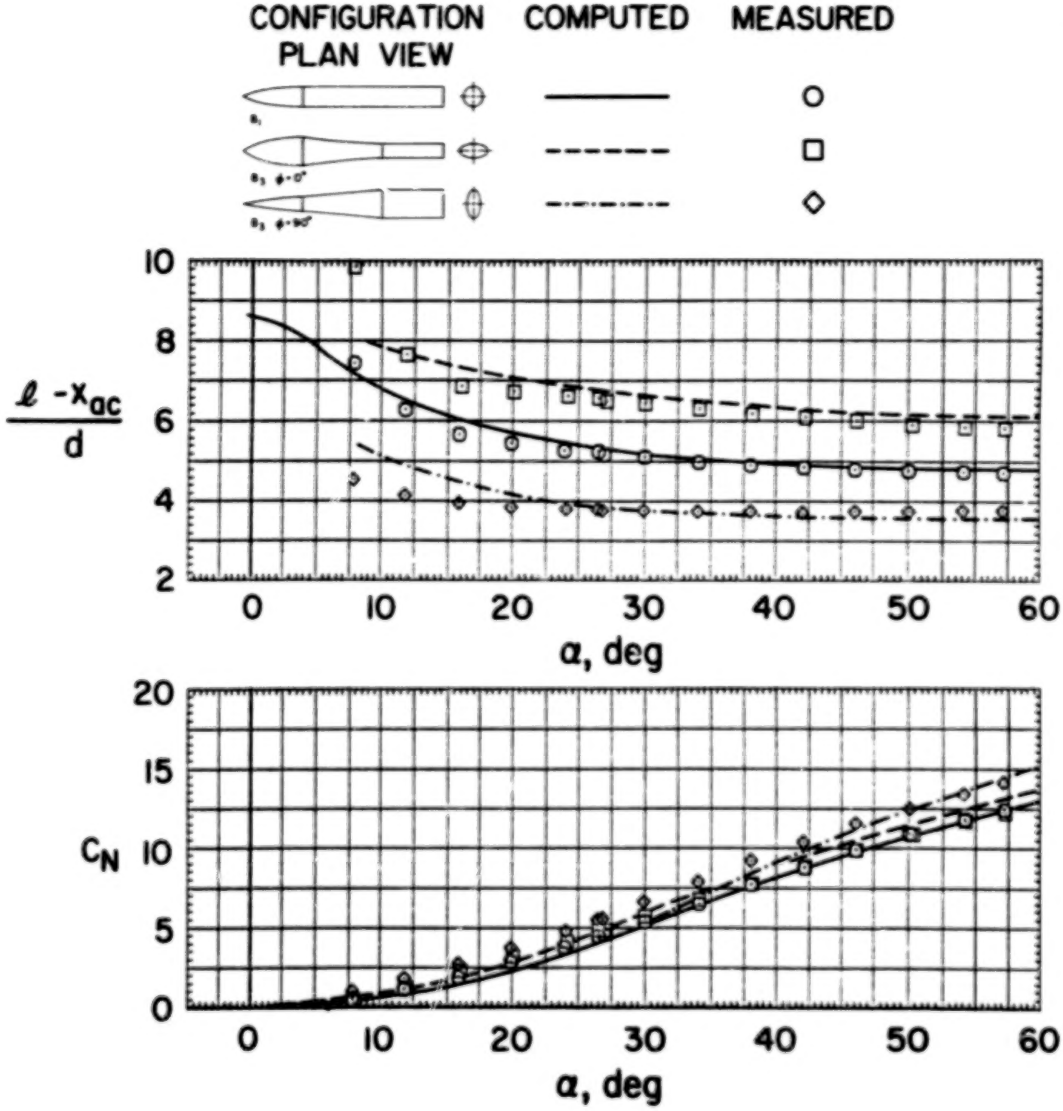

(e) $M_\infty = 2.0$, Re = 3.8×10^5.

Figure 27.– Concluded.

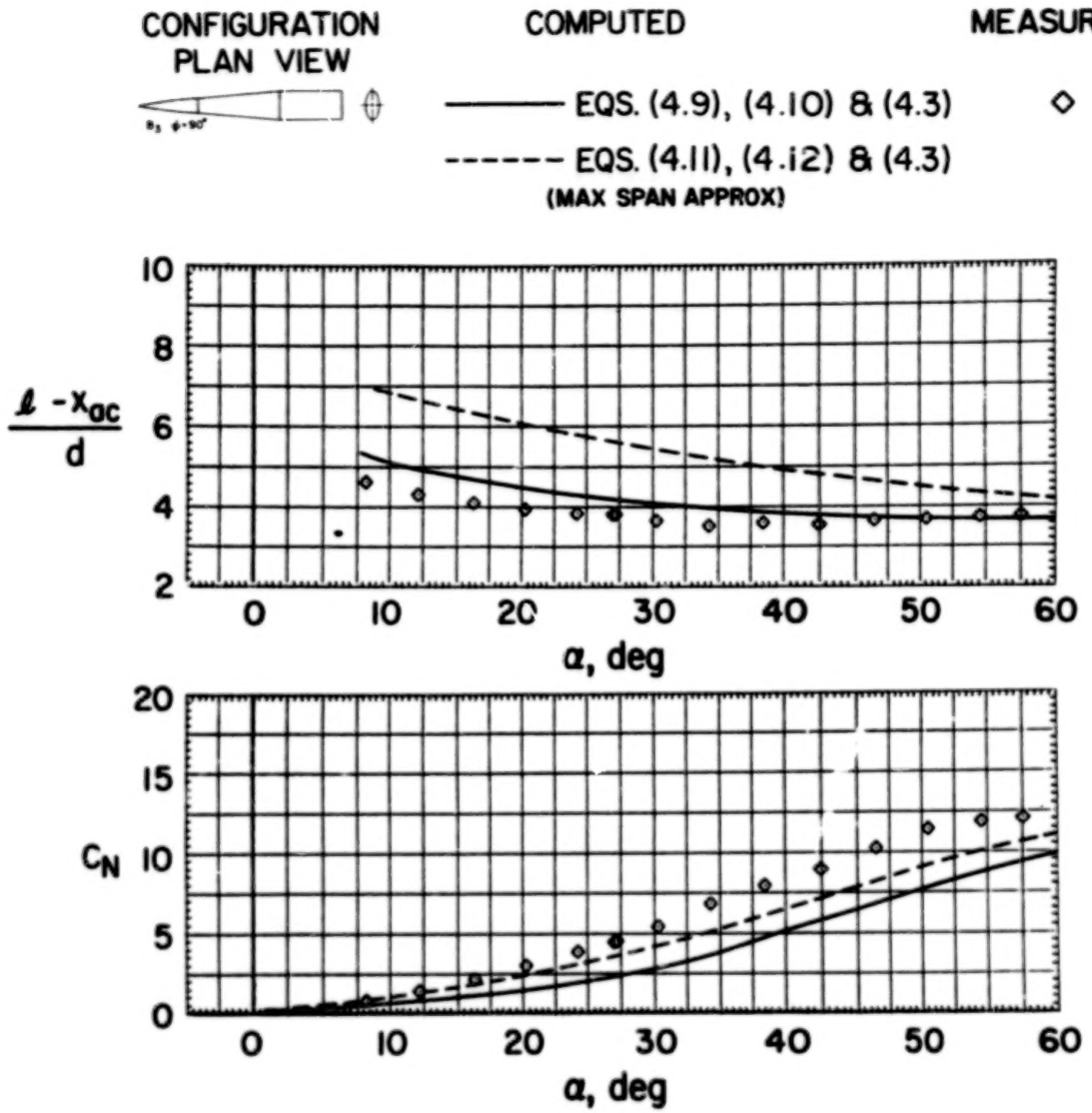

(a) $M_\infty = 0.6$, Re = 6.5×10^5.

Figure 28.– Comparison of computed with measured aerodynamic characteristics for body B_3 at $\phi = 90°$; $0.6 \leq M_\infty \leq 2.0$.

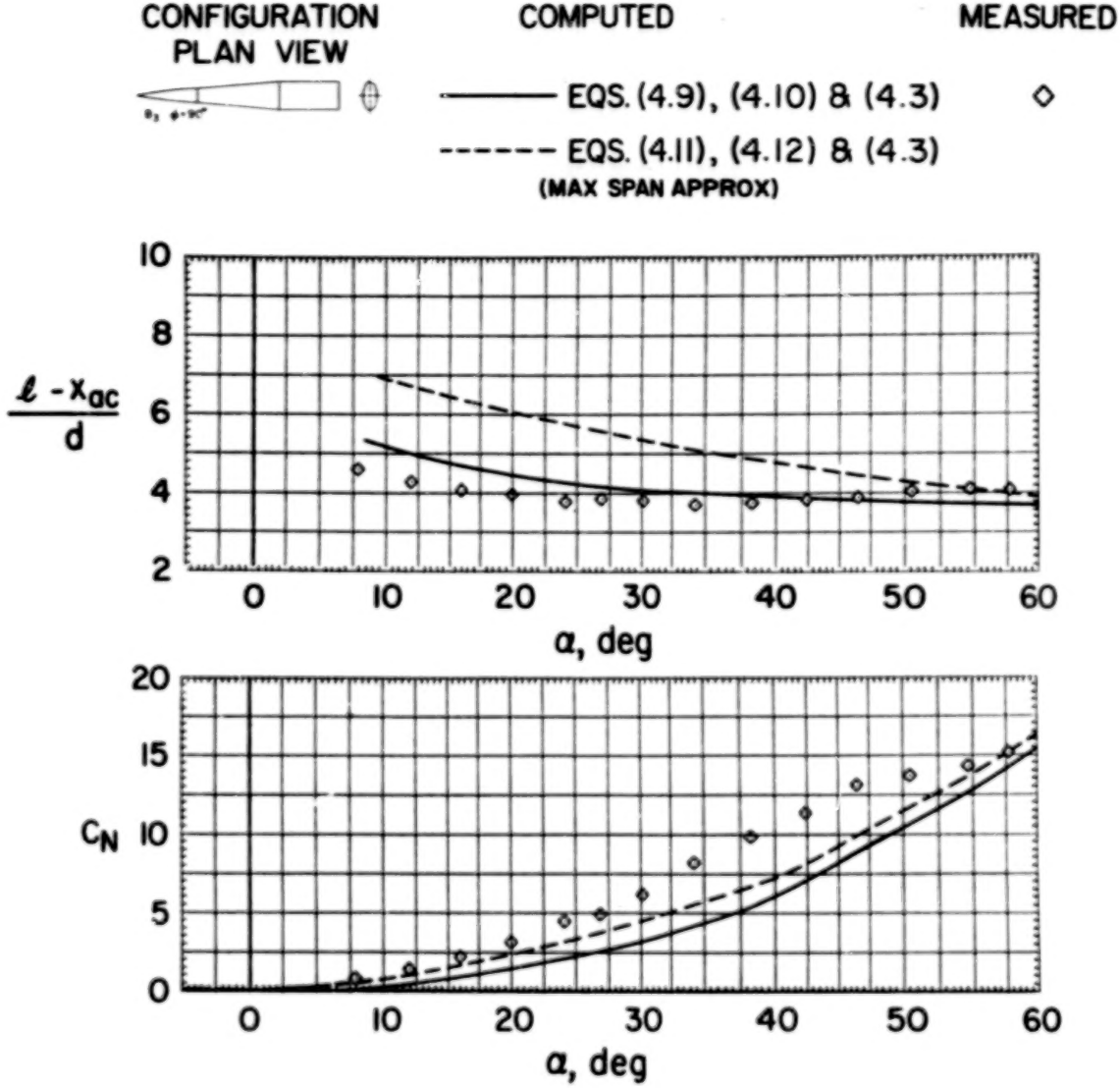

(b) $M_\infty = 0.9$, Re = 6.5×10^5.

Figure 28.– Continued.

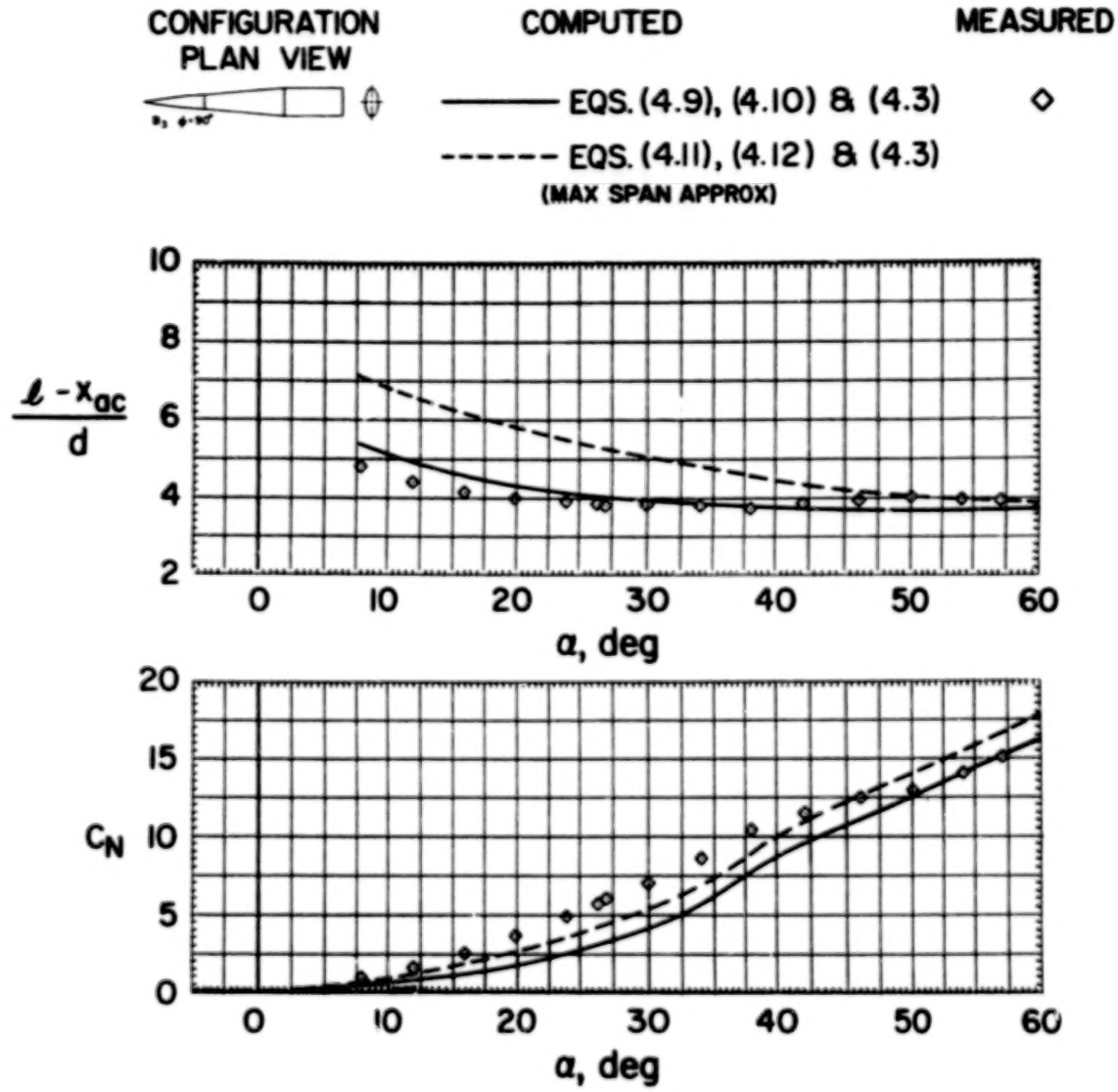

(c) $M_\infty = 1.2$, Re = 3.8×10^5.

Figure 28.– Continued.

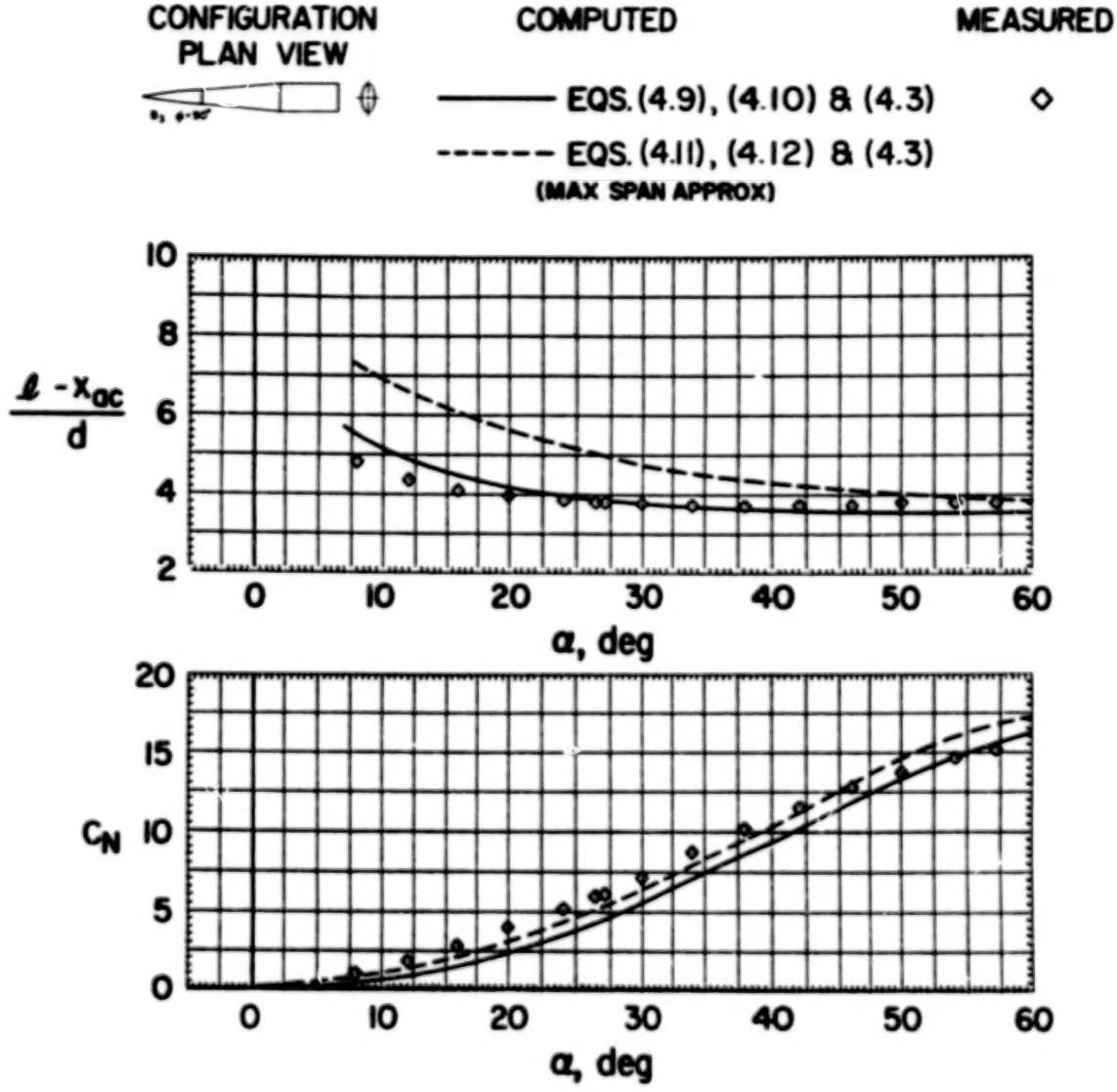

(d) $M_\infty = 1.5$, Re = 3.8×10^5.

Figure 28.– Continued.

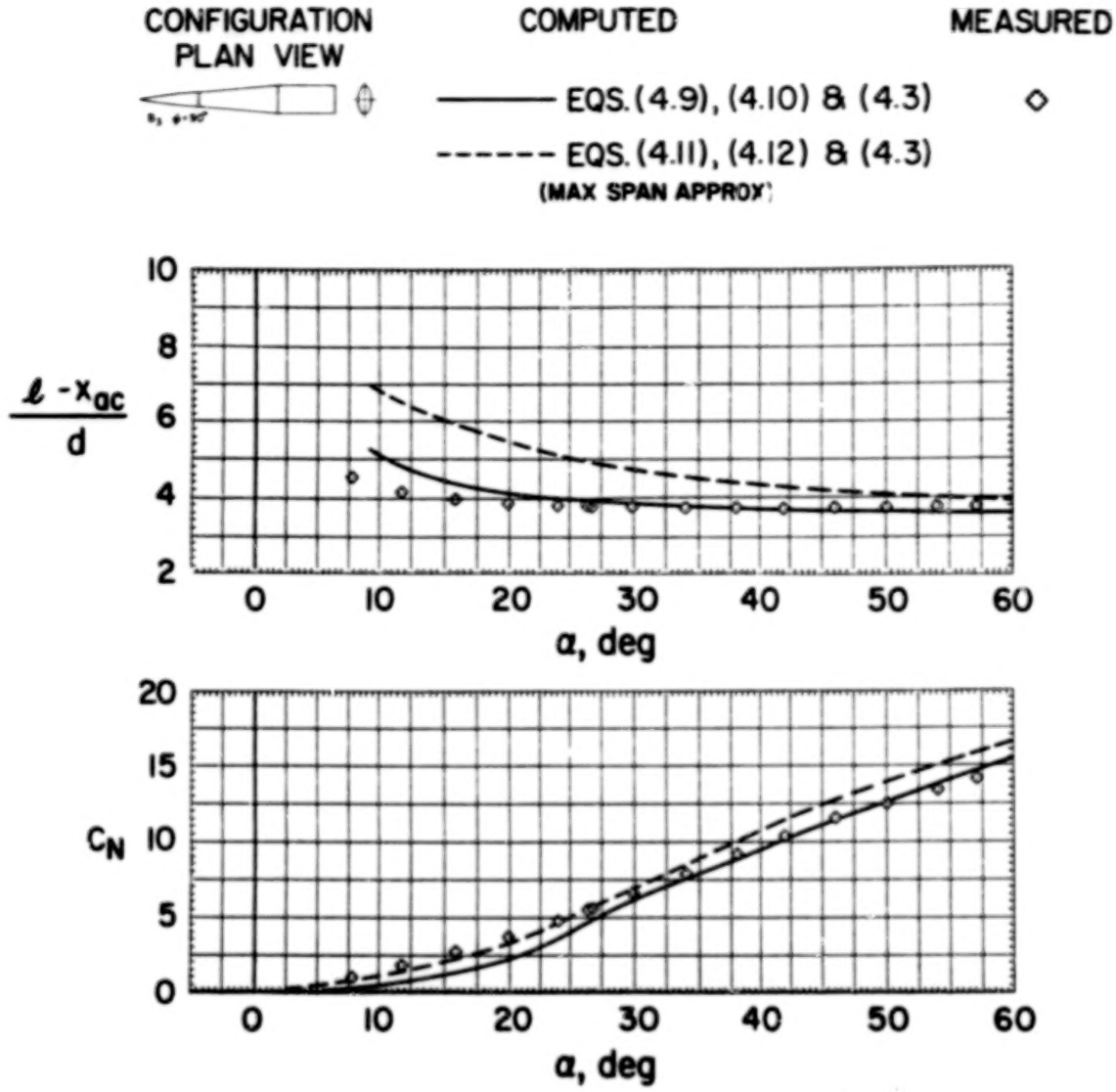

(e) $M_\infty = 2.0$, Re = 3.8×10^5.

Figure 28.– Concluded.

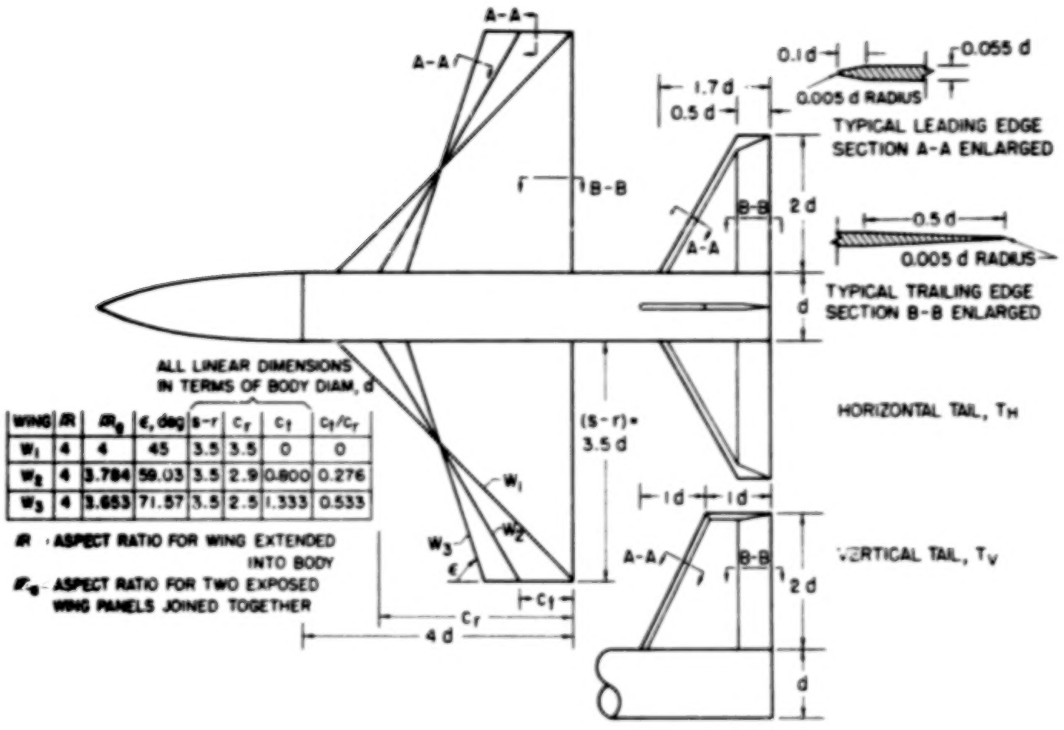

WING	$\mathcal{R}$	$\mathcal{R}_e$	ϵ, deg	s-r	c_r	c_t	c_t/c_r
W_1	4	4	45	3.5	3.5	0	0
W_2	4	3.784	59.03	3.5	2.9	0.800	0.276
W_3	4	3.653	71.57	3.5	2.5	1.333	0.533

$\mathcal{R}$ - ASPECT RATIO FOR WING EXTENDED INTO BODY

$\mathcal{R}_e$ - ASPECT RATIO FOR TWO EXPOSED WING PANELS JOINED TOGETHER

(a) Body B_1 with aspect-ratio 4 wings of various taper ratios and tail arrangement.

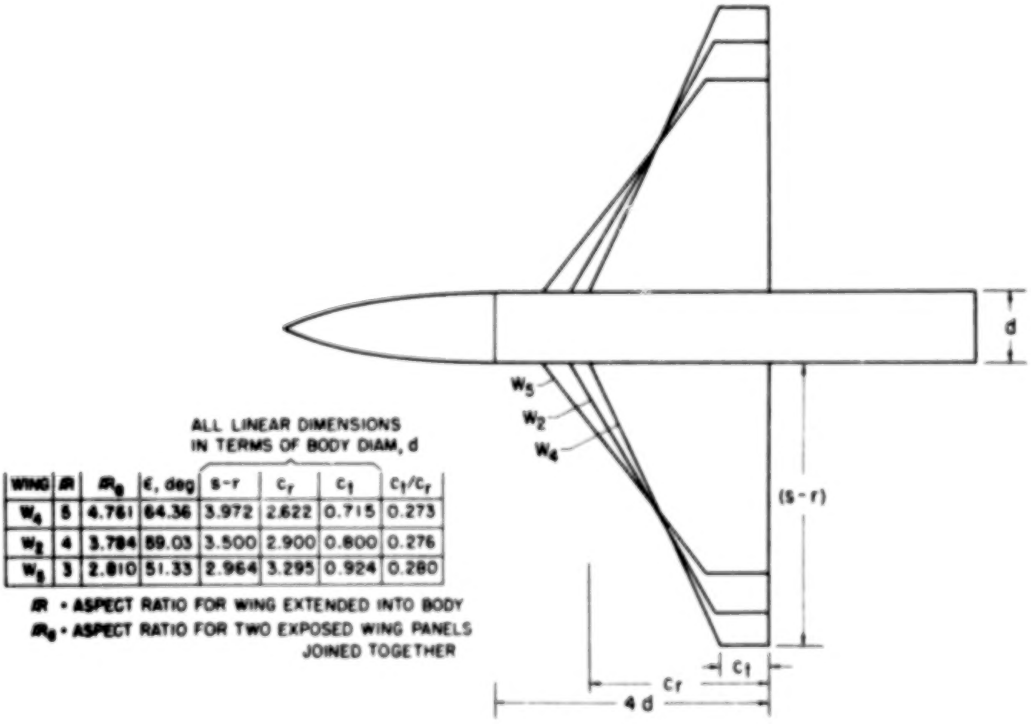

WING	$\mathcal{R}$	$\mathcal{R}_e$	ϵ, deg	s-r	c_r	c_t	c_t/c_r
W_4	5	4.761	64.36	3.972	2.622	0.715	0.273
W_2	4	3.784	59.03	3.500	2.900	0.800	0.276
W_5	3	2.810	51.33	2.964	3.295	0.924	0.280

$\mathcal{R}$ - ASPECT RATIO FOR WING EXTENDED INTO BODY

$\mathcal{R}_e$ - ASPECT RATIO FOR TWO EXPOSED WING PANELS JOINED TOGETHER

(b) Body B_1 with wings of aspect ratio 3, 4, and 5 (W_5, W_2, and W_4).

Figure 29.– Components for body-wing and body-wing-tail models tested in references 20 and 21.

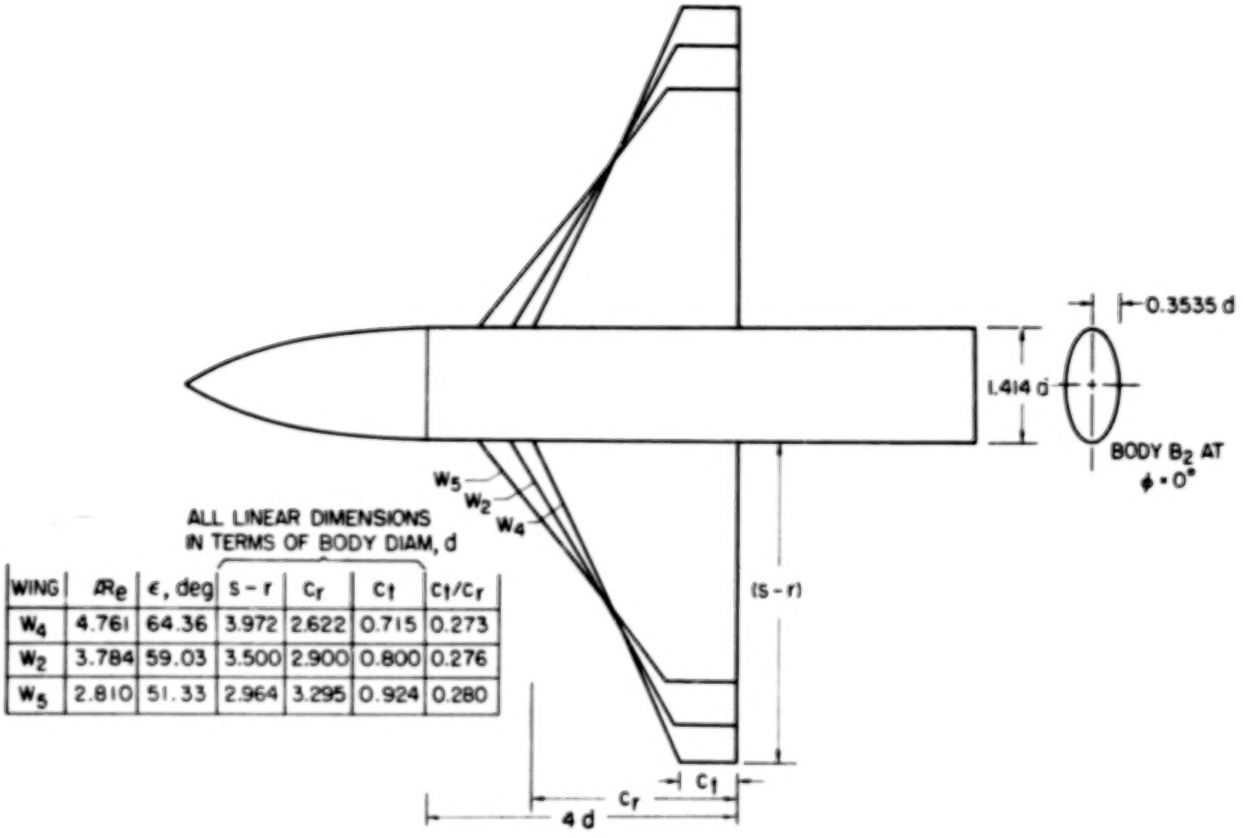

WING	AR_e	ϵ, deg	s - r	c_r	c_t	c_t/c_r
W_4	4.761	64.36	3.972	2.622	0.715	0.273
W_2	3.784	59.03	3.500	2.900	0.800	0.276
W_5	2.810	51.33	2.964	3.295	0.924	0.280

(c) Body B_2 with wings W_2, W_4, and W_5.

Figure 29.– Concluded.

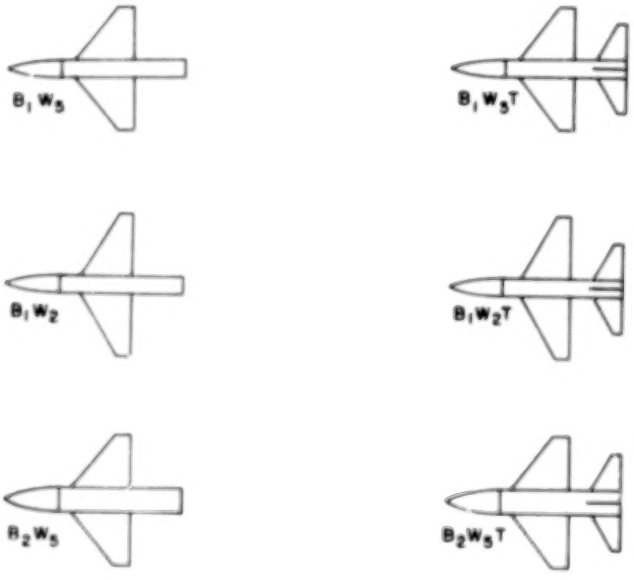

Figure 30.– Planform views of configurations for which the aerodynamic characteristics were measured in references 20 and 21 and computed in this study.

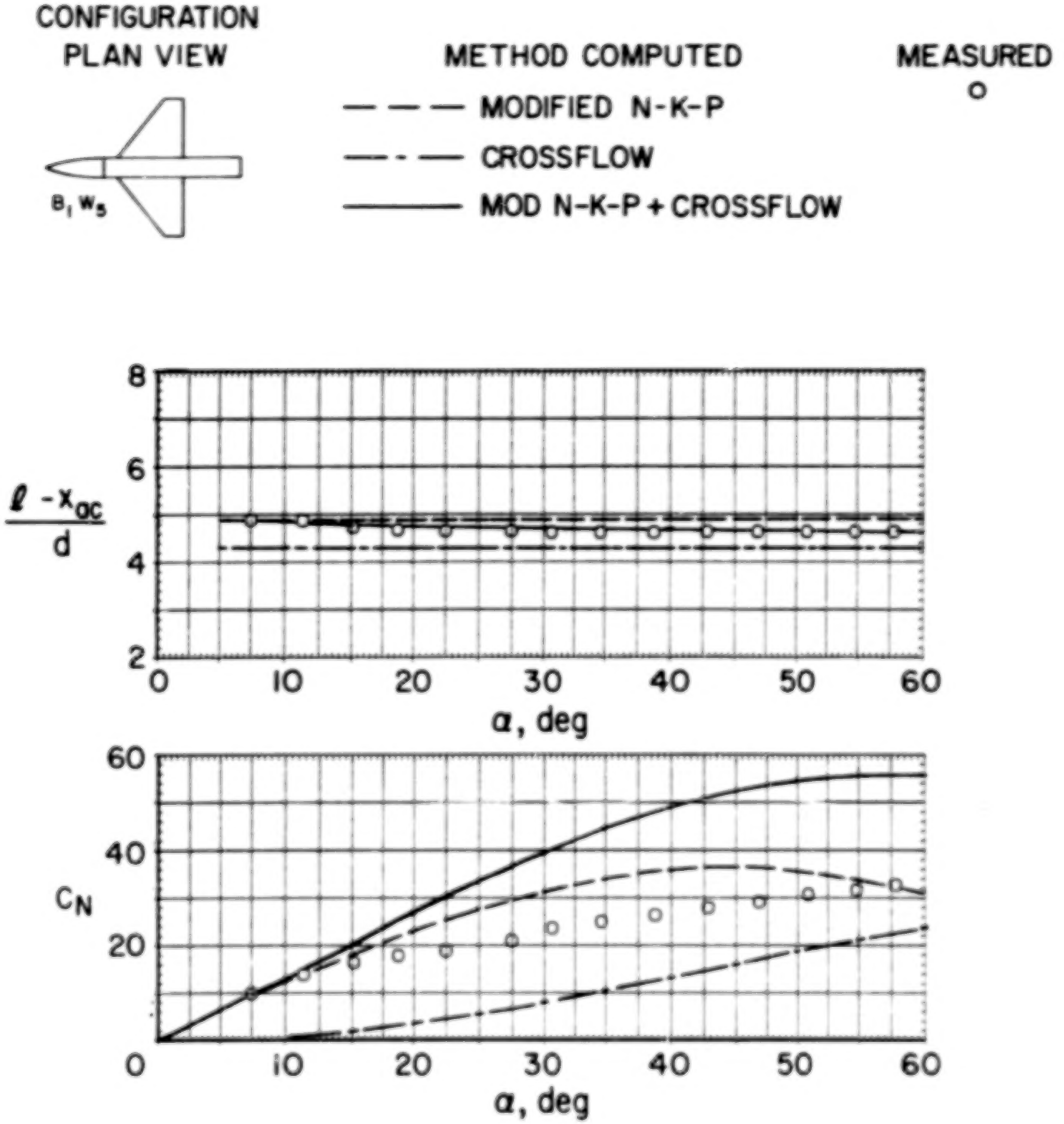

(a) $M_\infty = 0.6$, Re = 4.3×10^5.

Figure 31.– Comparison of computed with measured aerodynamic characteristics for body-wing model $B_1 W_5$.

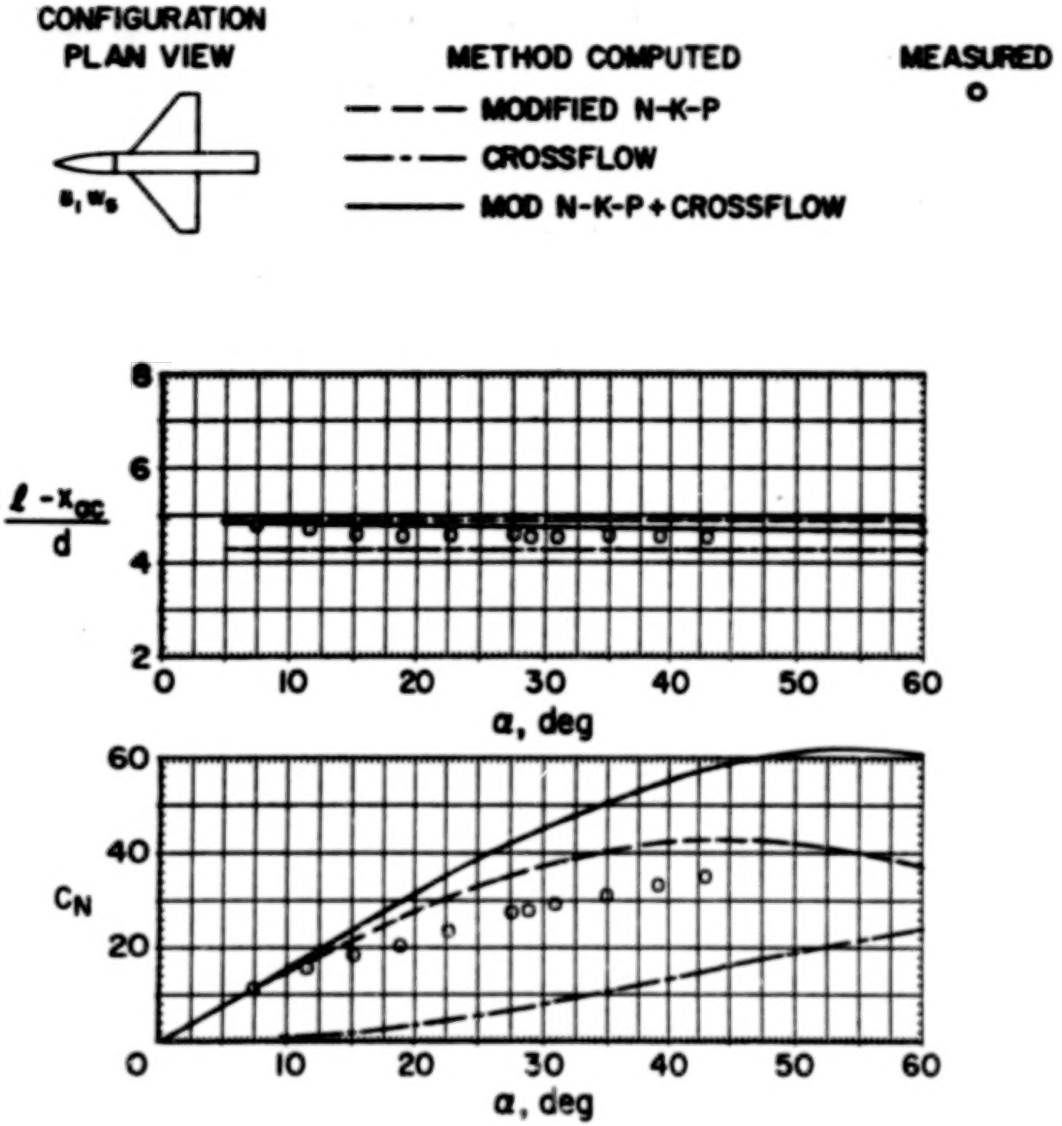

(b) $M_\infty = 0.9$, Re = 4.3×10^5.

Figure 31.– Continued.

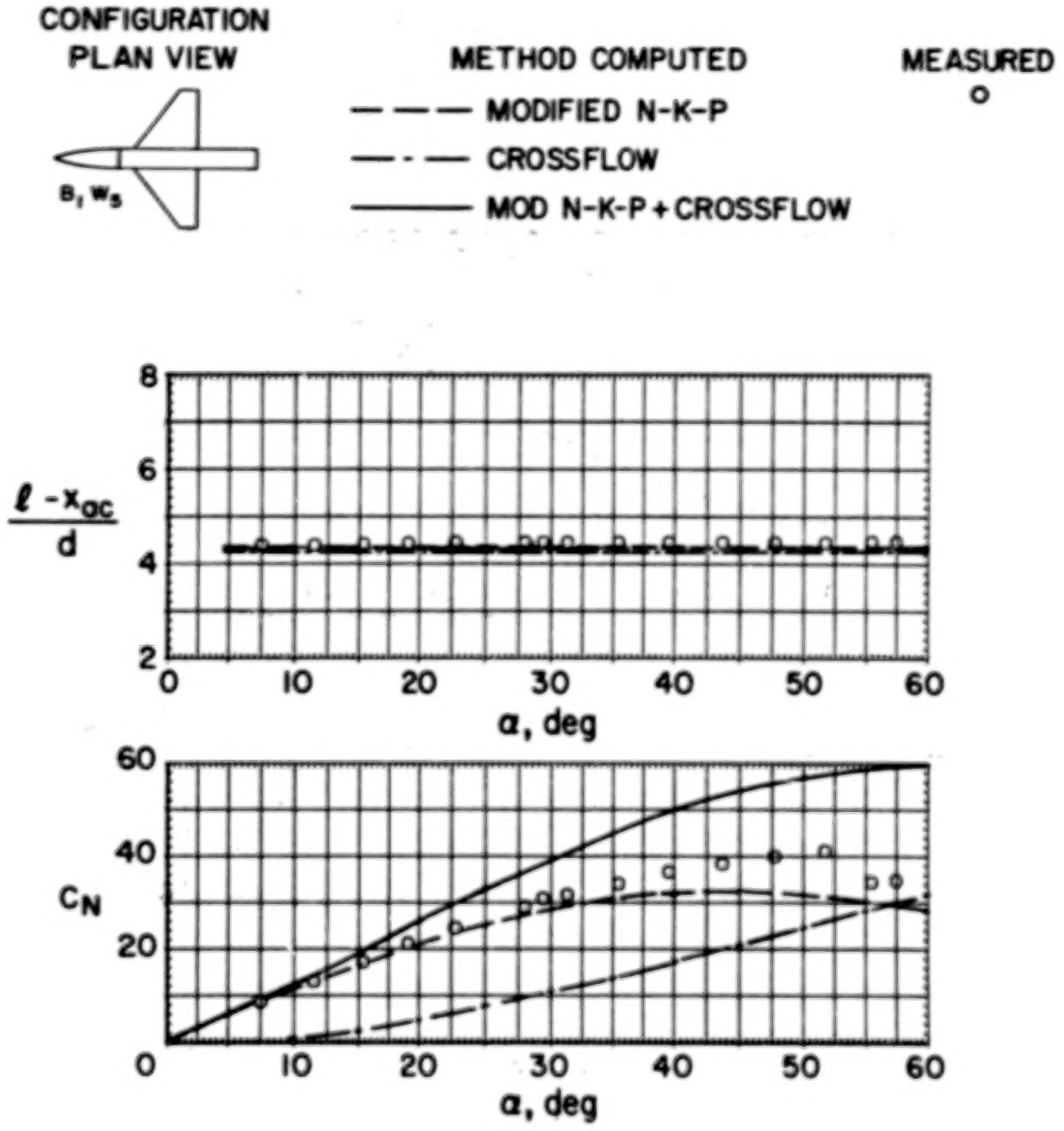

(c) $M_\infty = 1.5$, Re = 3.8×10^6.

Figure 31.– Continued.

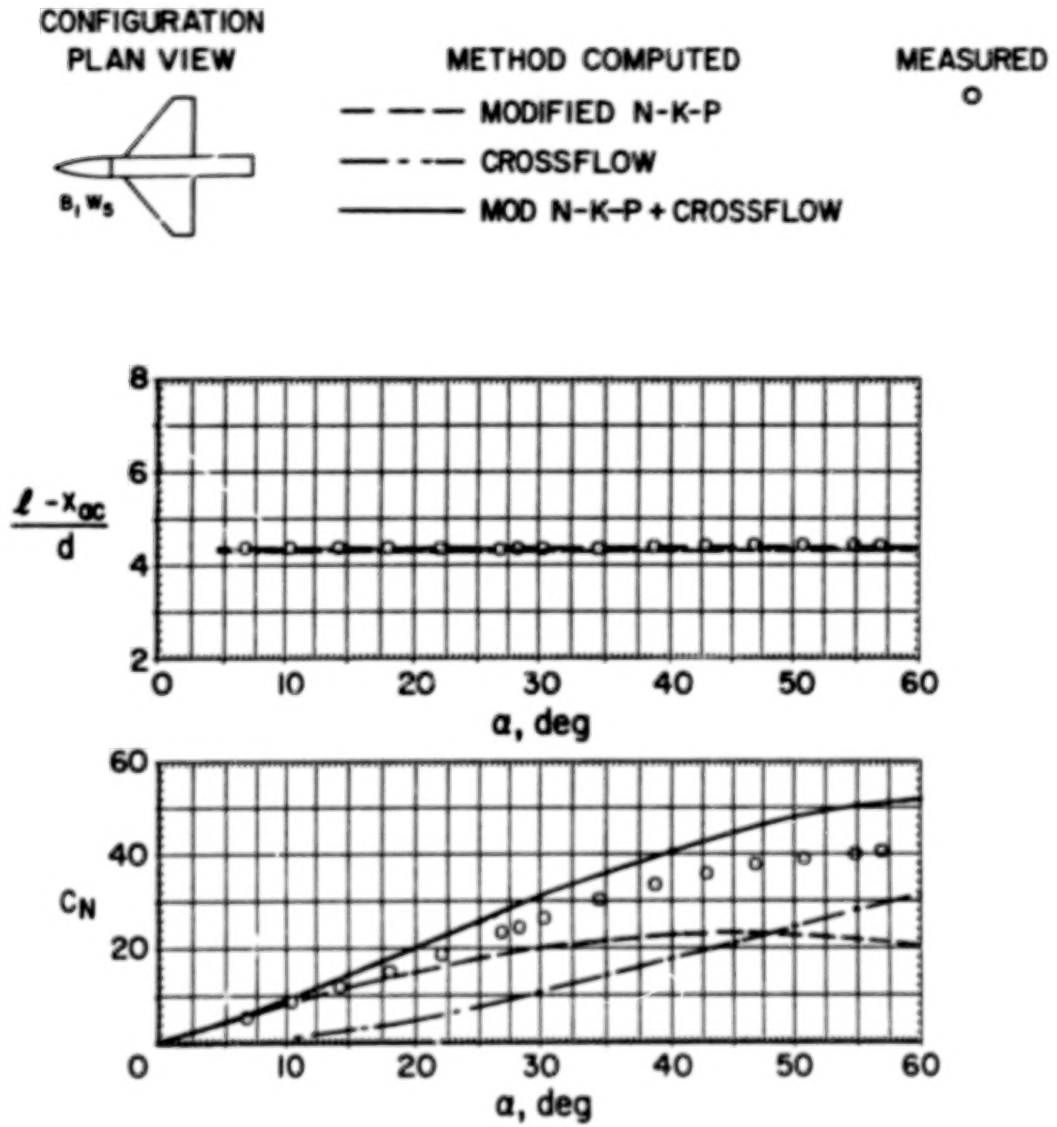

(d) $M_\infty = 2.0$, Re = 3.8×10^5.

Figure 31.– Concluded.

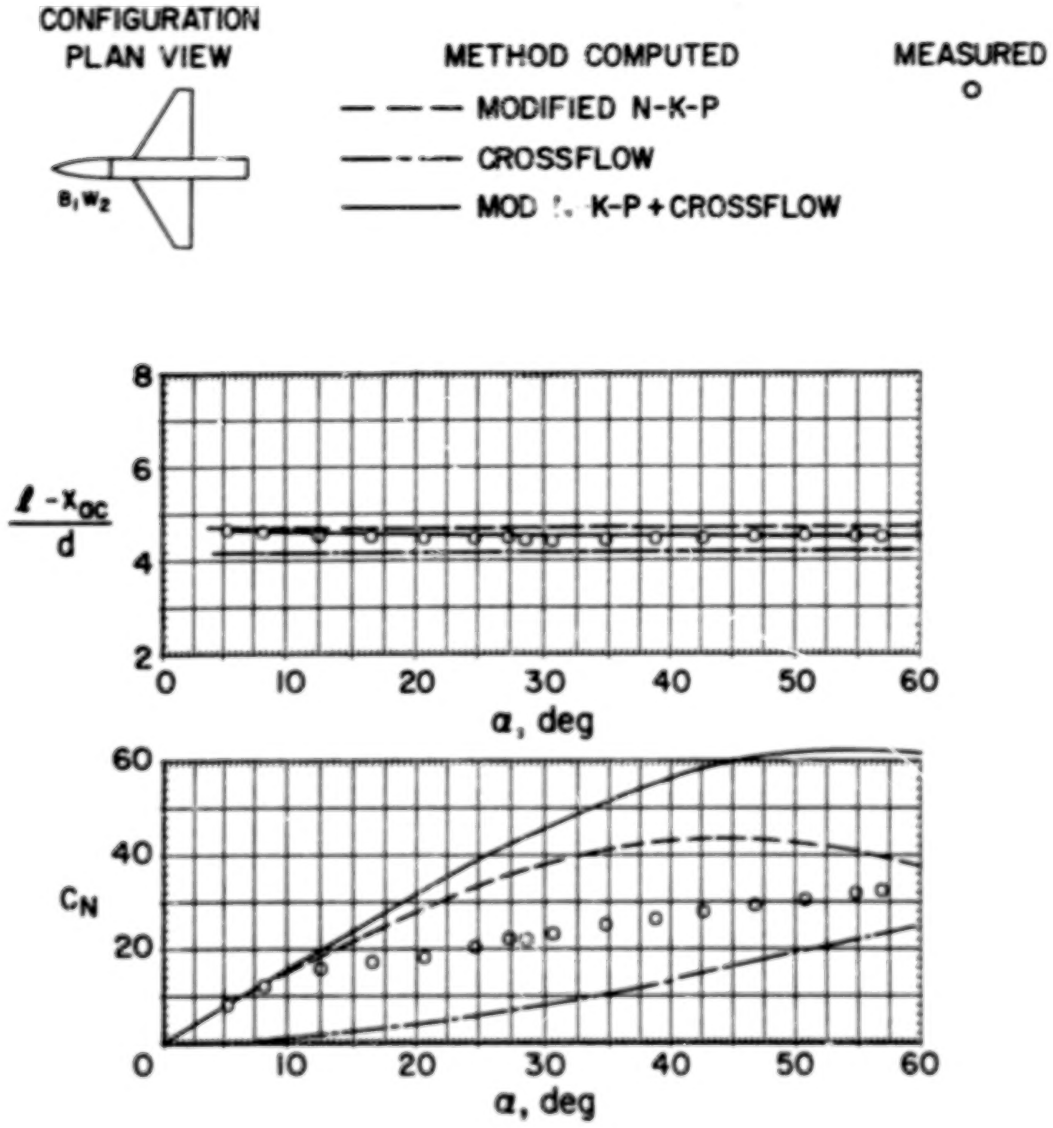

(a) $M_\infty = 0.6$, Re = 4.3×10^5.

Figure 32.– Comparison of computed with measured aerodynamic characteristics for body-wing model $B_1 W_2$.

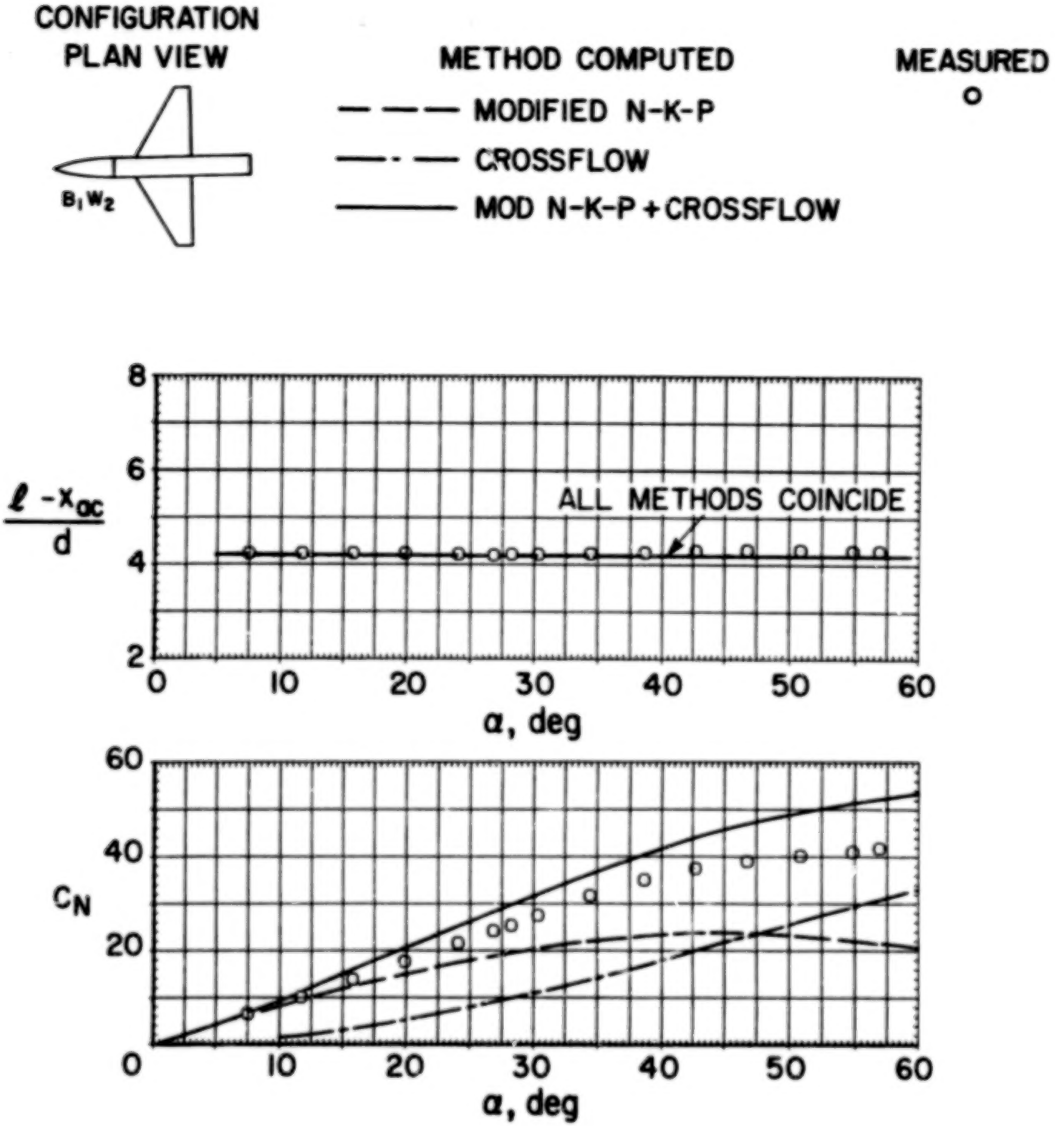

(b) $M_\infty = 2.0$, Re = 3.8×10^5.

Figure 32.– Concluded.

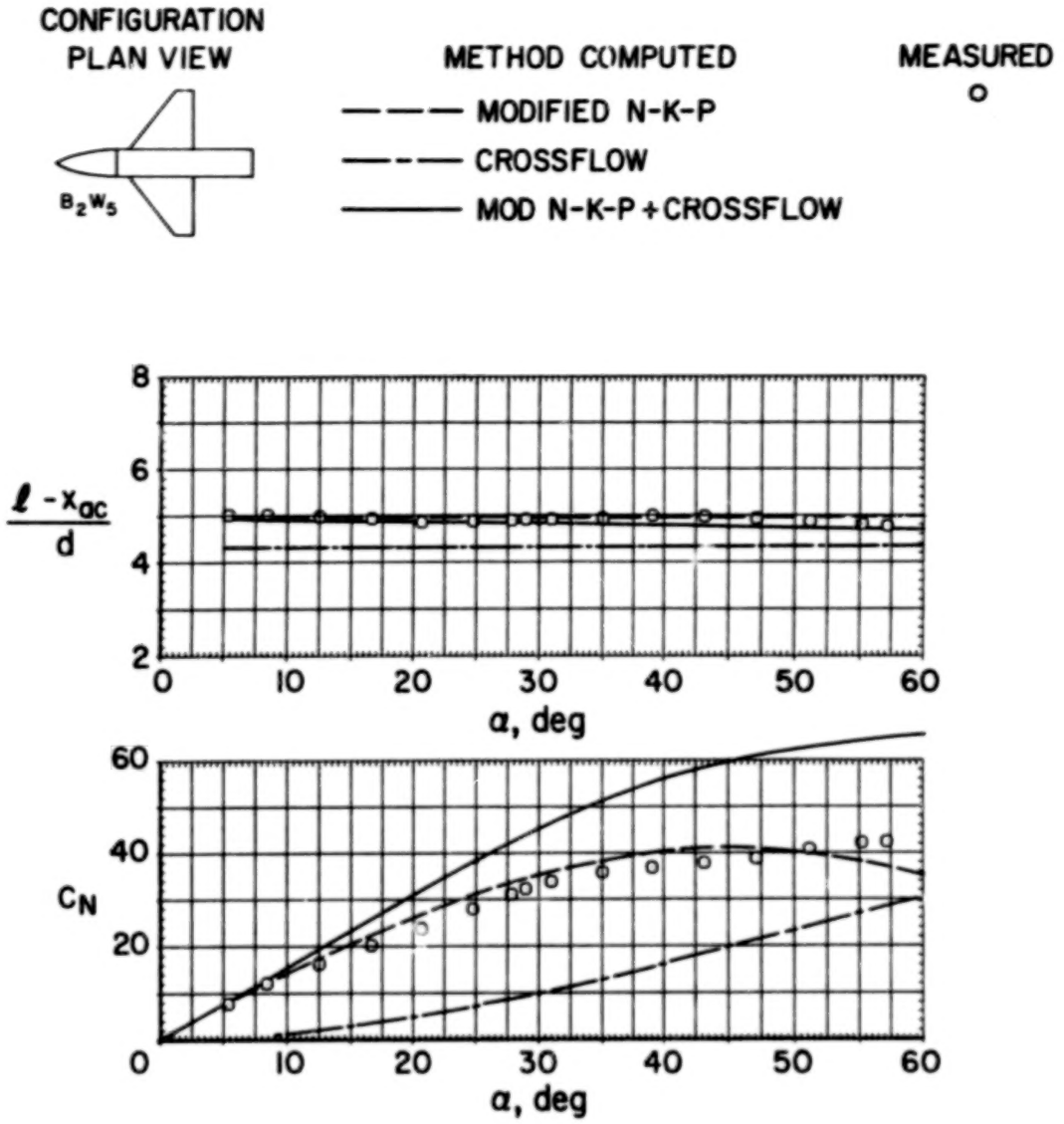

(a) $M_\infty = 0.6$, Re = 4.3×10^5.

Figure 33.– Comparison of computed with measured aerodynamic characteristics for body-wing model $B_2 W_5$.

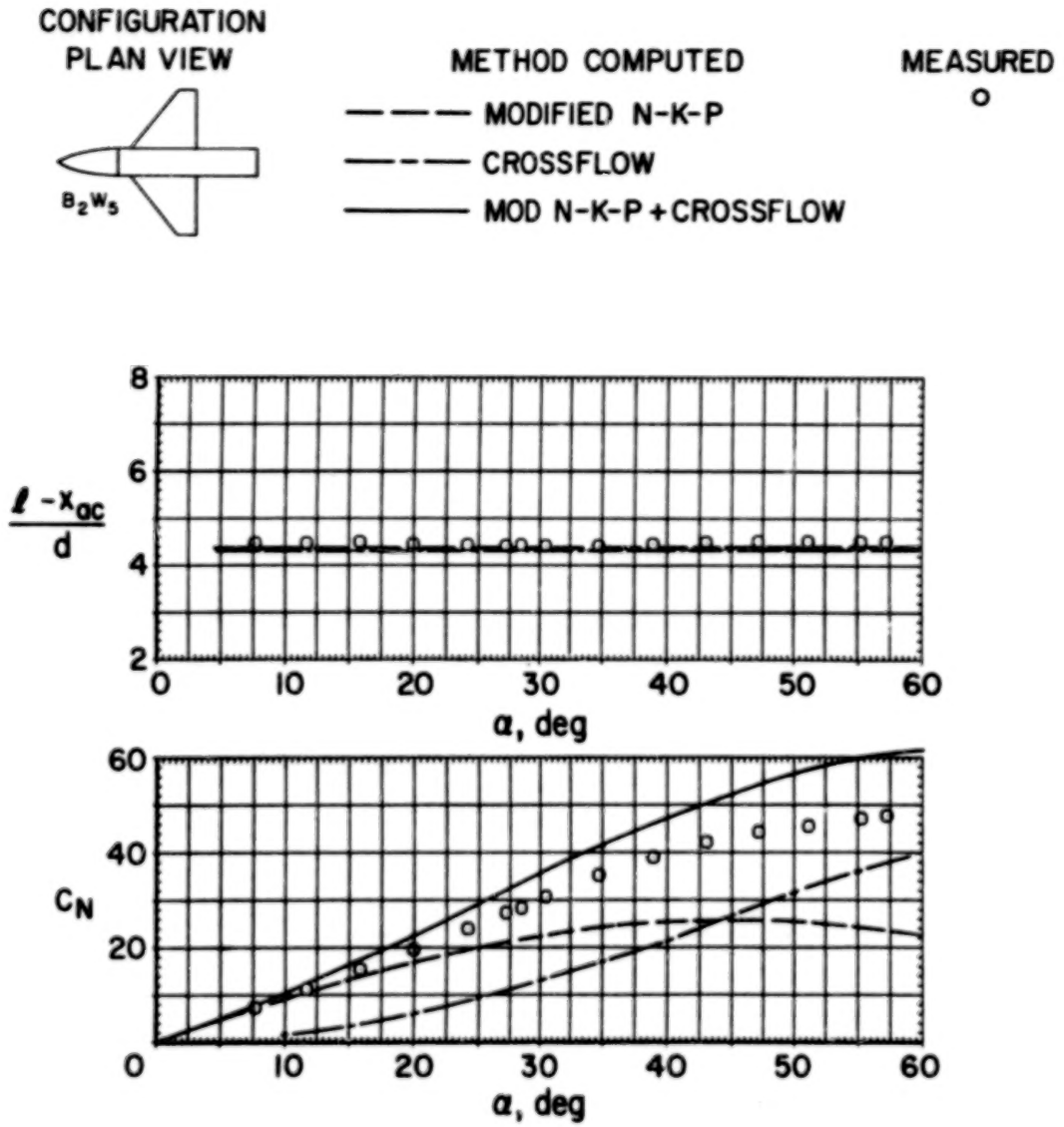

(b) $M_\infty = 2.0$, Re = 3.8×10^5.

Figure 33.– Concluded.

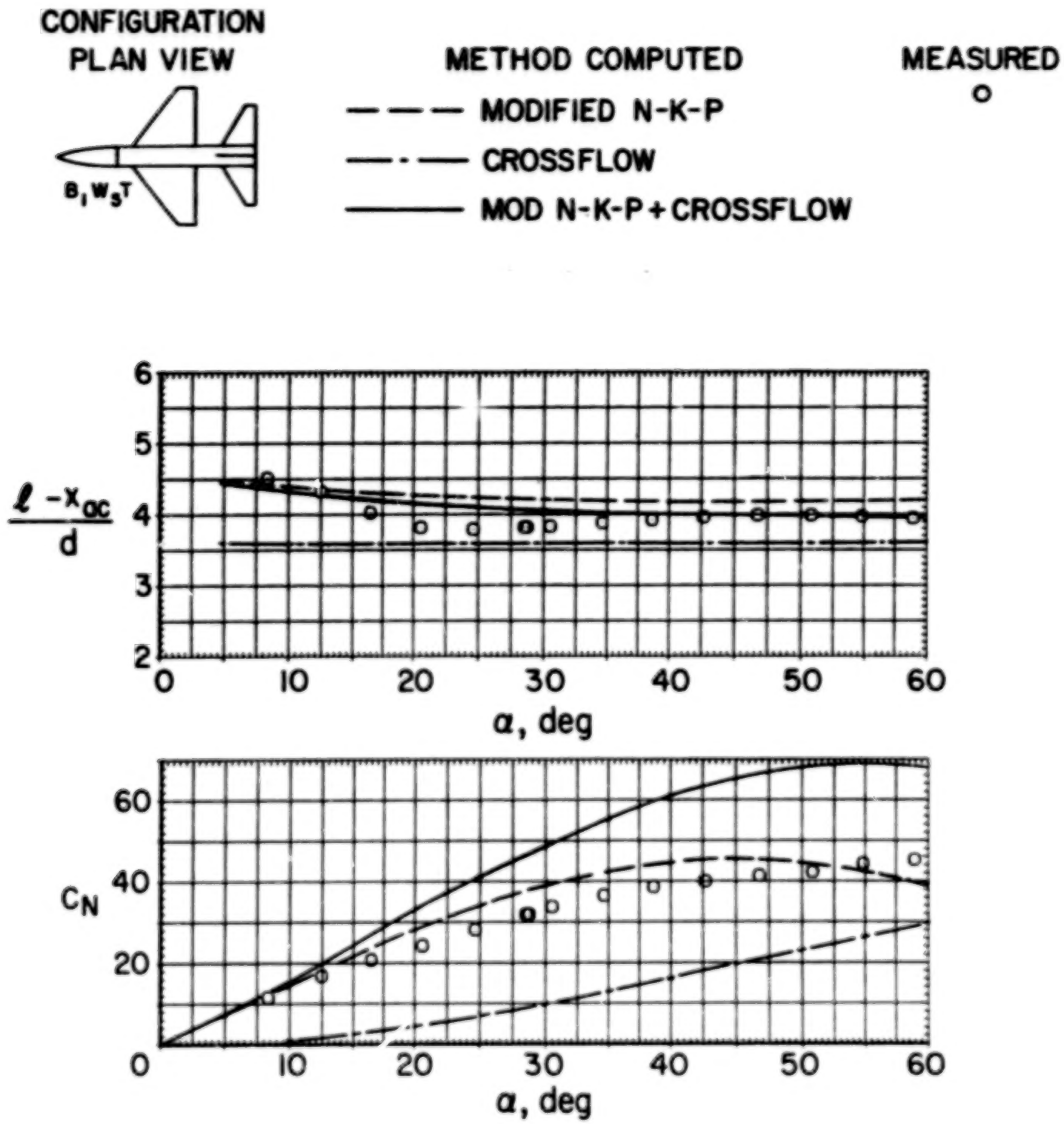

(a) $M_\infty = 0.6$, Re = 4.3×10^{6}.

Figure 34.– Comparison of computed with measured aerodynamic characteristics for body-wing-tail model $B_1 W_5 T$.

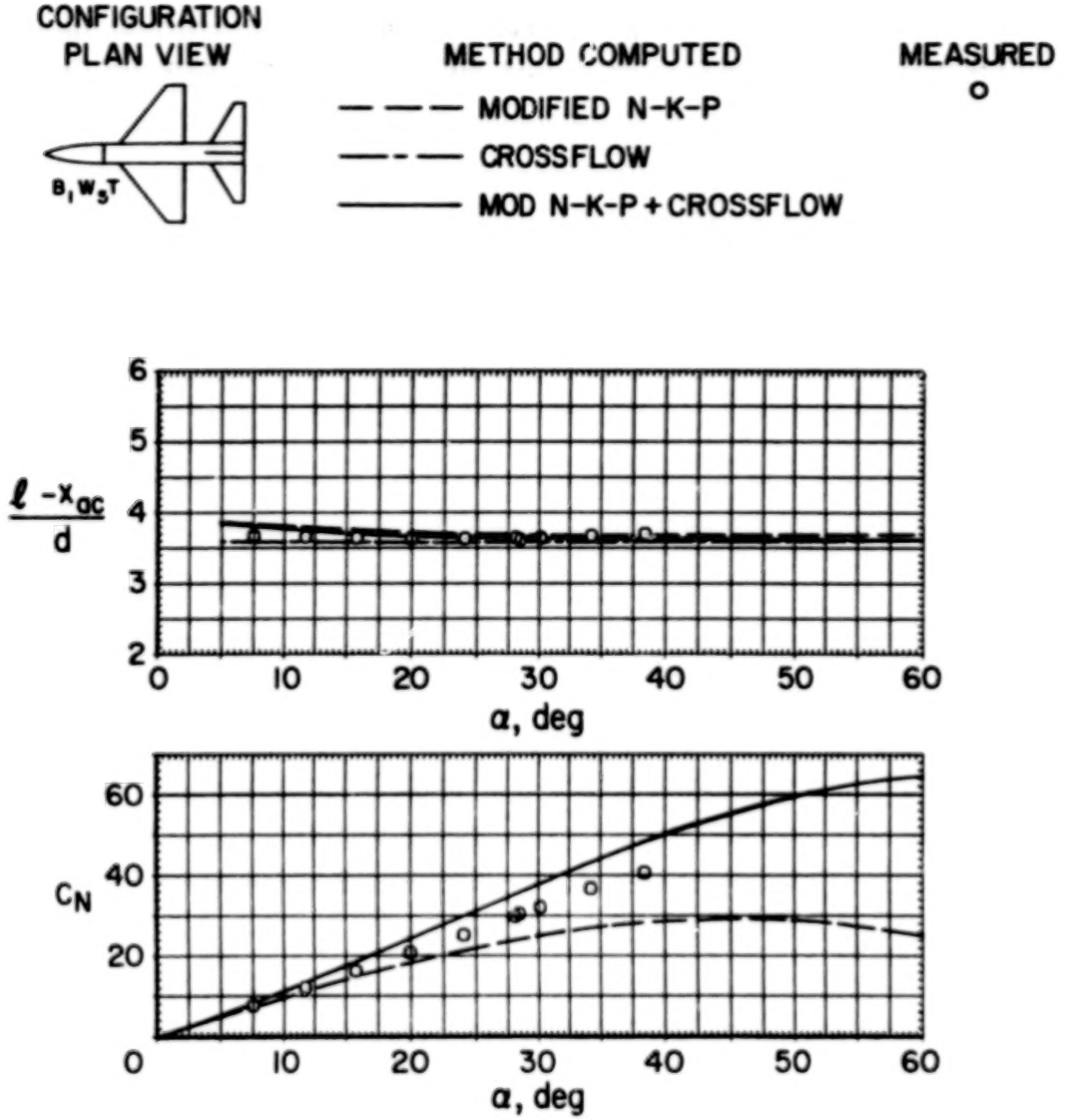

(b) $M_\infty = 2.0$, Re = 3.8×10^5.

Figure 34.– Concluded.

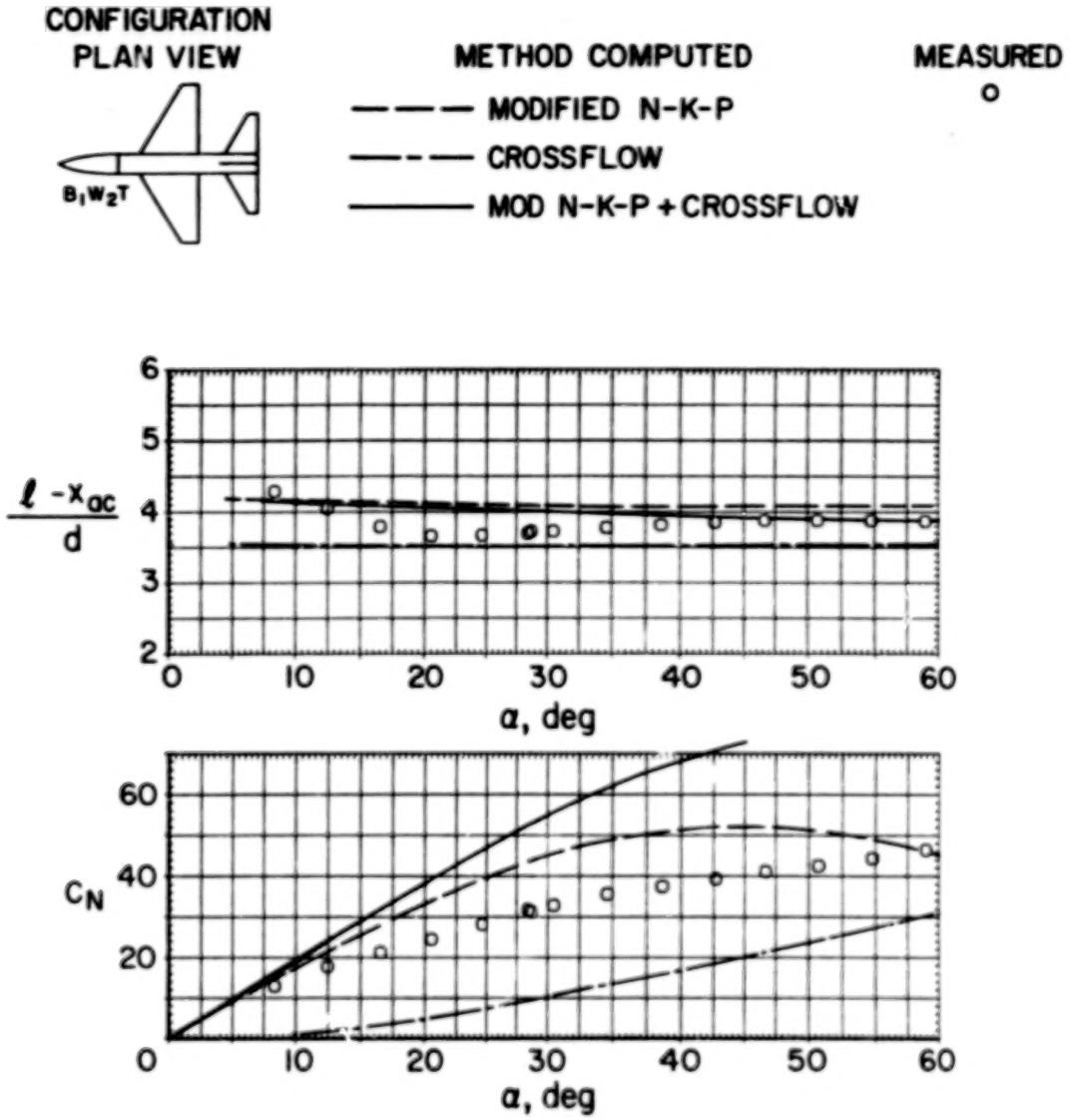

(a) $M_\infty = 0.6$, Re = 4.3×10^5.

Figure 35.– Comparison of computed with measured aerodynamic characteristics for body-wing-tail model $B_1 W_2 T$.

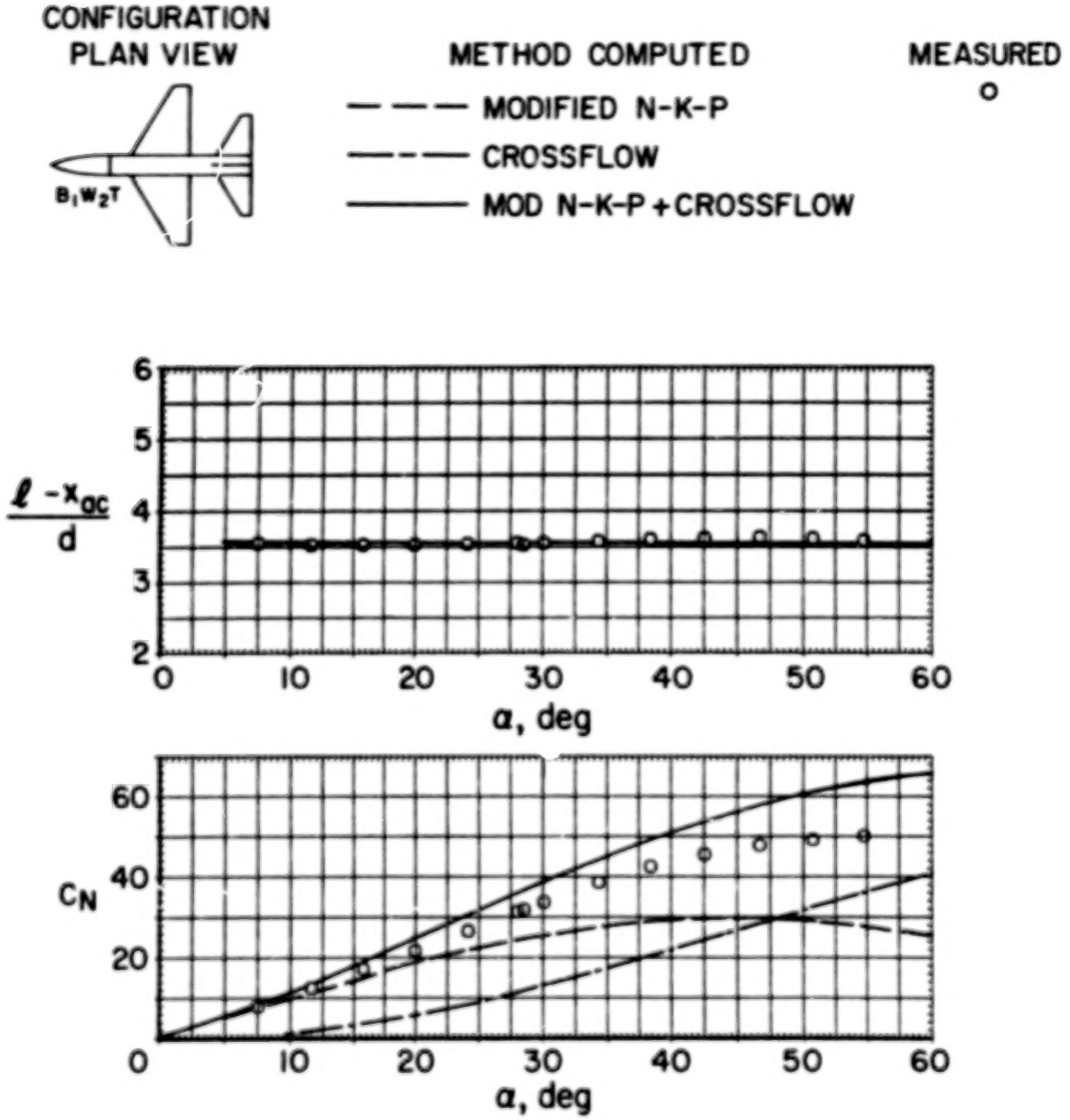

(b) $M_\infty = 2.0$, Re = 3.8×10^5.

Figure 35.– Concluded.

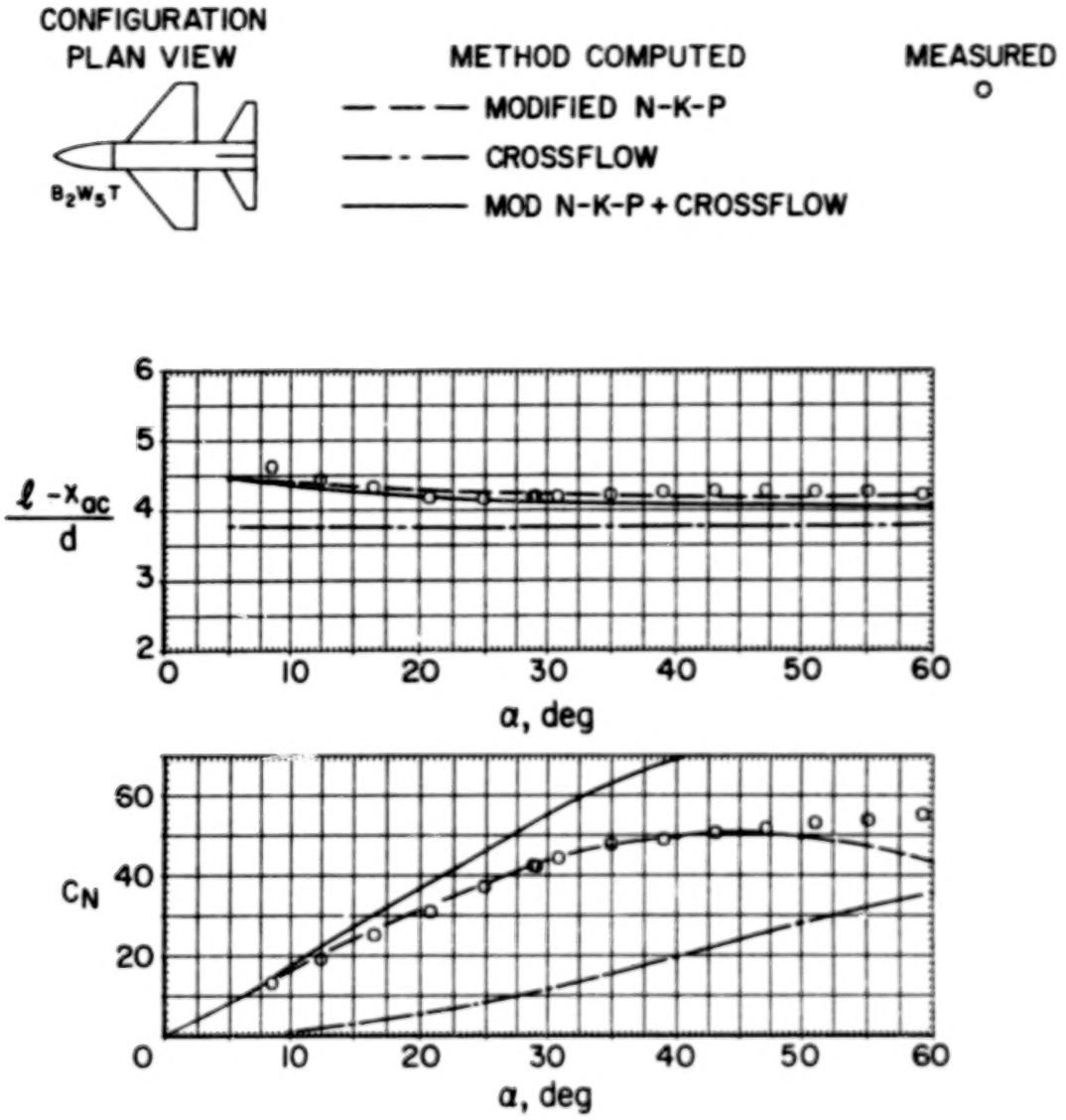

(a) $M_\infty = 0.6$, Re = 4.3×10^5.

Figure 36.– Comparison of computed with measured aerodynamic characteristics for body-wing-tail model $B_2 W_5 T$.

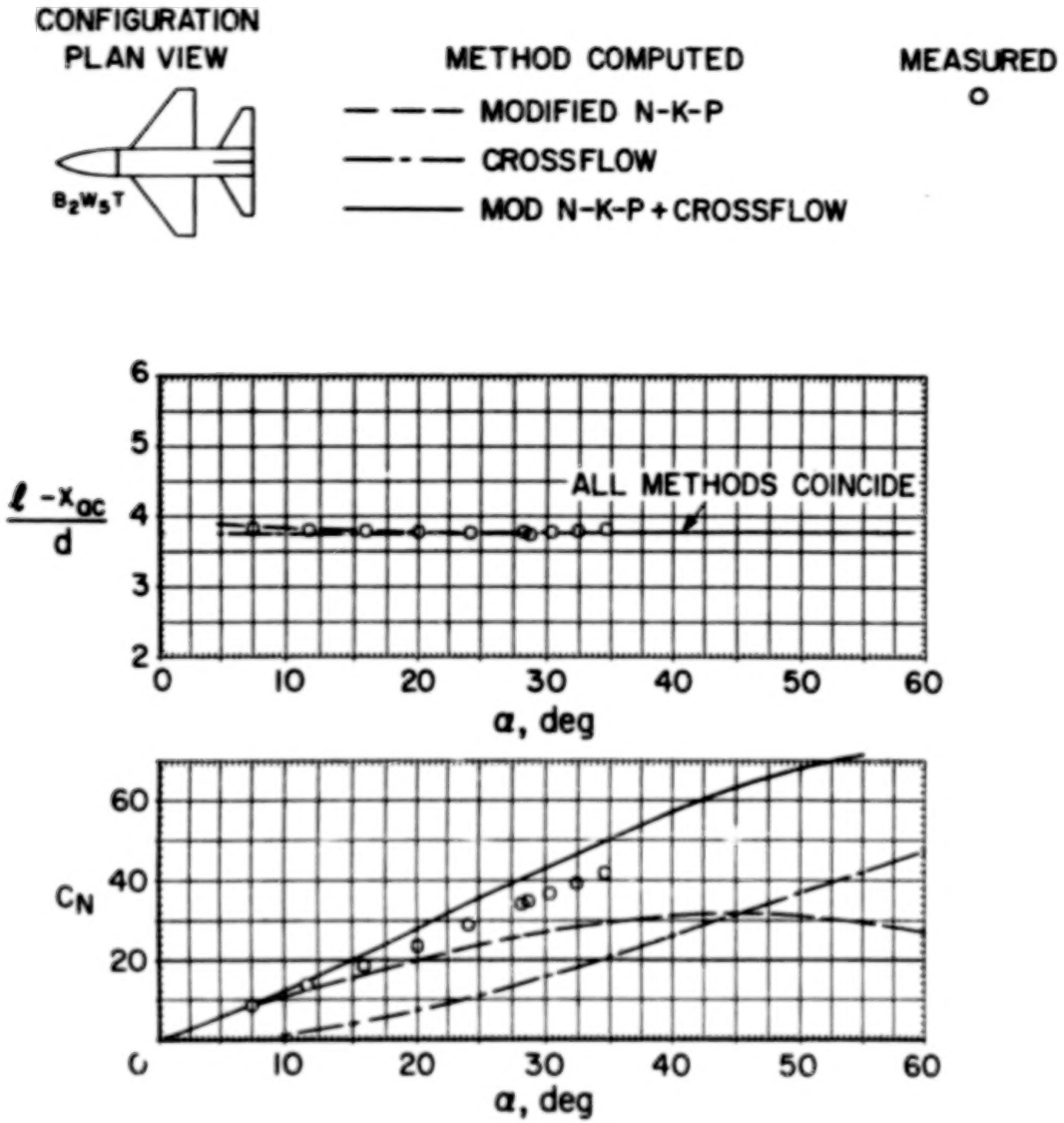

(b) $M_\infty = 2.0$, Re = 3.8×10^5.

Figure 36.– Concluded.

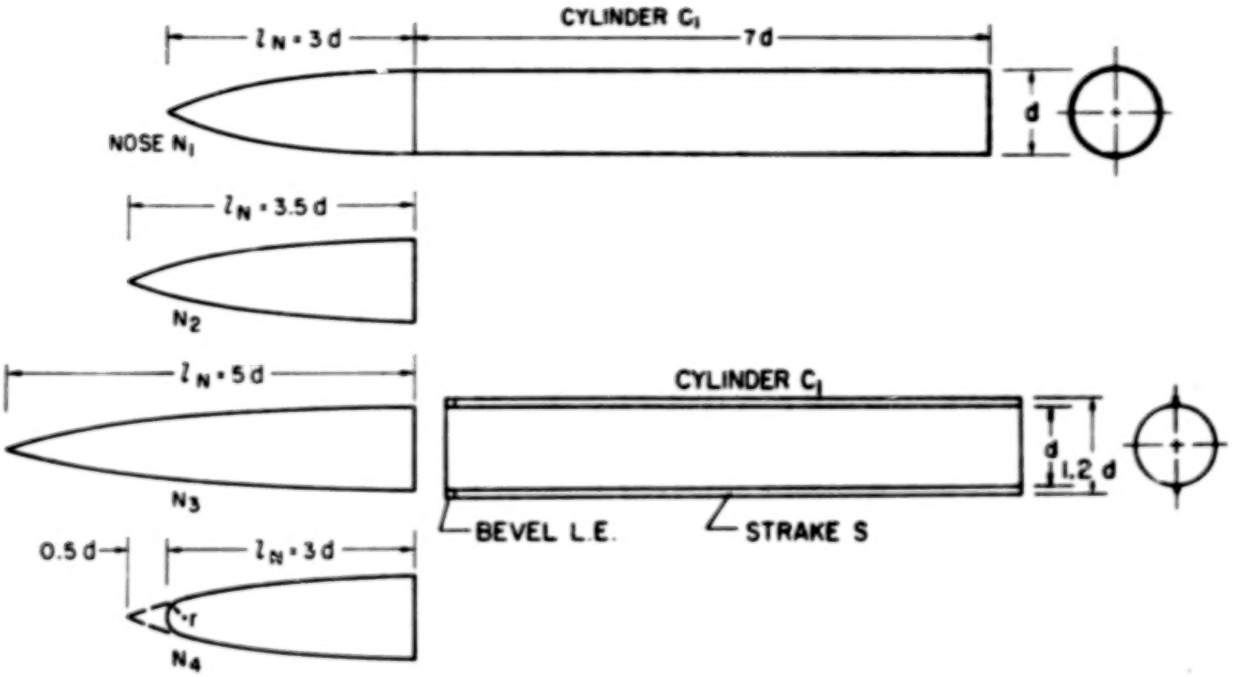

Figure 37.– Additional tangent ogive noses and strake for modification of body B_1.

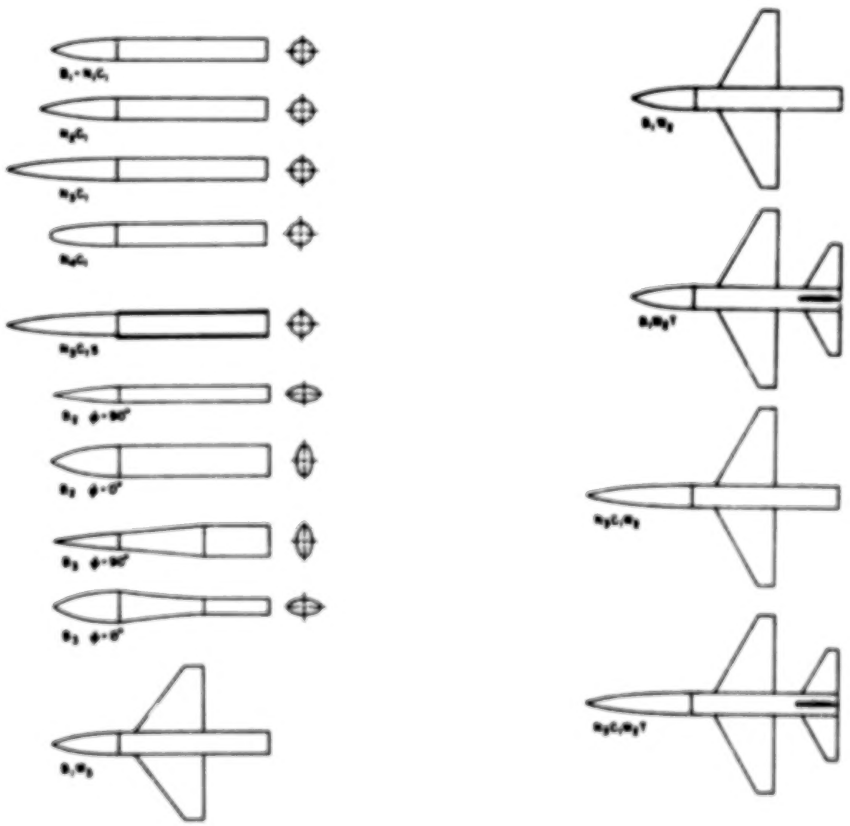

Figure 38.– Plan-view sketches of configurations used for vapor-screen and oil-flow studies.

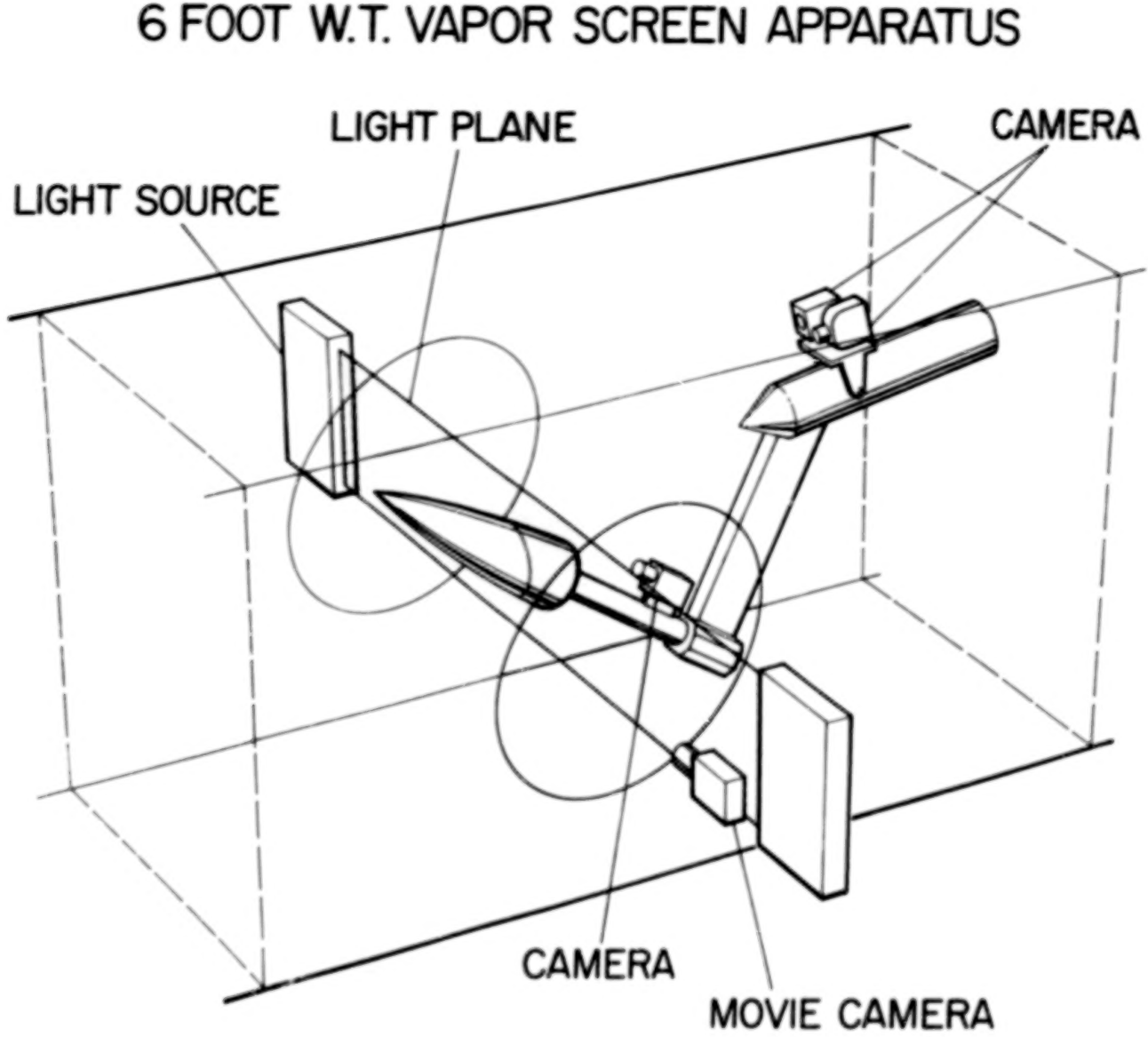

(a) Schematic drawing of equipment.

Figure 39.– Apparatus for vapor-screen tests in the Ames 6- by 6-Foot Wind Tunnel.

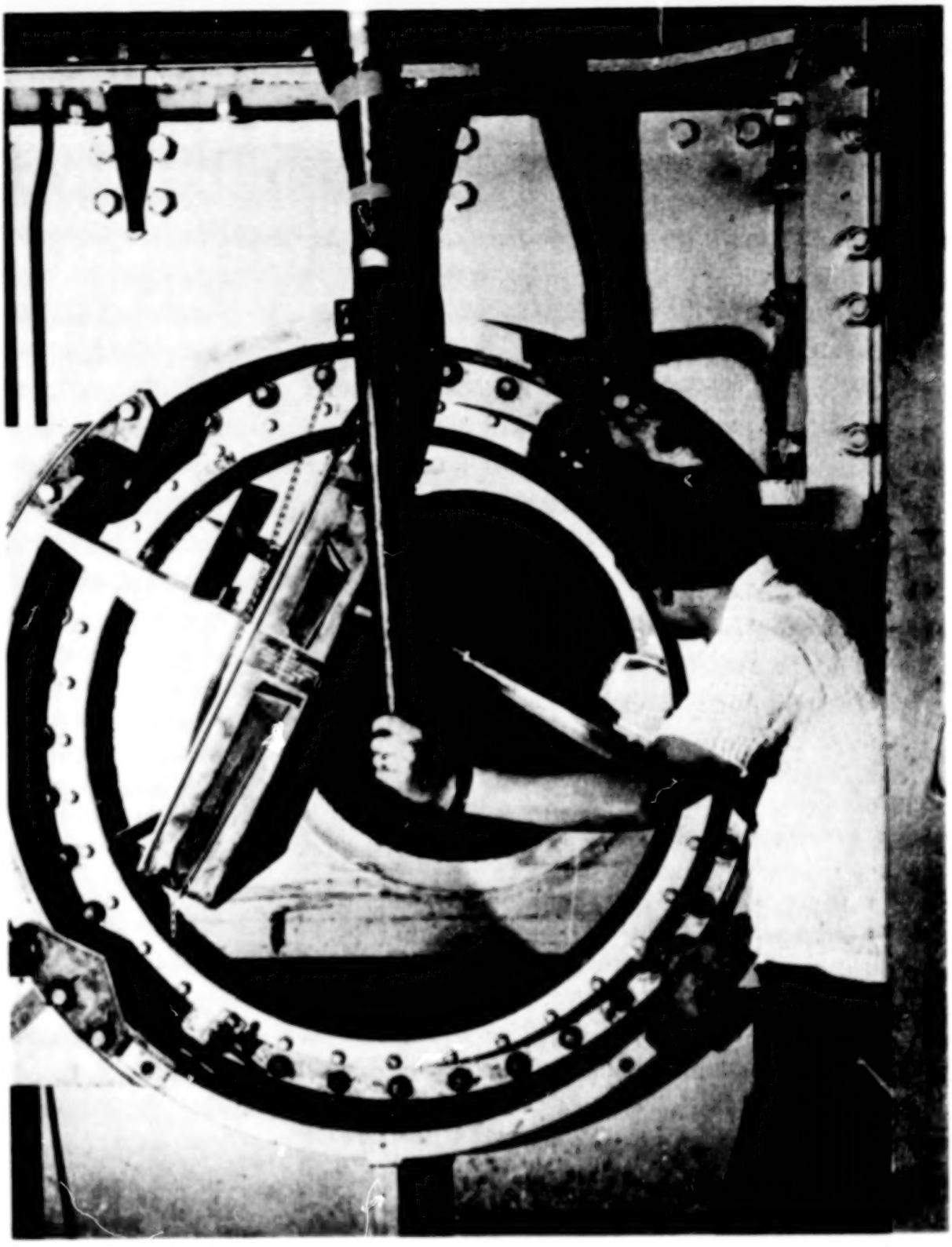

(b) Picture of light-box installation.

Figure 39.– Continued.

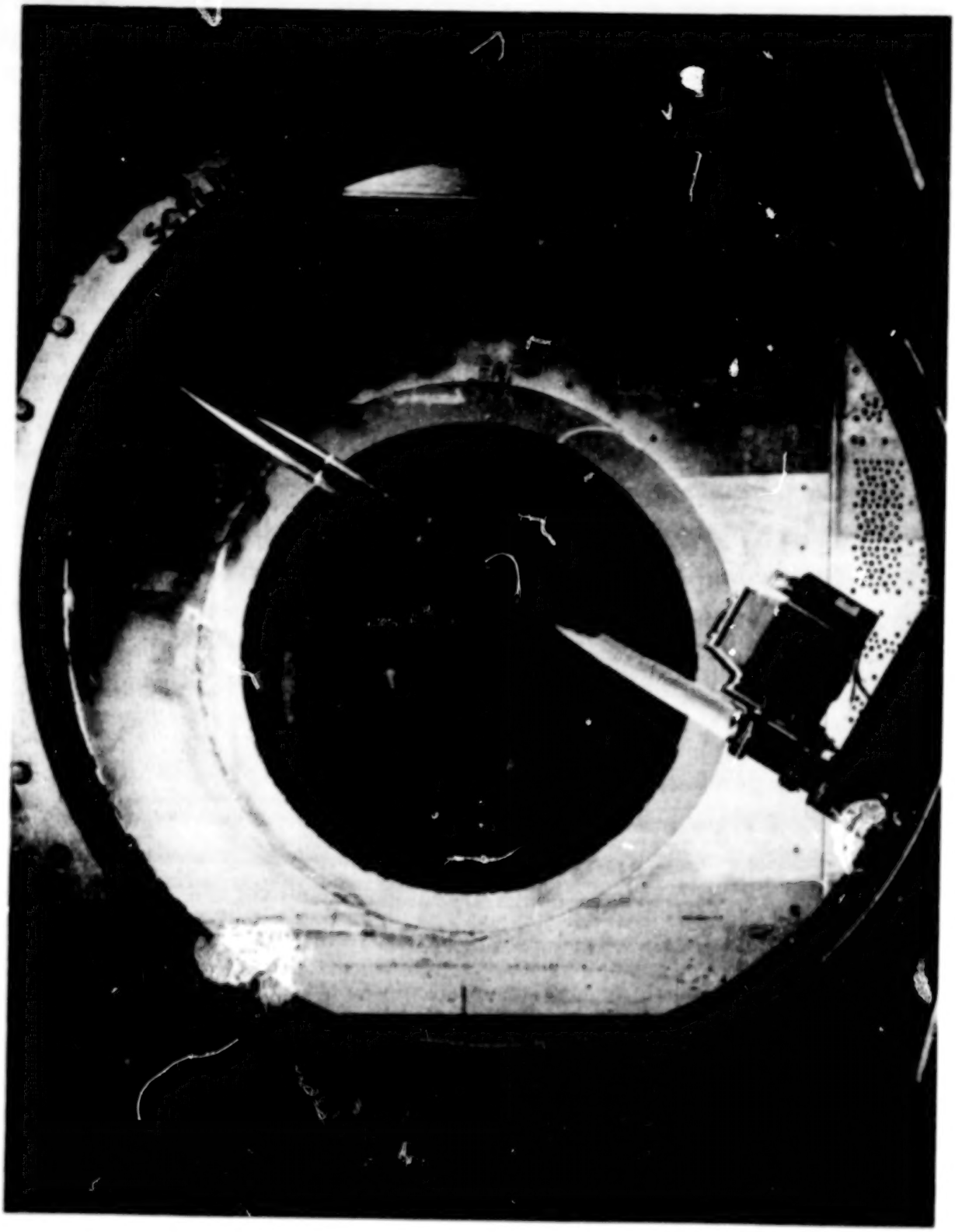

(c) Picture of model and camera installation.

Figure 39.– Concluded.

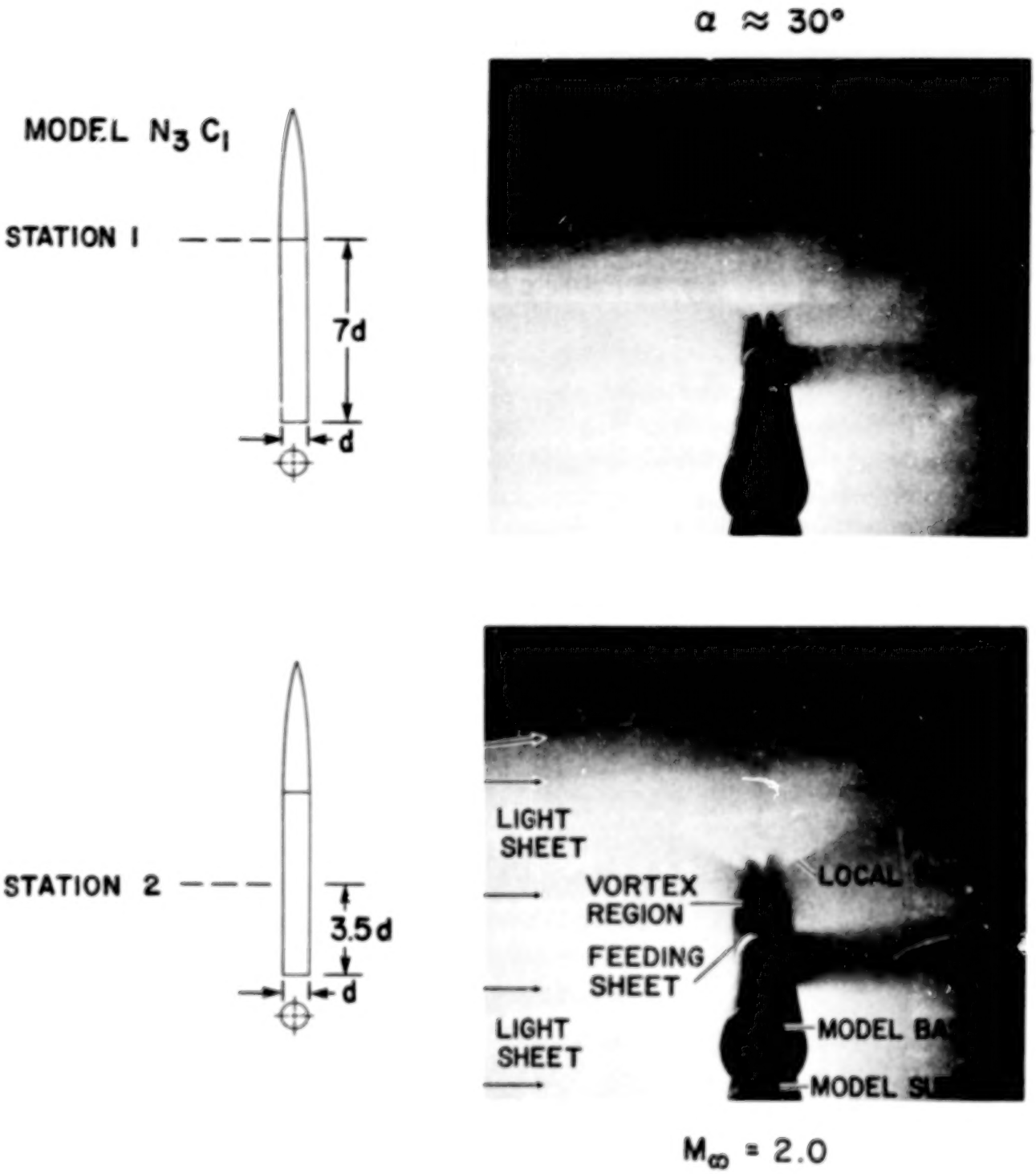

Figure 40.– Identification of typical items shown in vapor-screen photographs taken for a body at $M_\infty = 2.0$.

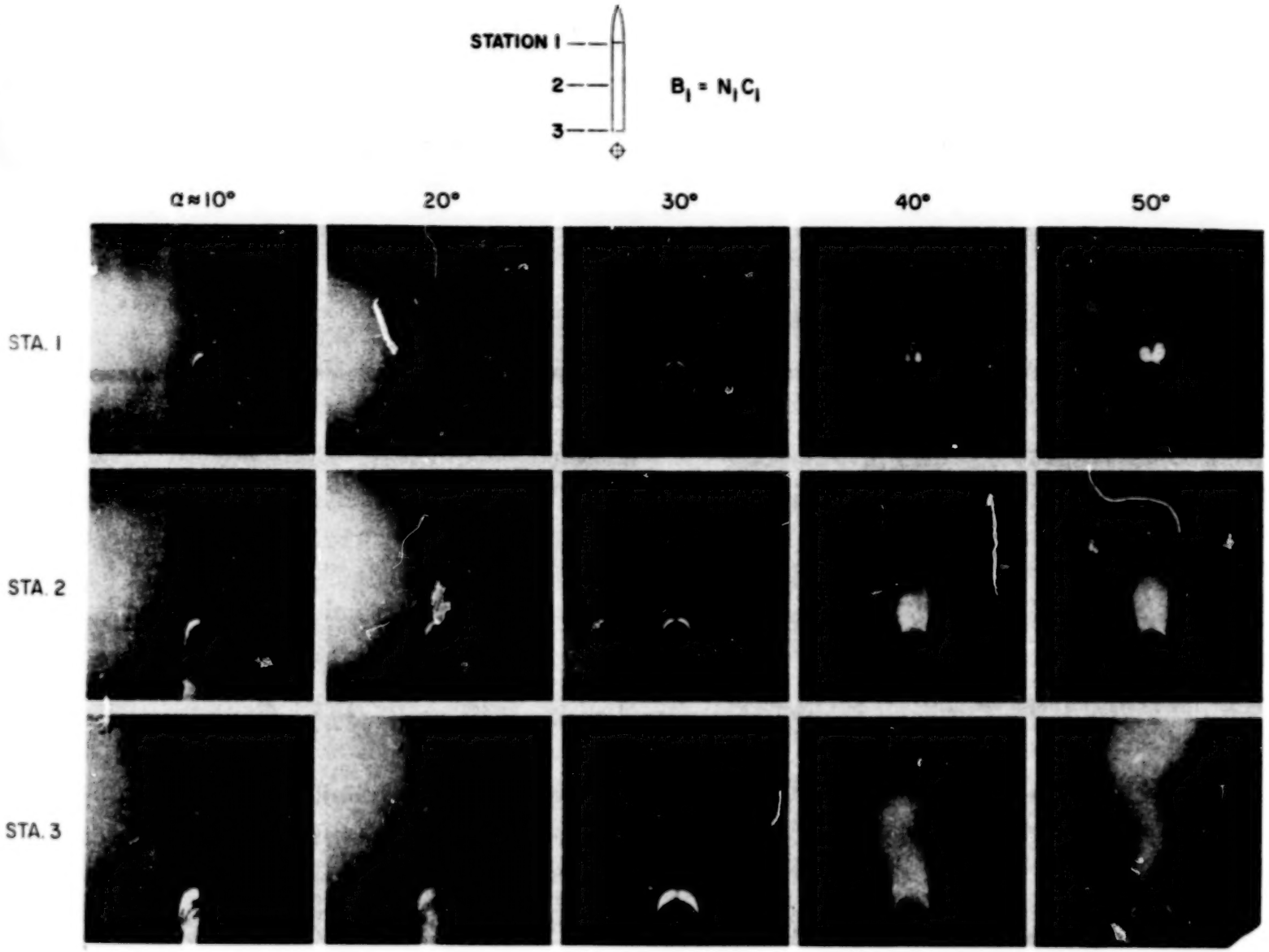

(a) $M_\infty = 0.6$.

Figure 41.-- Vapor-screen photographs for $B_1 = N_1 C_1$ (body with fineness-ratio-3 nose).

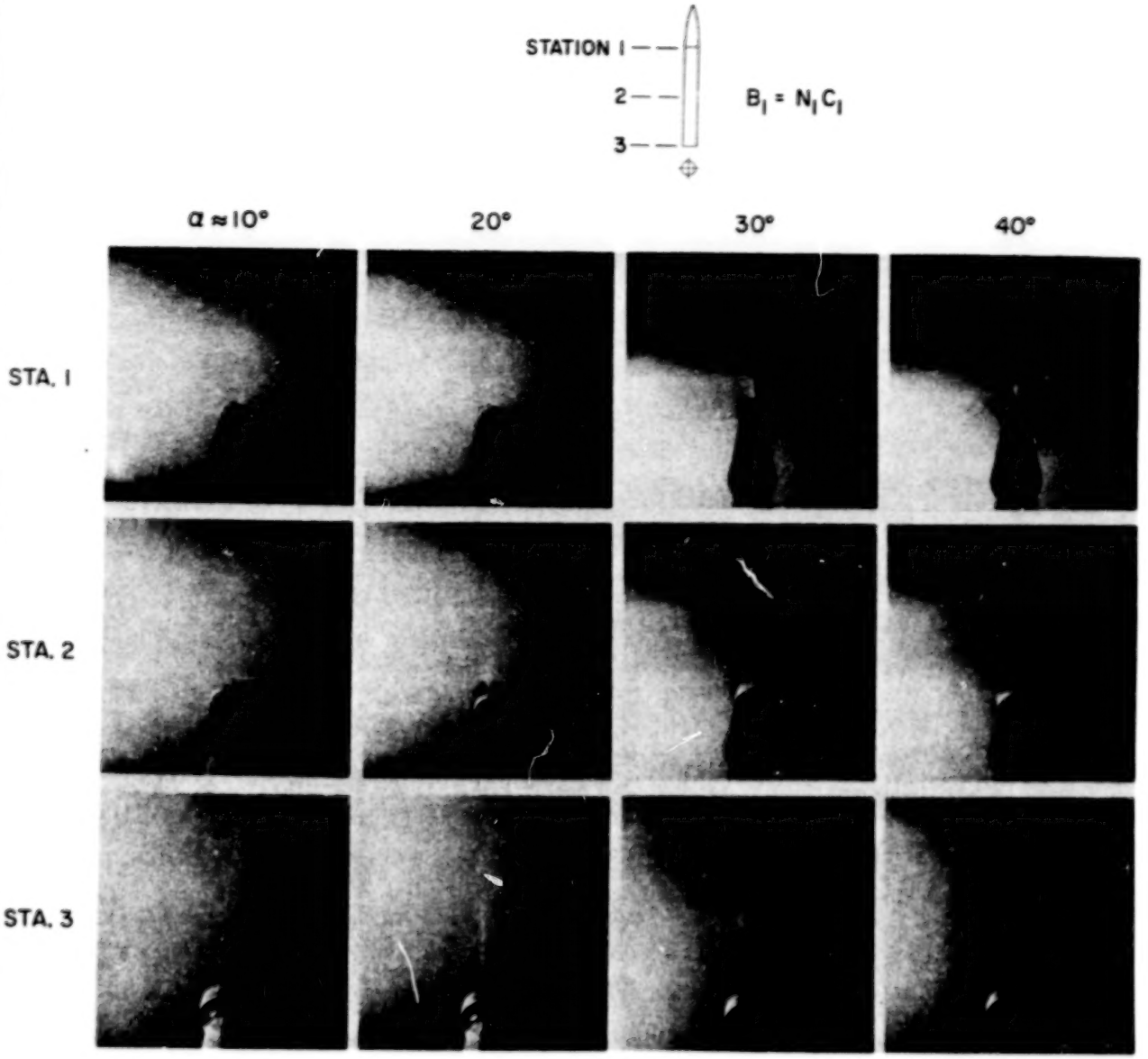

(b) $M_\infty = 0.9$.

Figure 41.– Continued.

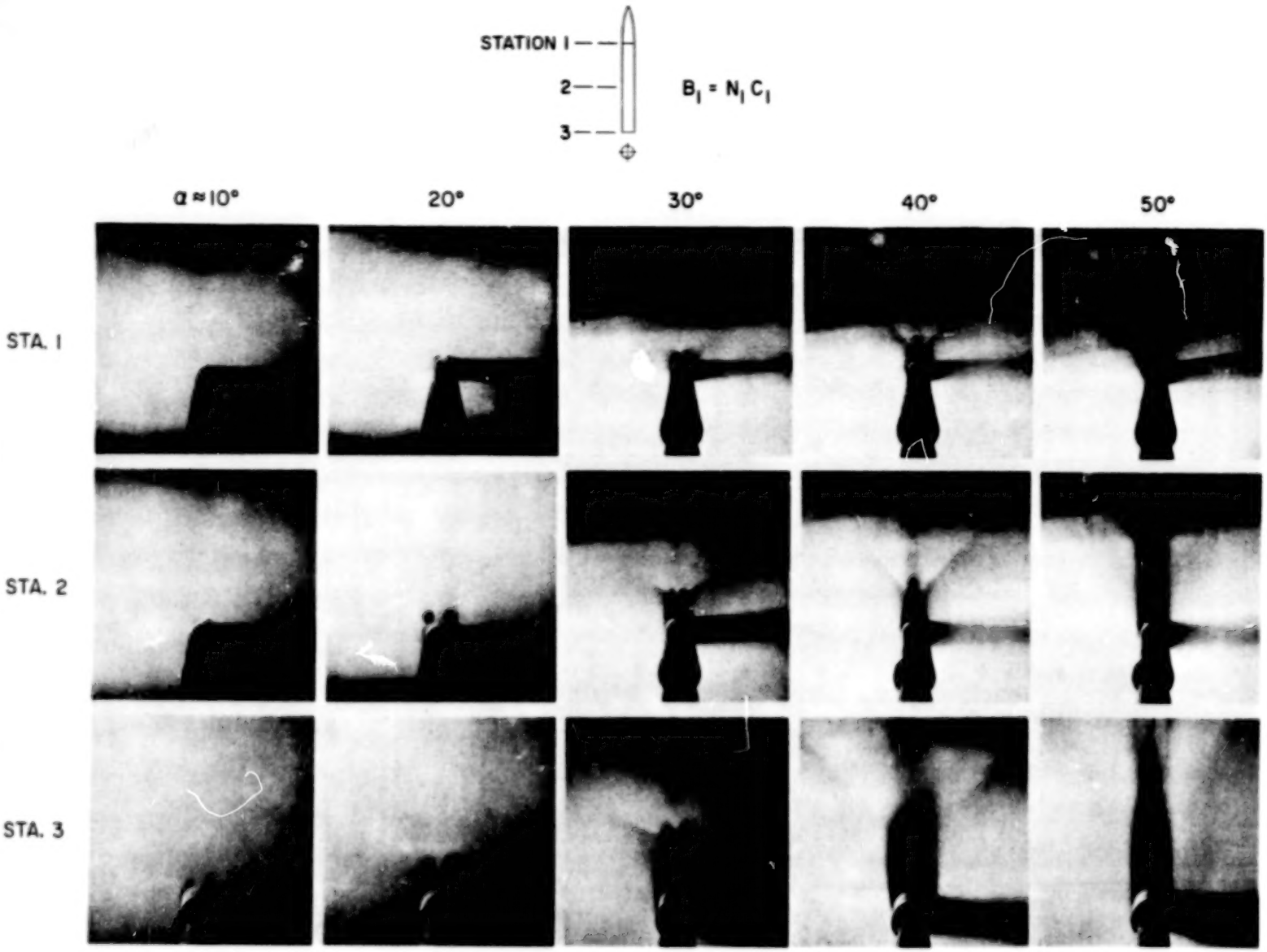

(c) $M_\infty = 2.0$.

Figure 41.– Concluded.

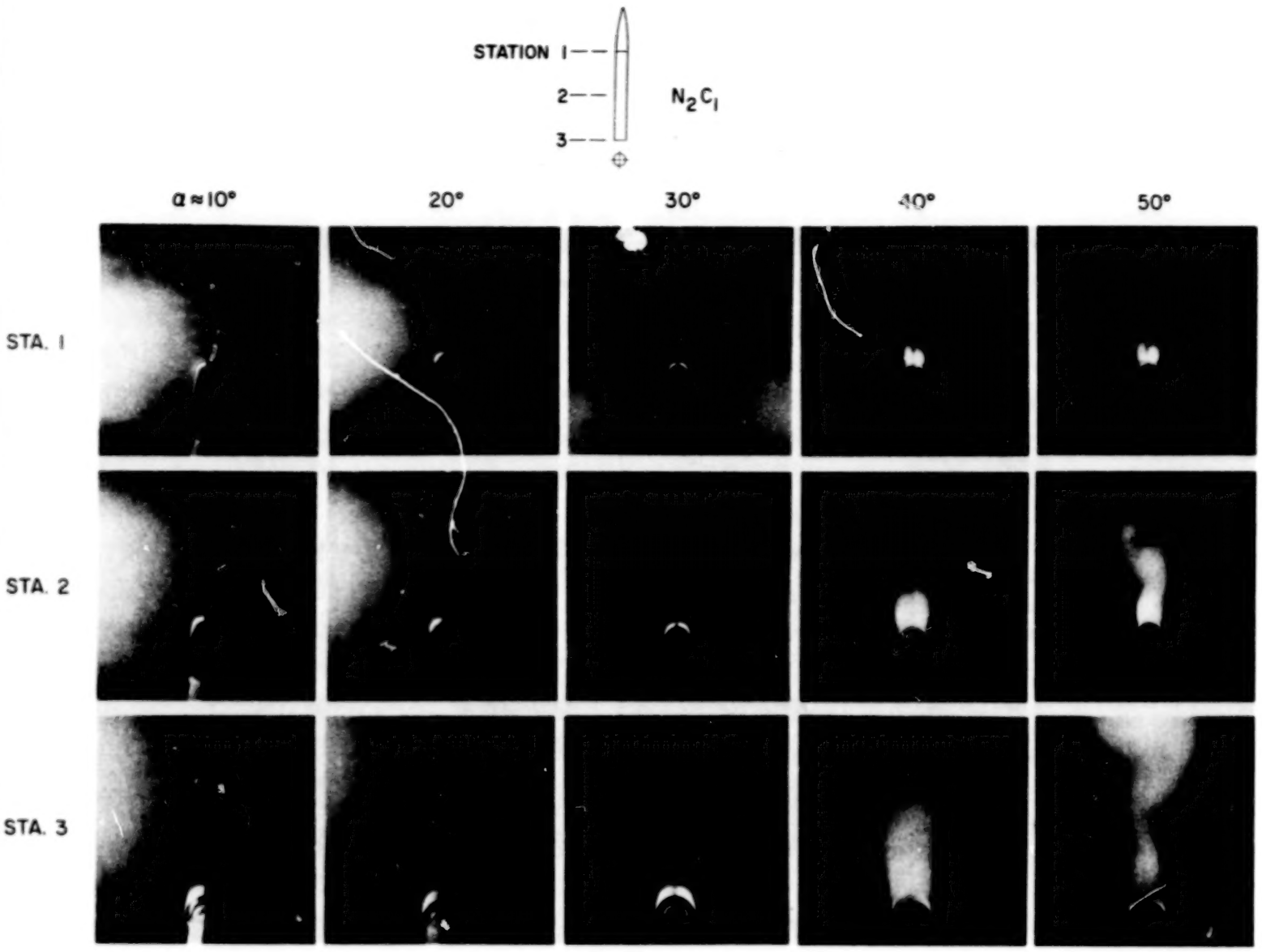

(a) $M_\infty = 0.6$.

Figure 42.– Vapor-screen photographs for N_2C_1 (body with fineness-ratio-3.5 nose).

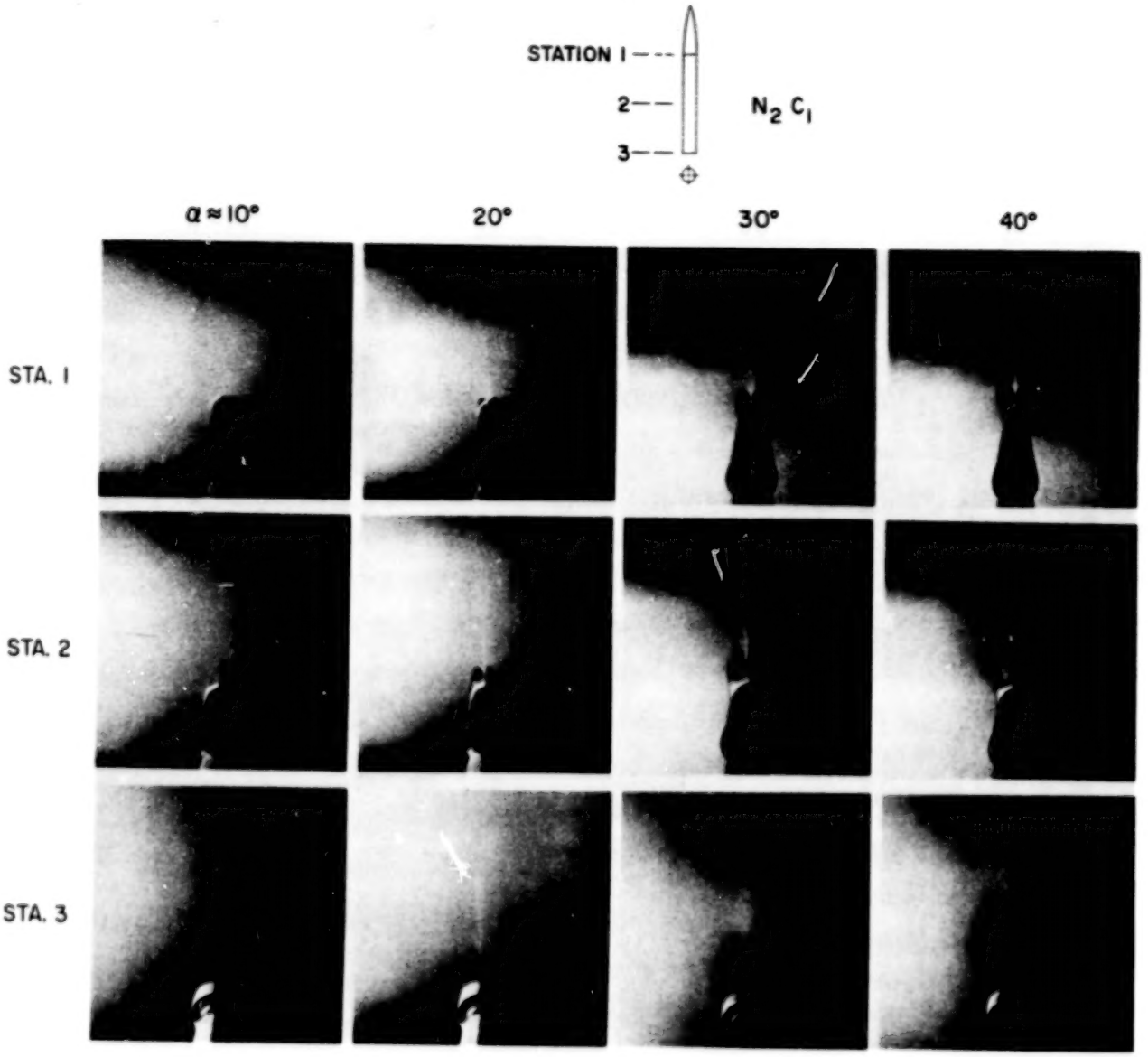

(b) $M_\infty = 0.9$.

Figure 42.– Continued.

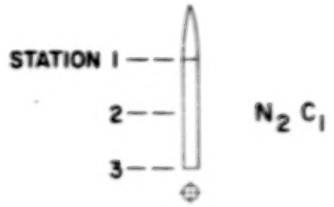

N_2 C_1

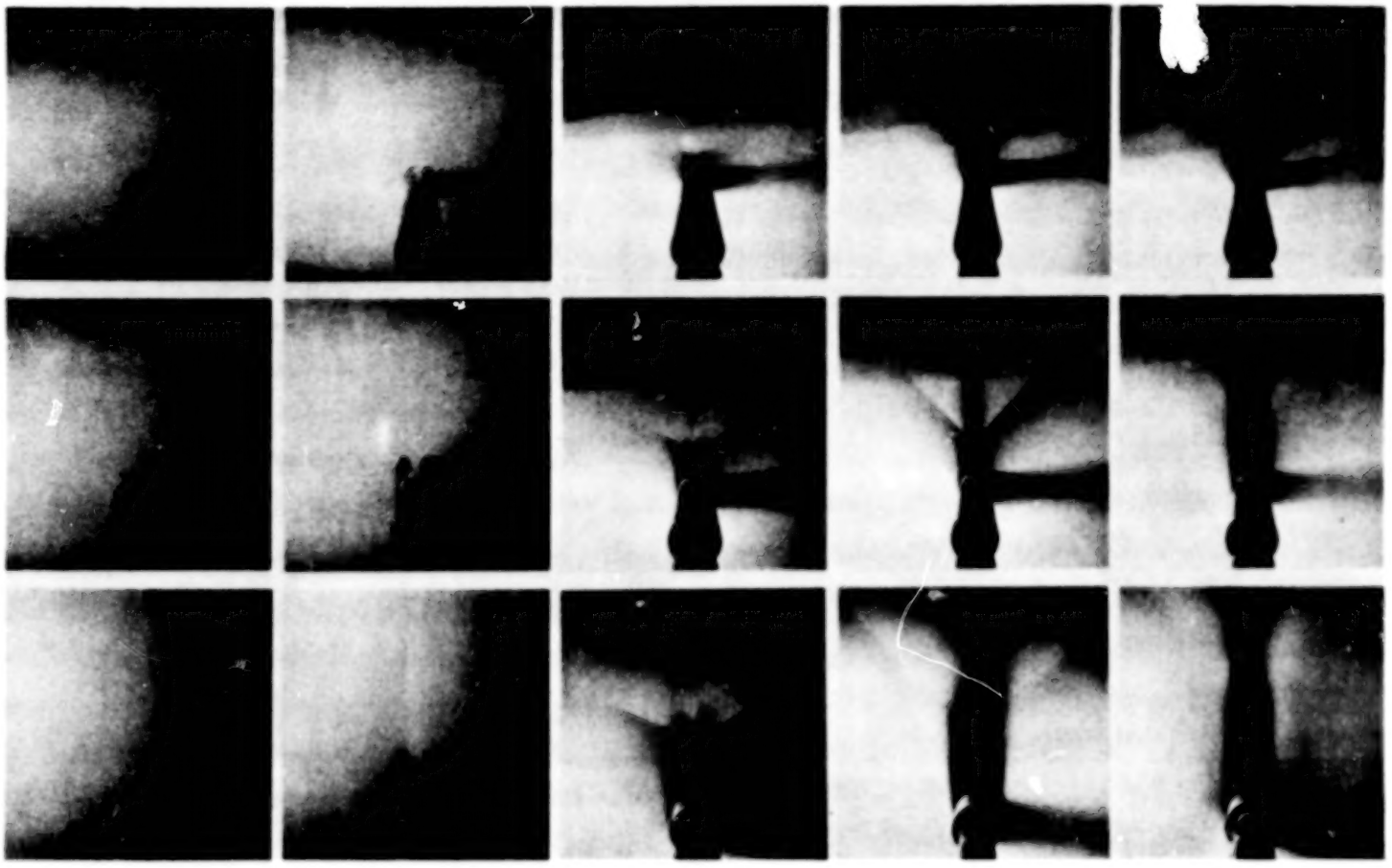

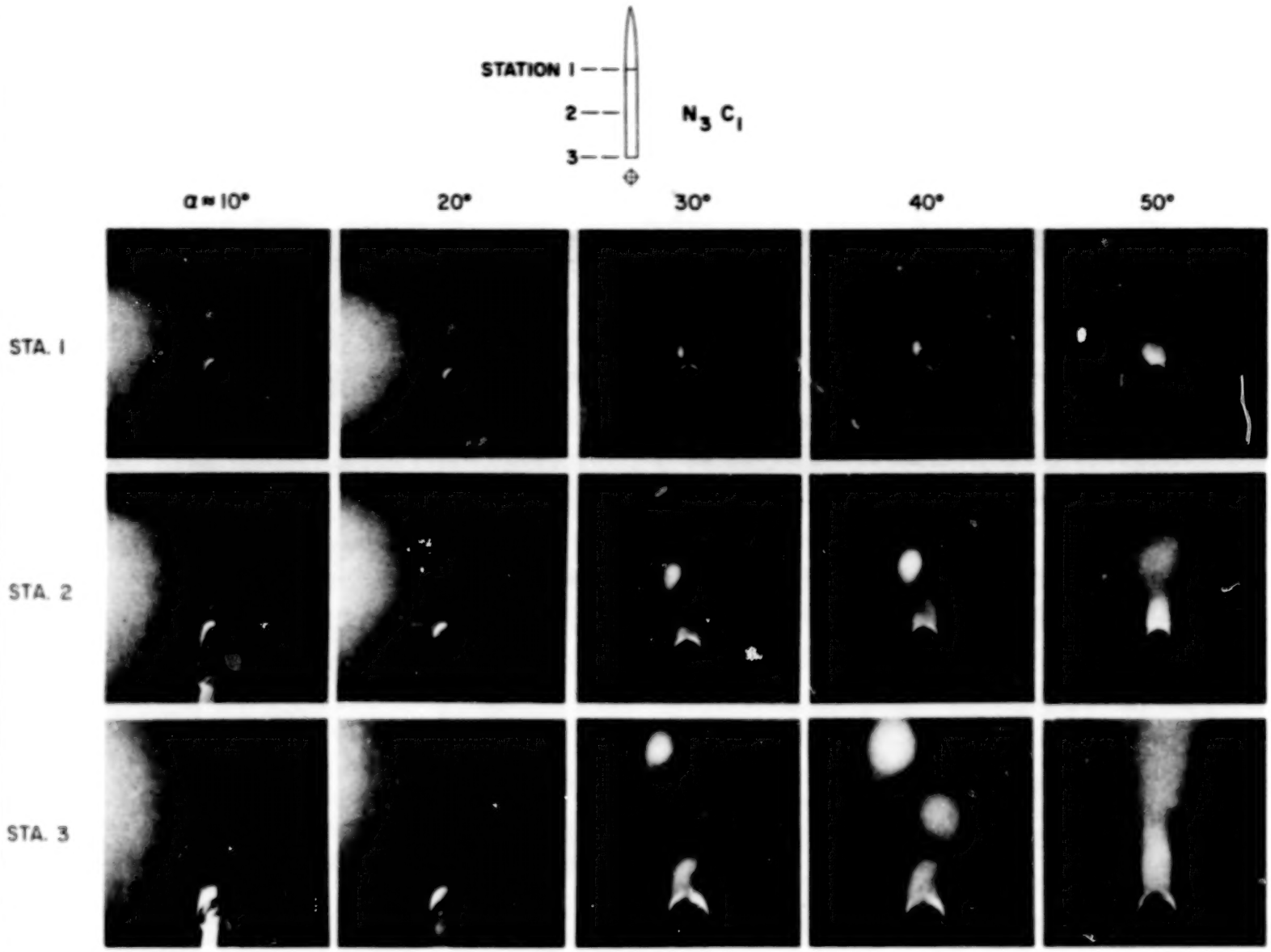

(a) $M_\infty = 0.6$.

Figure 43.– Vapor-screen photographs for N_3C_1 (body with fineness-ratio-5 nose).

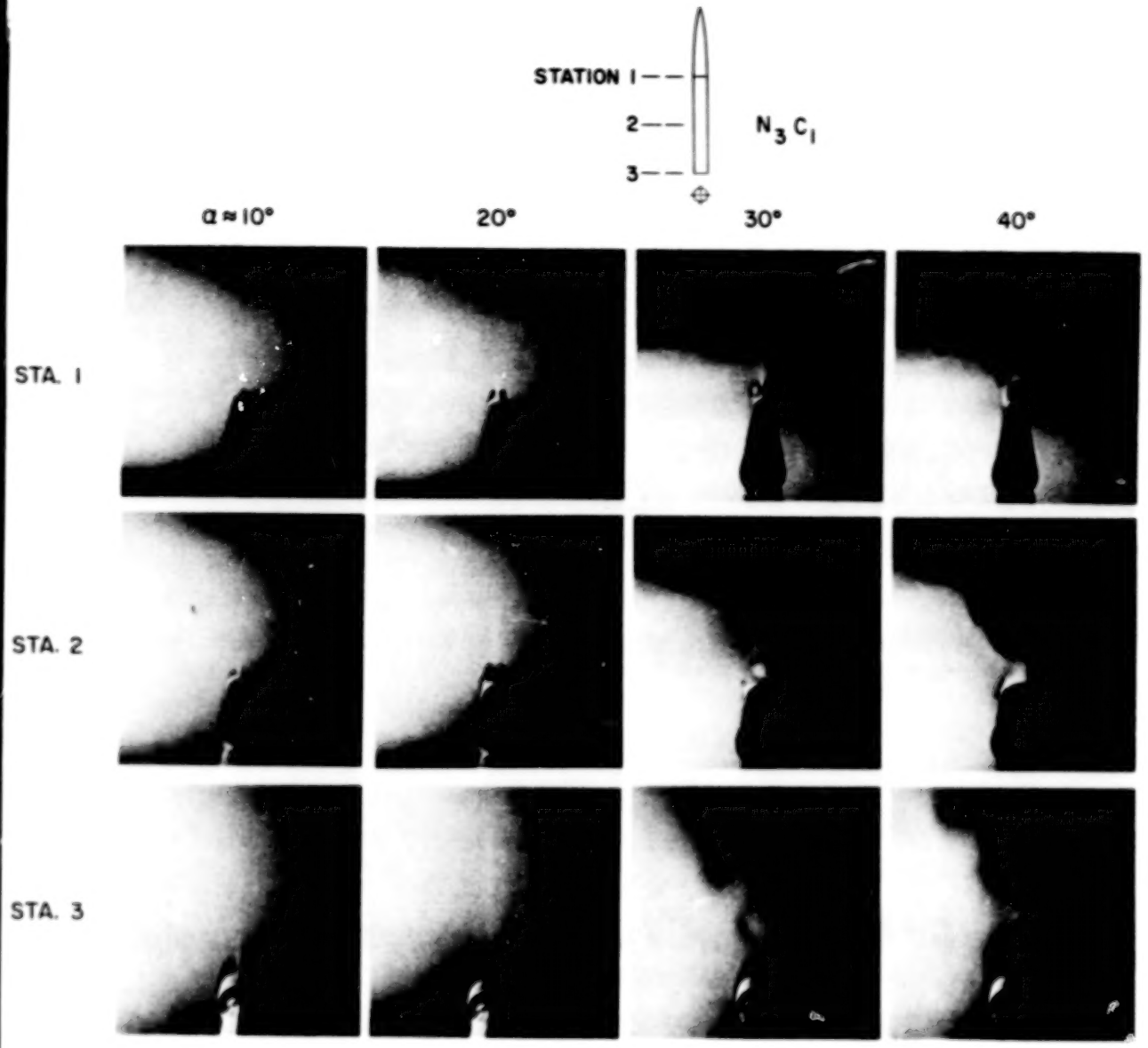

(b) $M_\infty = 0.9$.

Figure 43.– Continued.

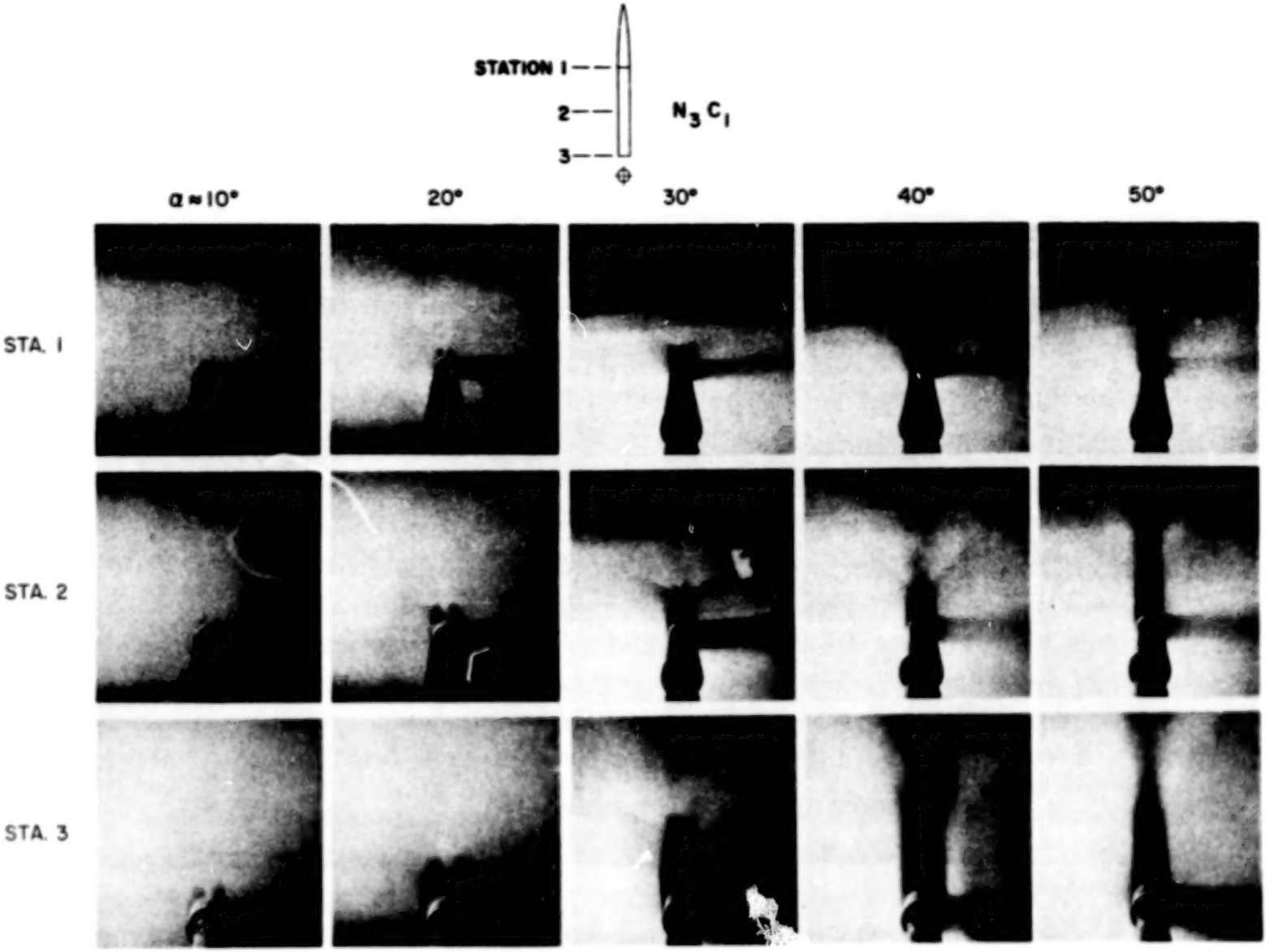

(c) $M_\infty = 2.0$.

Figure 43.– Concluded.

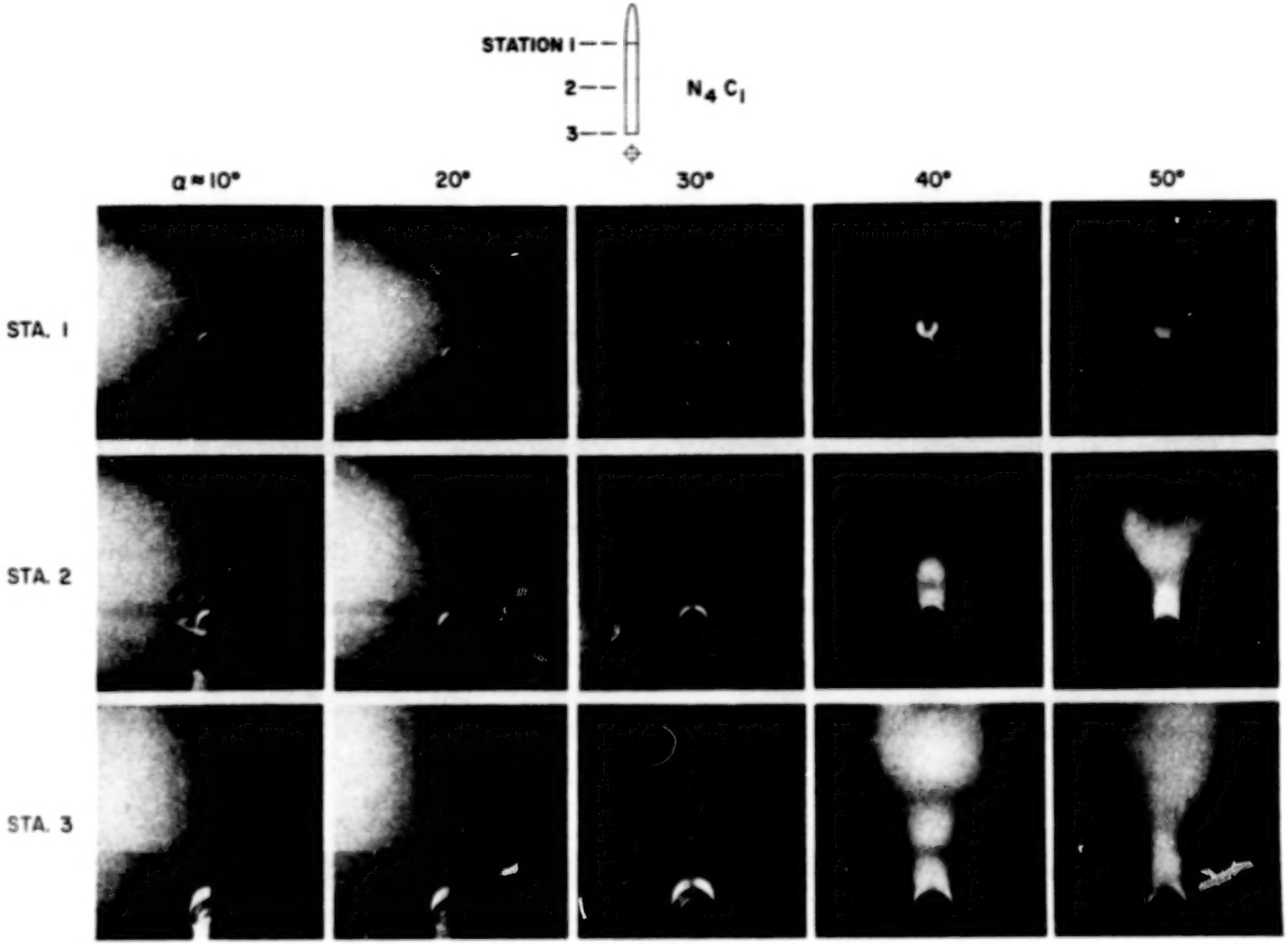

(a) $M_\infty = 0.6$.

Figure 44.– Vapor-screen photographs for $N_4 C_1$ (body with blunt nose of fineness ratio 3).

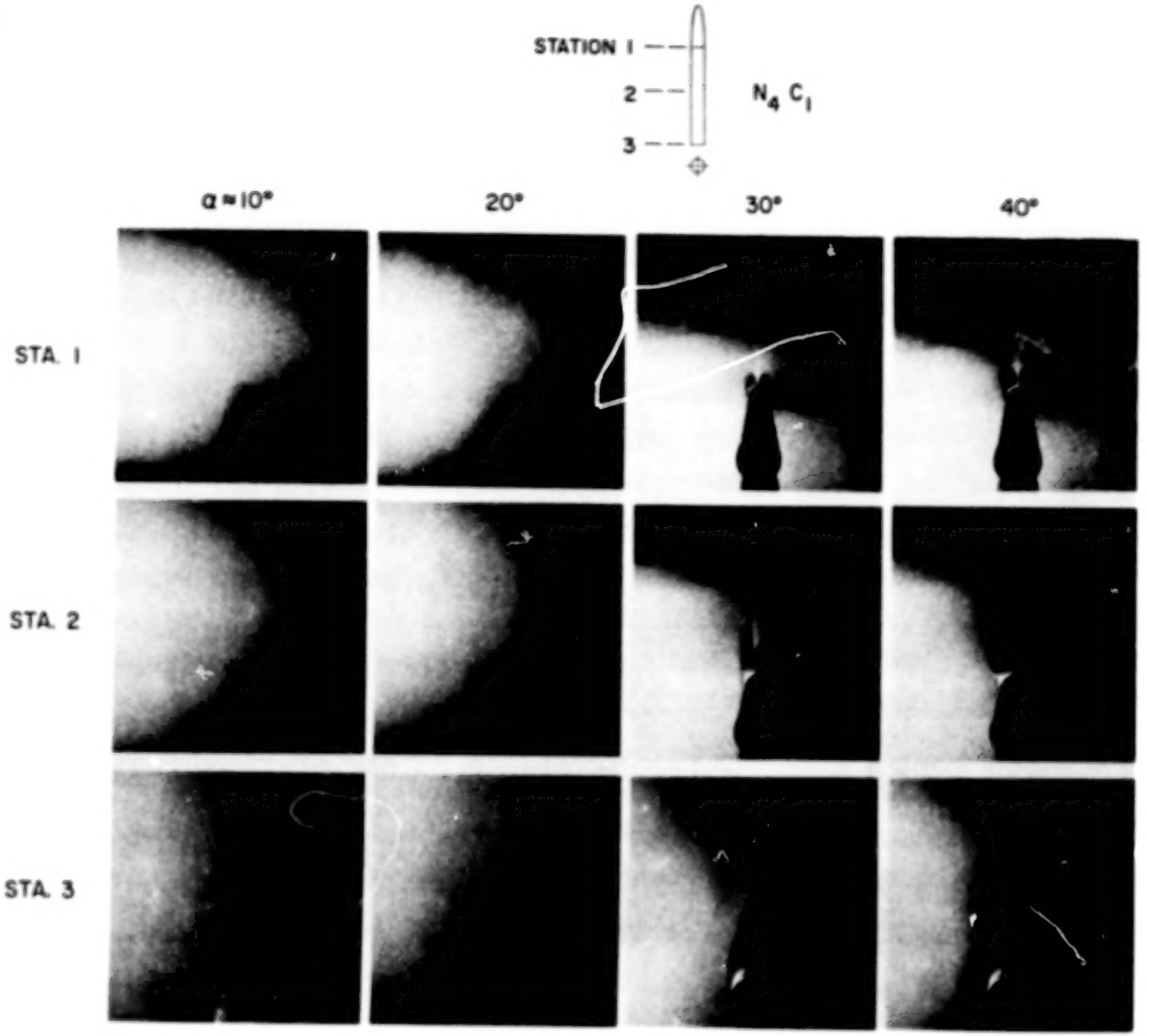

(b) $M_\infty = 0.9$.

Figure 44.– Continued.

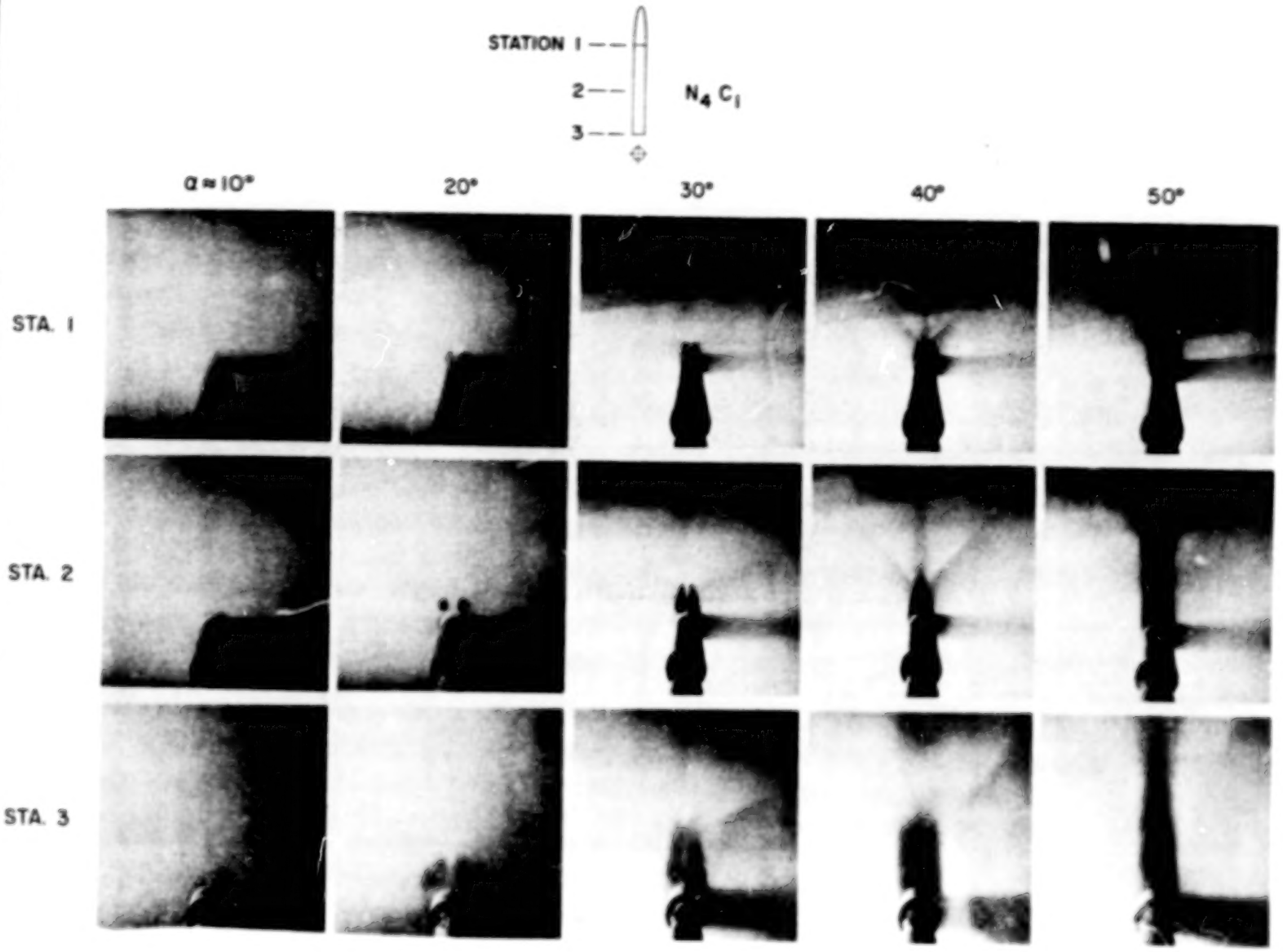

(c) $M_\infty = 2.0$.

Figure 44.– Concluded.

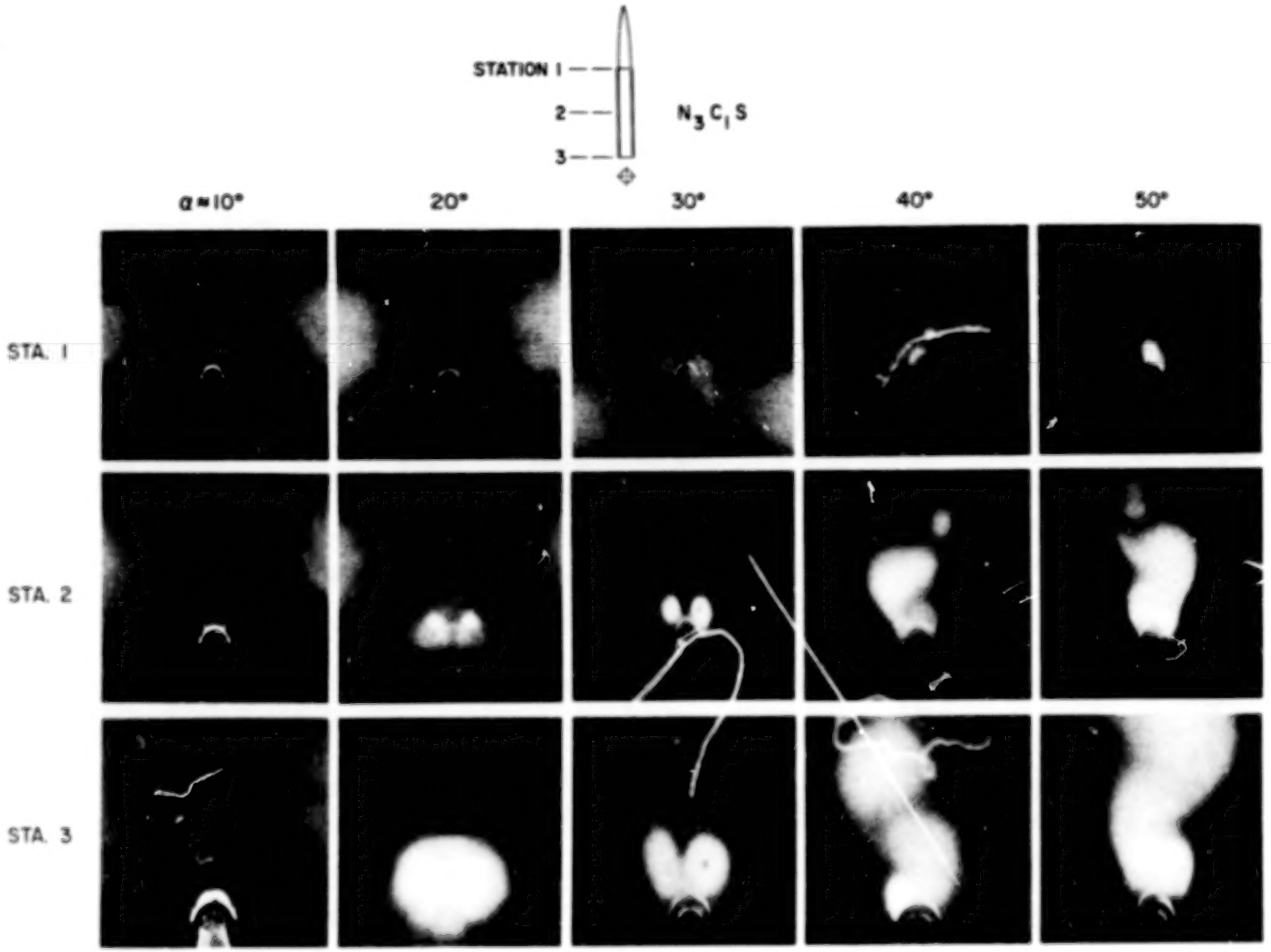

(a) $M_\infty = 0.6$.

Figure 45.– Vapor-screen photographs for $N_3 C_1 S$ (body with fineness-ratio-5 nose and afterbody strake).

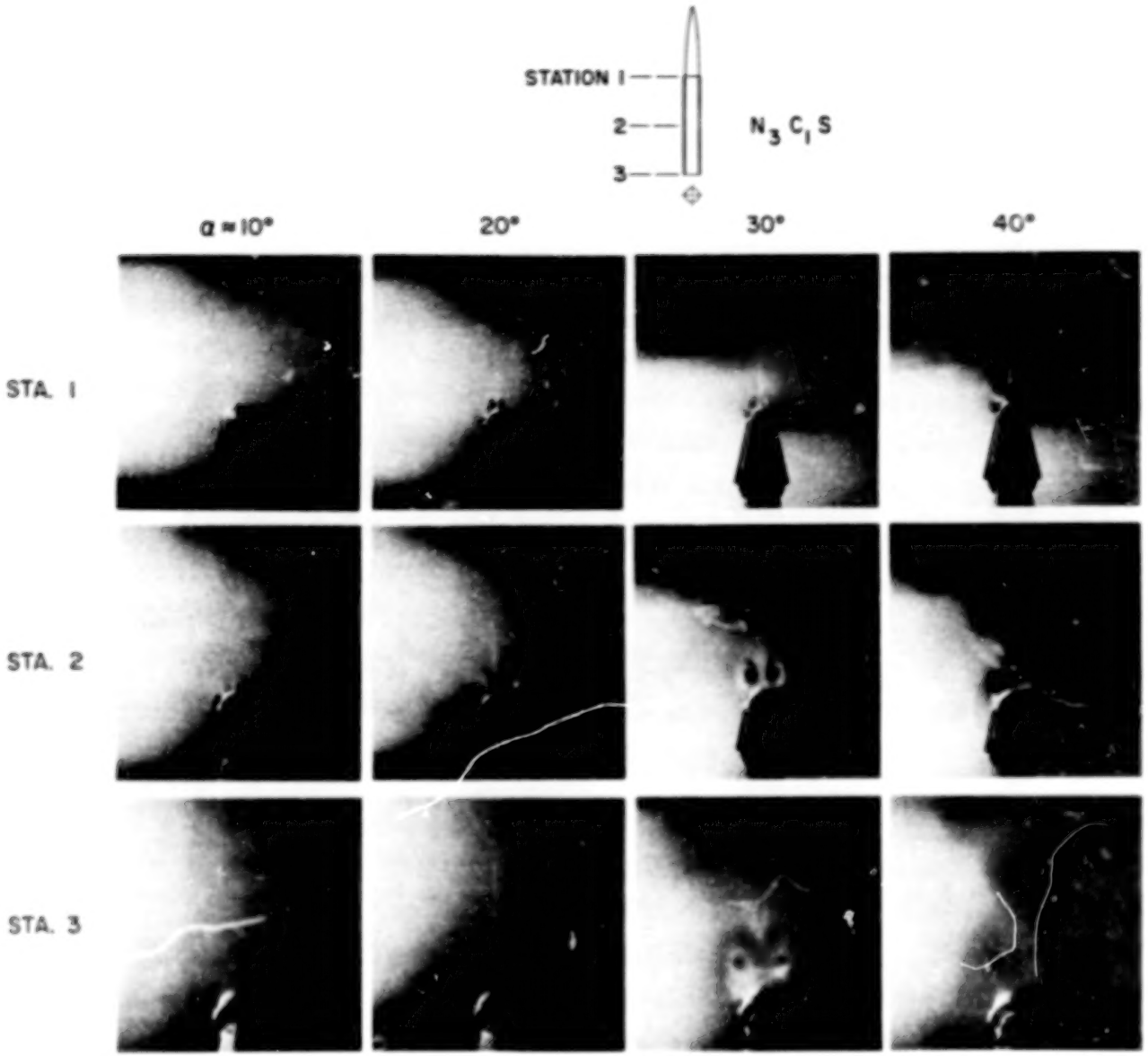

(b) $M_\infty = 0.9$.

Figure 45.– Continued.

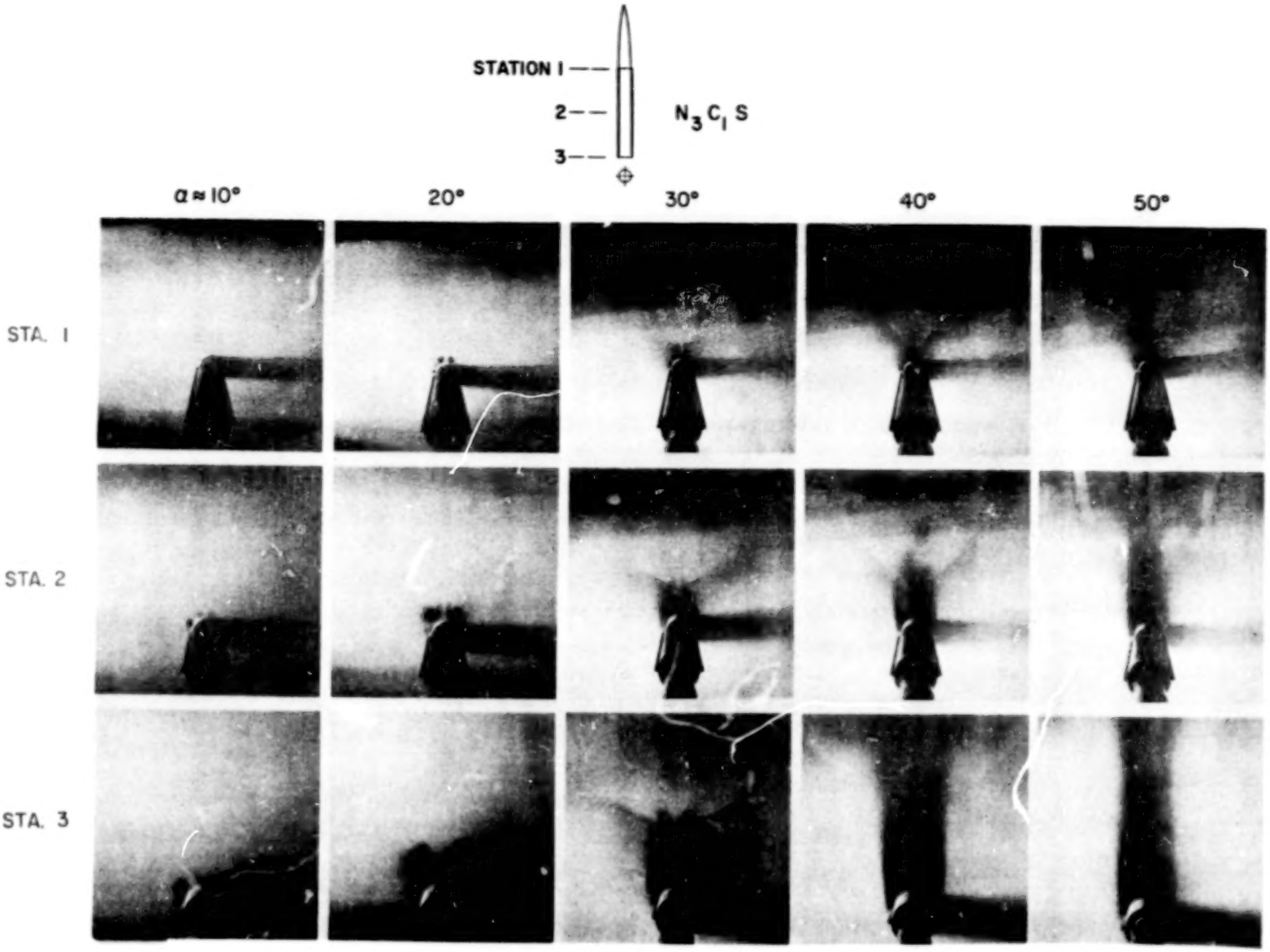

(c) $M_\infty = 2.0$.

Figure 45.– Concluded.

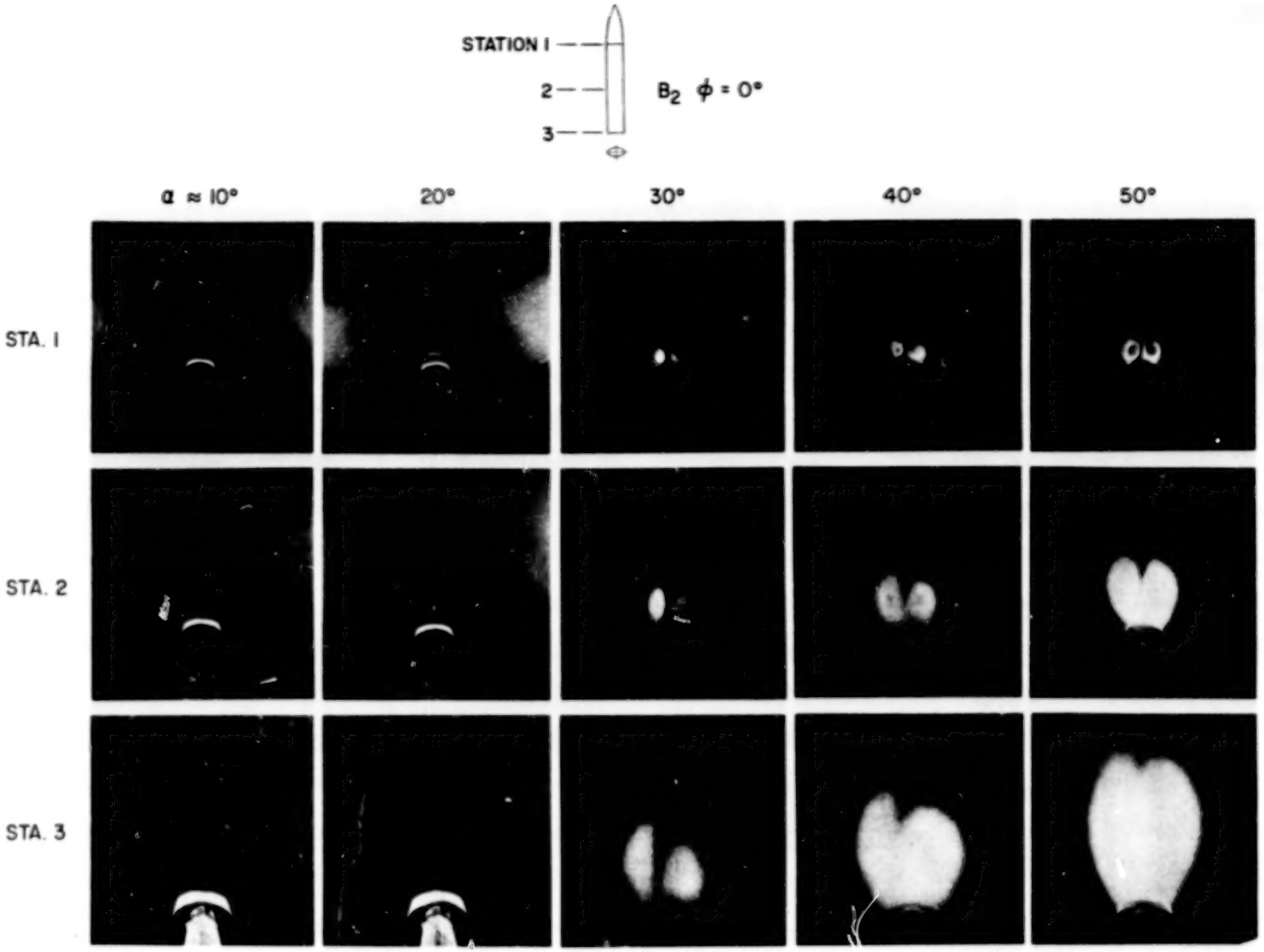

(a) $M_\infty = 0.6$.

Figure 46.– Vapor-screen photographs for B_2 at $\phi = 0°$ (body with constant a/b cross sections).

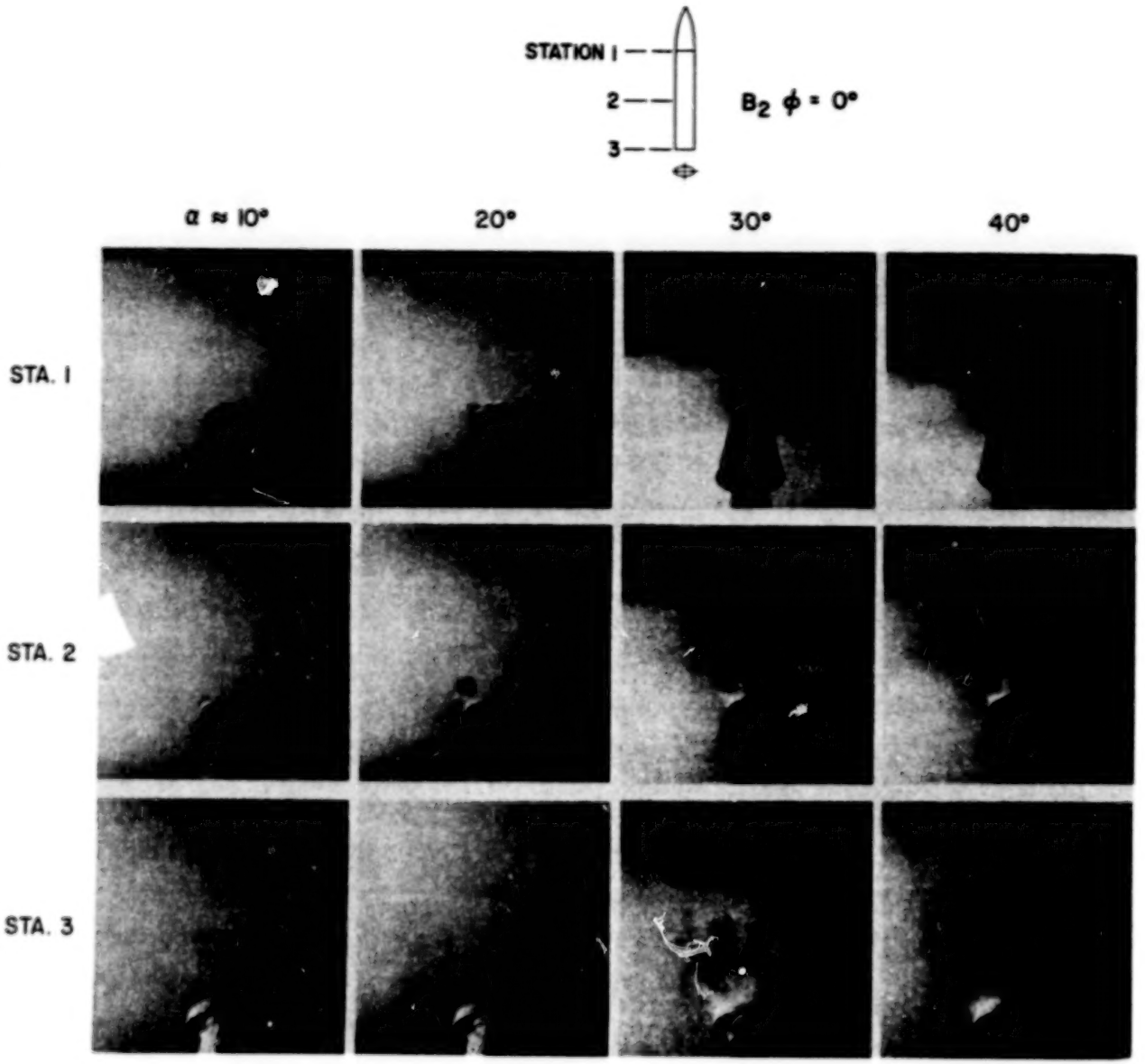

(b) $M_\infty = 0.9$.

Figure 46.– Continued.

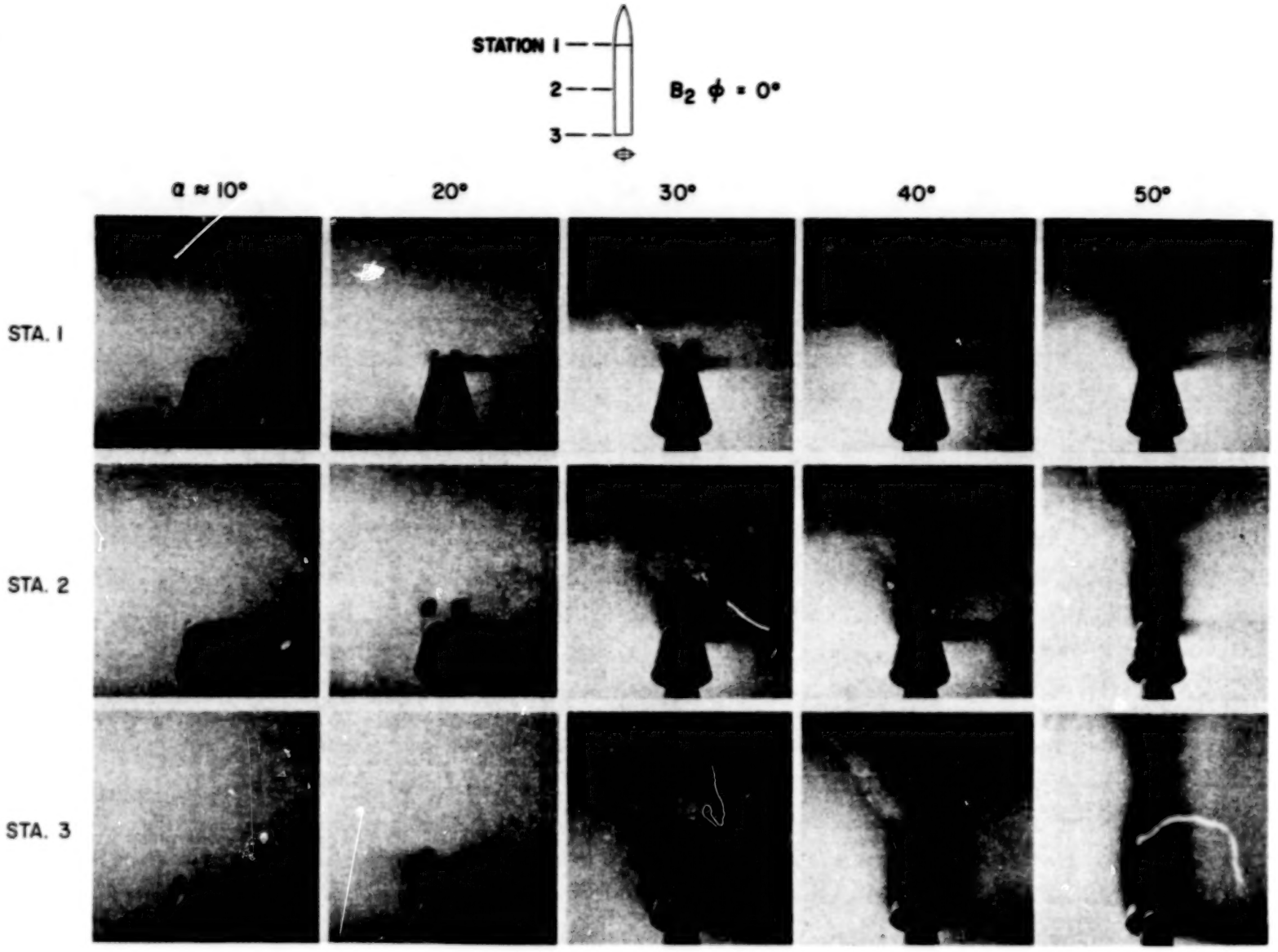

(c) $M_\infty = 2.0$.

Figure 46.– Concluded.

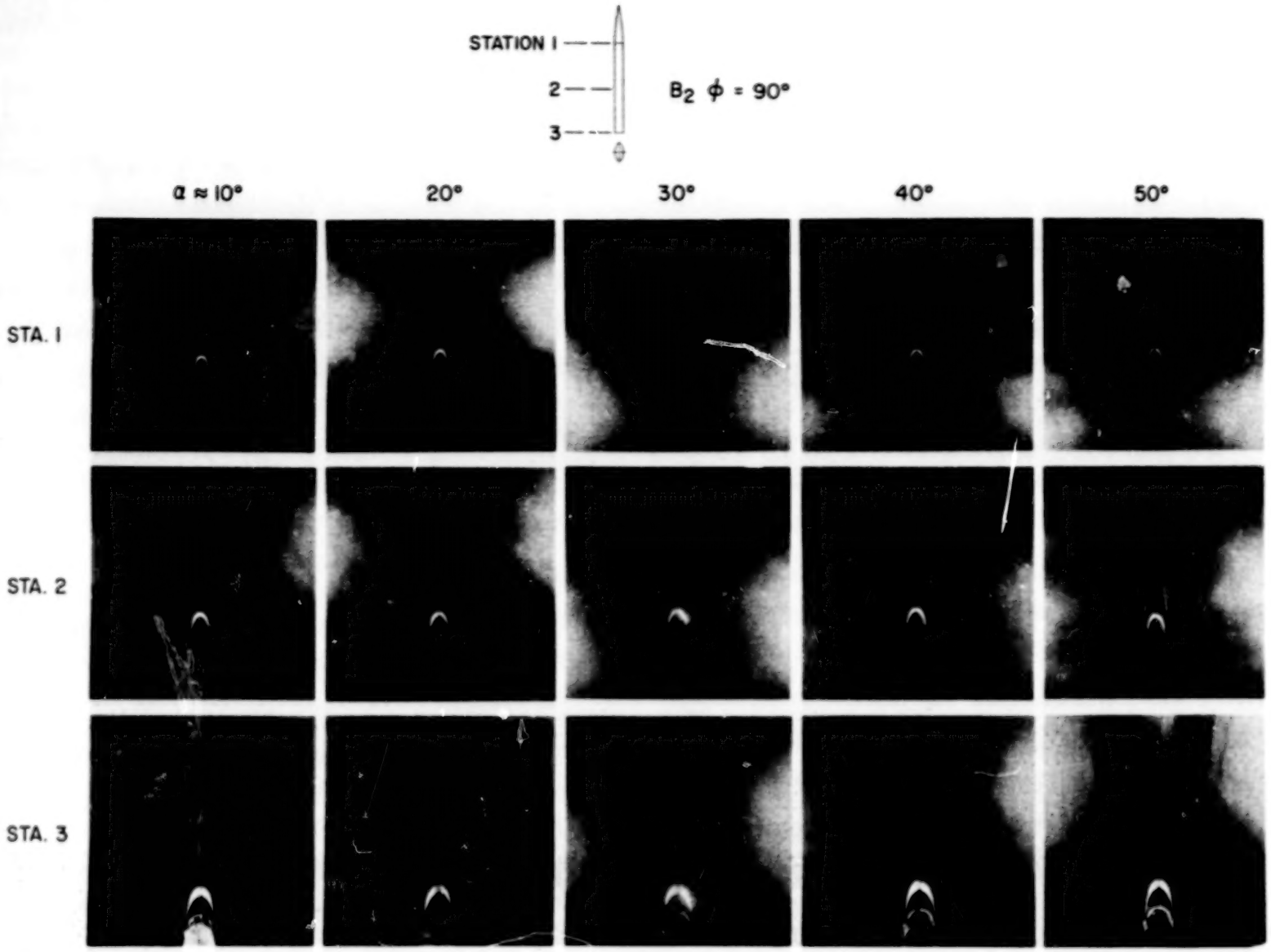

(a) $M_\infty \approx 0.6$.

Figure 47.-- Vapor-screen photographs for B_2 at $\phi = 90°$ (body with constant a/b cross sections).

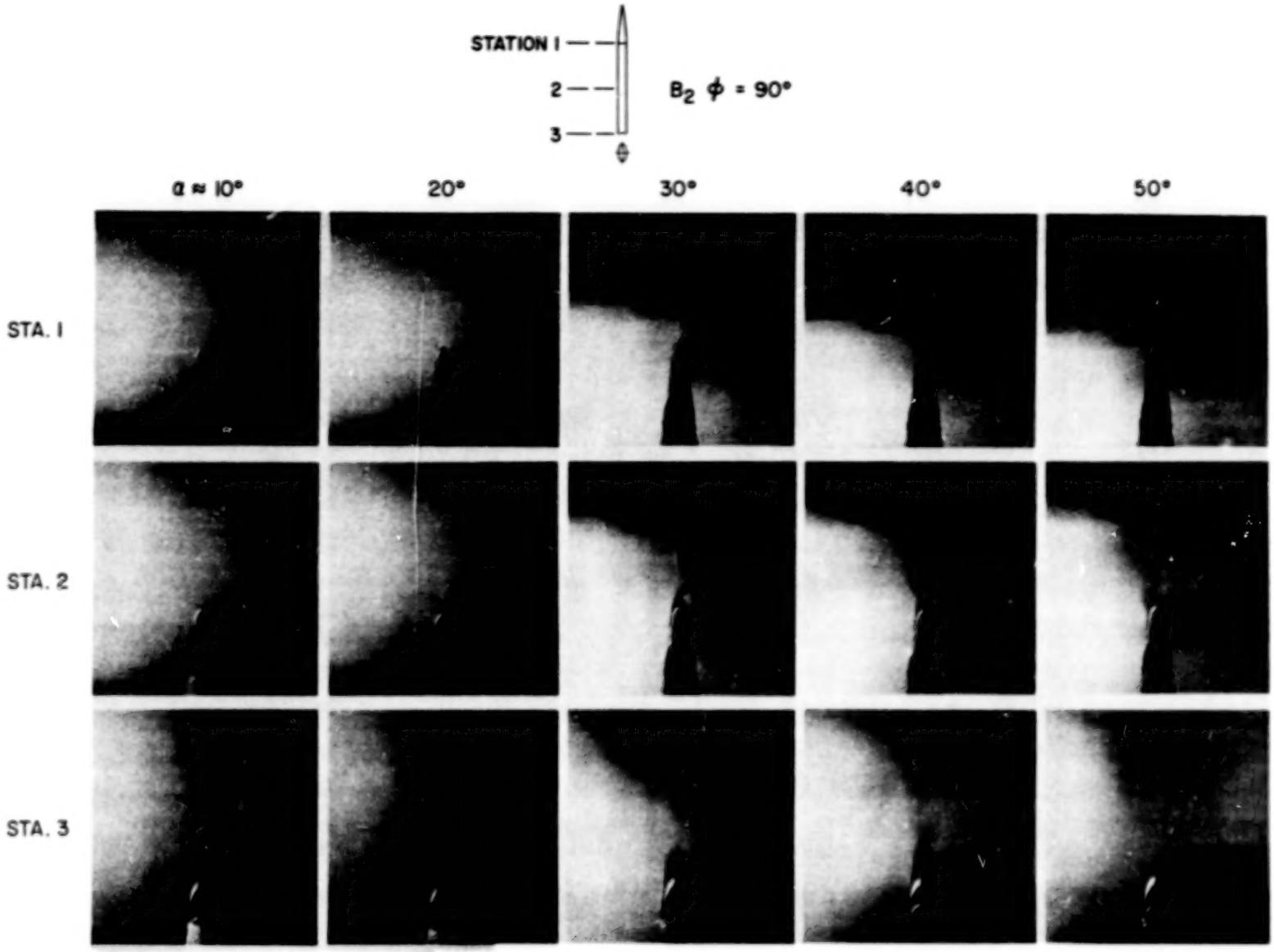

(b) $M_\infty = 0.9$.

Figure 47.– Continued.

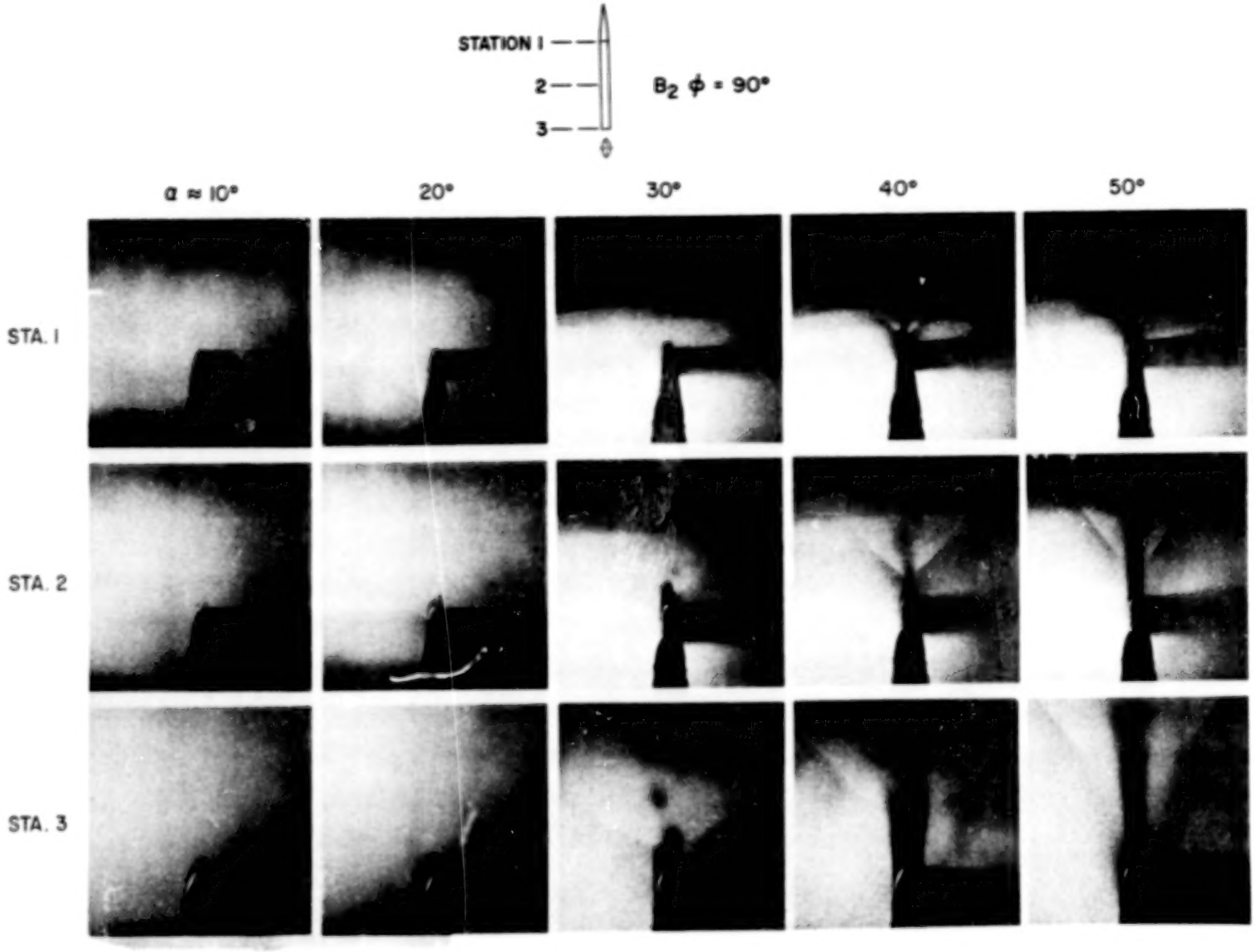

(c) $M_\infty = 2.0$.

Figure 47.– Concluded.

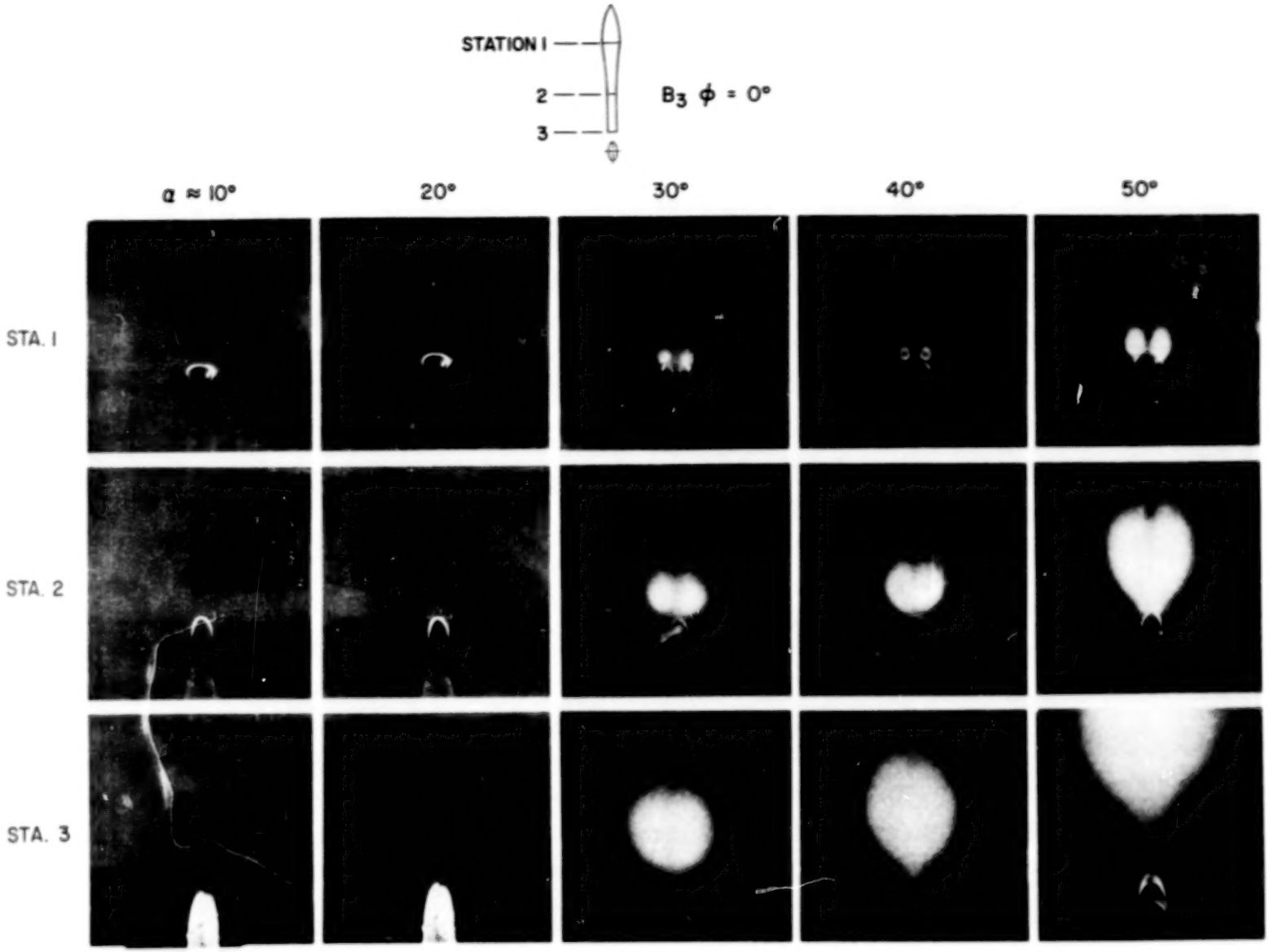

(a) $M_\infty = 0.6$.

Figure 48.– Vapor-screen photographs for B_3 at $\phi = 0°$ (body with variable a/b cross sections).

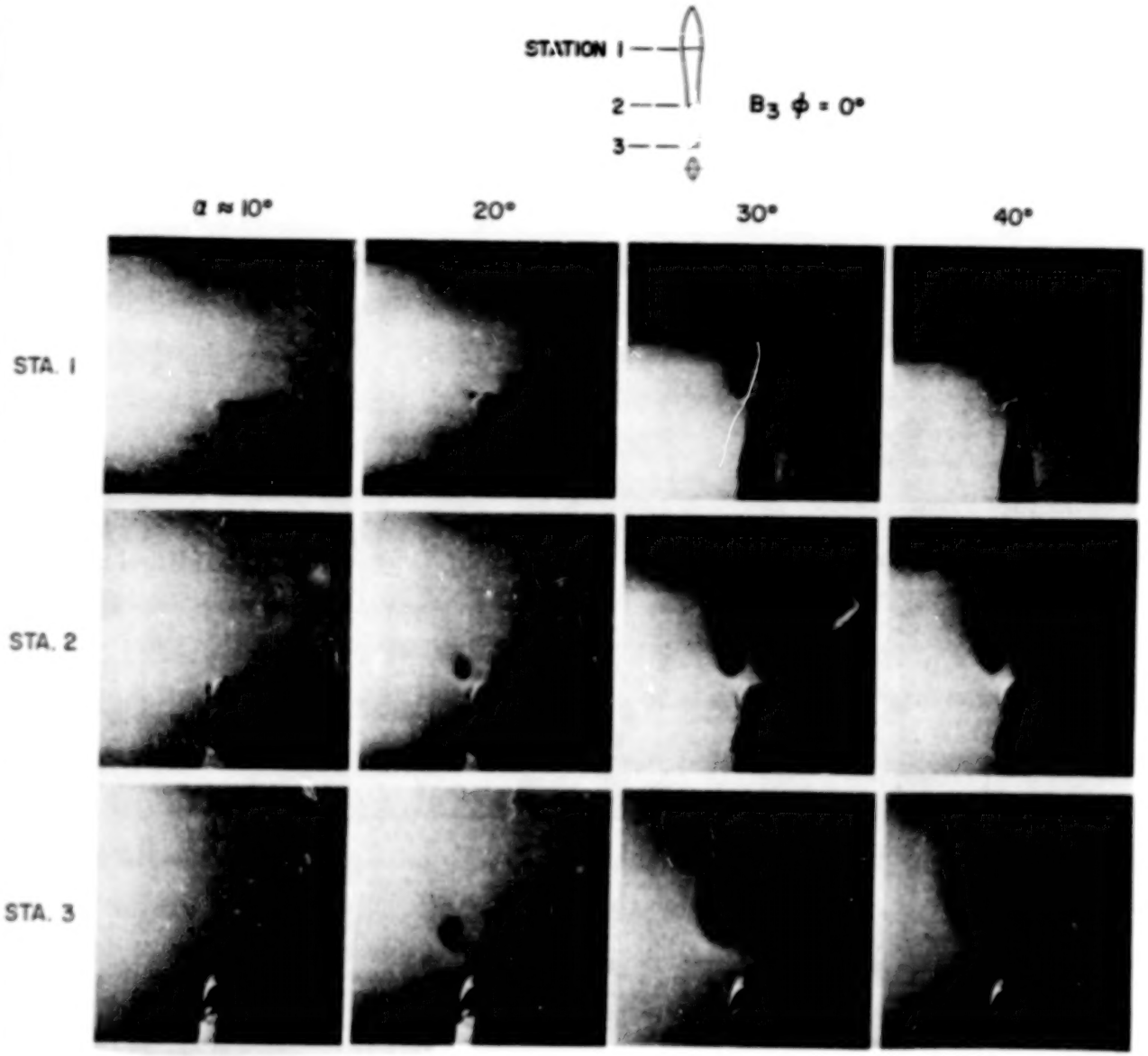

(b) $M_\infty = 0.9$.

Figure 48.– Continued.

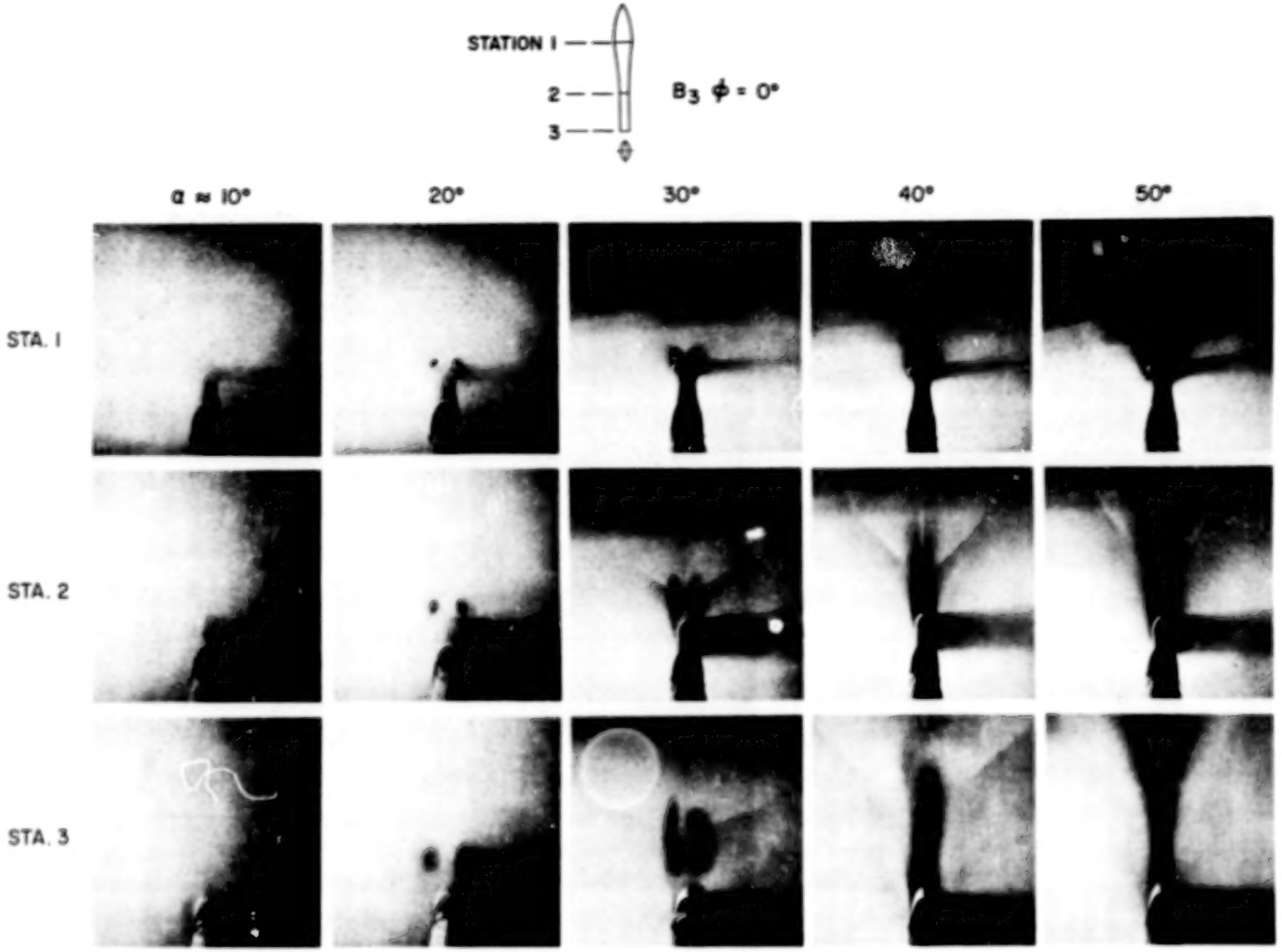

(c) $M_\infty = 2.0$.

Figure 48.– Concluded.

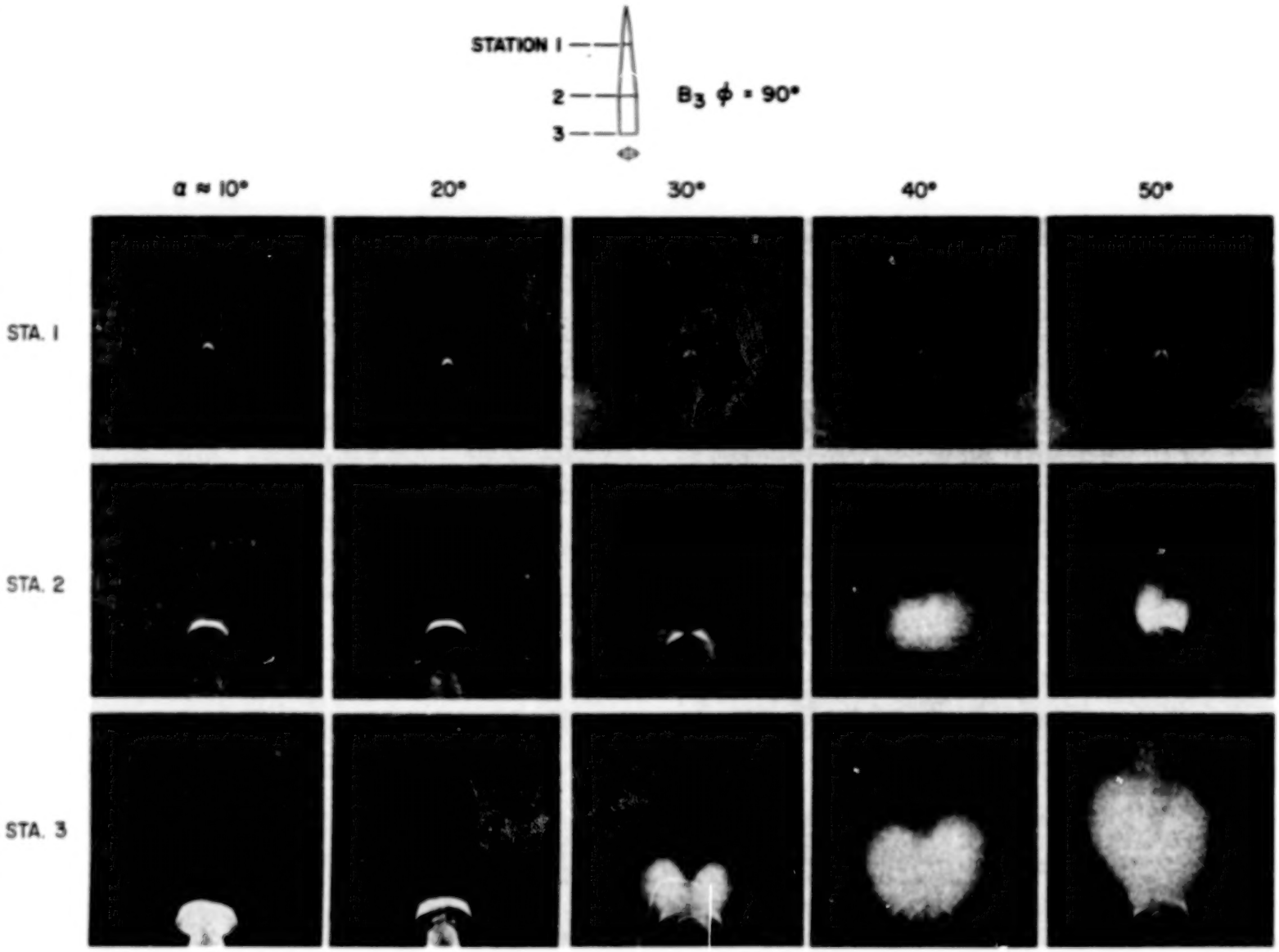

(a) $M_\infty = 0.6$.

Figure 49.– Vapor-screen photographs for B_3 at $\phi = 90°$ (body with variable a/b cross sections).

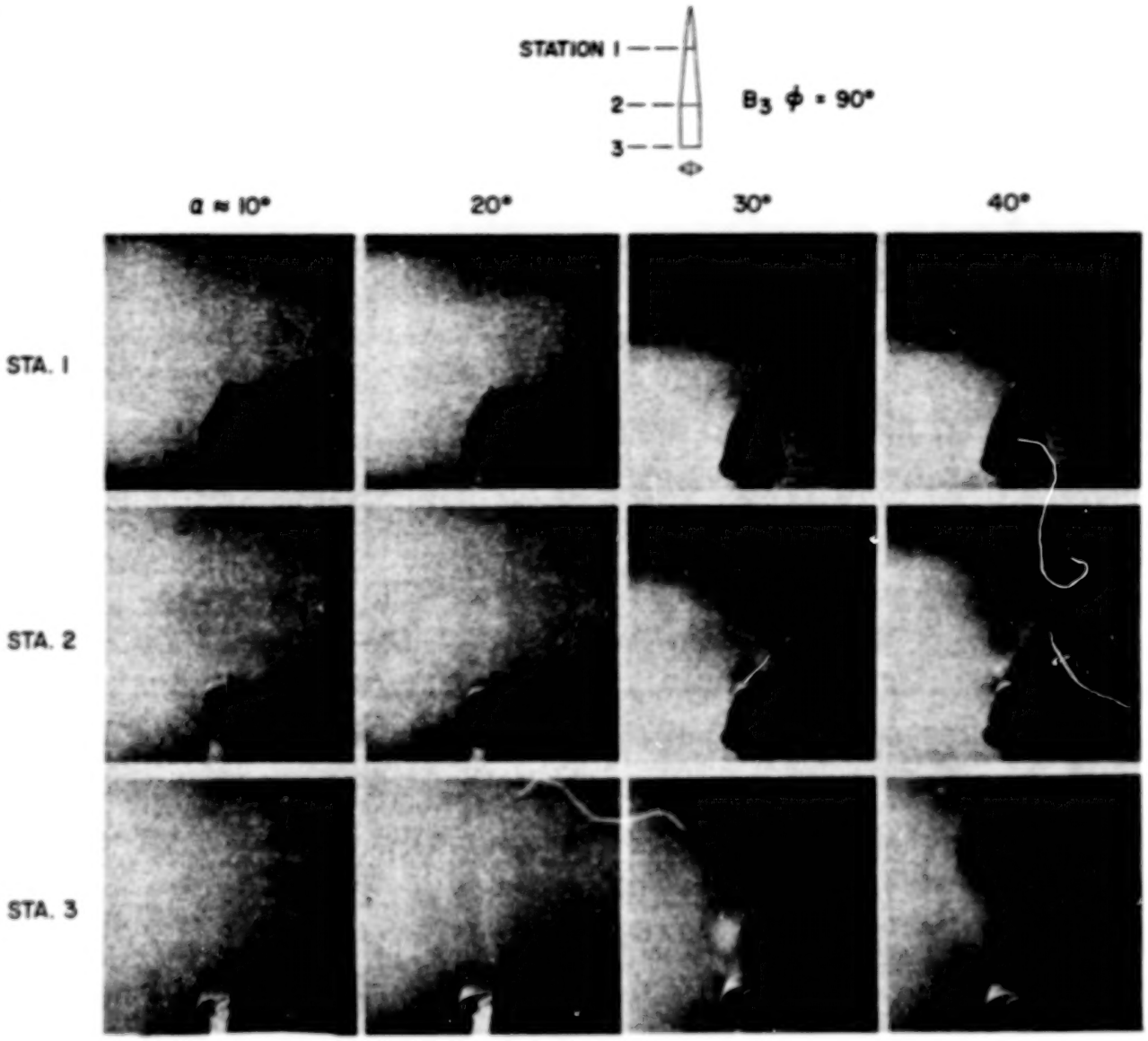

(b) $M_\infty = 0.9$.

Figure 49.– Continued.

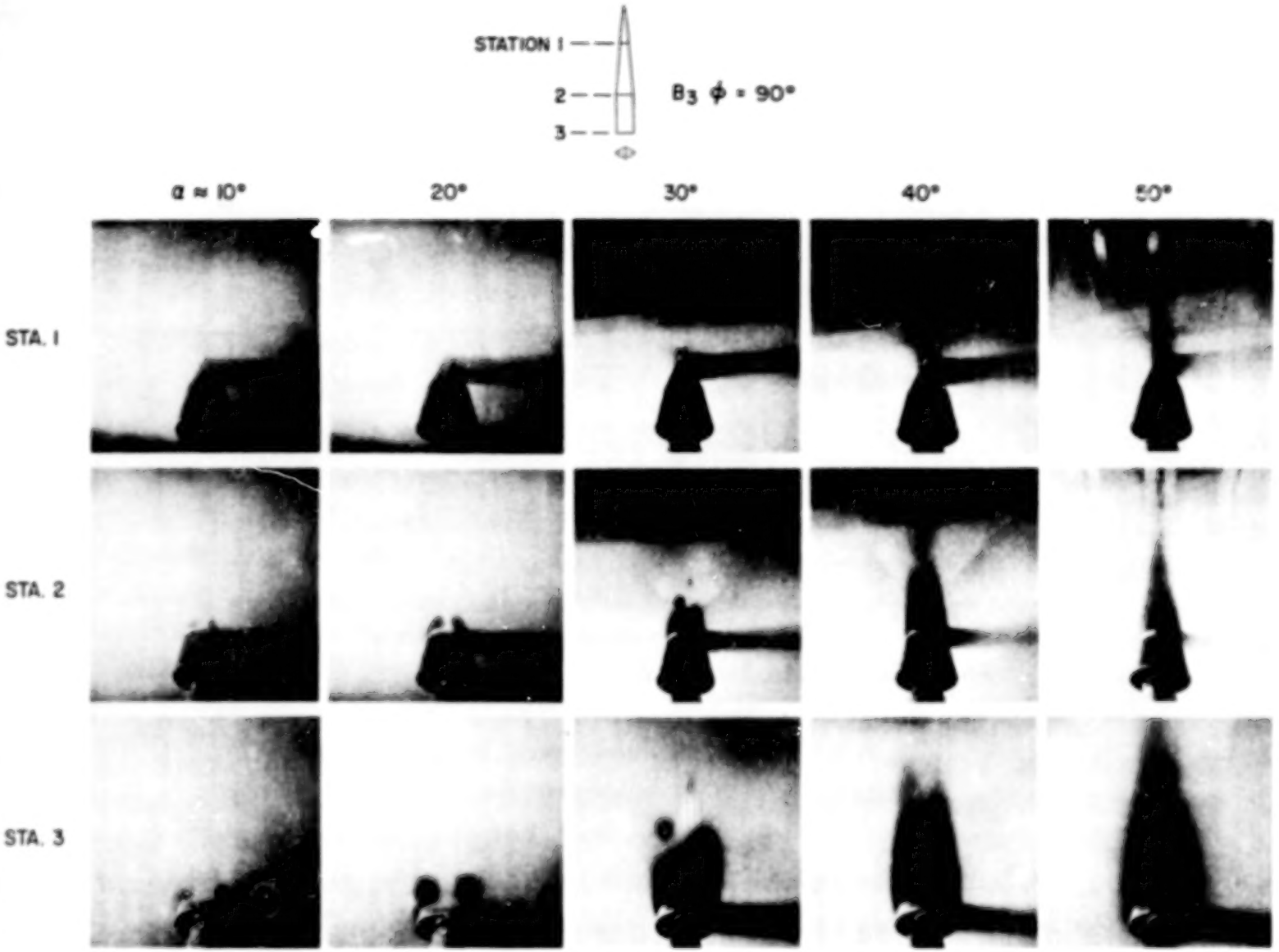

(c) $M_\infty \simeq 2.0$.

Figure 49.– Concluded.

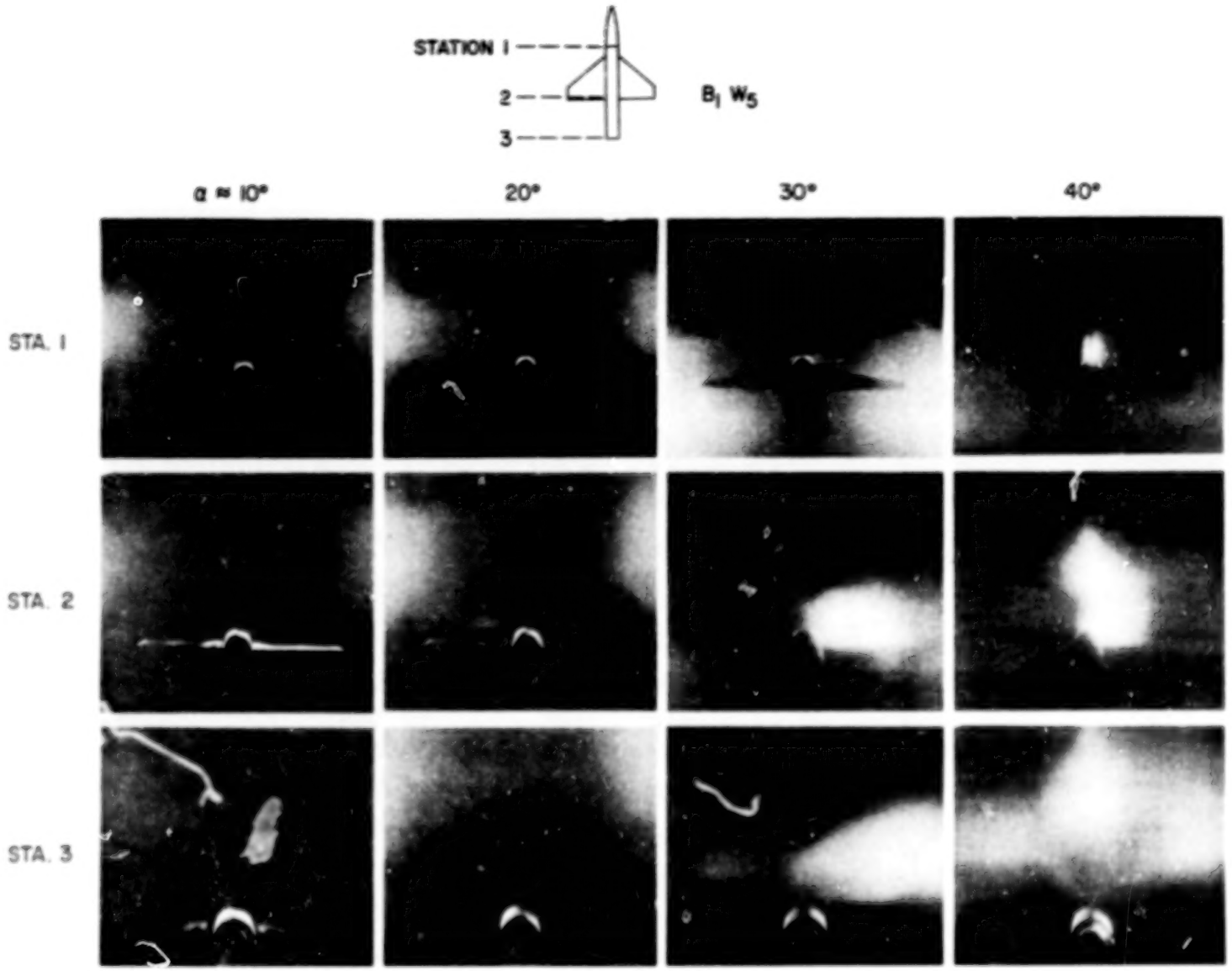

(a) $M_\infty = 0.6$.

Figure 50.– Vapor-screen photographs for $B_1 W_5 = N_1 C_1 W_5$ (body with fineness-ratio-3 nose and aspect-ratio-3 wing).

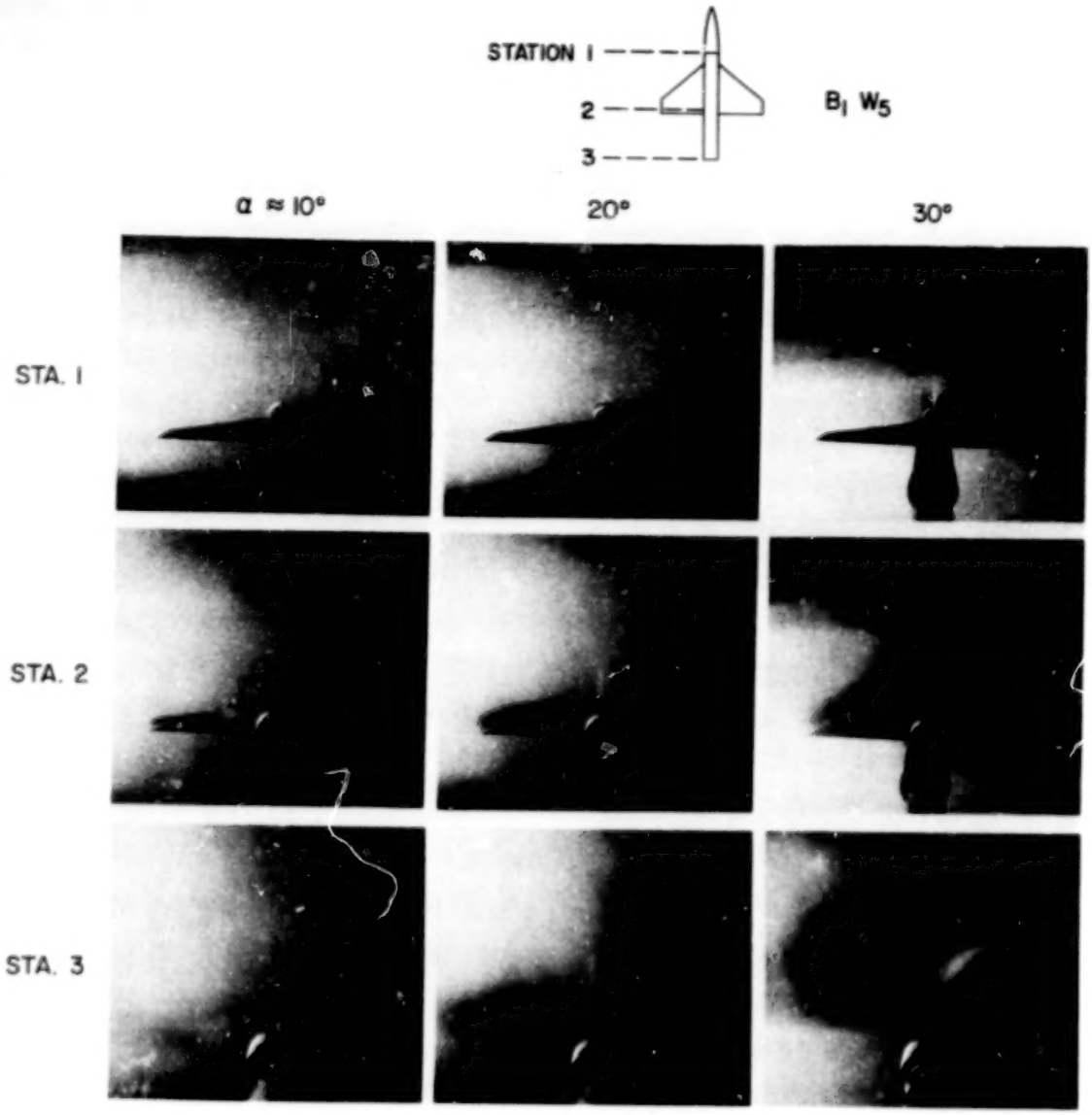

(b) $M_\infty = 0.9$.

Figure 50.– Continued.

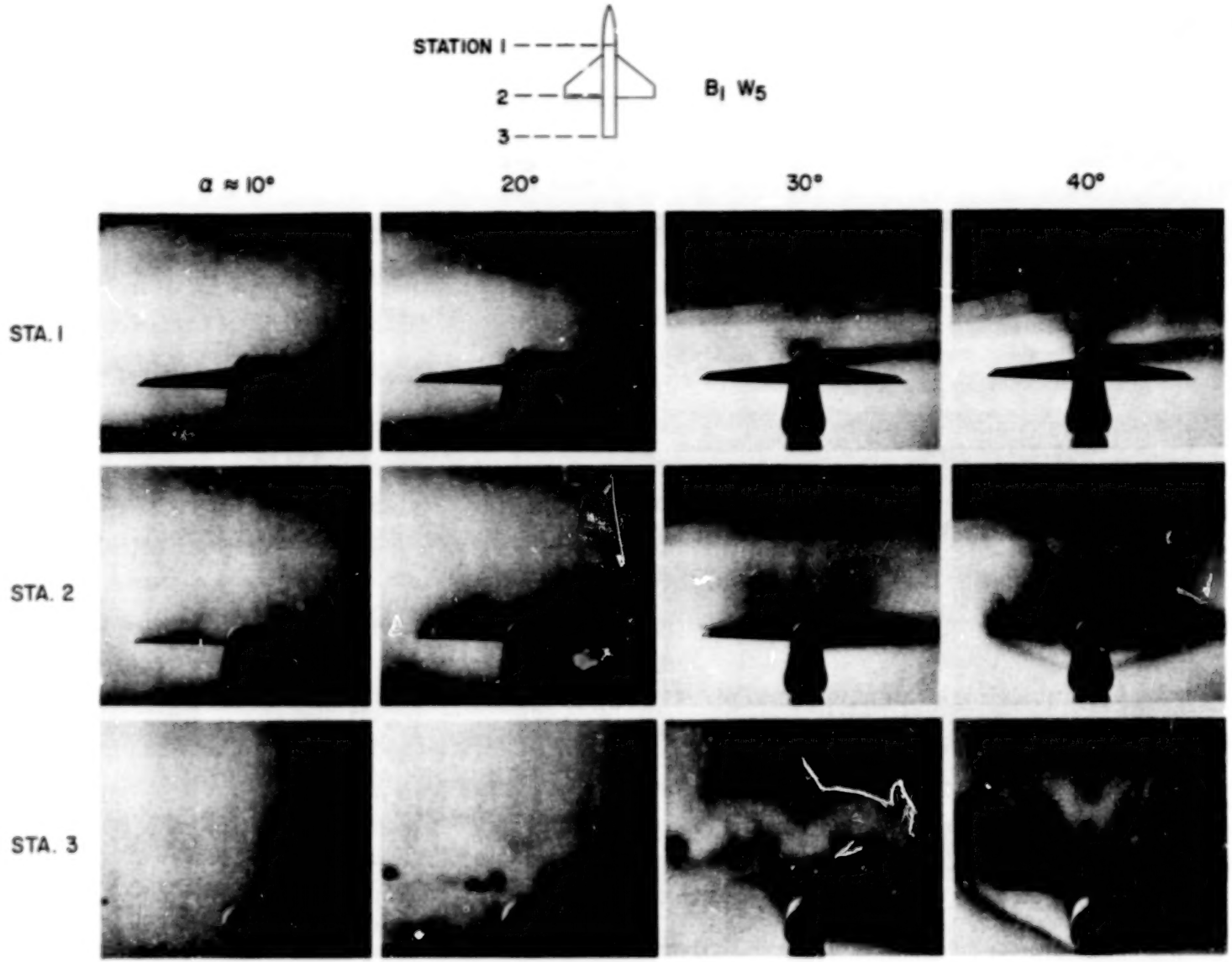

(c) $M_\infty = 2.0$.

Figure 50.– Concluded.

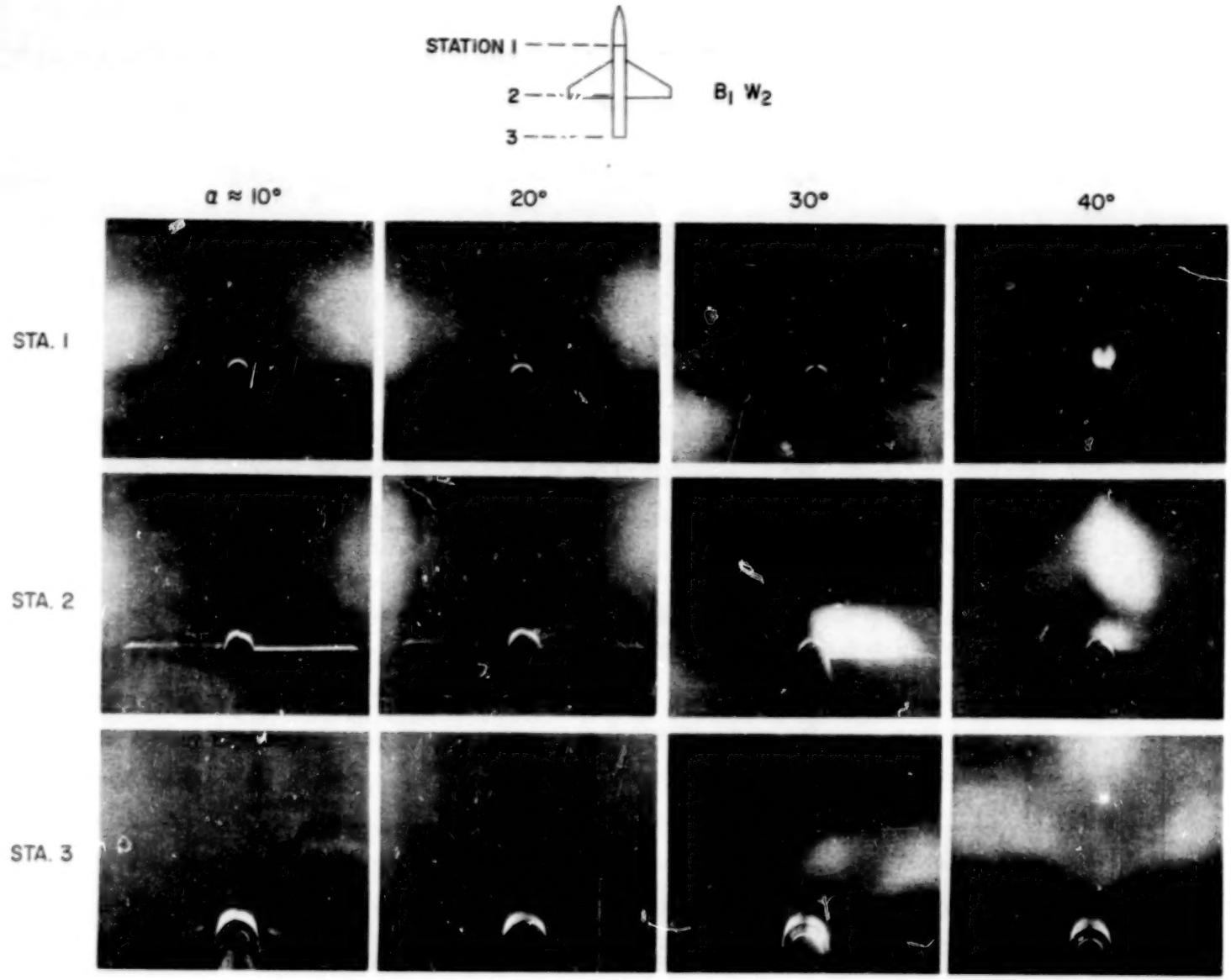

(a) $M_\infty = 0.6$.

Figure 51.– Vapor-screen photographs for $B_1 W_2 = N_1 C_1 W_2$ (body with fineness-ratio-3 nose and aspect-ratio-4 wing).

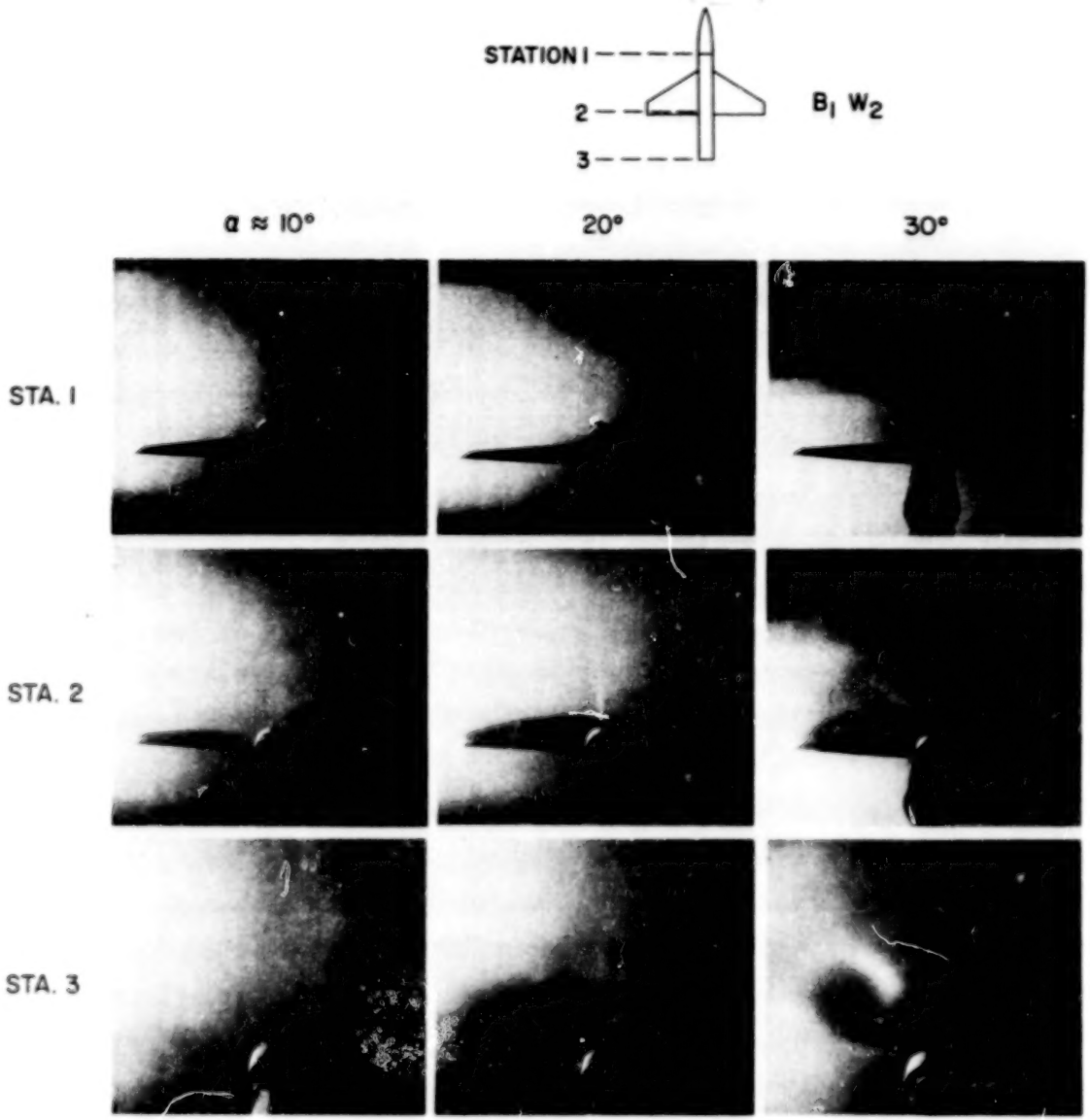

(b) $M_\infty = 0.9$.

Figure 51.– Continued.

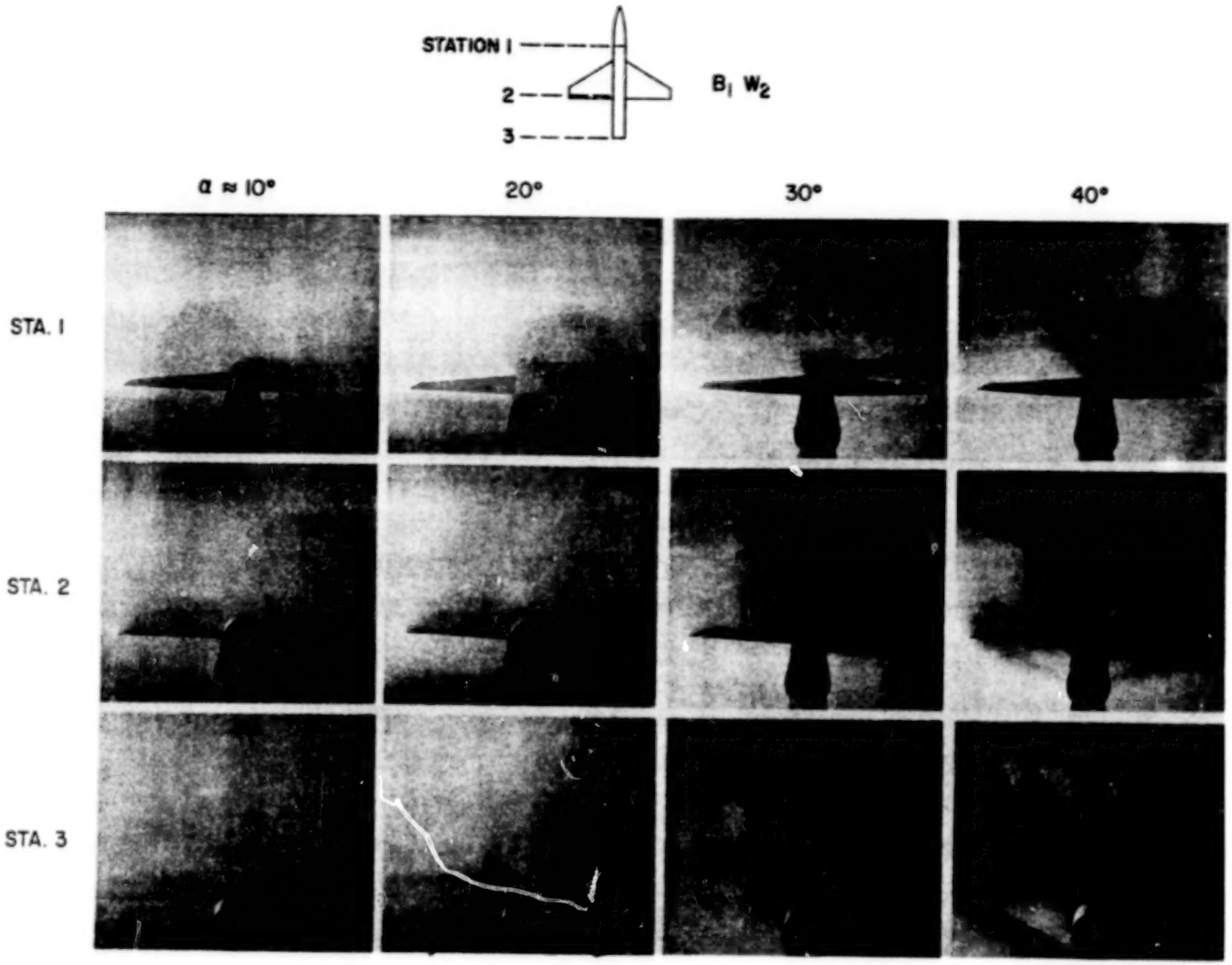

(c) $M_\infty = 2.0$.

Figure 51.– Concluded.

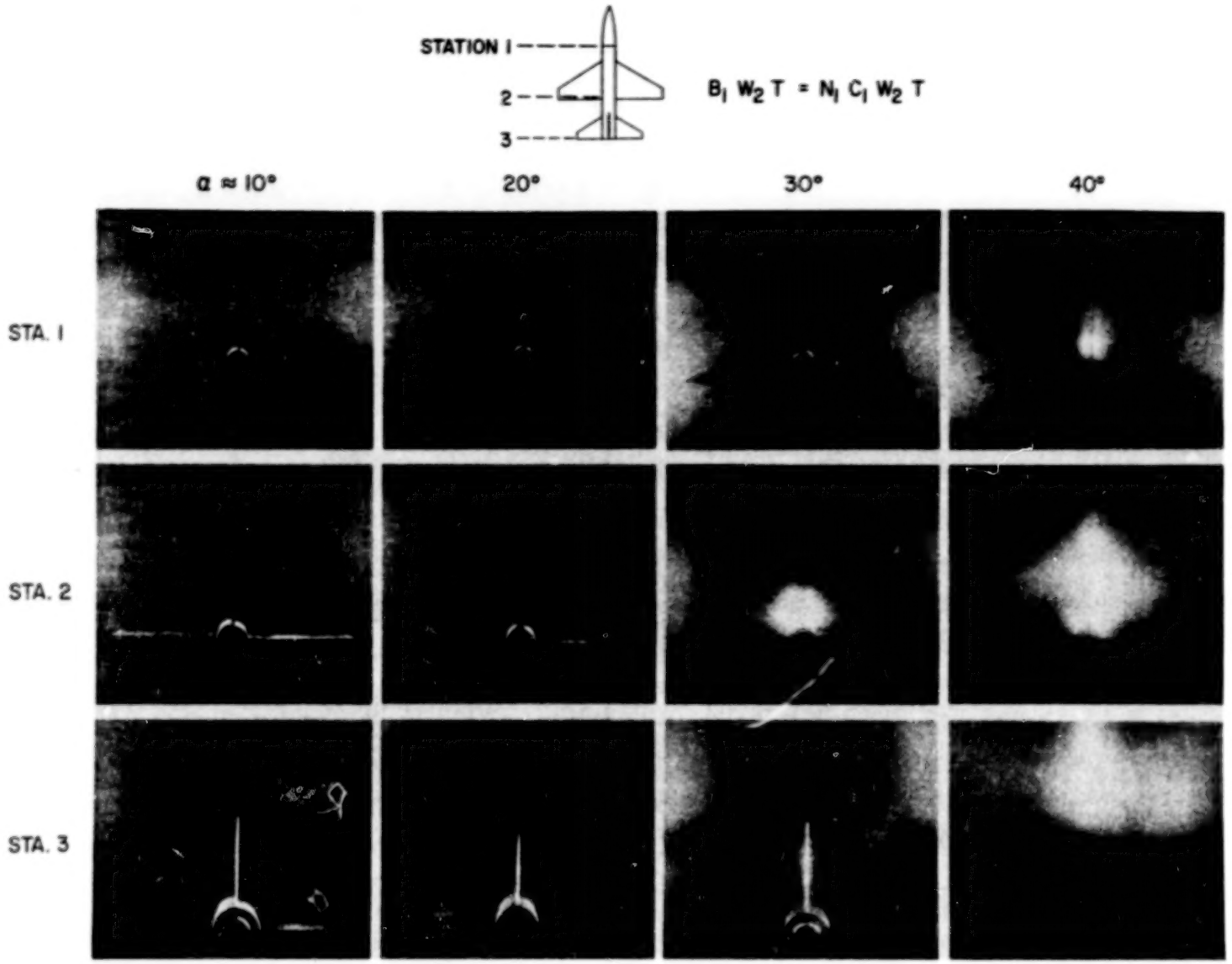

(a) $M_\infty = 0.6$.

Figure 52.– Vapor-screen photographs for $B_1 W_2 T = N_1 C_1 W_2 T$ (body with fineness-ratio-3 nose, aspect-ratio-4 wing, and tail).

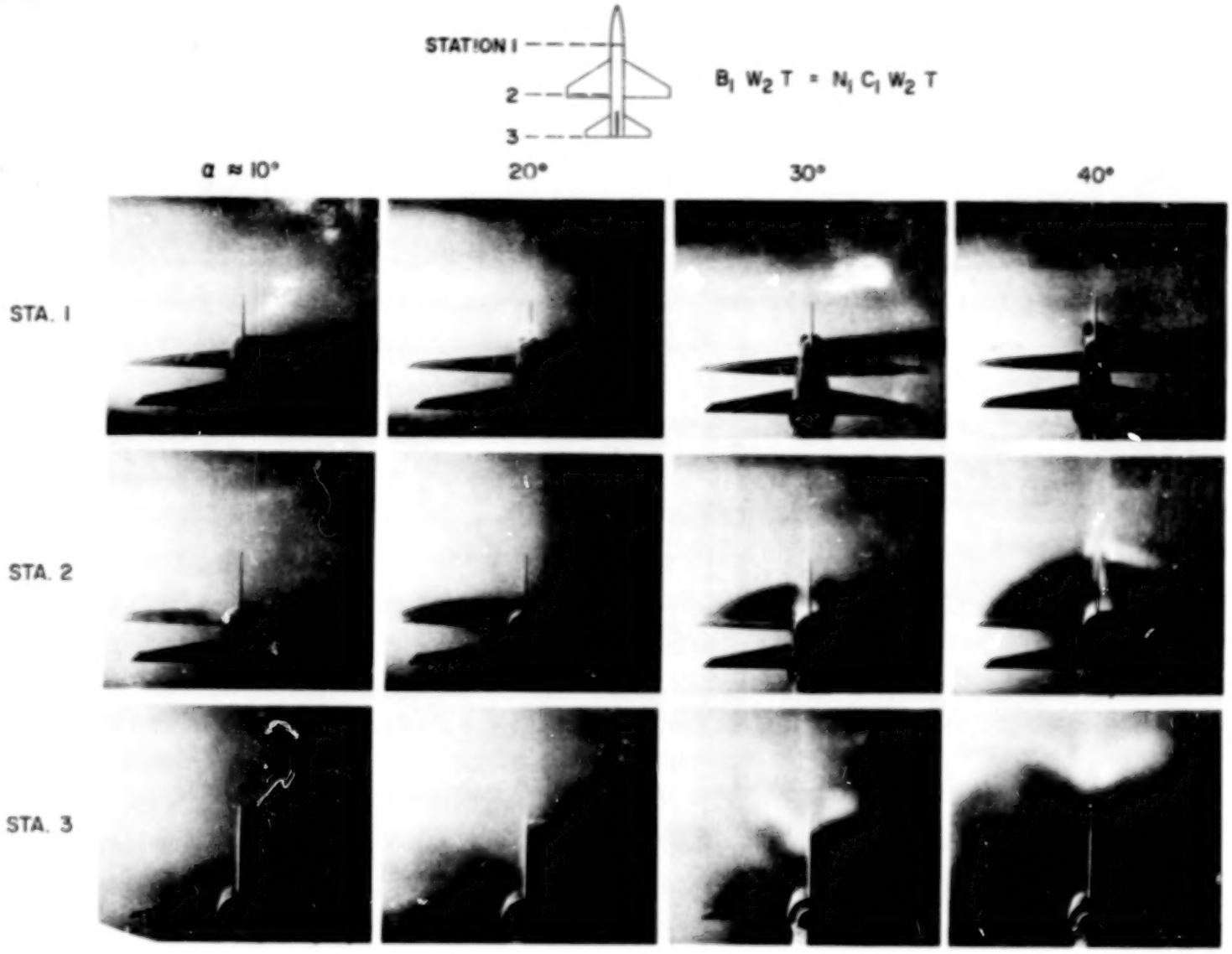

(b) $M_\infty = 0.9$.

Figure 52.– Continued.

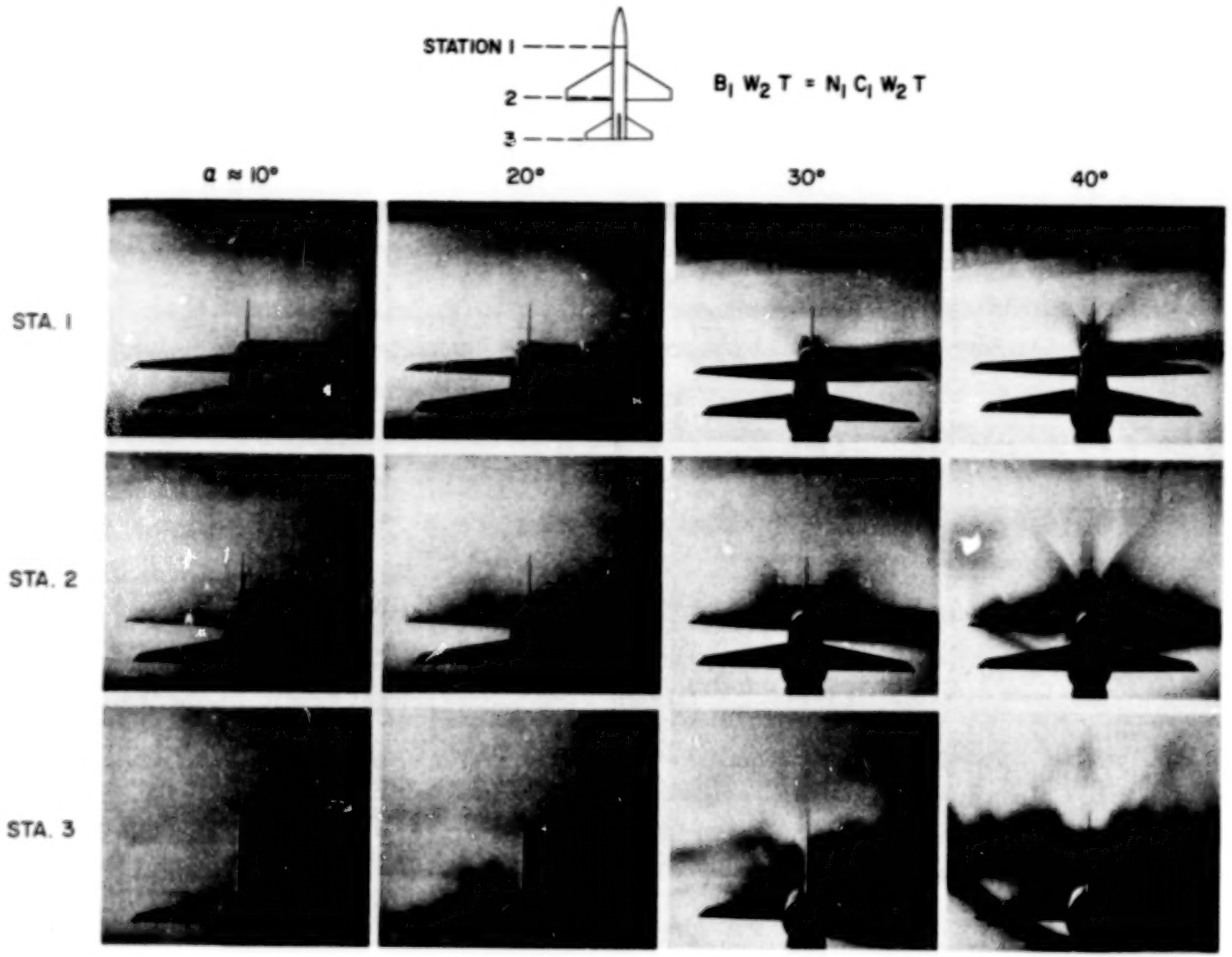

(c) $M_\infty = 2.0$.

Figure 52.– Concluded.

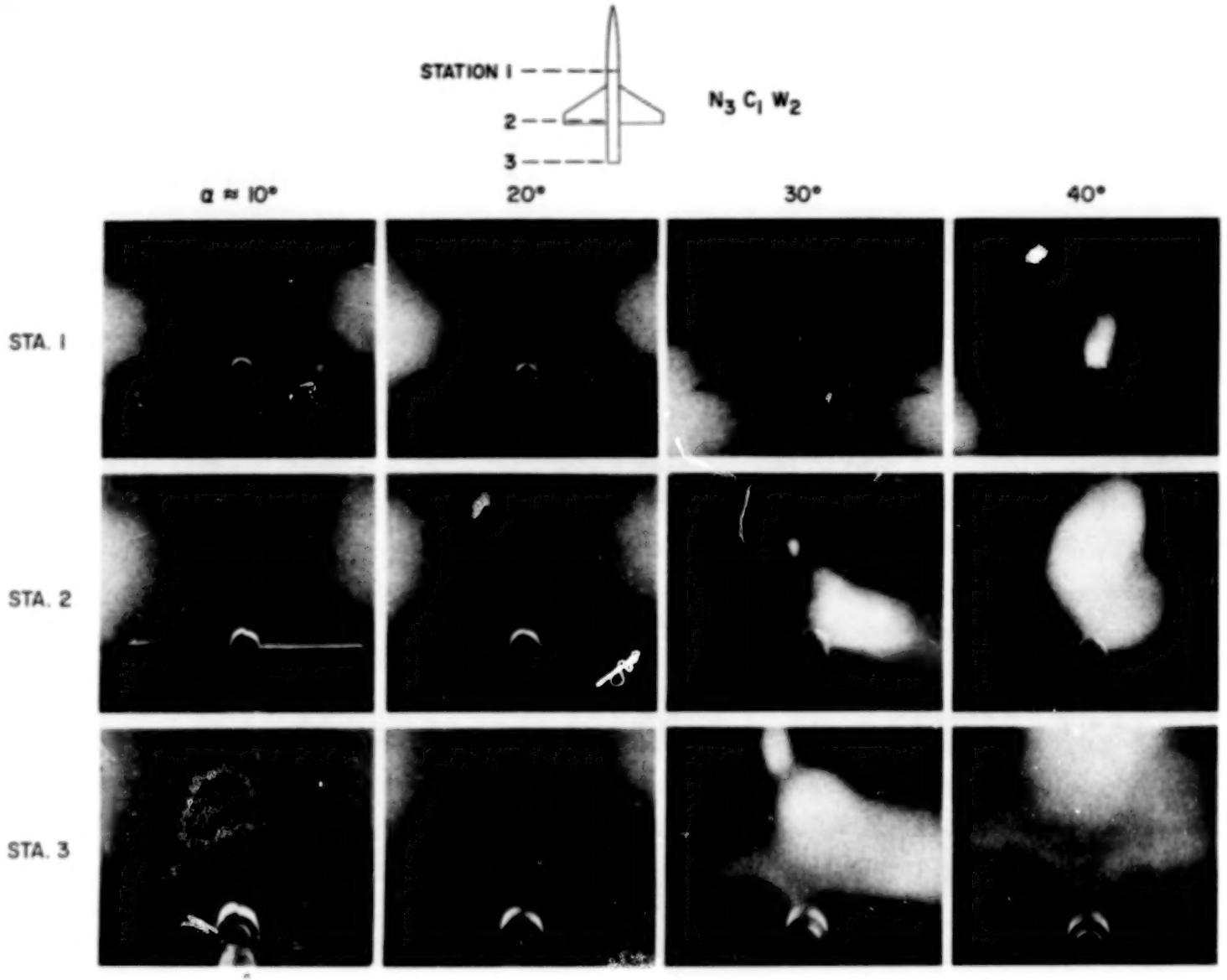

(a) $M_\infty = 0.6$.

Figure 53.– Vapor-screen photographs for $N_3 C_1 W_2$ (body with fineness-ratio-5 nose and aspect-ratio-4 wing)

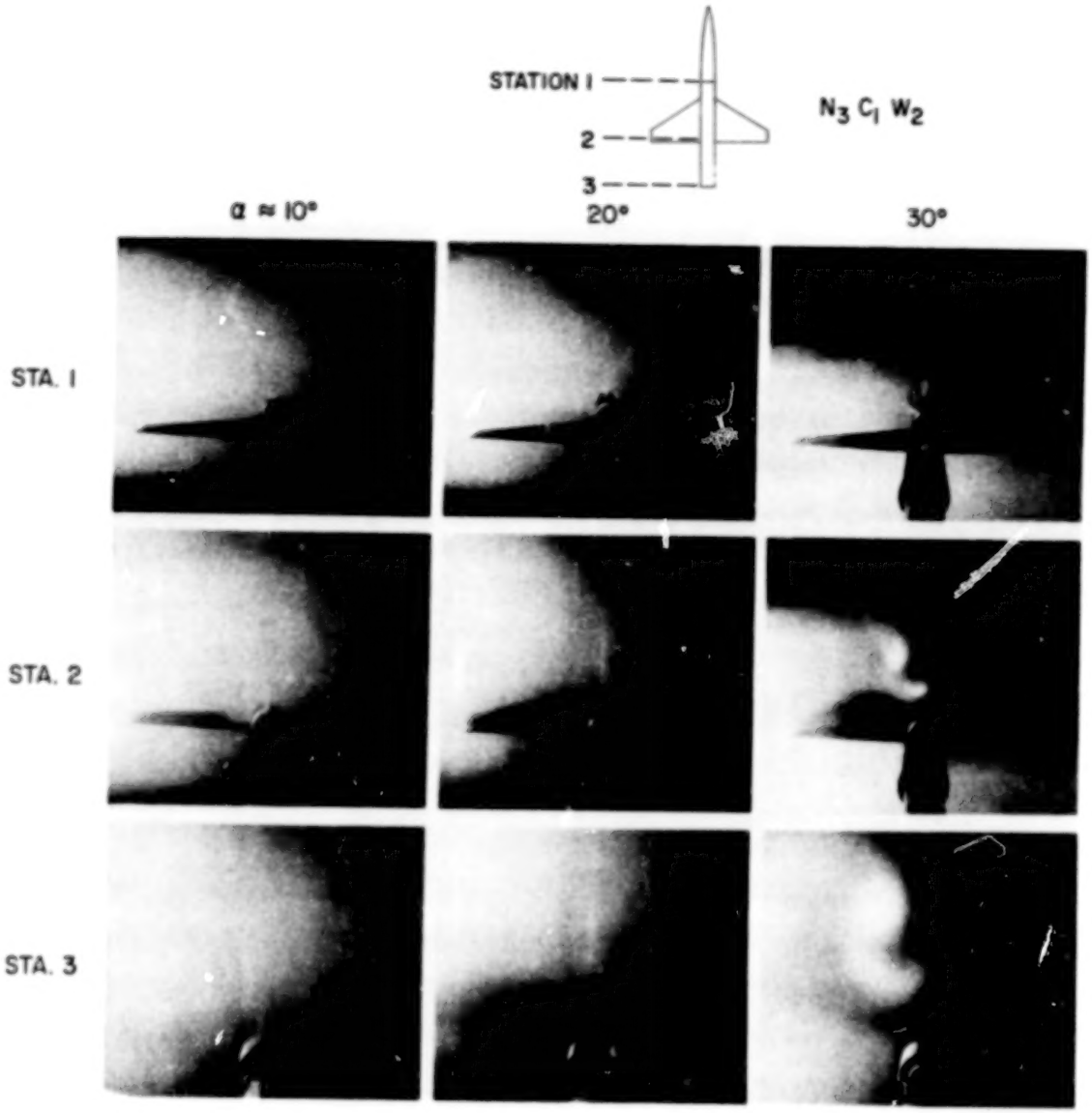

(b) $M_\infty = 0.9$.

Figure 53.– Continued.

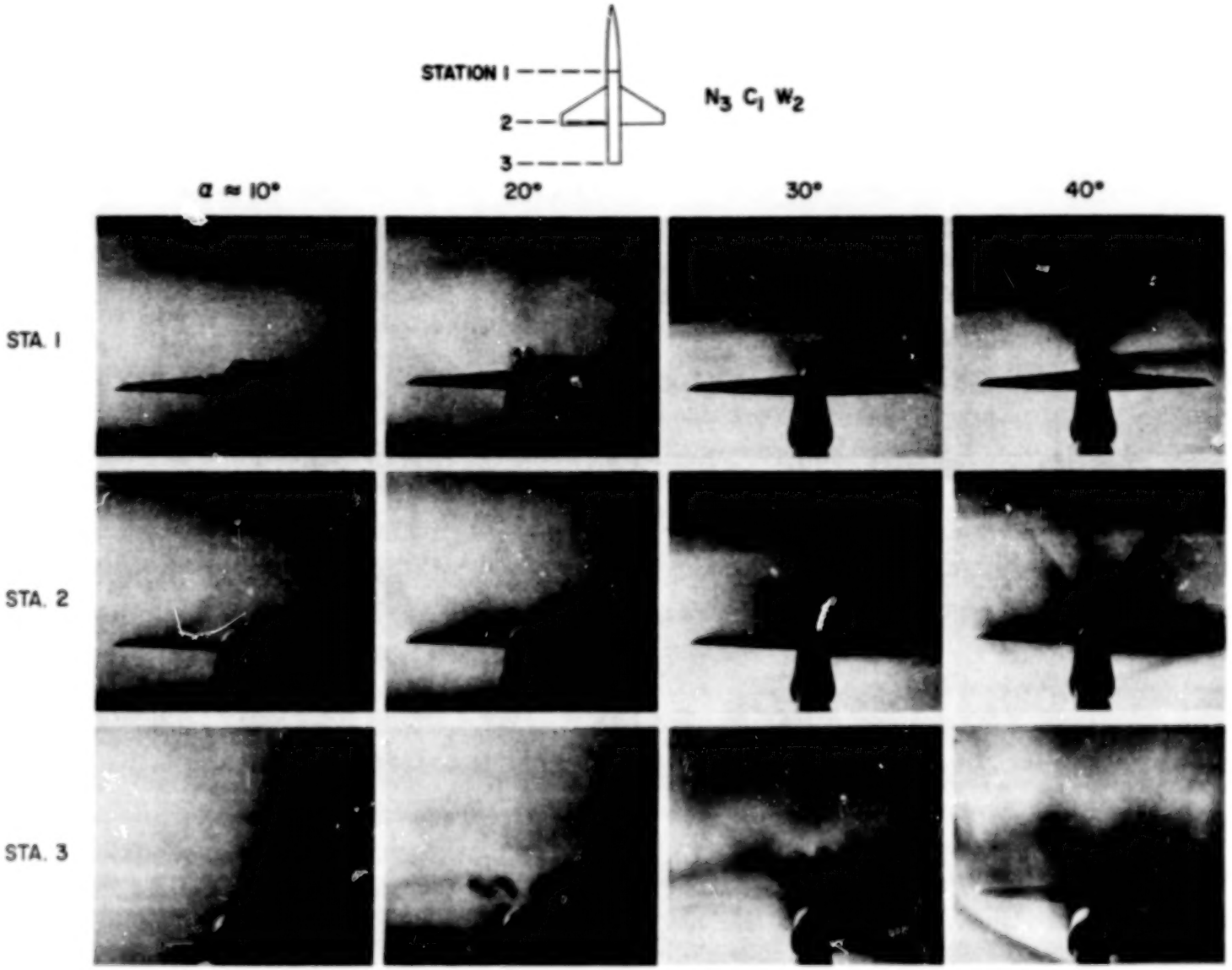

(c) $M_\infty = 2.0$.

Figure 53.– Concluded.

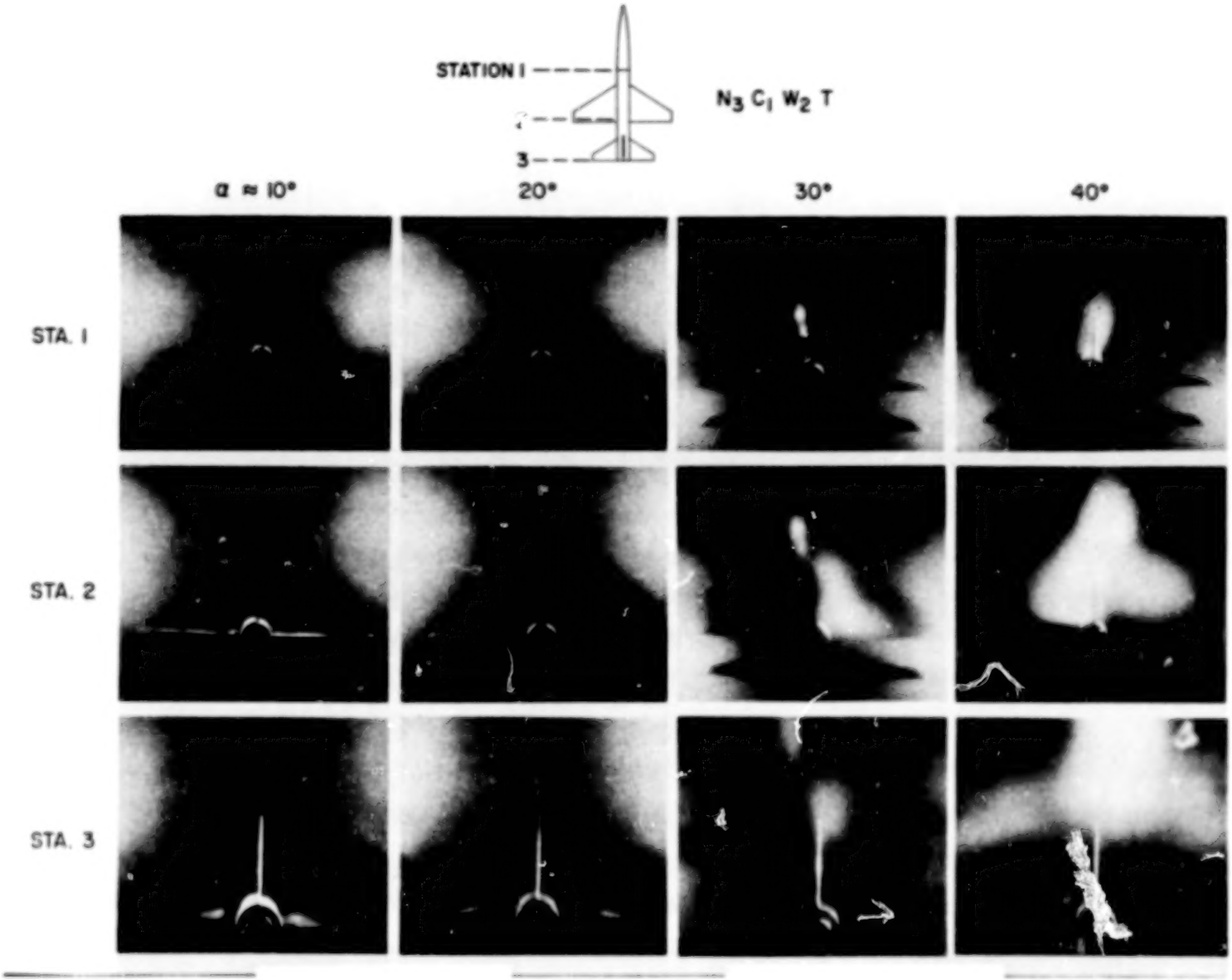

(a) $M_\infty = 0.6$.

Figure 54.– Vapor-screen photographs for $N_3 C_1 W_2 T$ (body with fineness-ratio-5 nose, aspect-ratio-4 wing, and tail)

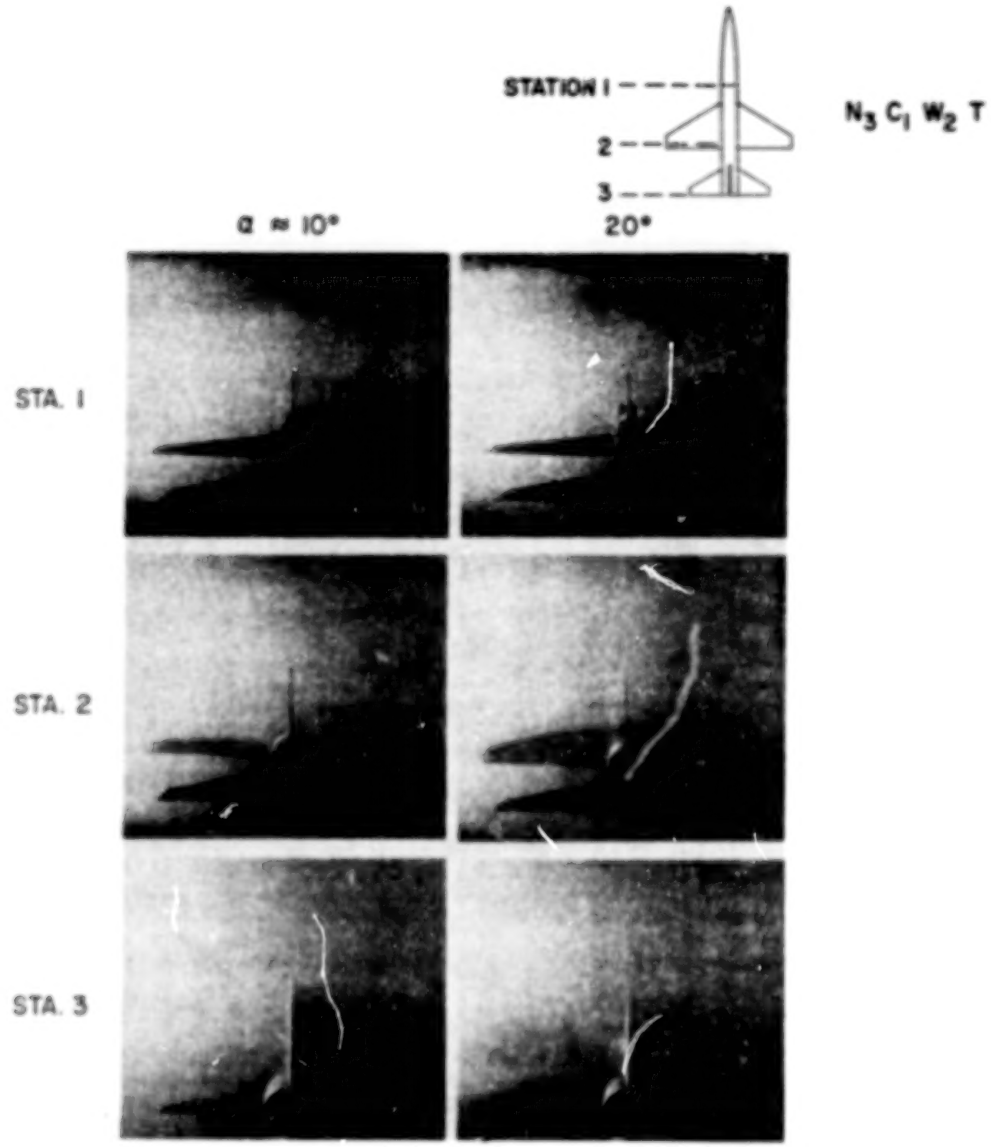

(b) $M_{\infty} = 0.9$.

Figure 54.– Continued.

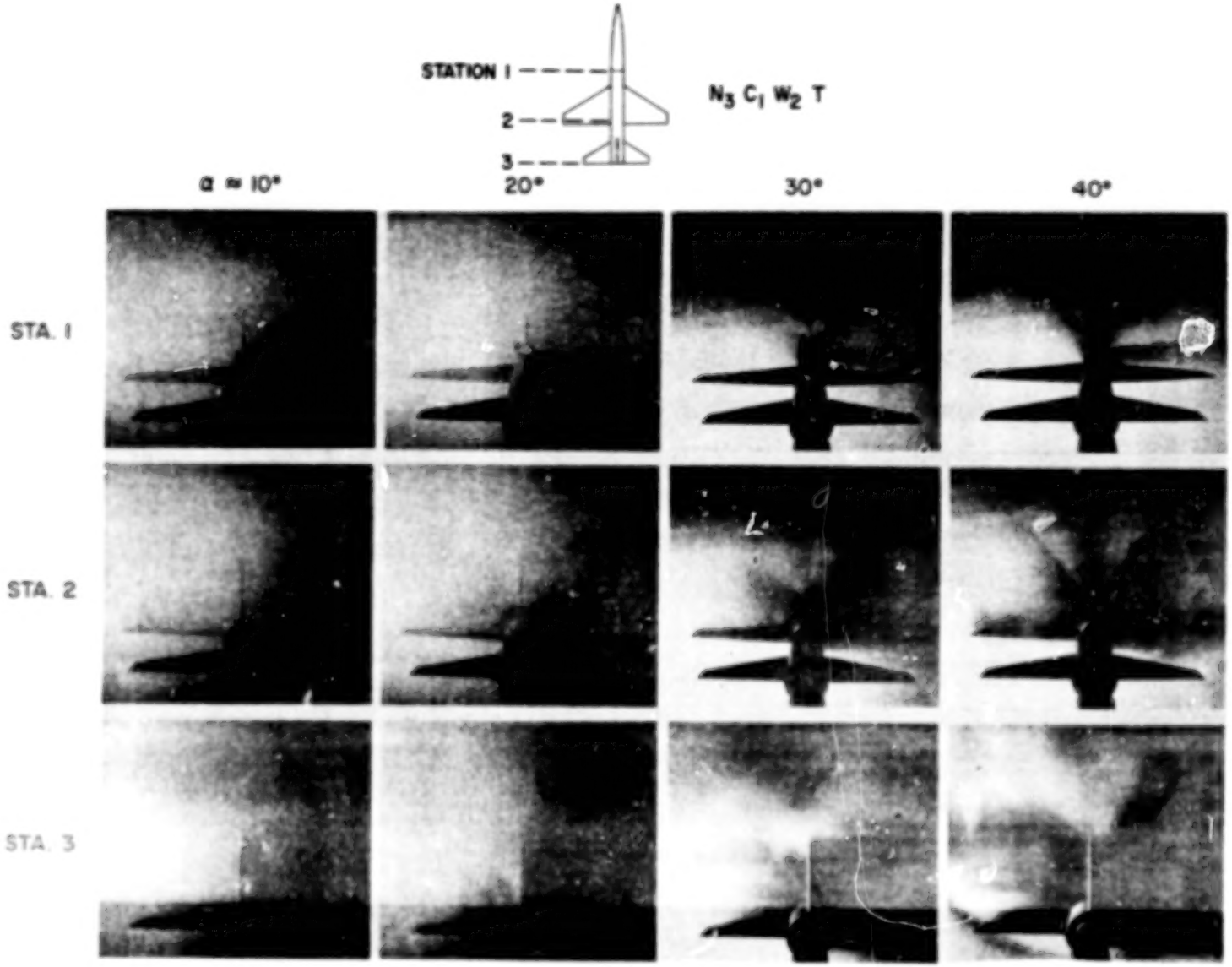

(c) $M_\infty = 2.0$.

Figure 54.– Concluded.

TABLE OF CONTENTS

	Page	
NOTATION	vi	1/A4
SUMMARY	1	1/A10
CHAPTER 1. INTRODUCTION	2	1/A11
CHAPTER 2. DERIVATION OF BASIC METHOD FOR COMPUTING C_N AND C_m CHARACTERISTICS	6	1/B1
2.1 Bodies of Revolution	6	1/B1
2.2 Bodies of Circular and Noncircular Cross Section Alone and With Lifting Surfaces	11	1/B6
2.3 Empirical Input Values	14	1/B9
2.3.1 Crossflow drag coefficient	14	1/B9
2.3.2 Crossflow drag proportionality factor	17	1/B12
2.4 Formulas and Values of $(C_n/C_{n_o})_{SB}$ and $(C_n/C_{n_o})_{Newt}$ for Various Cross Sections	18	1/B13
2.4.1 Formulas of $(C_n/C_{n_o})_{SB}$	18	1/B13
2.4.2 Formulas of $(C_n/C_{n_o})_{Newt}$	19	1/B14
2.4.3 Values of $(C_n/C_{n_o})_{SB}$ and $(C_n/C_{n_o})_{Newt}$	20	1/C1
2.5 Relative Influence of Crossflow Terms	21	1/C2
CHAPTER 3. METHOD APPLIED TO BODIES OF REVOLUTION	23	1/C4
3.1 Cone-Cylinder and Ogive-Cylinder Bodies at $M_\infty = 2.9$	23	1/C4
3.2 Ogive-Cylinder Bodies at $M_\infty = 0.6$ to 2.0	24	1/C5
3.3 Predicted Effect of Change in Crossflow Reynolds Number from Subcritical to Supercritical	26	1/C7
CHAPTER 4. METHOD APPLIED TO BODIES OF ELLIPTIC CROSS SECTION	28	1/C9
4.1 Bodies Studied and Tests at $M_\infty = 0.6$ to 2.0	28	1/C9
4.2 Equations Used to Compute C_N and C_m for Each Body	29	1/C9
4.2.1 Equations for bodies with constant a/b cross sections (bodies B_1 and B_2)	31	1/C12
4.2.2 Equations for body with variable a/b cross sections (body B_3)	31	1/C12

	Page	
4.3 Comparison of Computed With Measured Normal-Force and Normal-Force-Center Characteristics	33	1/C14
4.3.1 Bodies with constant a/b cross sections (bodies B_1 and B_2)	33	1/C14
4.3.2 Body with variable a/b cross sections (body B_3)	33	1/C14
CHAPTER 5. METHOD APPLIED TO BODY-WING AND BODY-WING-TAIL CONFIGURATIONS	35	1/D2
5.1 Configurations Studied and Tests at M_∞ = 0.6 to 2.0	35	1/D2
5.2 Methodology Used to Compute C_N and C_m	36	1/D3
5.3 Comparison of Computed with Measured Normal-Force and Normal-Force-Center Characteristics	39	1/D6
5.3.1 Body-wing configurations	39	1/D6
5.3.2 Body-wing-tail configurations	41	1/D8
CHAPTER 6. VISUAL OBSERVATION OF FLOWS OVER MODELS	43	1/D10
6.1 Models Considered	44	1/D11
6.2 Vapor-Screen and Oil-Flow Techniques	45	1/D12
6.2.1 Vapor-screen technique	45	1/D12
6.2.2 Oil-flow technique	46	1/D13
6.3 Photographs Obtained from Vapor-Screen and Oil-Flow Techniques	47	1/D14
6.3.1 Photographs from vapor-screen technique	47	1/D14
6.3.2 Photographs from oil-flow technique	49	1/E2
CHAPTER 7. EXPERIMENTAL SIDE FORCES ON MODELS AT β = 0°	52	1/E5
7.1 Bodies Alone	52	1/E5
7.1.1 Effects of nose fineness ratio and Mach number	52	1/E5
7.1.2 Effect of nose-tip rounding	54	1 /E7
7.1.3 Effect of afterbody side strakes	54	1/E7
7.1.4 Effect of elliptic cross section	54	1/E7
7.2 Body-Wing and Body-Wing-Tail Configurations	55	1/E8
7.2.1 Effects of adding a wing and a wing plus tail to a body	55	1/E8
7.2.2 Effects of wing aspect ratio and taper ratio	55	1/E8
CHAPTER 8. CONCLUDING REMARKS	56	1/E9

Page

APPENDIX A – DERIVATION OF $(C_n/C_{n_o})_{Newt}$ FOR WINGED-CIRCULAR AND WINGED-ELLIPTIC CROSS SECTIONS 59 1/E12

Winged-Circular Cross Section with Wing Planform Perpendicular to Crossflow Velocity 59 1/E12

Winged-Elliptic Cross Section with Semimajor Axis and Wing Planform Perpendicular to Crossflow Velocity 60 1/E13

Winged-Elliptic Cross Section with Semiminor Axis and Wing Planform Perpendicular to Crossflow Velocity 62 1/F1

APPENDIX B – DERIVATION OF $(C_n/C_{n_o})_{Newt}$ FOR WINGED-SQUARE CROSS SECTIONS WITH ROUNDED CORNERS 64 1/F3

APPENDIX C – FORMULAS TO COMPUTE GEOMETRIC PARAMETERS FOR TANGENT OGIVES. 67 1/F6

REFERENCES 68 1/F7

FIGURES 75 1/F14

NOTATION

A	body cross-sectional area
A_b	body base area (at $x = \ell$)
A_p	planform area
A_r	reference area (taken as A_b for the comparisons of computed with experimental results)
A_s	surface wetted area
A_w	exposed wing planform area (2 panels)
a	speed of sound
a,b	semimajor and semiminor axes of elliptic cross section
C_A	axial-force coefficient, $\frac{F_a}{q_\infty A_r}$
C_{d_n}	crossflow drag coefficient of circular cylinder section, $\frac{F_n}{q_n(\Delta\ell_{cy})d_{cy}}$
C_D	drag coefficient, $\frac{\text{drag}}{q_\infty A_r}$
C_L	lift coefficient, $\frac{\text{lift}}{q_\infty A_r}$
C_m	pitching-moment coefficient about station at x_m from nose, $\frac{\text{pitching moment}}{q_\infty A_r X}$
C_N	normal-force coefficient, $\frac{F_n}{q_\infty A_r}$
C_n	local normal-force coefficient per unit length
C_p	pressure coefficient, $\frac{p - p_\infty}{q_\infty}$
C_Y	side-force coefficient, $\frac{F_y}{q_\infty A_r}$
d	body cross-section diameter
f	cross force per unit length along body length
f_p	potential cross force per unit length along body length
f_v	viscous cross force per unit length along body length

F_a, F_n, F_y	axial, normal, and side force
k	corner rounding for body cross section, $\frac{r}{w}$
K_1, K_2	longitudinal and transverse apparent mass coefficients
ℓ	body length
ℓ_A	body aftersection length
ℓ_N	body nose length
M_n	Mach number component normal to body axis, $M_\infty \sin \alpha$
M_∞	free-stream Mach number
p	pressure
p_∞	free-stream static pressure
q_n	dynamic pressure component normal to body axis, $q_\infty \sin^2 \alpha$
q_∞	free-stream dynamic pressure, $\frac{1}{2} \rho V_\infty^2$
r	body cross-section radius or corner radius
r_a	arc radius of ogive
S	displacement of crossflow
s	semispan
t	time
Re	free-stream Reynolds number, $\frac{\rho V_\infty X}{\mu}$
Re_n	Reynolds number component normal to body axis, $Re \frac{d}{X} \sin \alpha$
V	body volume
V_n	velocity component normal to body axis, $V_\infty \sin \alpha$
V_∞	free-stream velocity
w	body width

X	reference length (generally taken as d for the comparisons of computed with experimental results)
x	axial distance from body nose
x_{ac}	axial distance from body nose to aerodynamic normal-force center (center of pressure)
x_c	axial distance from body nose to centroid of body planform area
x_m	axial distance from body nose to pitching-moment reference center
x_{sf}	axial distance from body nose to aerodynamic side-force center
α	angle of attack
β	angle of sideslip
ϵ	wing planform semiapex angle
η	crossflow drag proportionality factor (ratio of crossflow drag for a finite-length cylinder to that for an infinite-length cylinder)
μ	viscosity coefficient of air
ρ	density of air
ϕ	angle of roll about body longitudinal axis

Subscripts

b	body base
cy	cylinder
$Newt$	Newtonian theory
$nose$	body nose
o	equivalent circular body or cross section
SB	slender-body theory
$stag$	stagnation

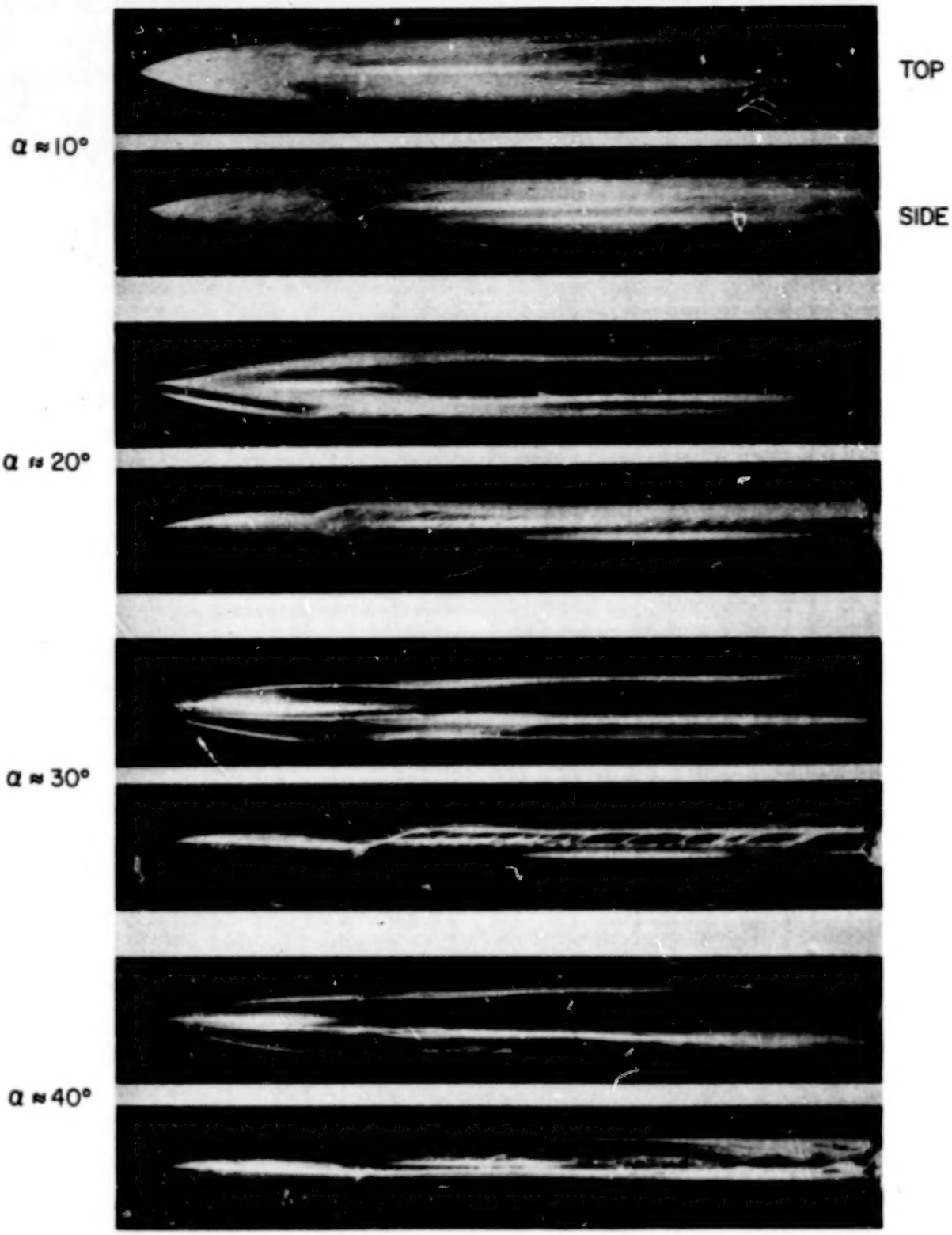

(a) $M_\infty = 0.6$.

Figure 55.– Oil-flow photographs for $B_1 = N_1 C_1$ (body with fineness-ratio-3 nose).

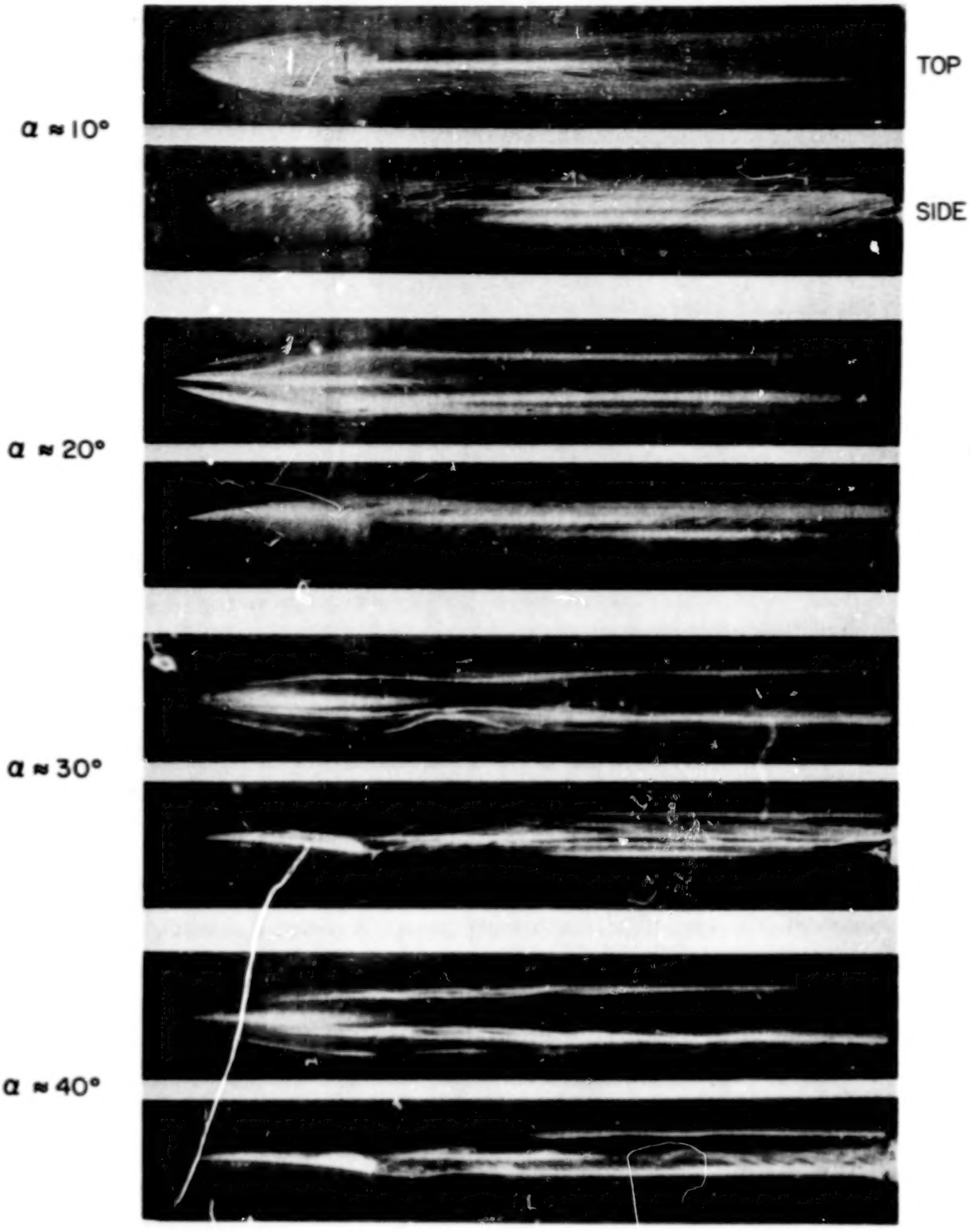

(b) $M_\infty = 0.9$.

Figure 55.– Continued.

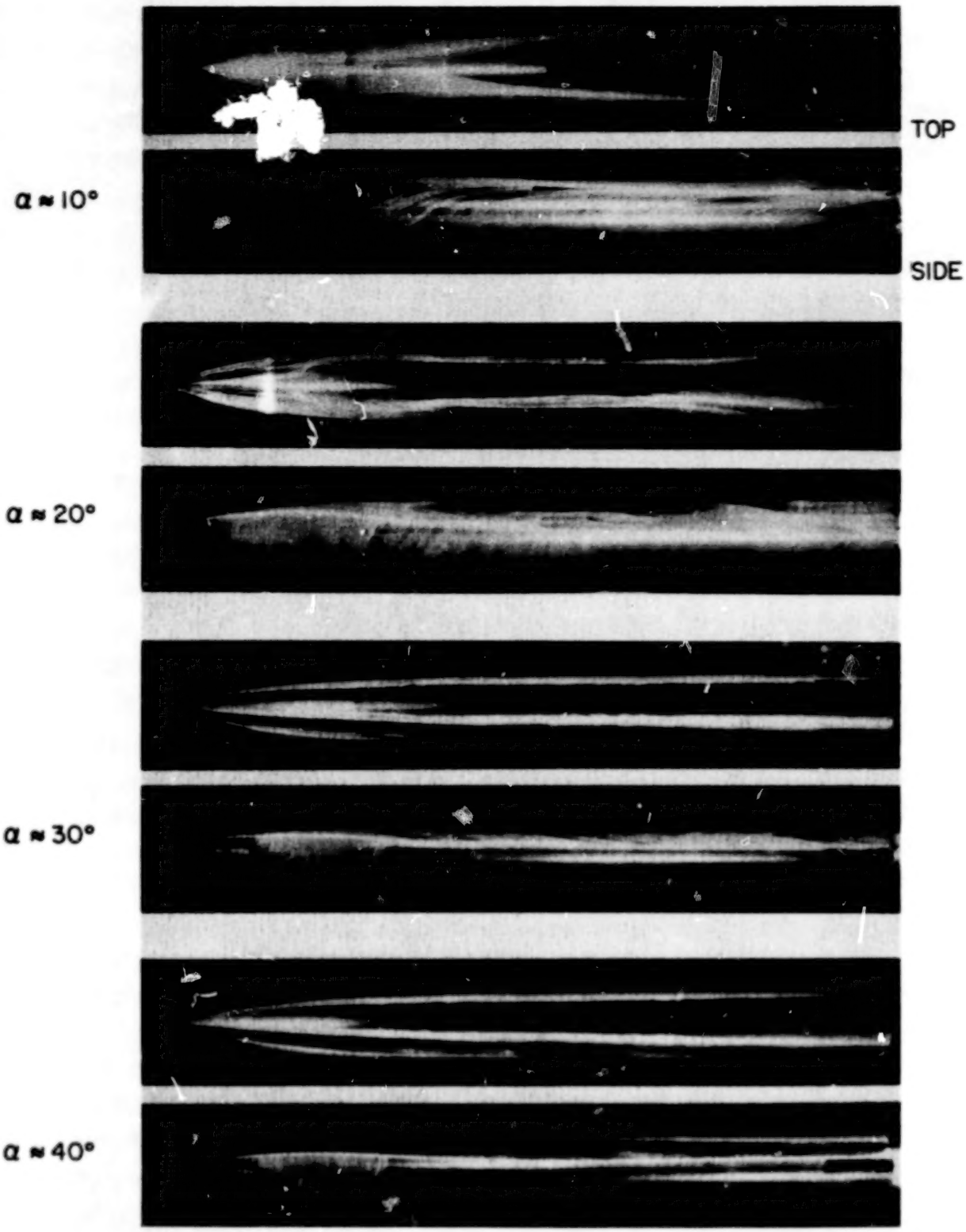

(c) $M_\infty = 2.0$.

Figure 55.– Concluded.

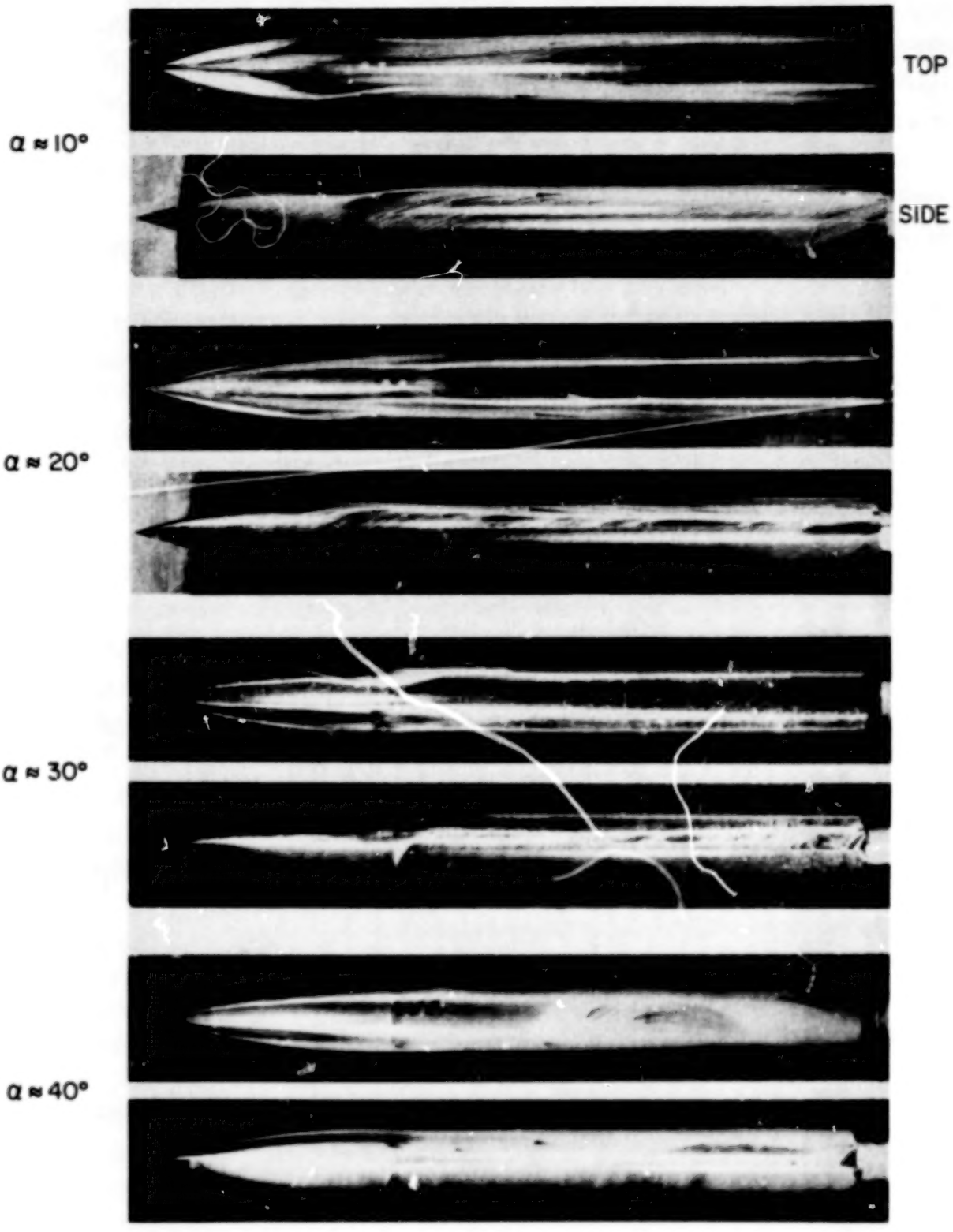

(a) $M_\infty = 0.6$.

Figure 56.– Oil-flow photographs for N_2C_1 (body with fineness-ratio-3.5 nose).

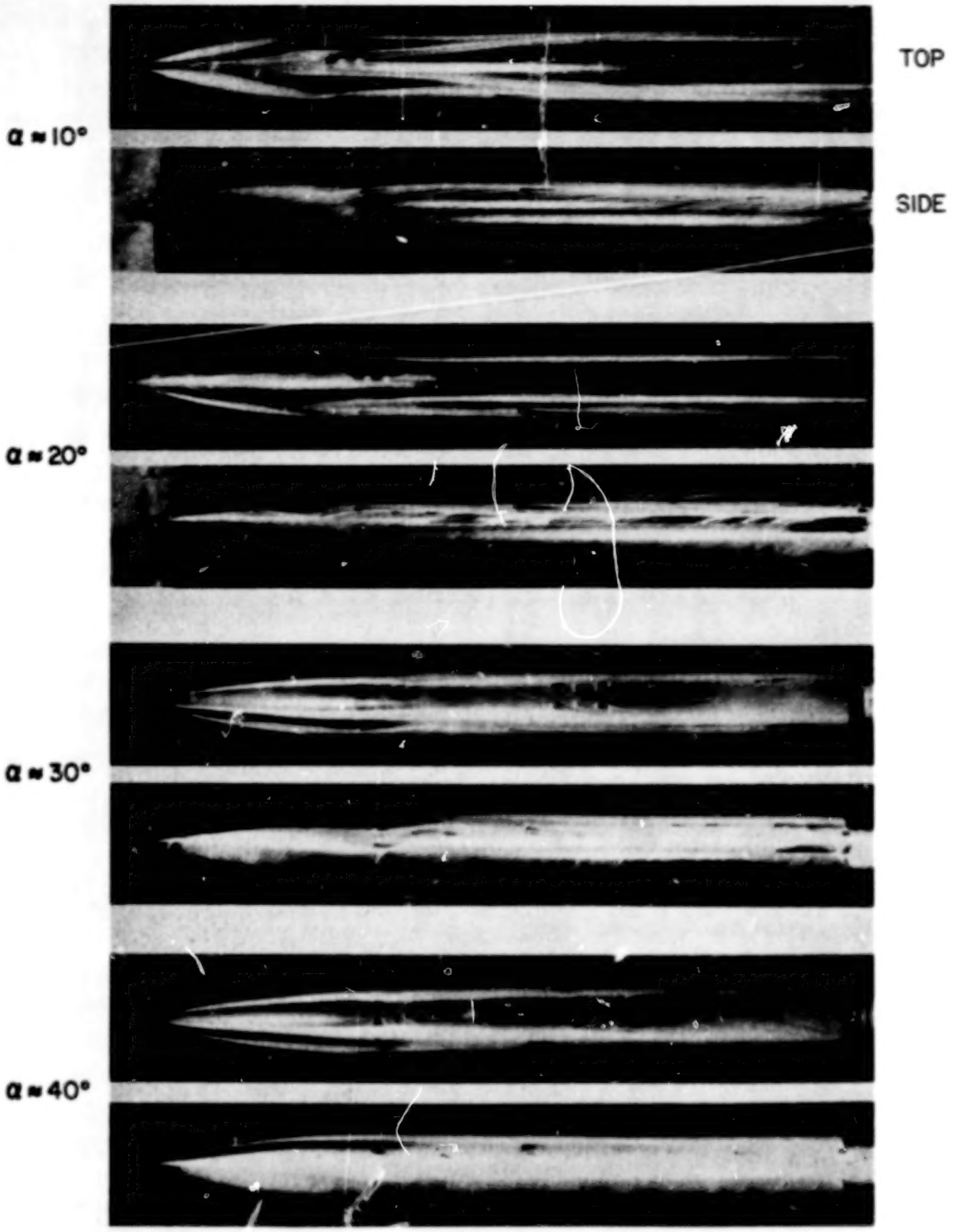

(b) $M_\infty = 0.9$.

Figure 56.– Continued.

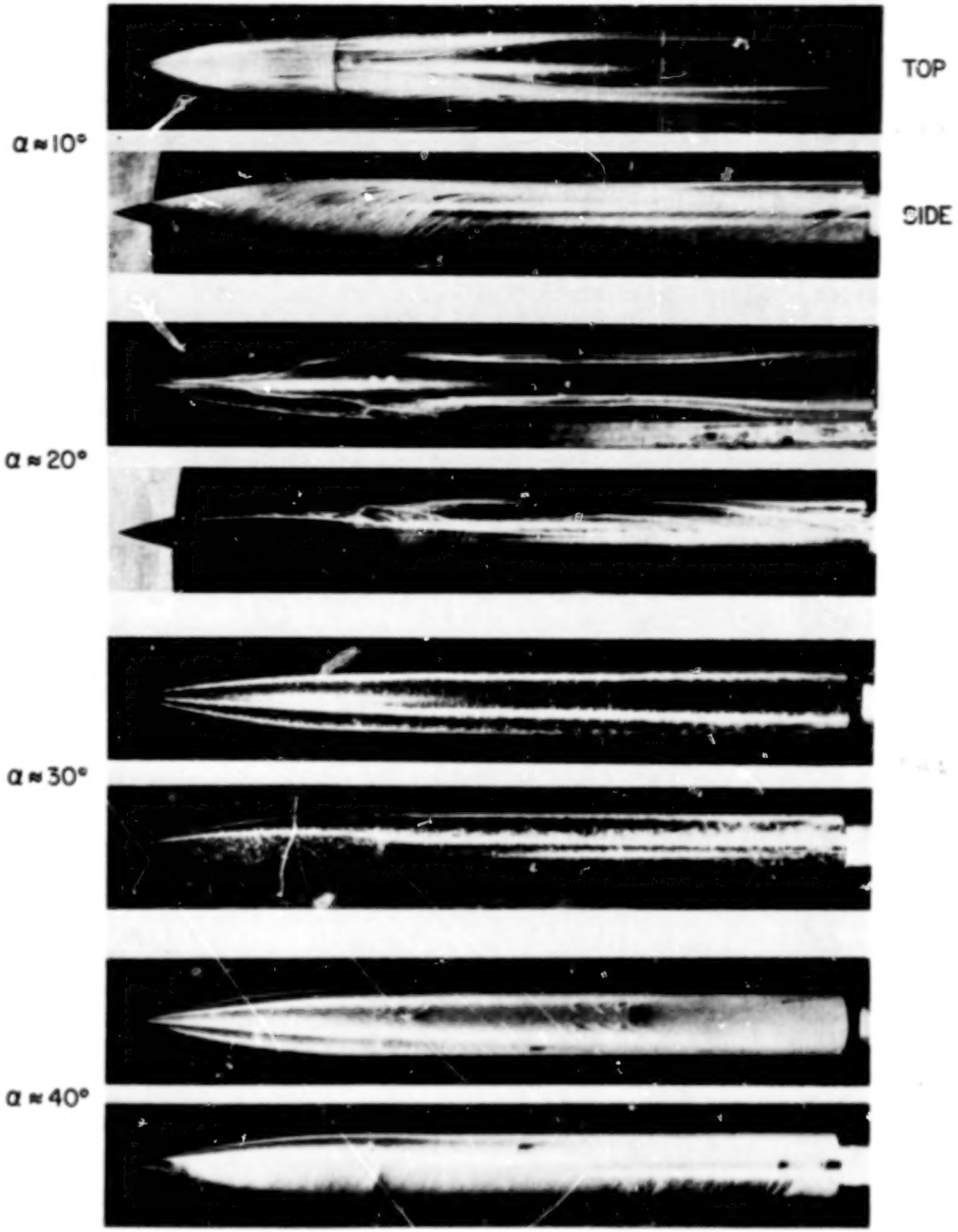

(c) $M_\infty = 2.0$.

Figure 56.– Concluded.

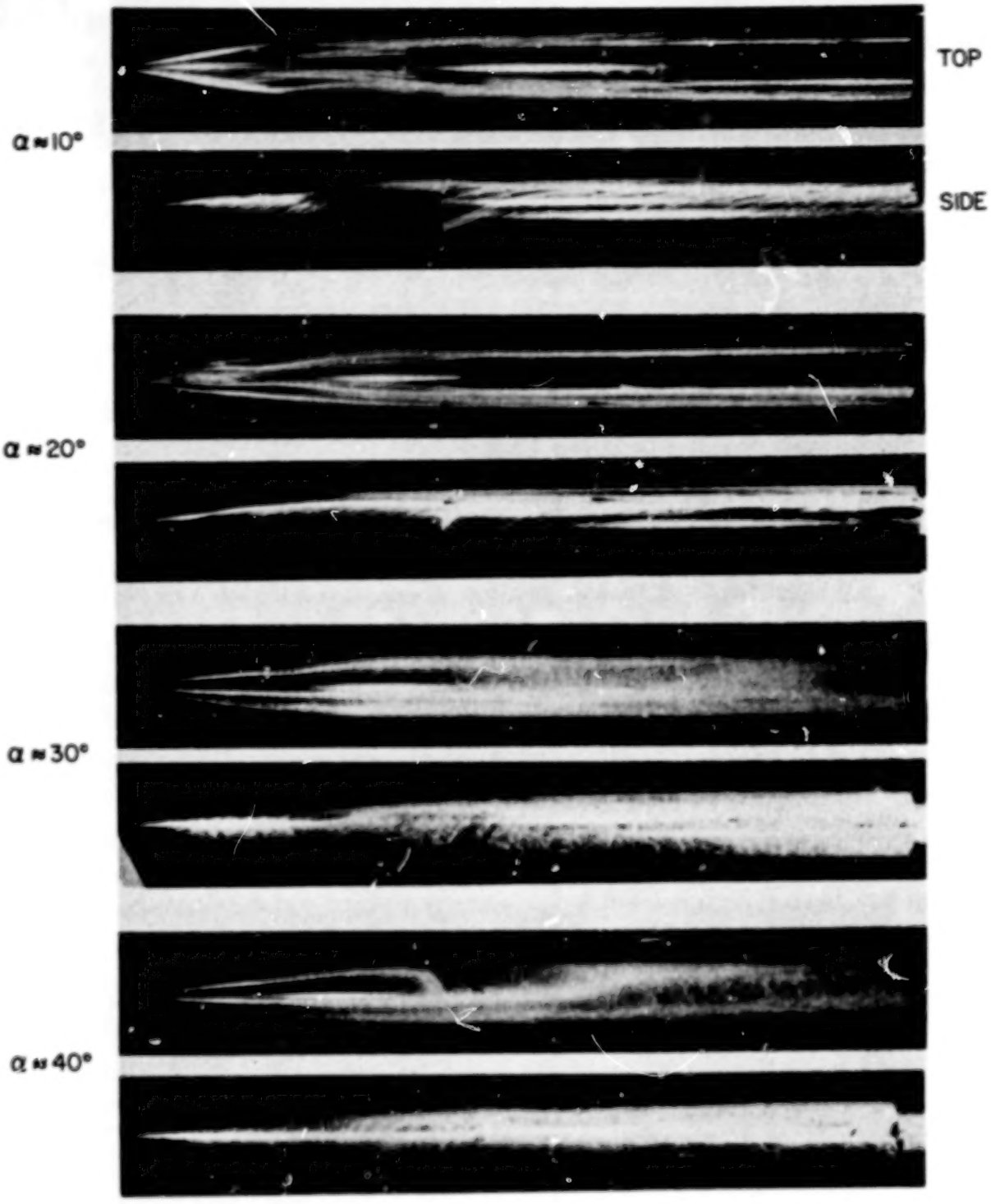

(a) $M_\infty = 0.6$.

Figure 57.– Oil-flow photographs for N_3C_1 (body with fineness-ratio-5 nose).

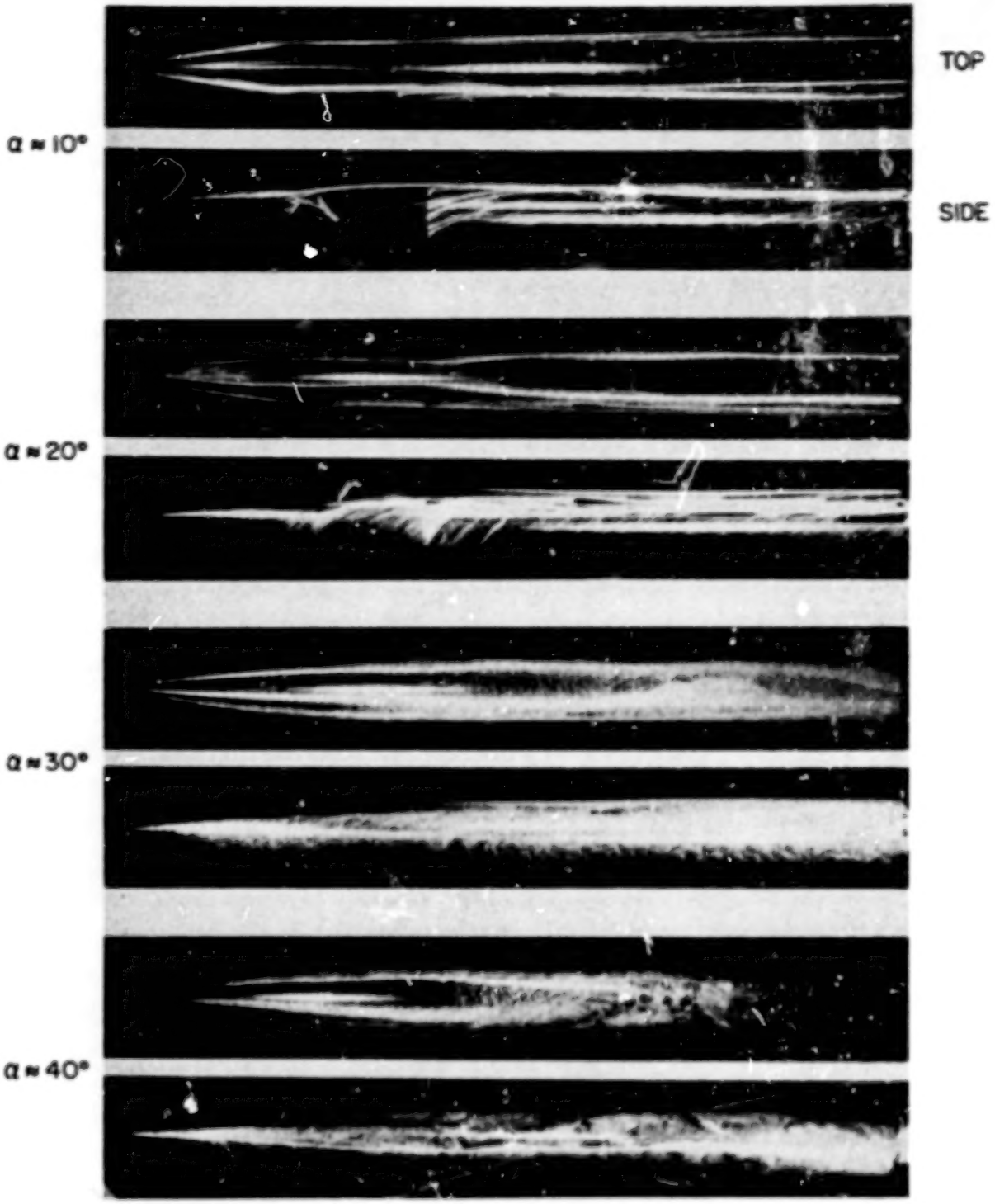

(b) $M_\infty = 0.9$.

Figure 57.– Continued.

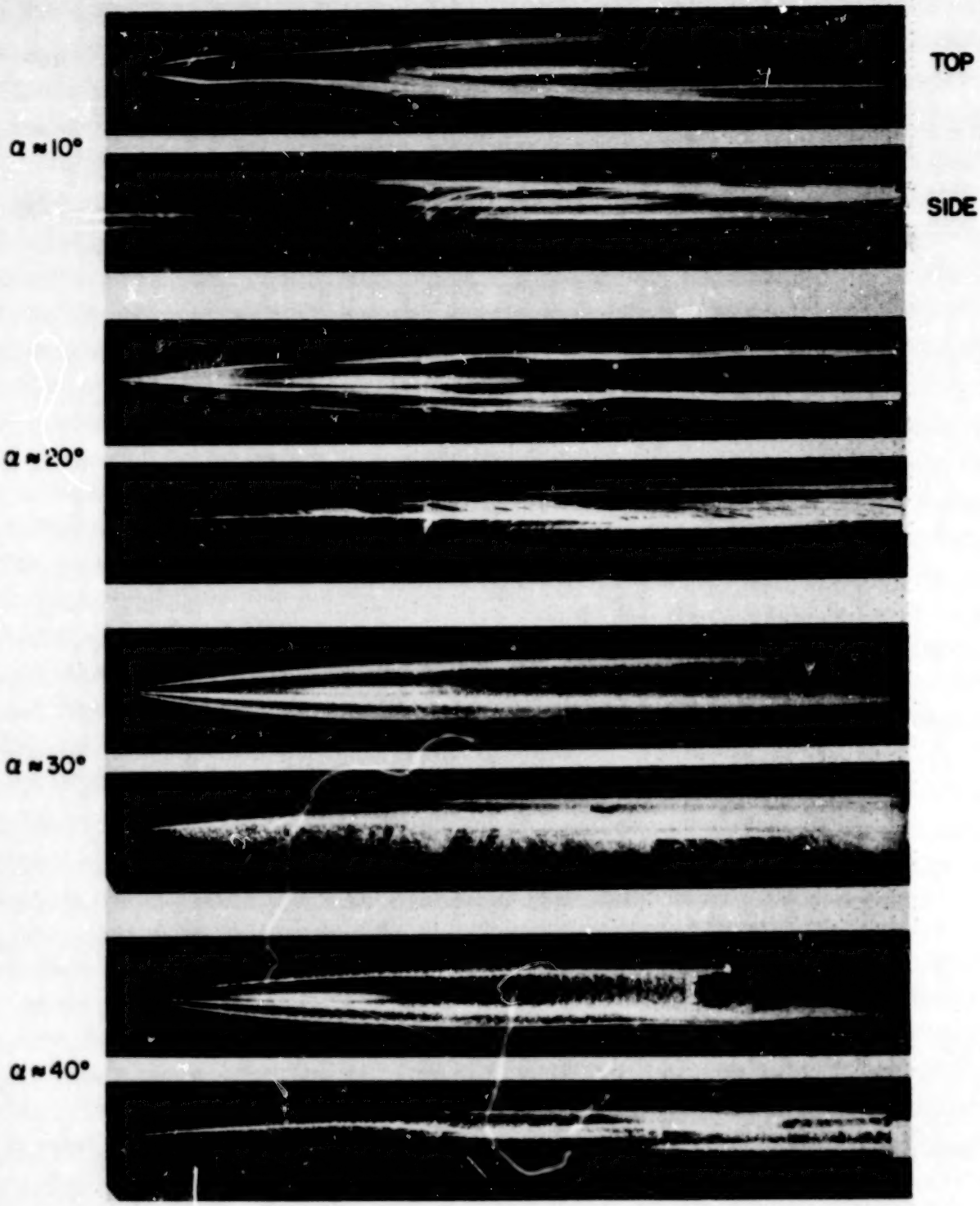

(c) $M_\infty = 2.0$.

Figure 57.– Concluded.

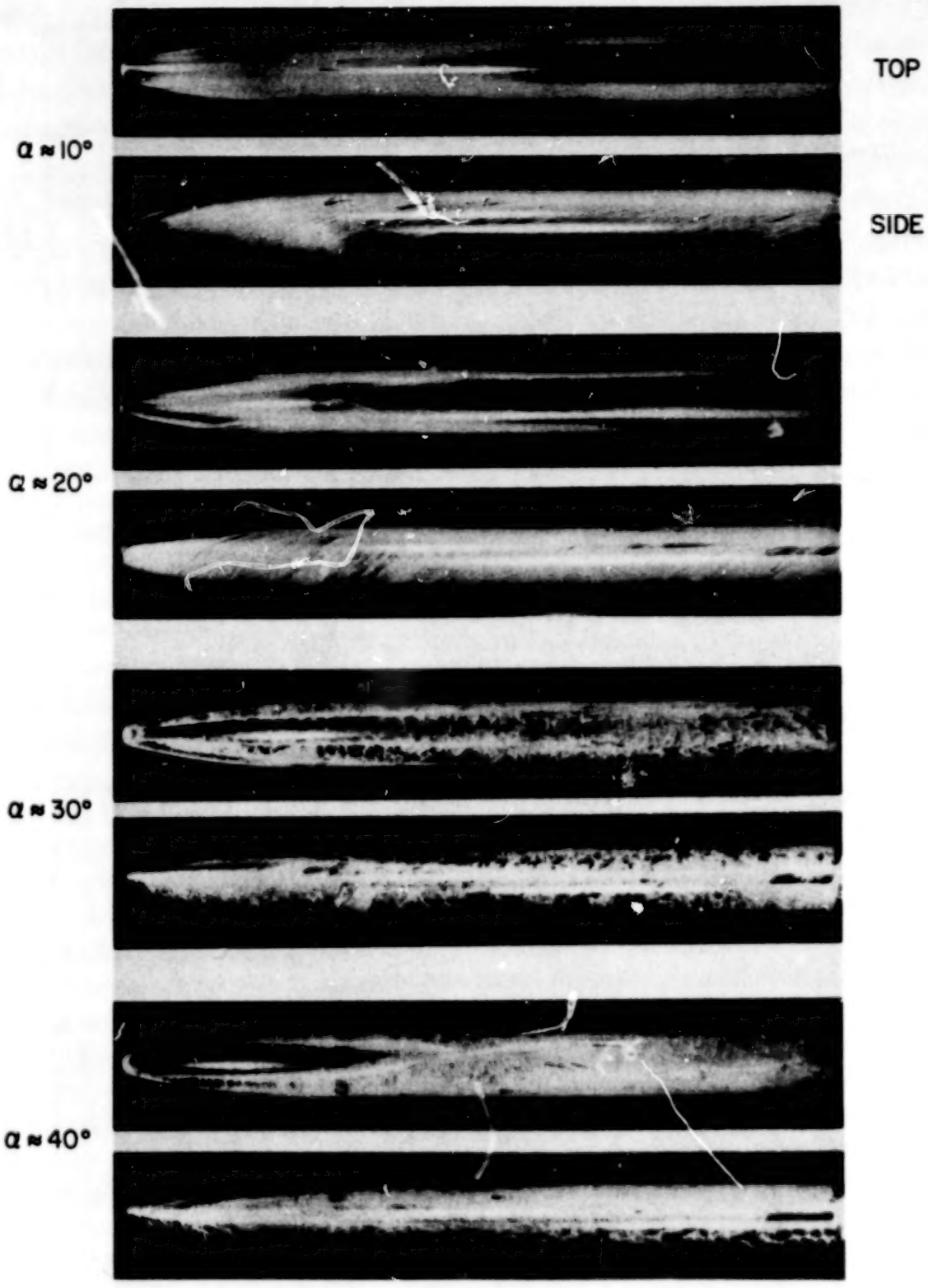

(a) $M_\infty = 0.6$.

Figure 58.– Oil-flow photographs for N_4C_1 (body with blunt nose of fineness ratio 3).

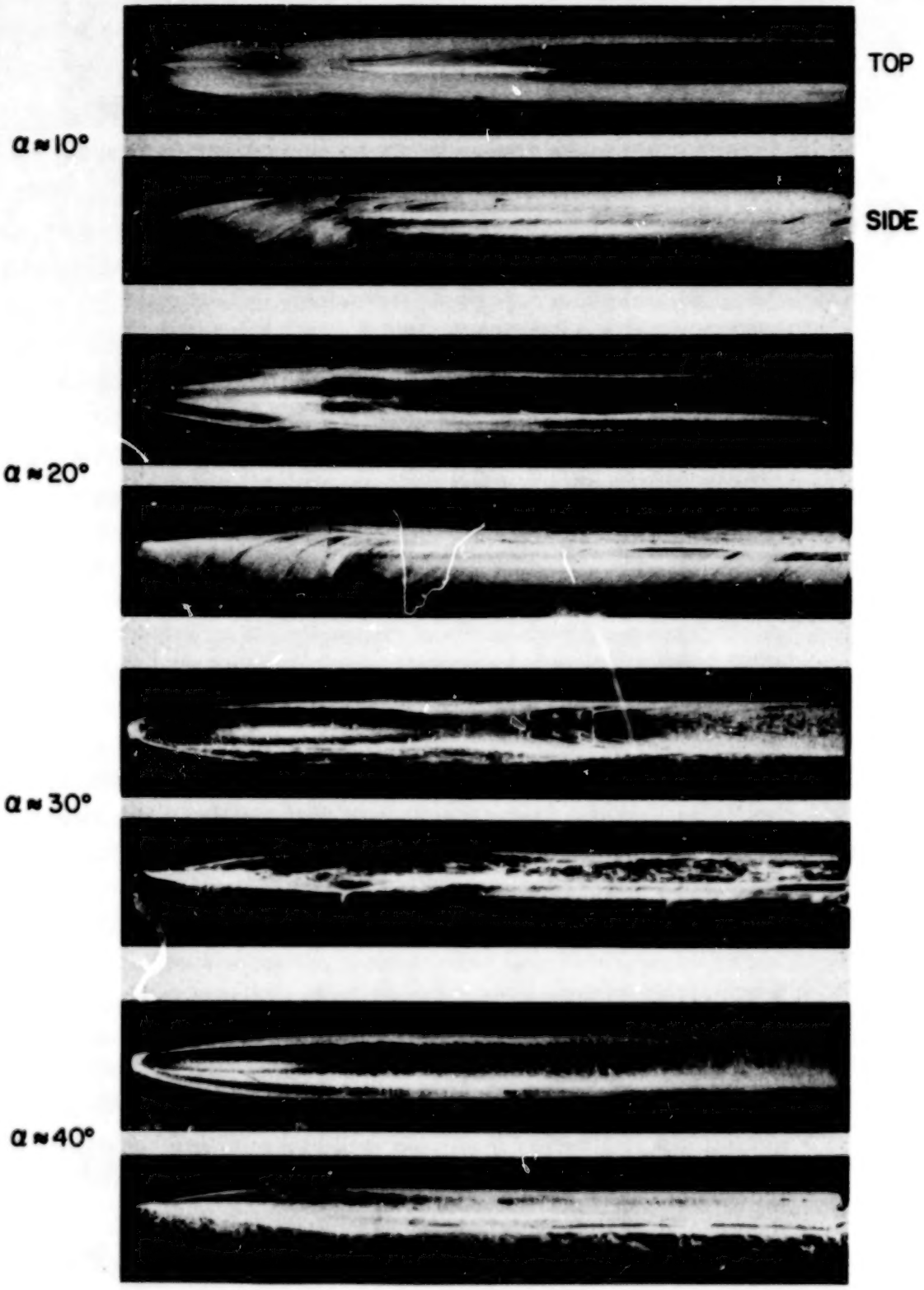

(b) $M_\infty = 0.9$.

Figure 58.– Continued.

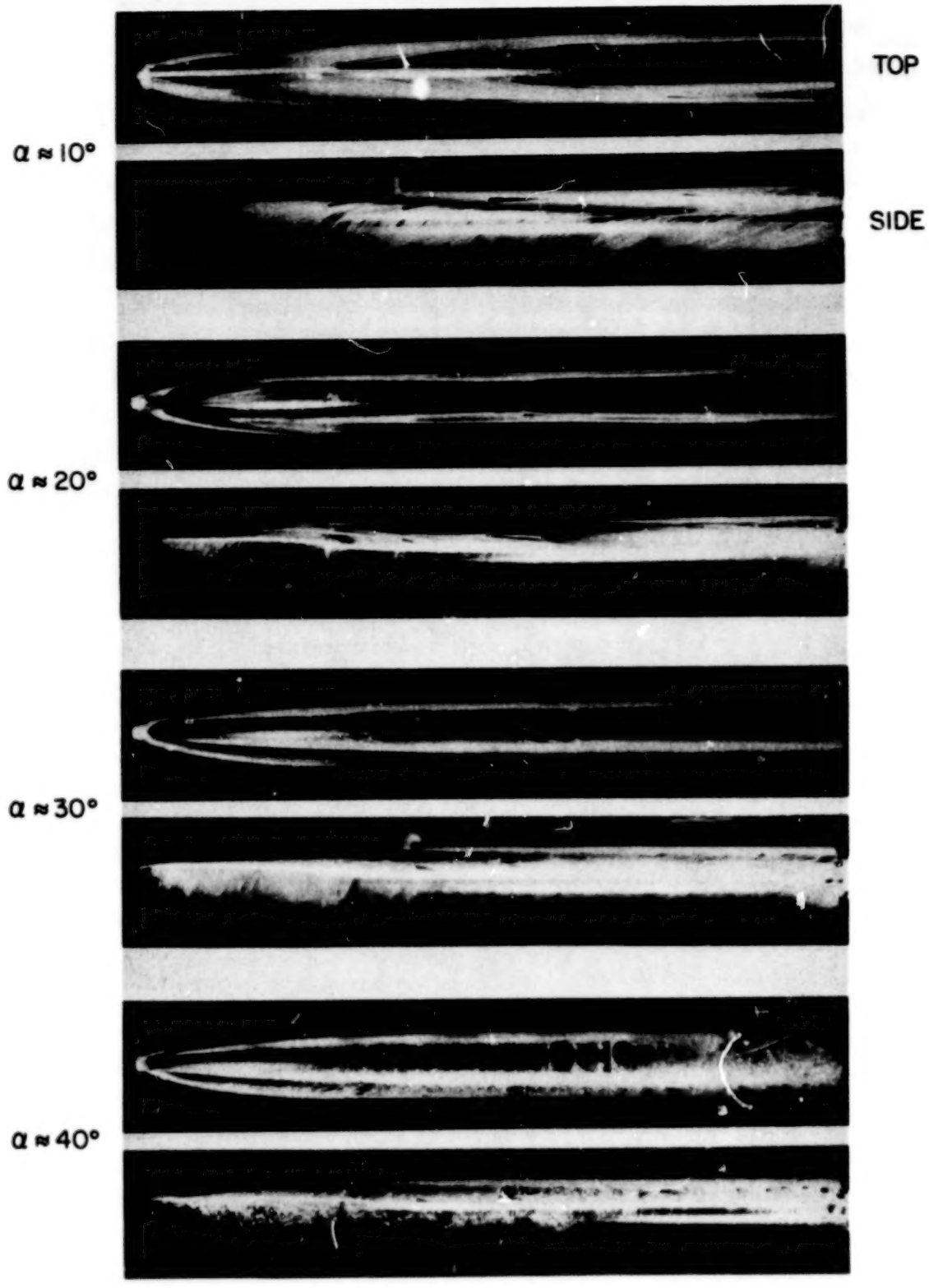

(c) $M_\infty = 2.0$.

Figure 58.– Concluded.

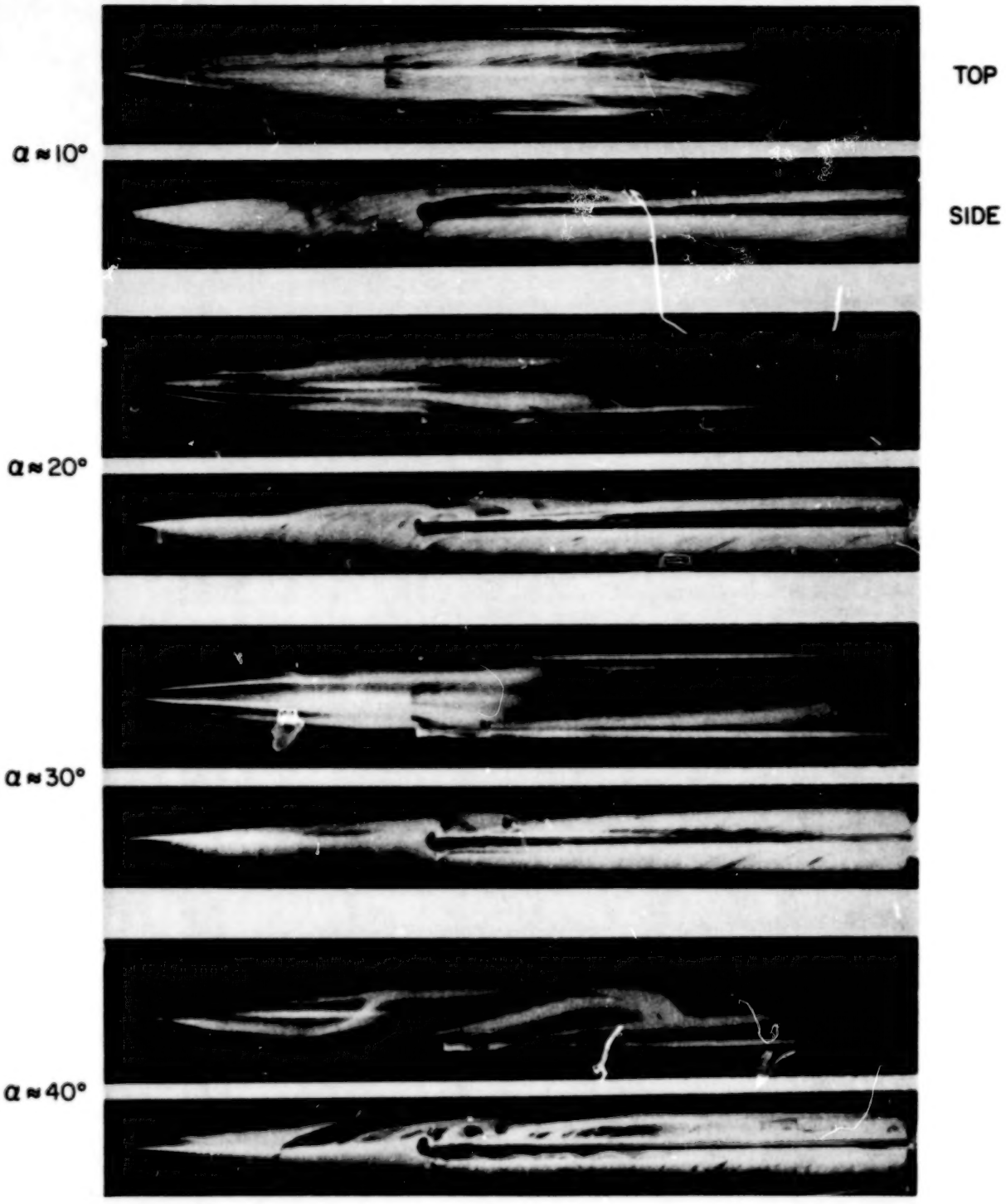

(a) $M_\infty = 0.6$.

Figure 59.– Oil-flow photographs for $N_3 C_1 S$ (body with fineness-ratio-5 nose and afterbody strake).

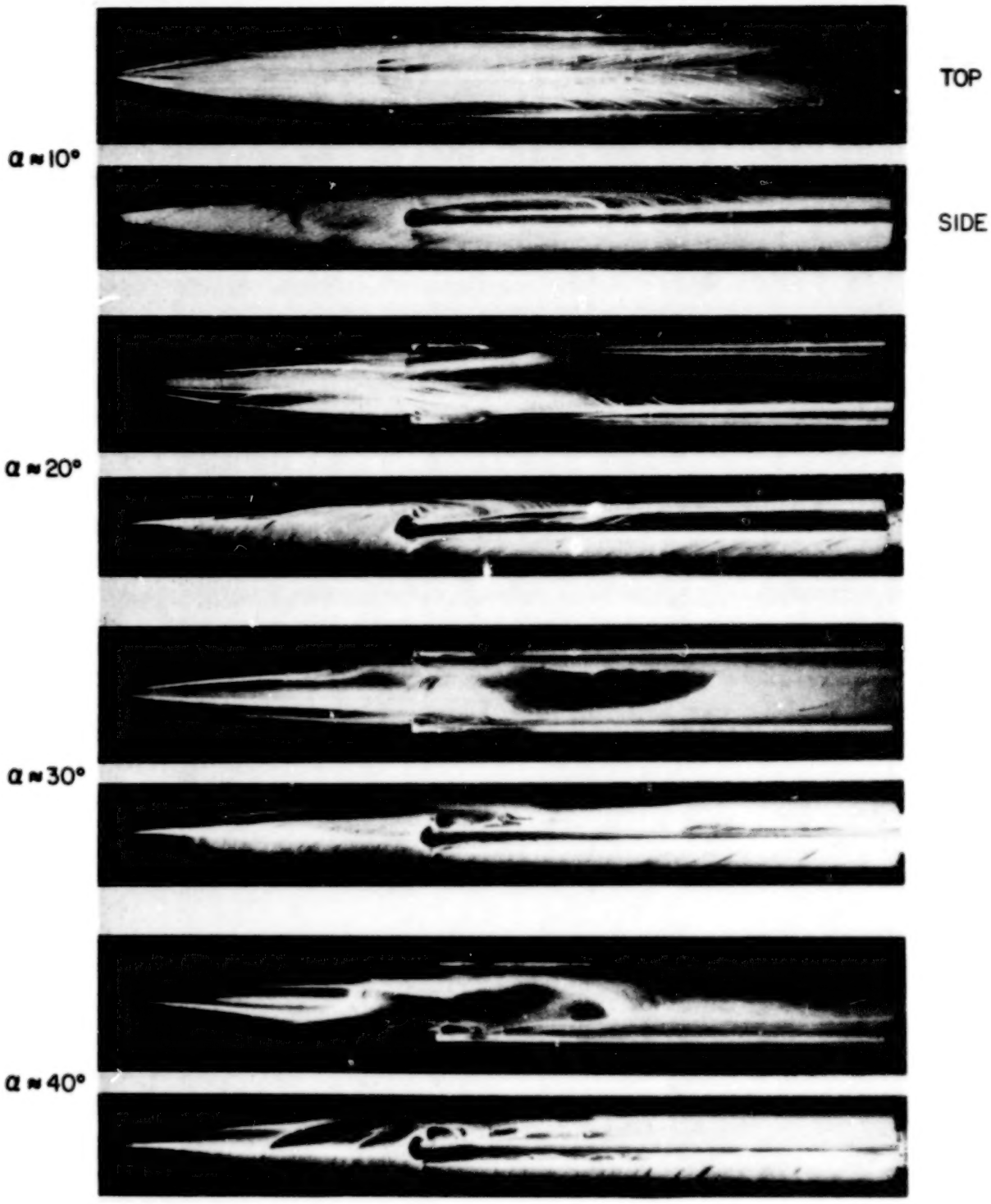

(b) $M_\infty = 0.9$.

Figure 59.– Continued.

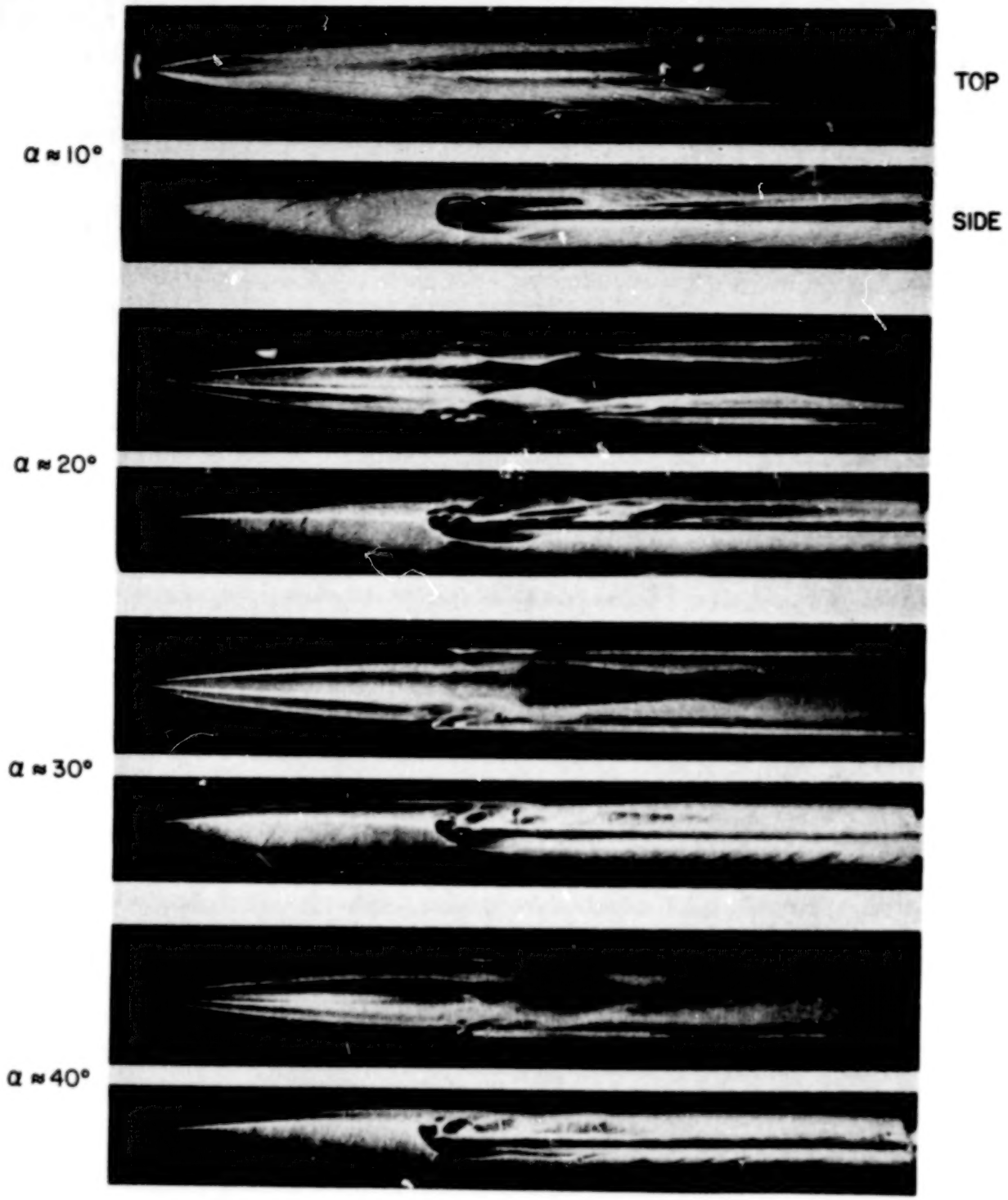

(c) $M_\infty \approx 2.0$.

Figure 59.– Concluded.

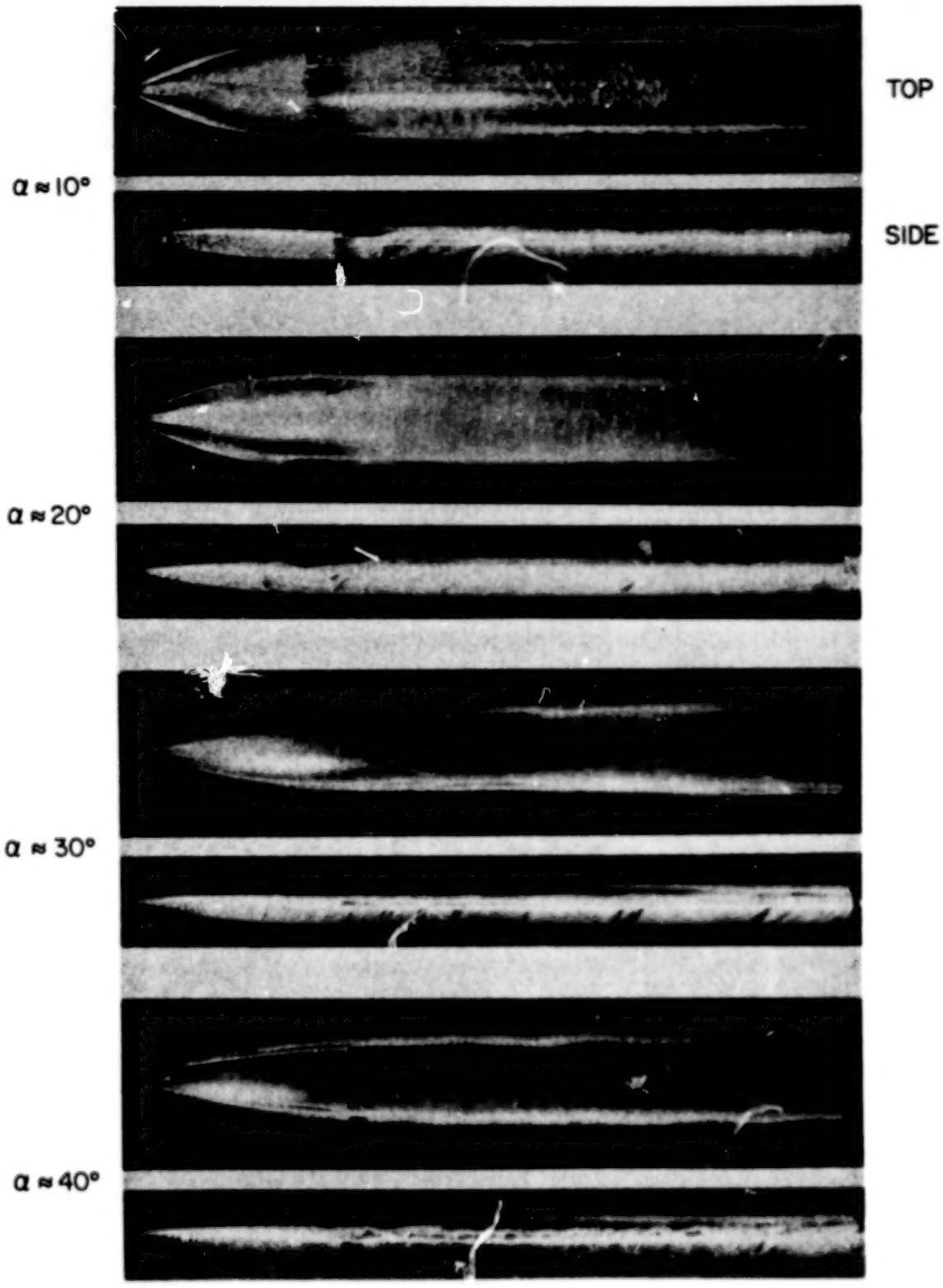

(a) $M_\infty = 0.6$.

Figure 60.– Oil-flow photographs for B_2 at $\phi = 0°$ (body with constant a/b cross sections).

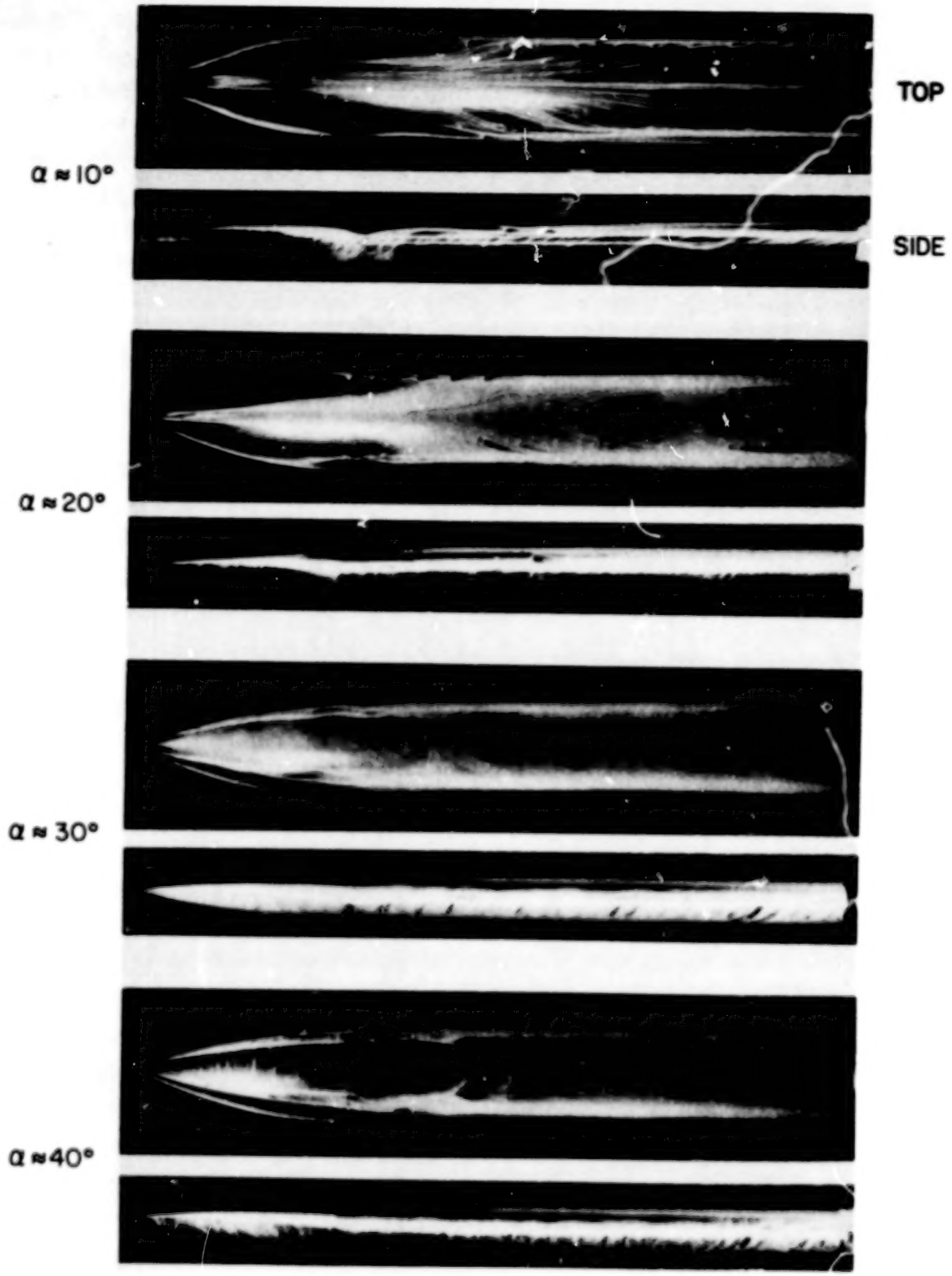

(b) $M_\infty = 0.9$.

Figure 60.– Continued.

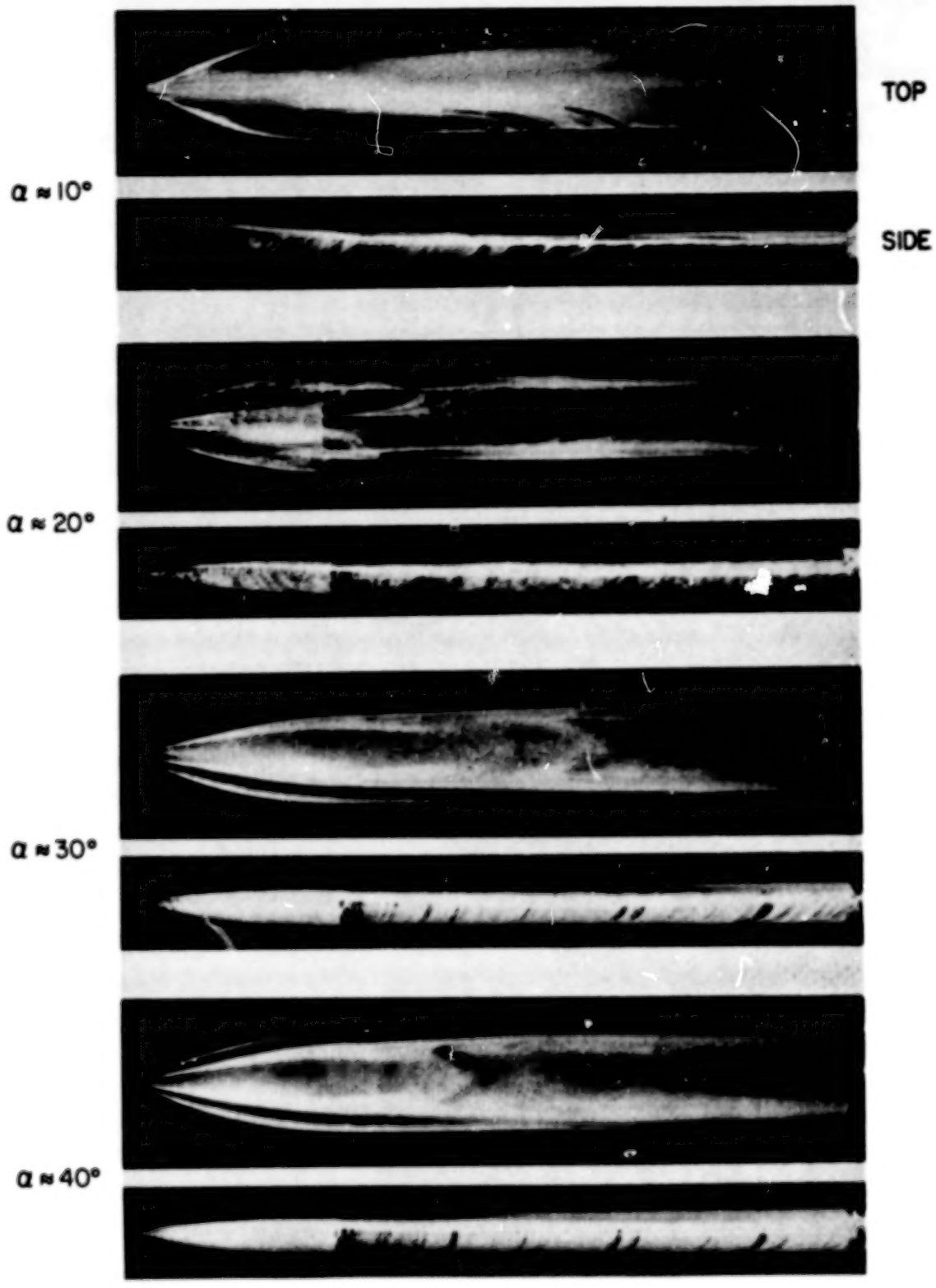

(c) $M_\infty = 2.0$.

Figure 60.– Concluded

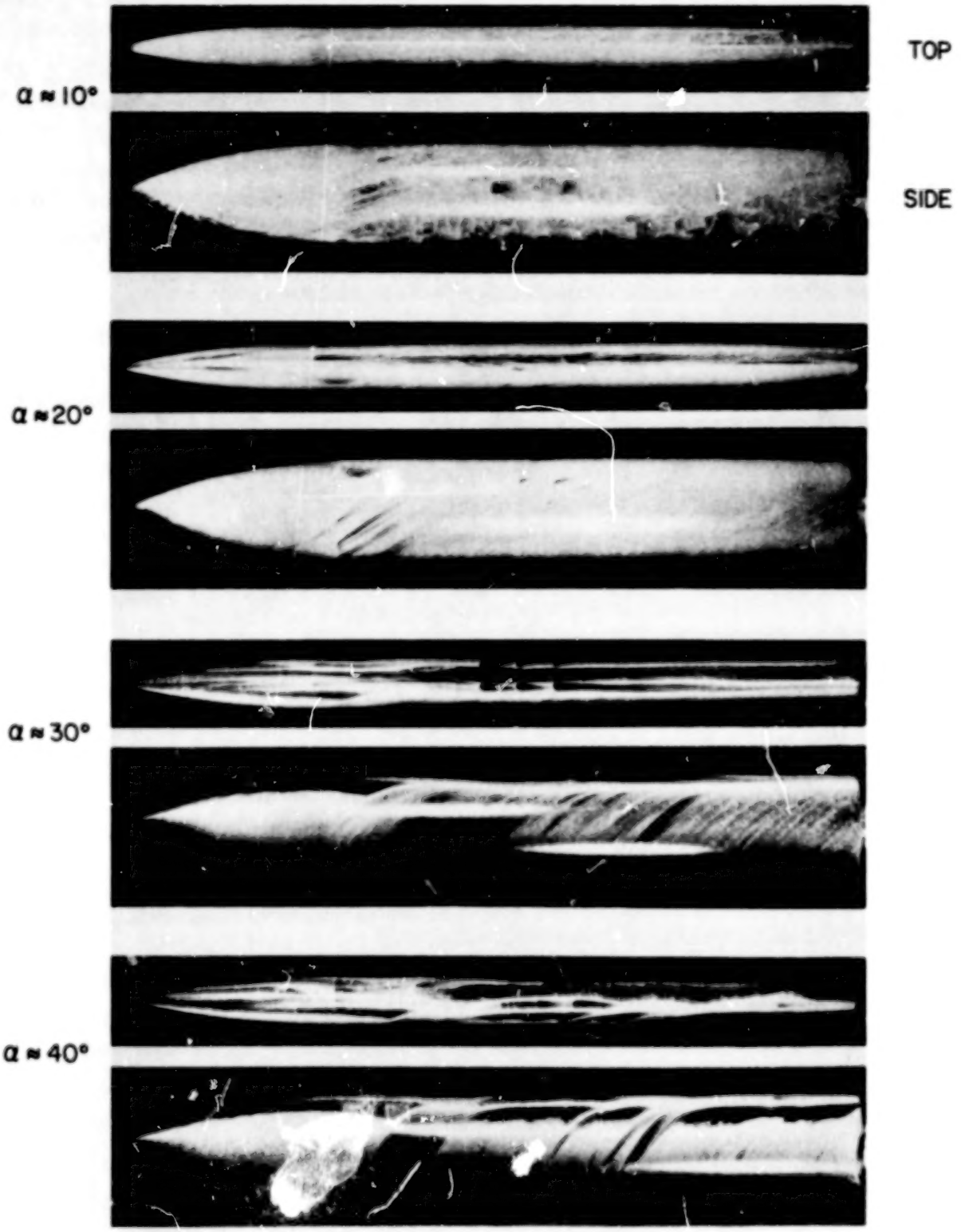

(a) $M_\infty = 0.6$.

Figure 61.– Oil-flow photographs for B_2 at $\phi = 90°$ (t[illegible]nstant a/b cross sections).

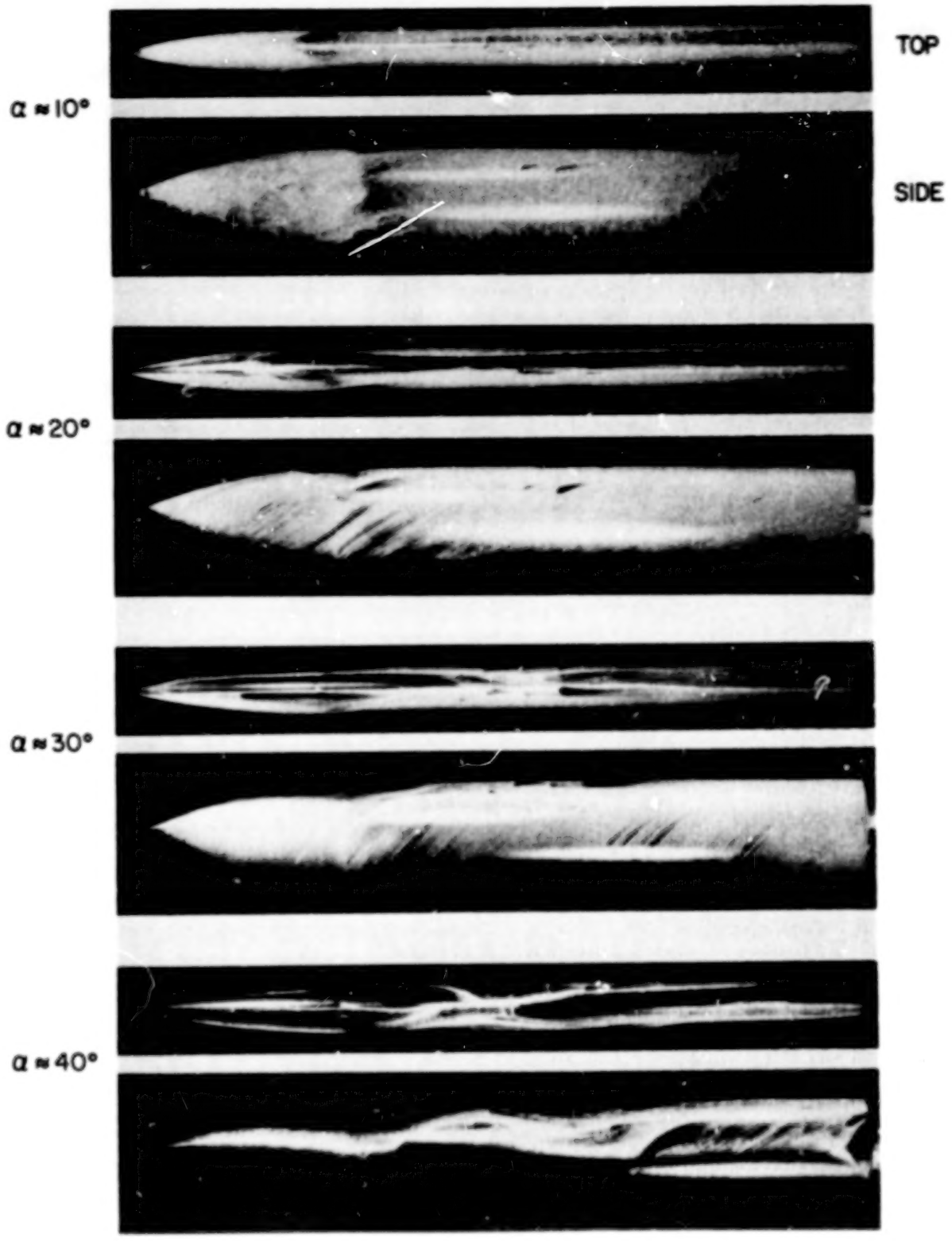

(b) $M_\infty = 0.9$.

Figure 61.– Continued.

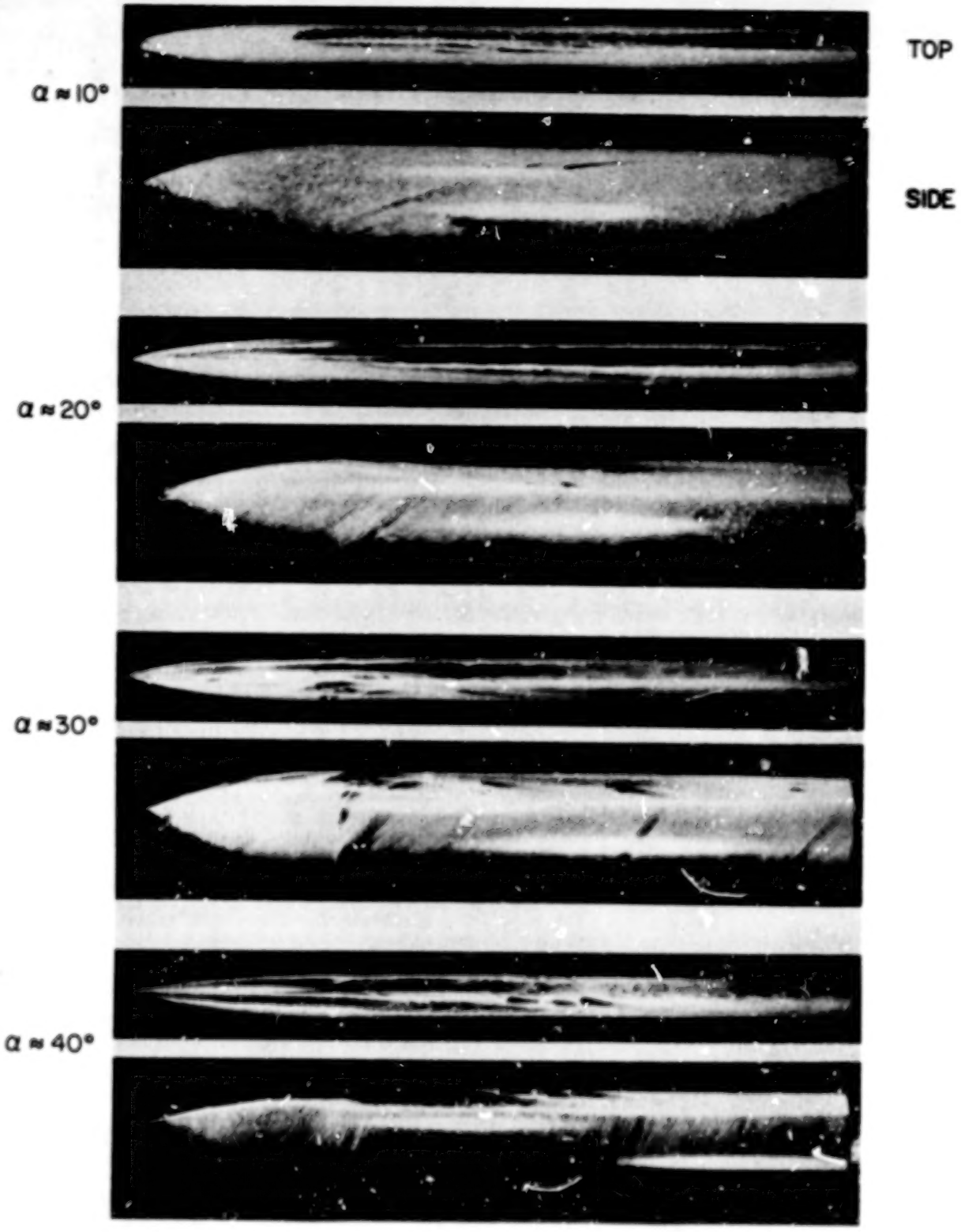

(c) $M_\infty = 2.0$.

Figure 61.– Concluded.

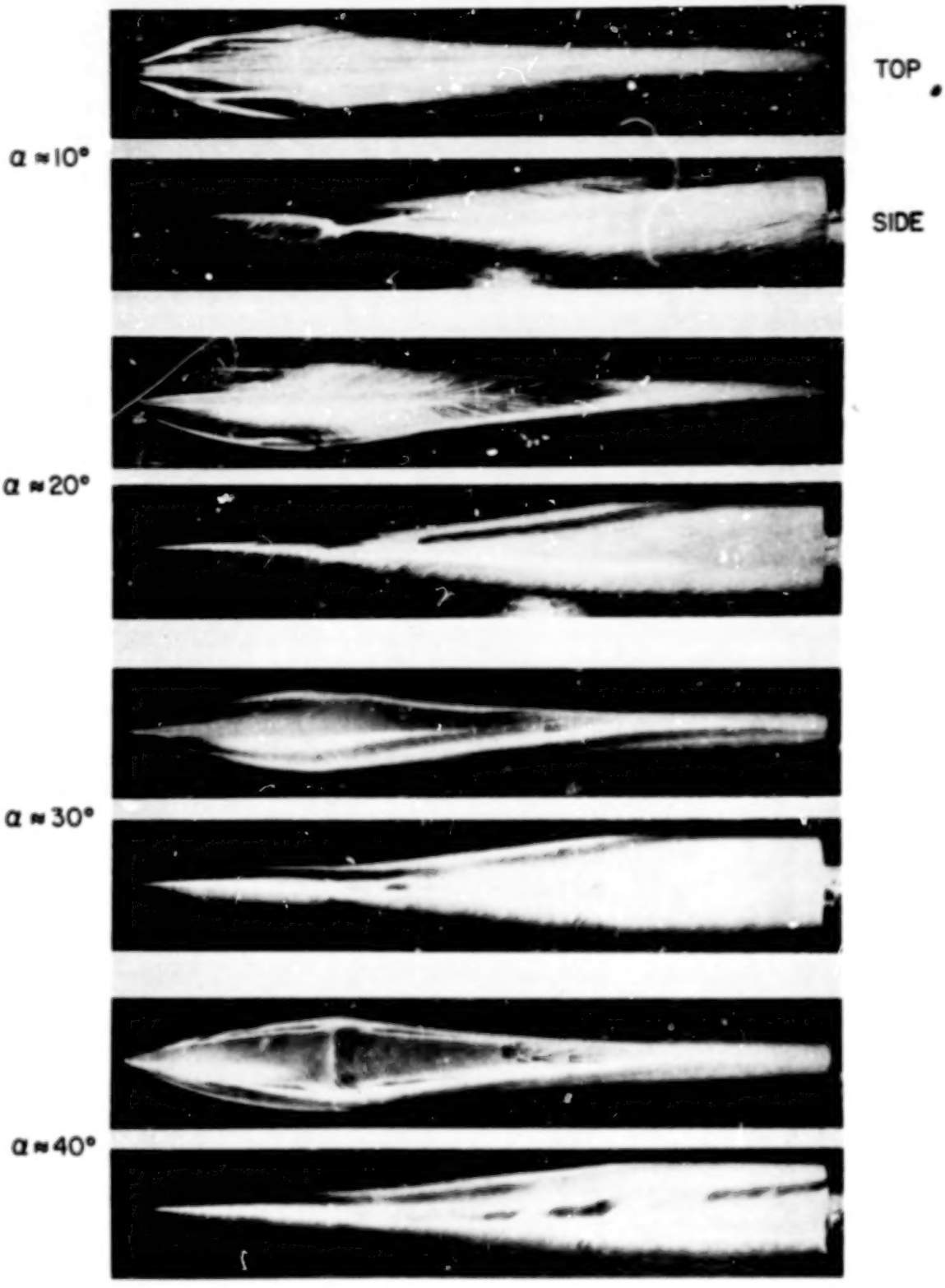

(a) $M_\infty = 0.6$.

Figure 62.– Oil-flow photographs for B_3 at $\phi = 0°$ (body with variable a/b cross sections).

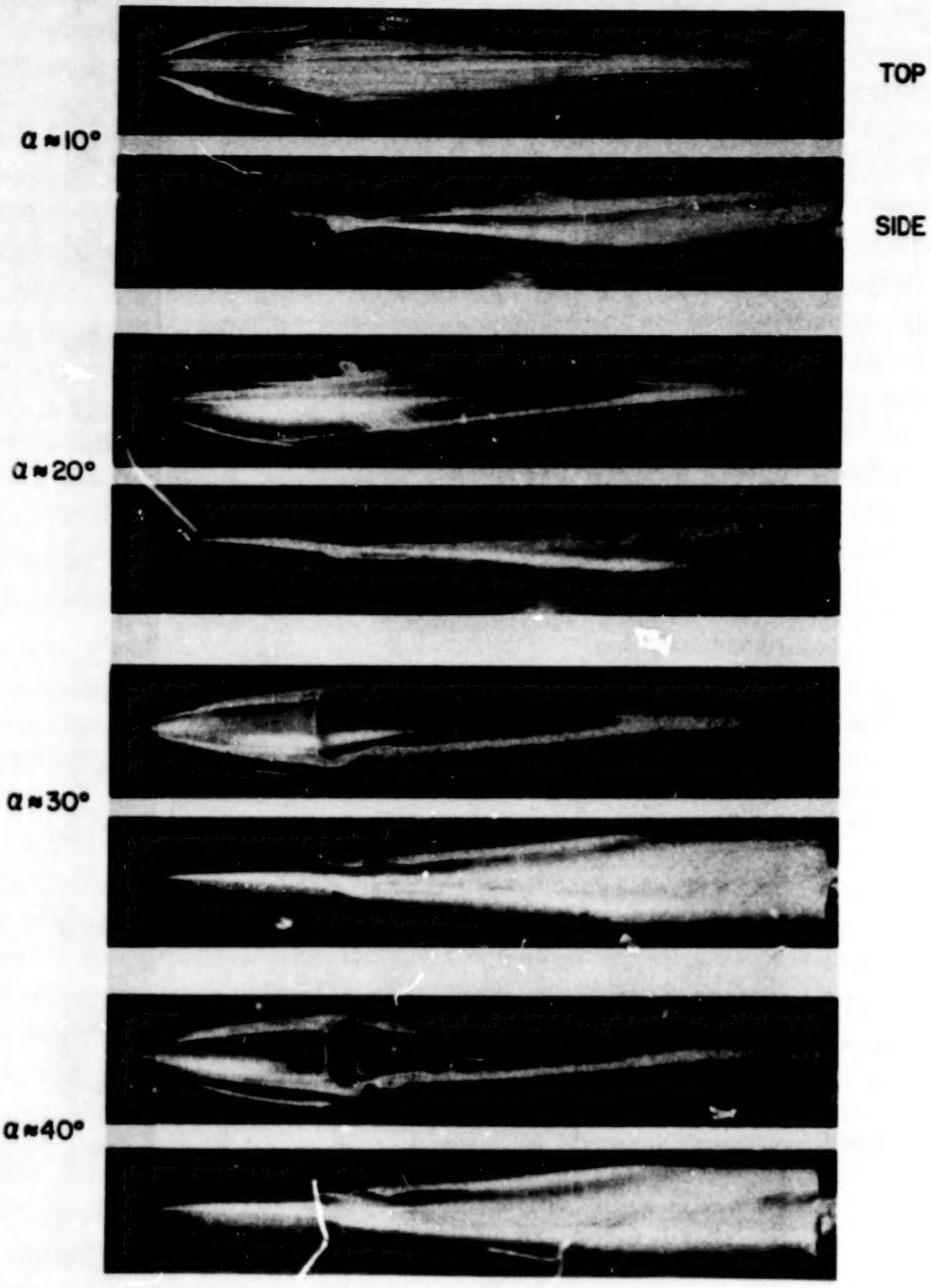

(b) $M_\infty = 0.9$.

Figure 62.– Continued.

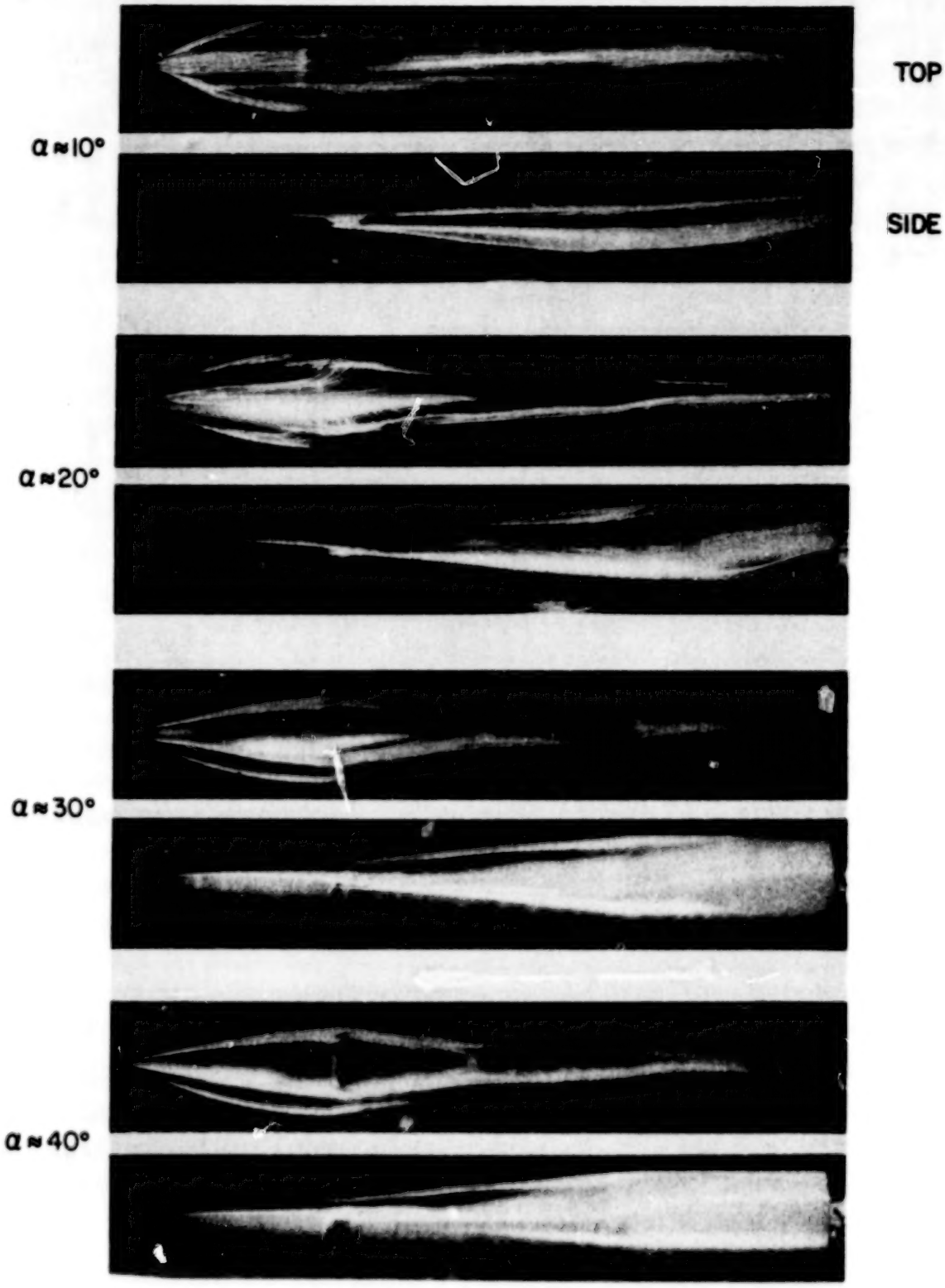

(c) $M_\infty = 2.0$.

Figure 62.– Concluded.

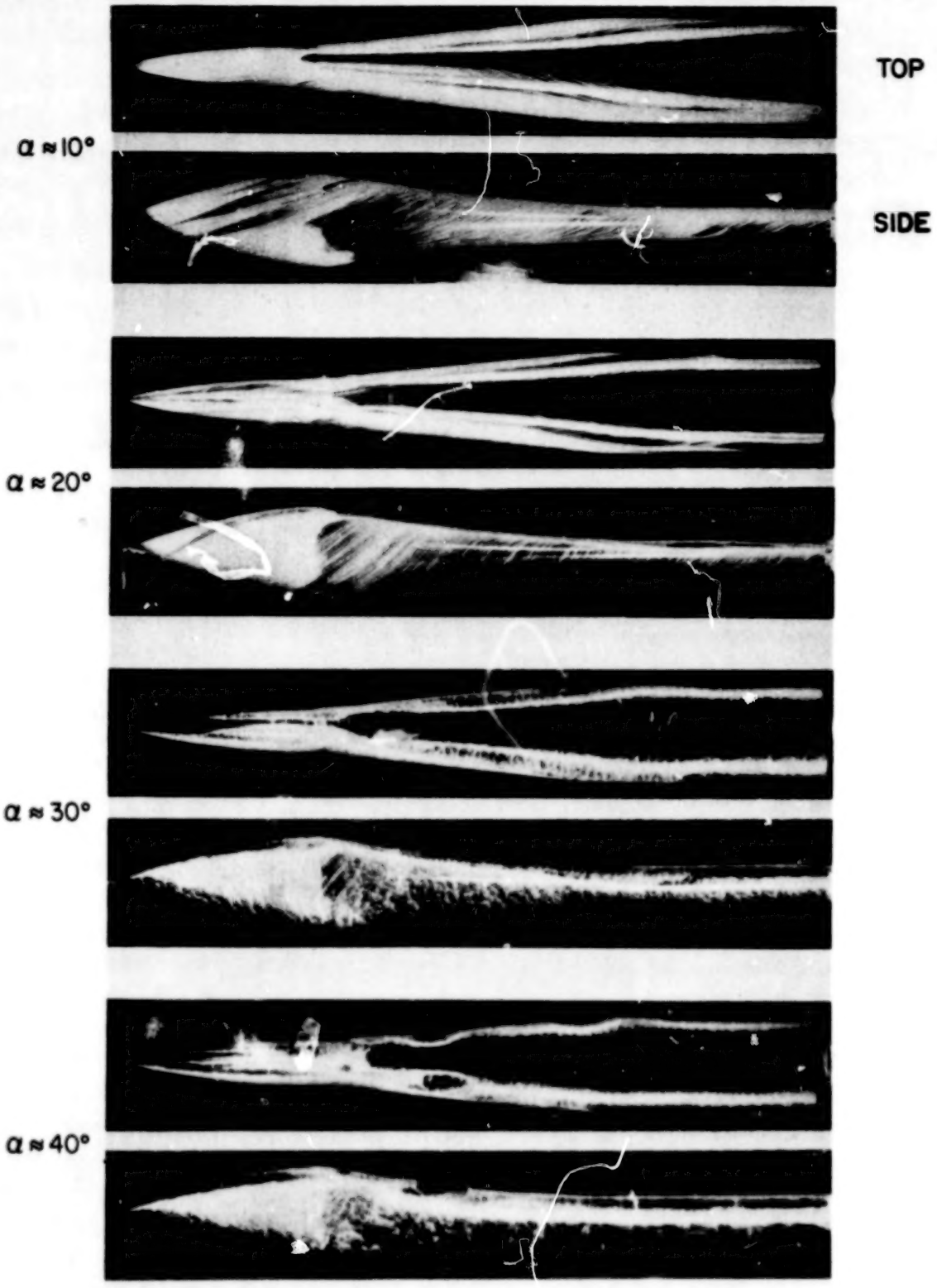

(a) $M_\infty = 0.6$.

Figure 63.– Oil-flow photographs for B_3 at $\phi = 90°$ (body with variable a/b cross sections).

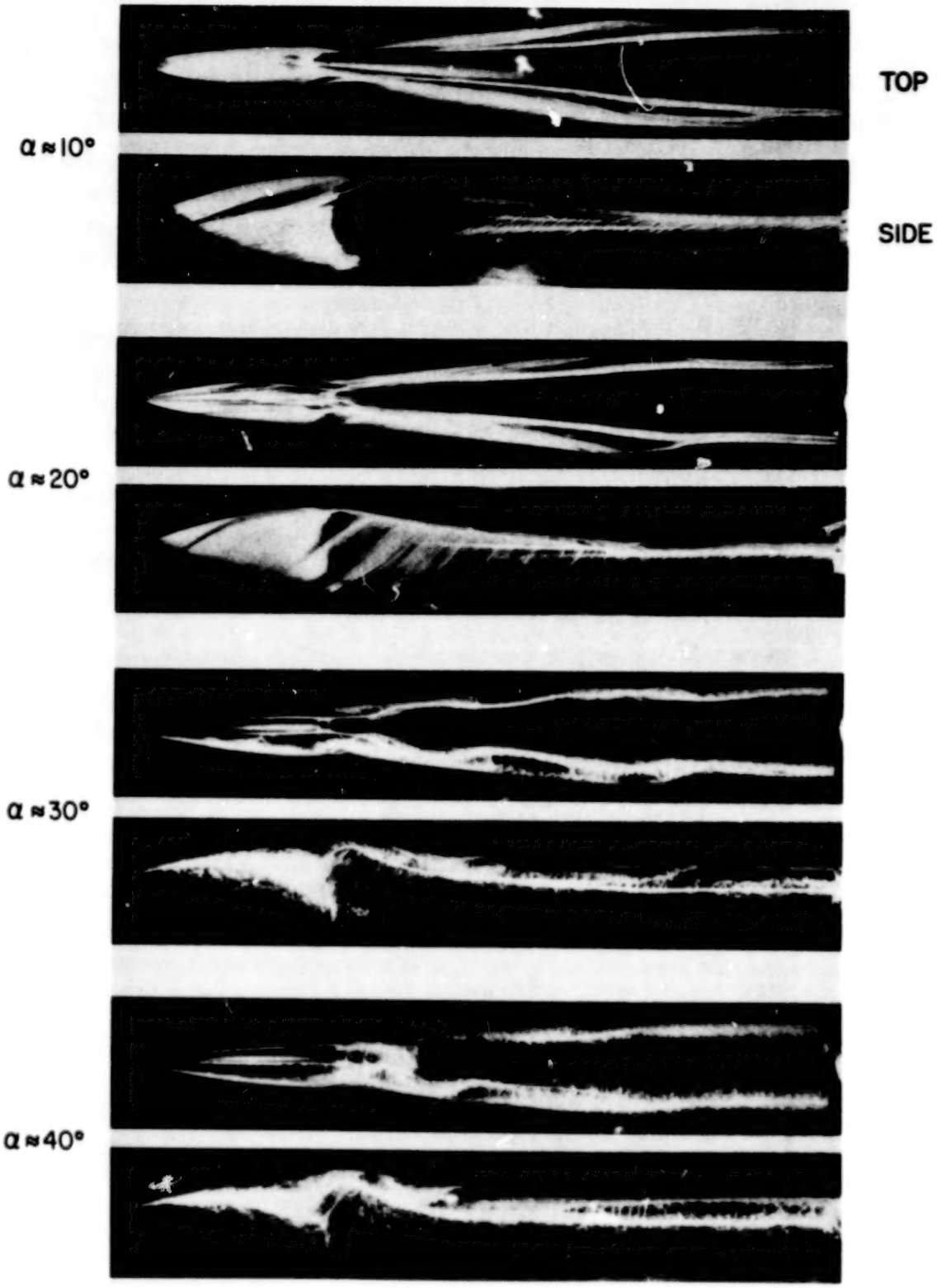

(b) $M_\infty = 0.9$.

Figure 63.– Continued.

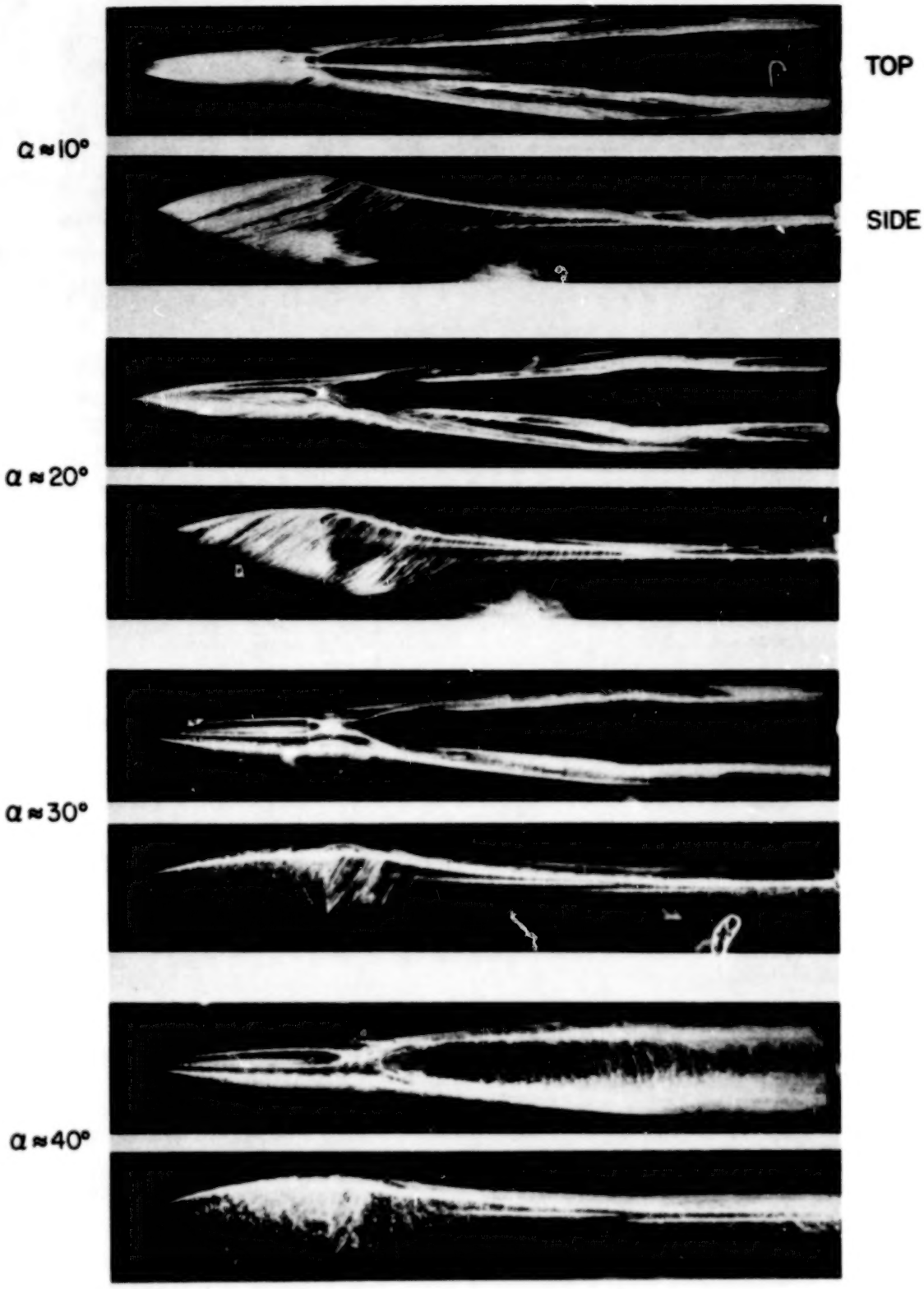

(c) $M_\infty = 2.0$.

Figure 63. – Concluded.

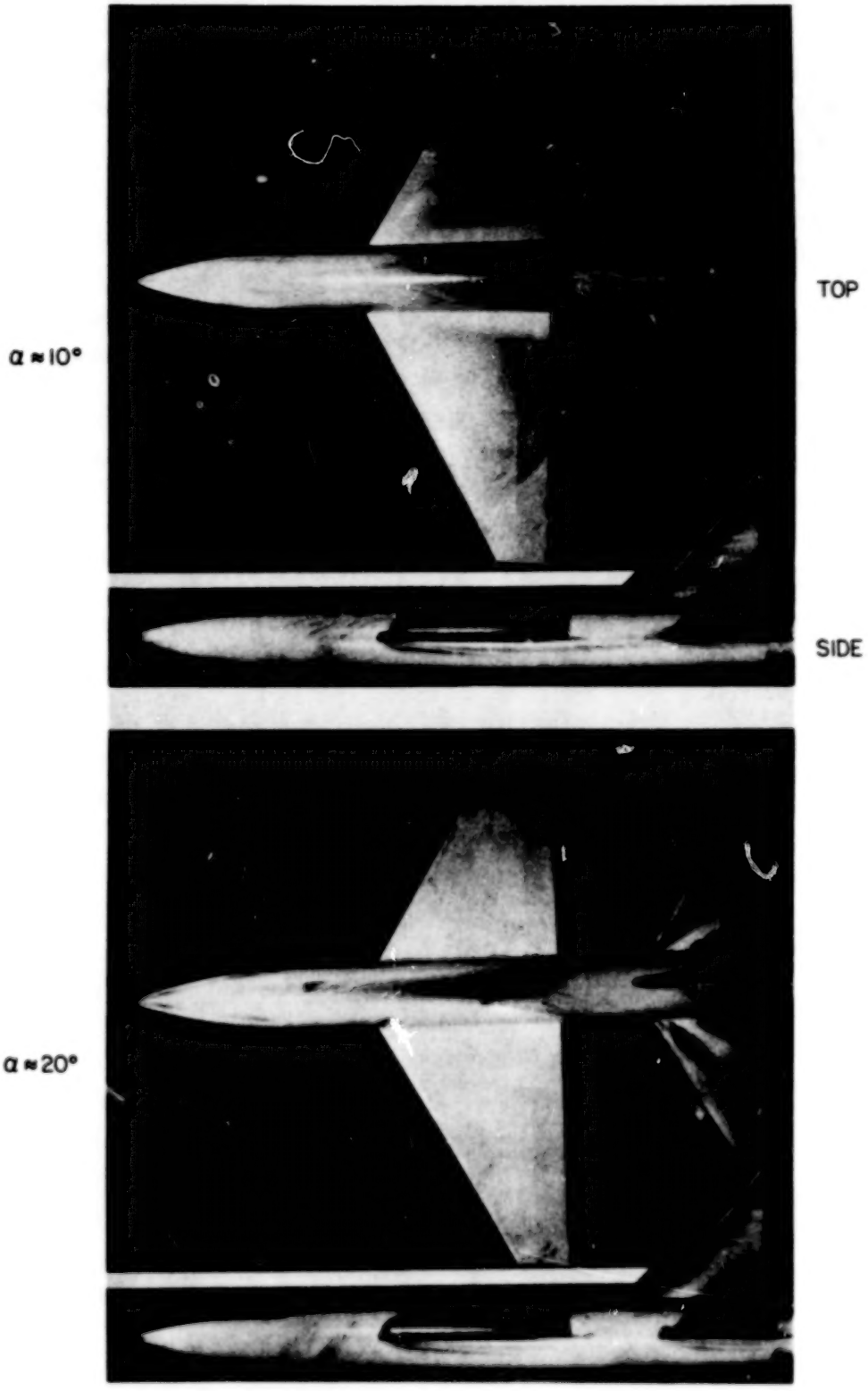

(a) $M_\infty = 0.6$.

Figure 64.– Oil-flow photographs for $B_1 W_2 T = N_1 C_1 W_2 T$ (body with fineness-ratio-3 nose, aspect-ratio-4 wing, and tail).

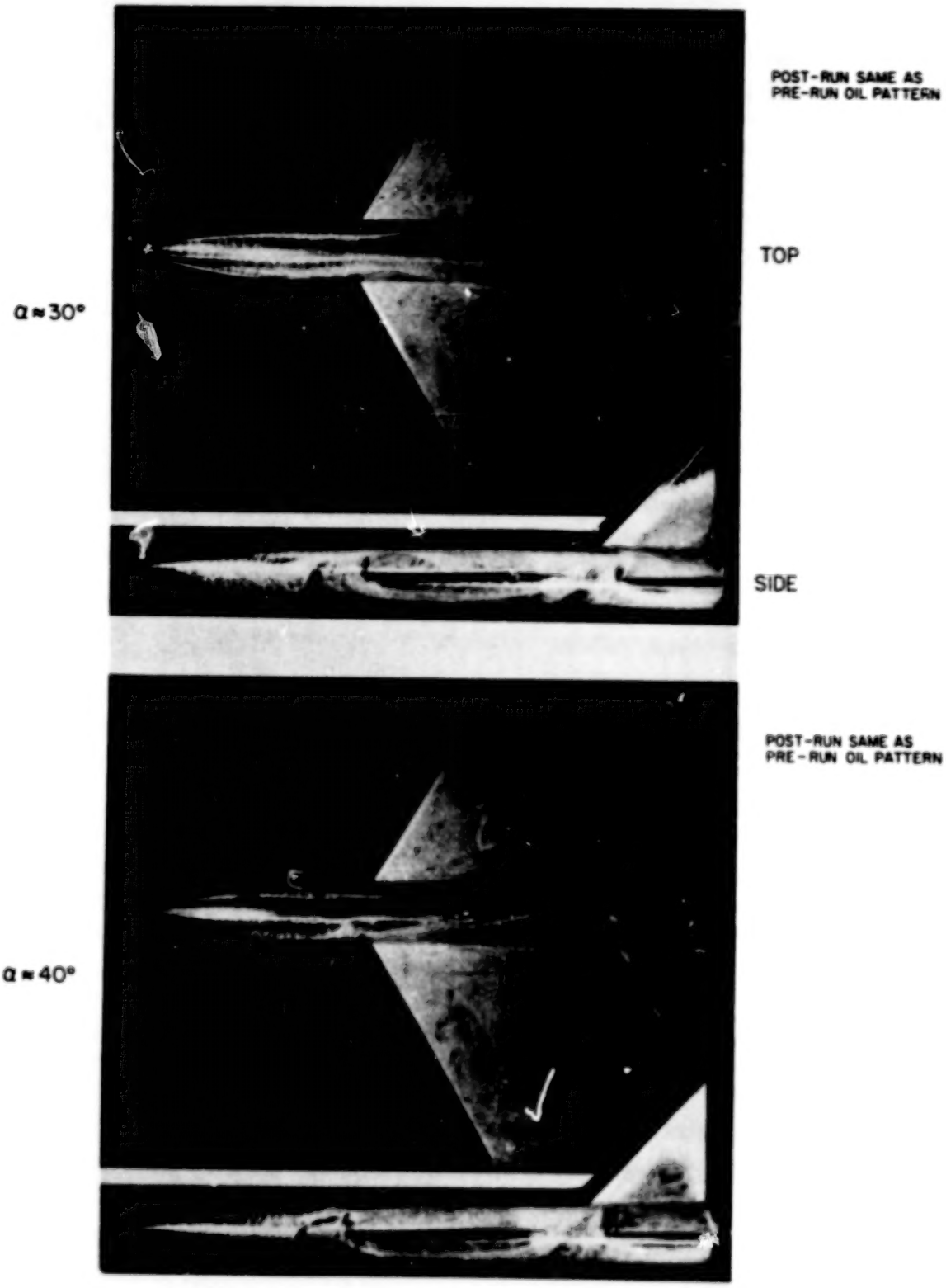

(a) $M_\infty = 0.6$ – Concluded.

Figure 64.– Continued.

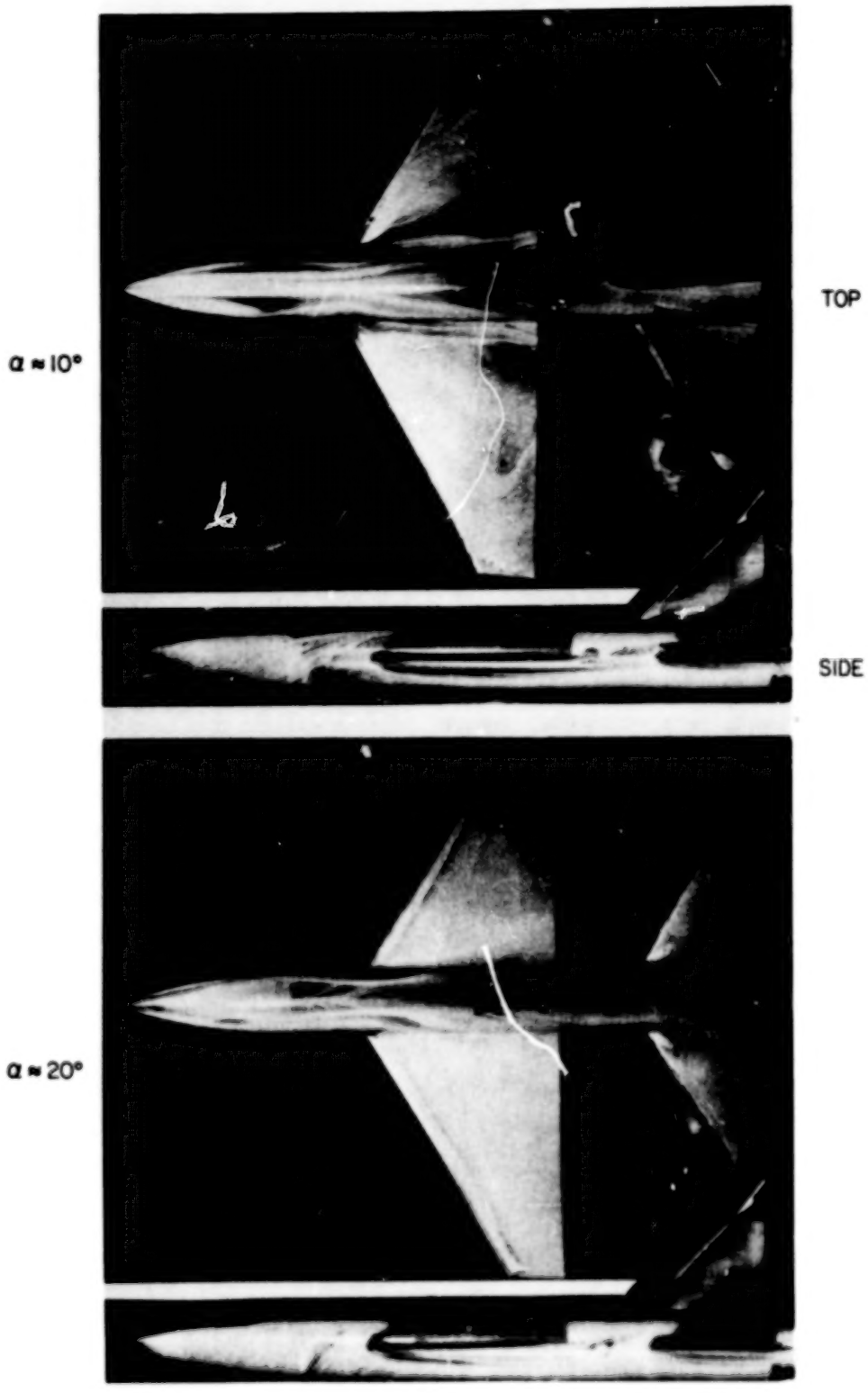

(b) $M_\infty = 0.9$.

Figure 64. - Continued.

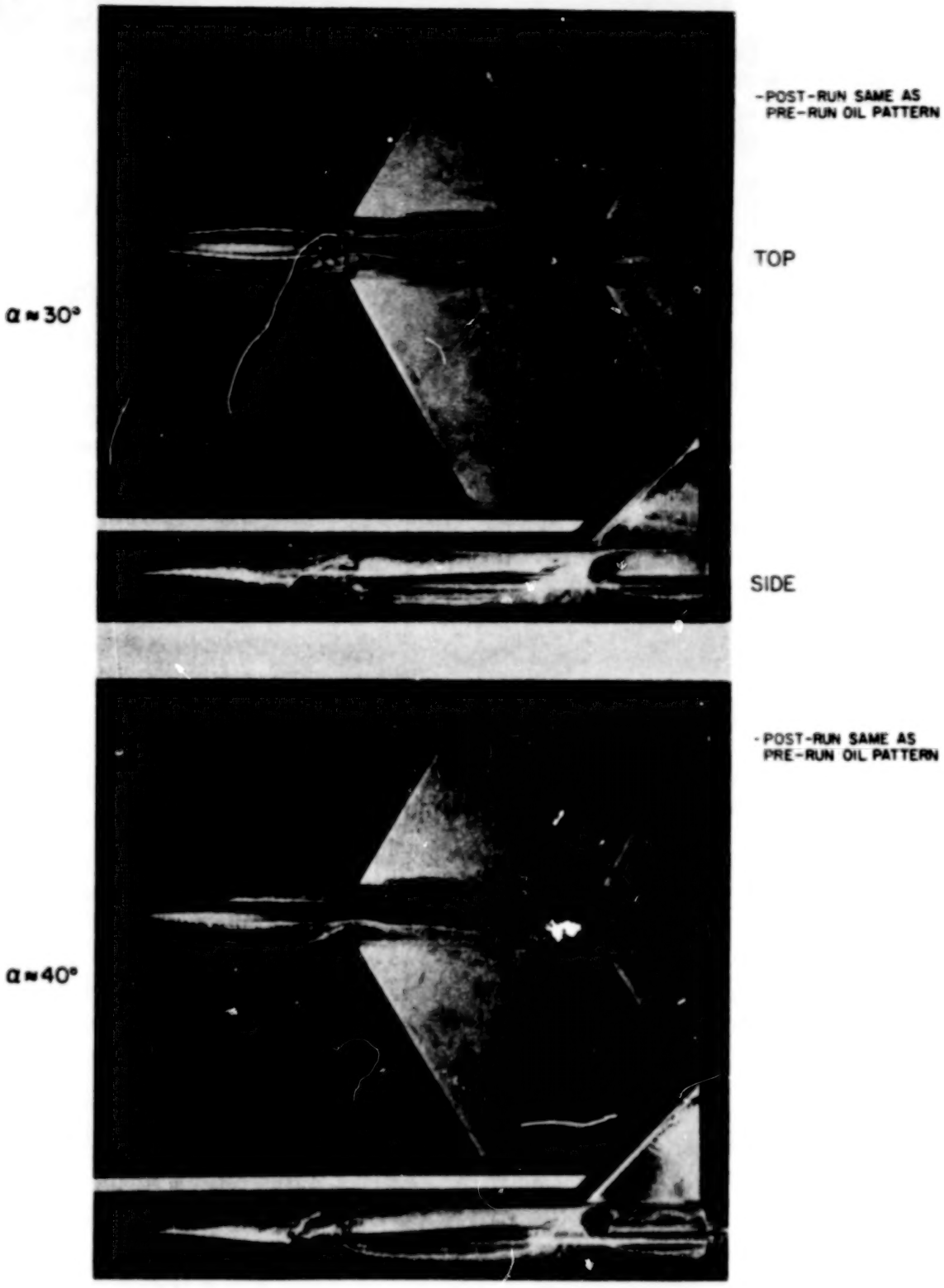

(b) $M_\infty = 0.9$ – Concluded.

Figure 64. – Continued.

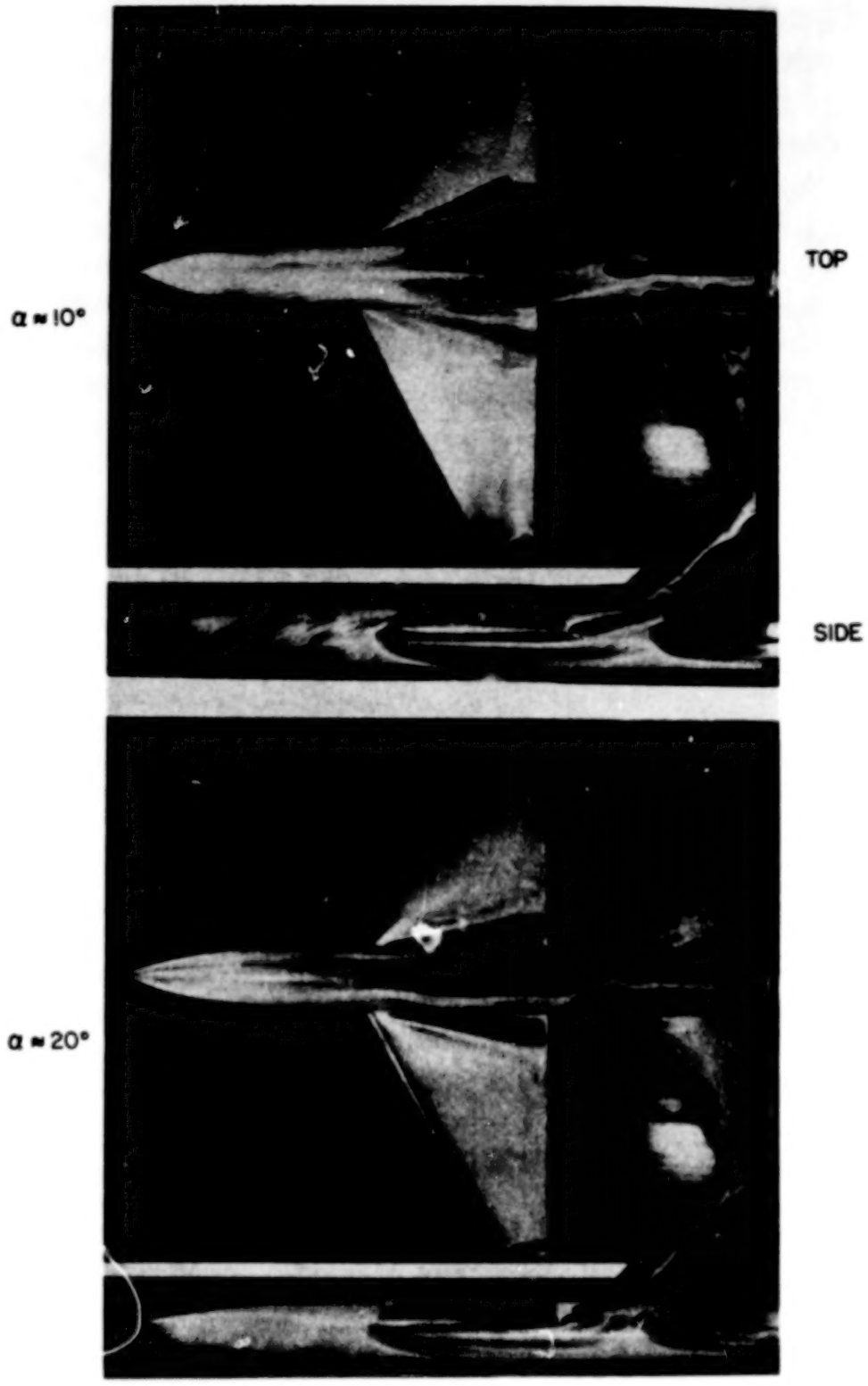

(c) $M_\infty = 2.0$.

Figure 64.– Continued.

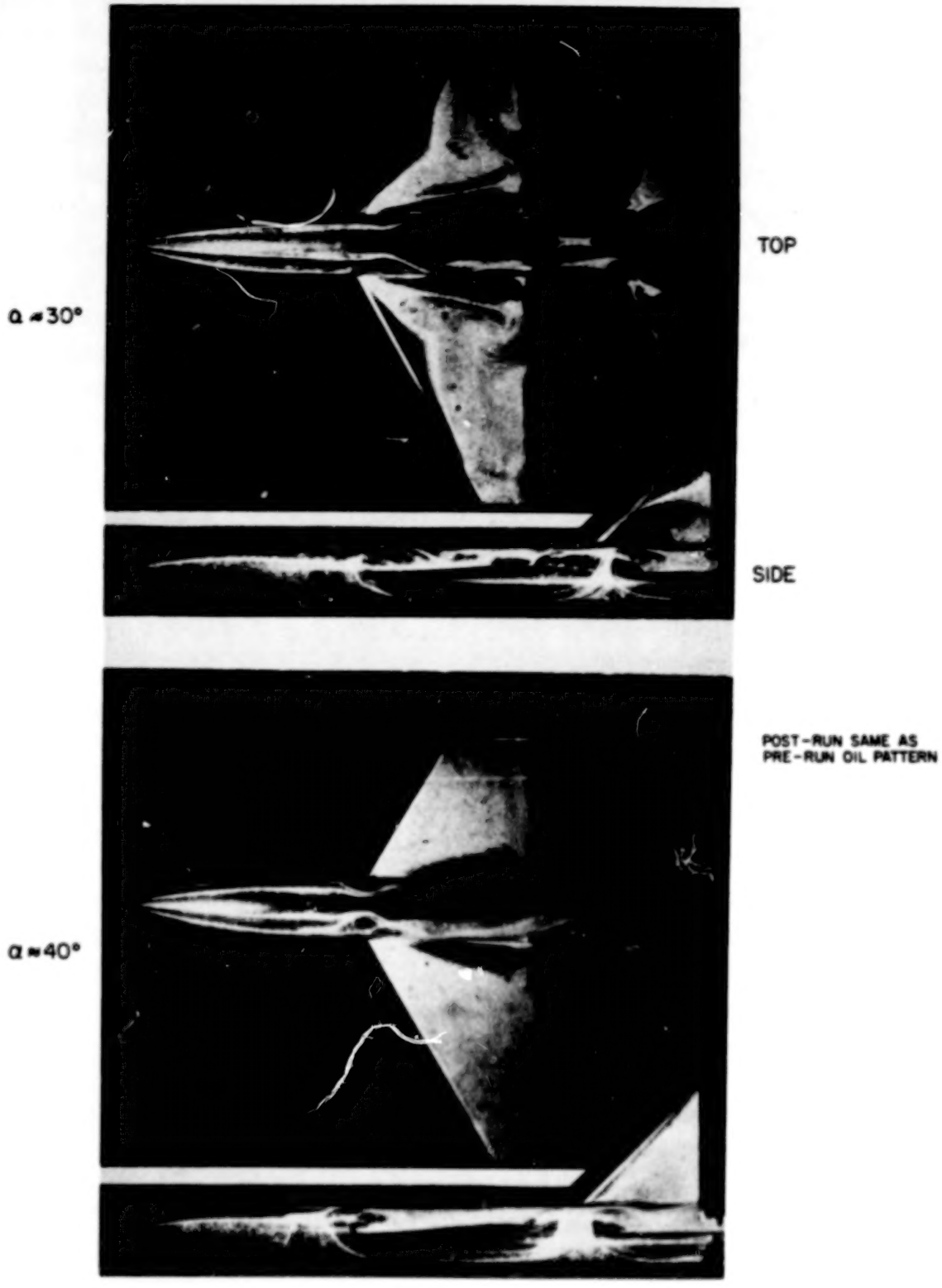

(c) $M_\infty = 2.0$ – Concluded.

Figure 64.– Concluded.

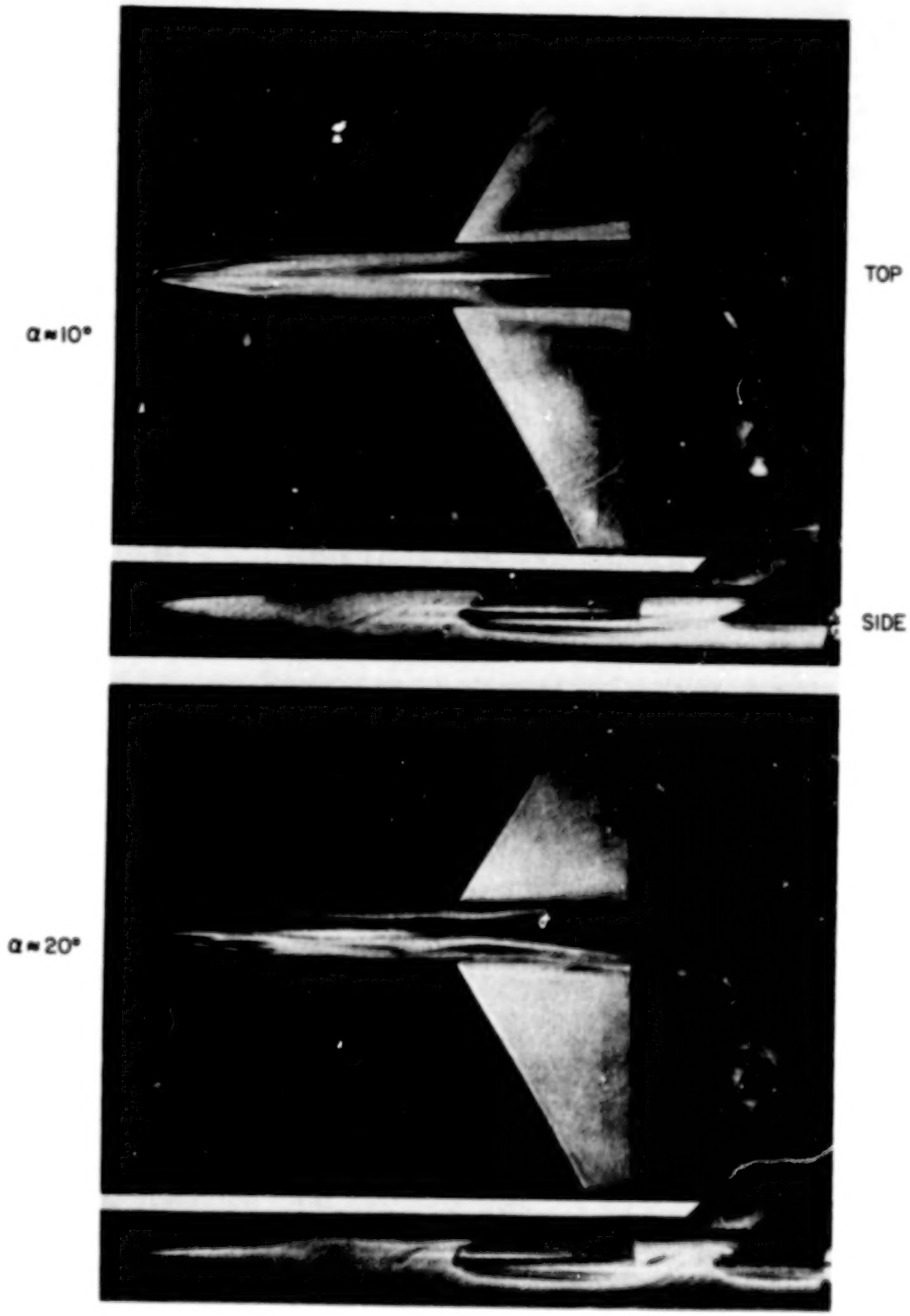

(a) $M_\infty = 0.6$.

Figure 65.– Oil-flow photographs for $N_3 C_1 W_2 T$ (body with fineness-ratio-5 nose, aspect-ratio-4 wing, and tail).

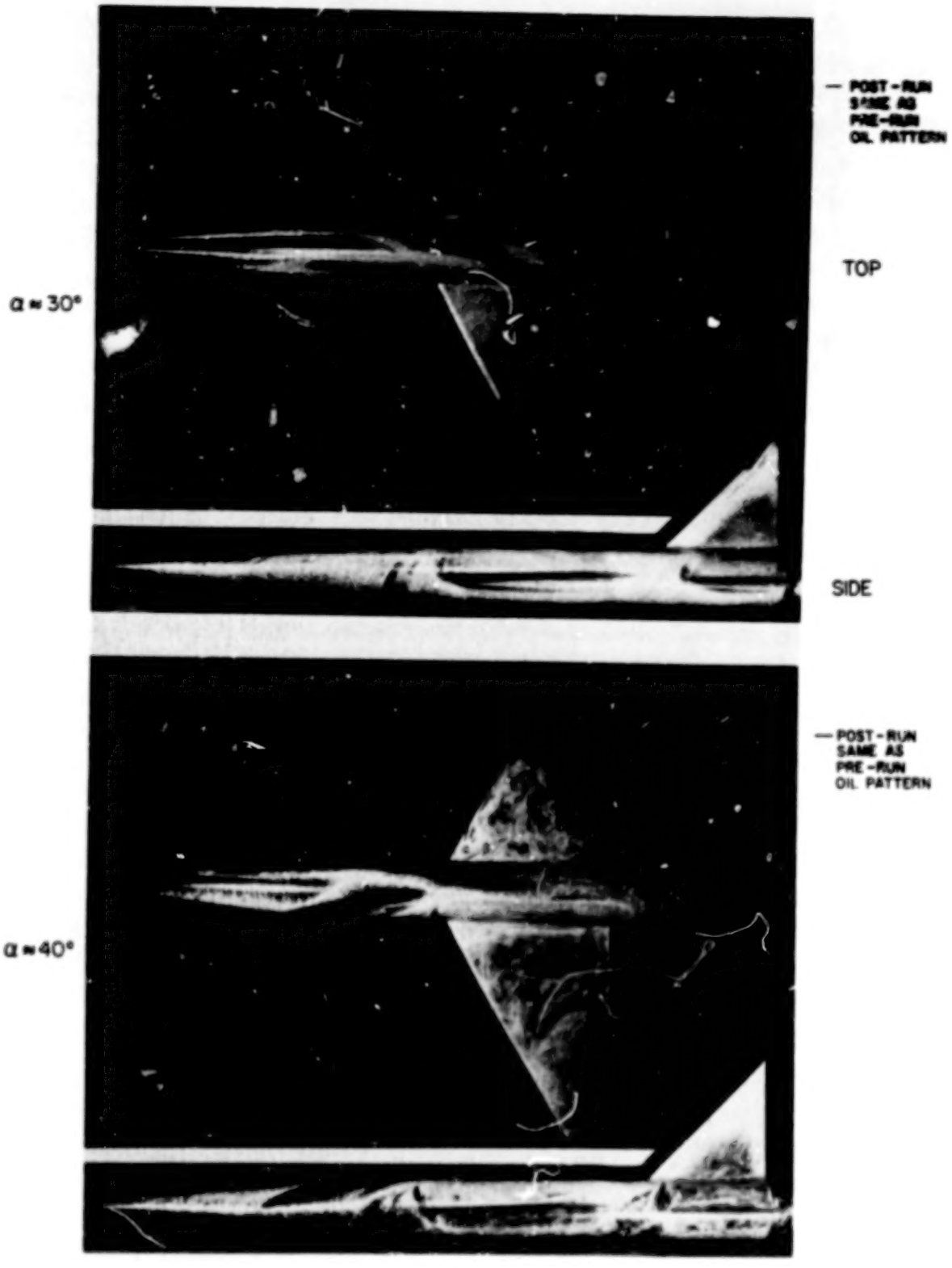

(a) $M_\infty = 0.6$ – Concluded

Figure 65. – Continued.

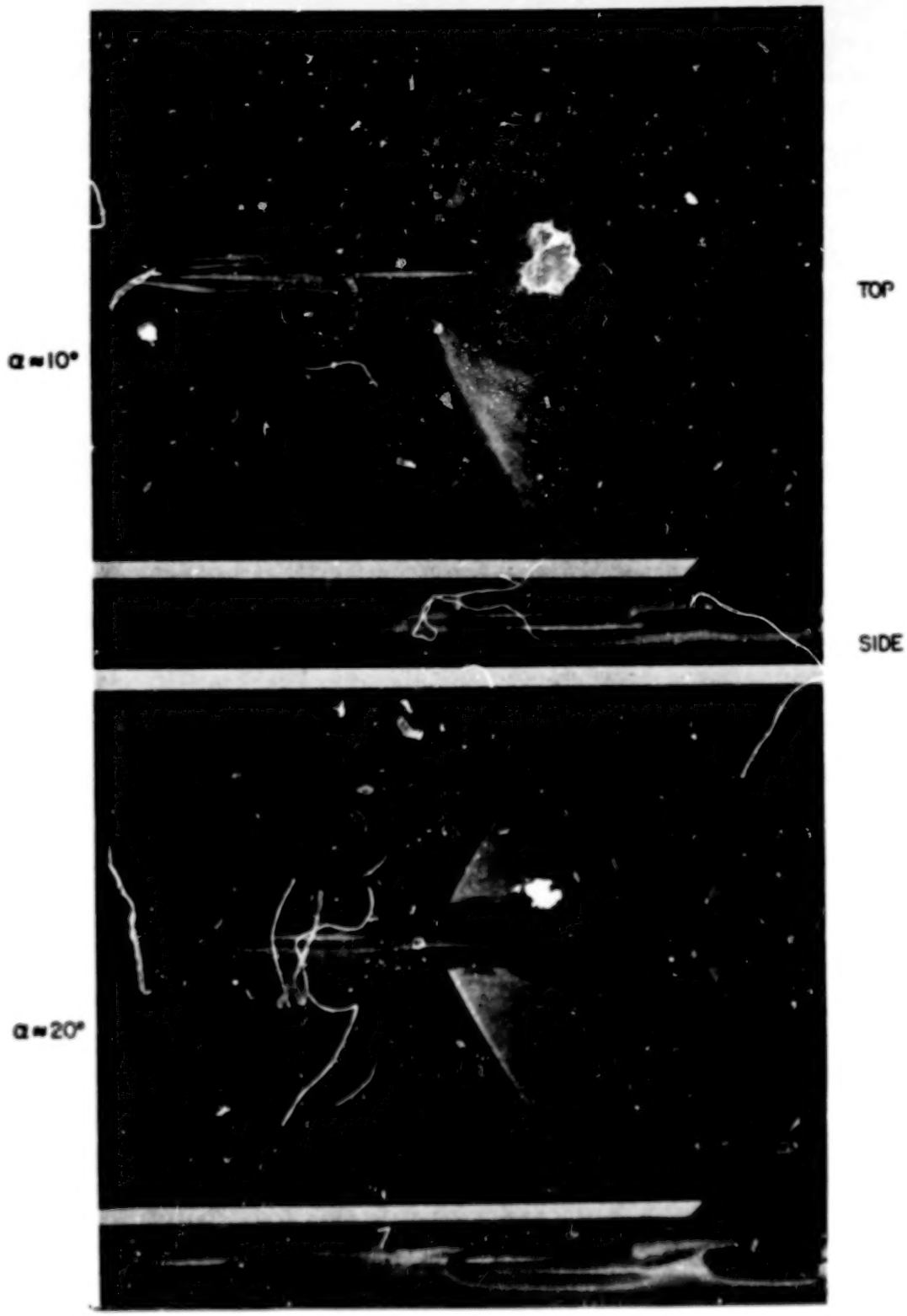

(b) $M_\infty = 0.9$.

Figure 65.– Continued.

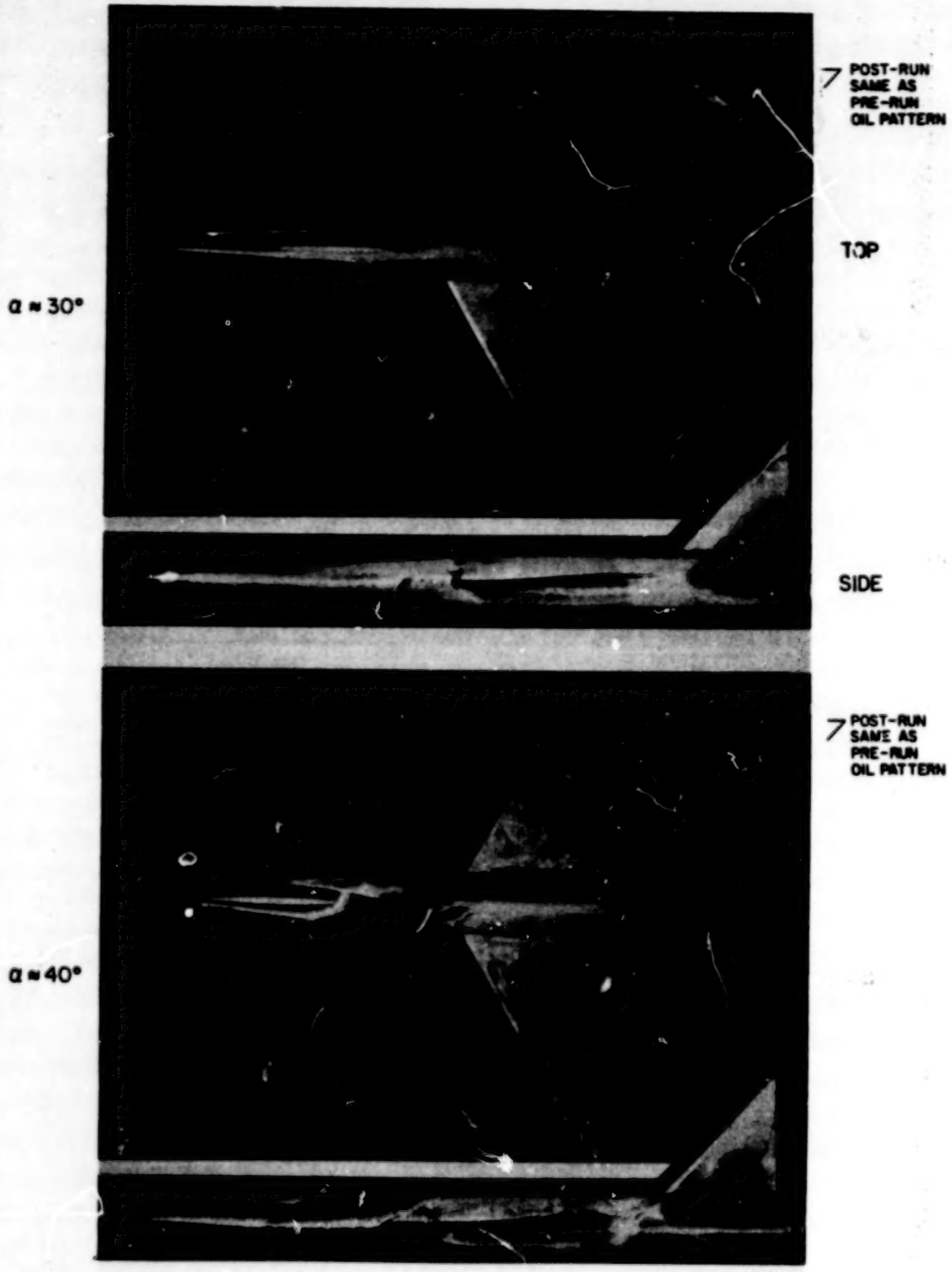

(b) $M_\infty = 0.9$ – Concluded

Figure 65.– Continued.

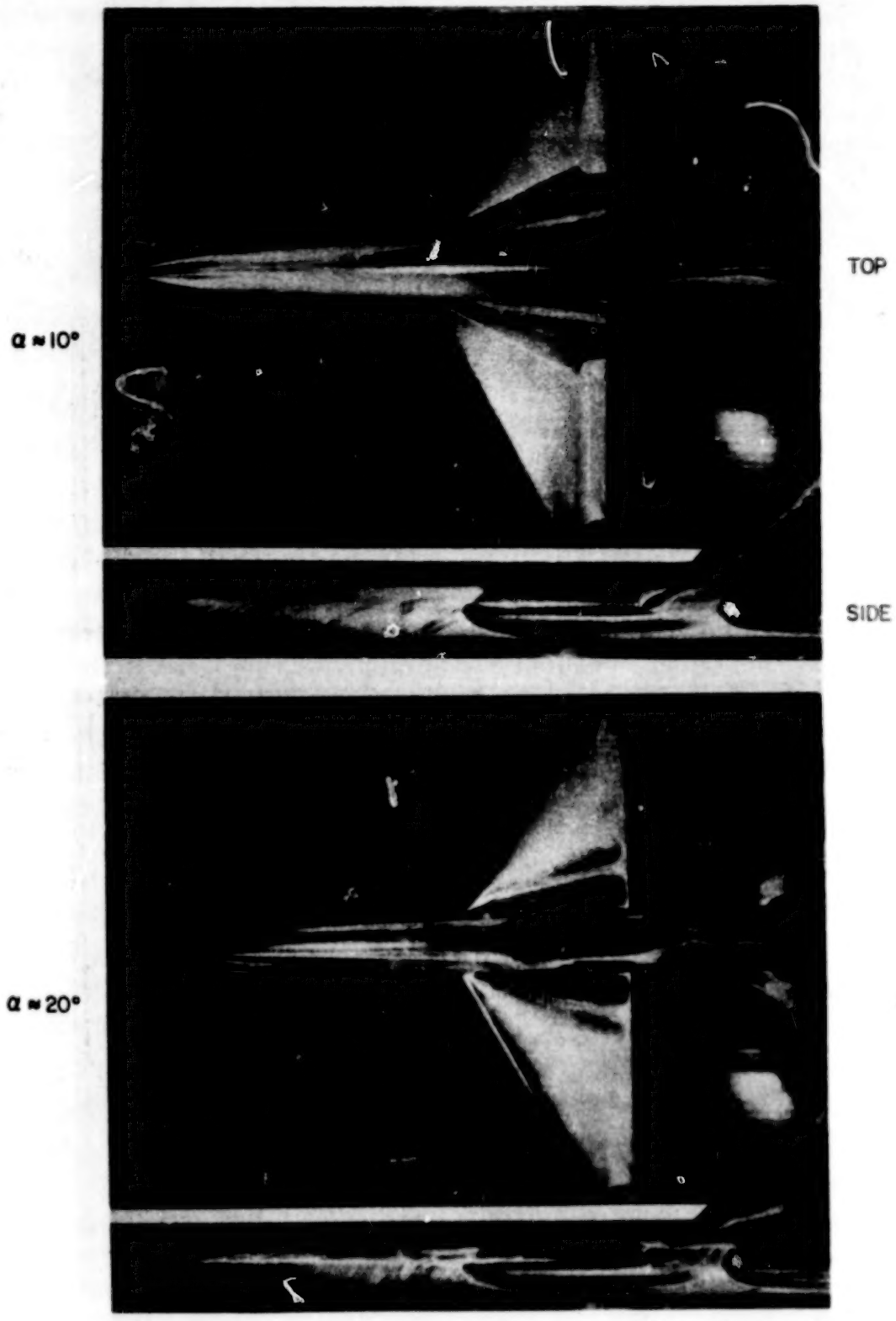

(c) $M_\infty = 2.0$.

Figure 65.– Continued.

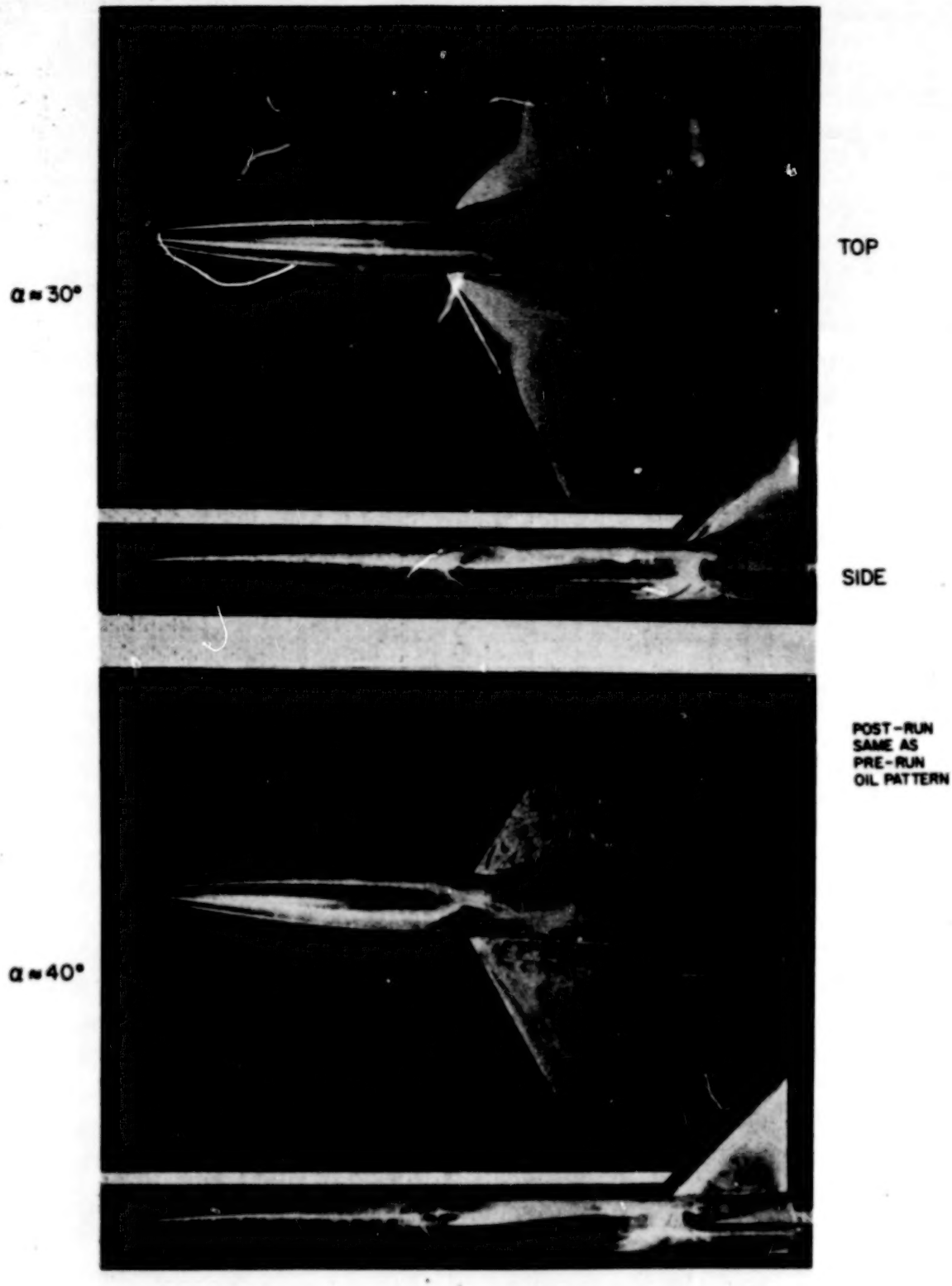

(c) $M_\infty = 2.0$ – Concluded.

Figure 65. – Concluded.

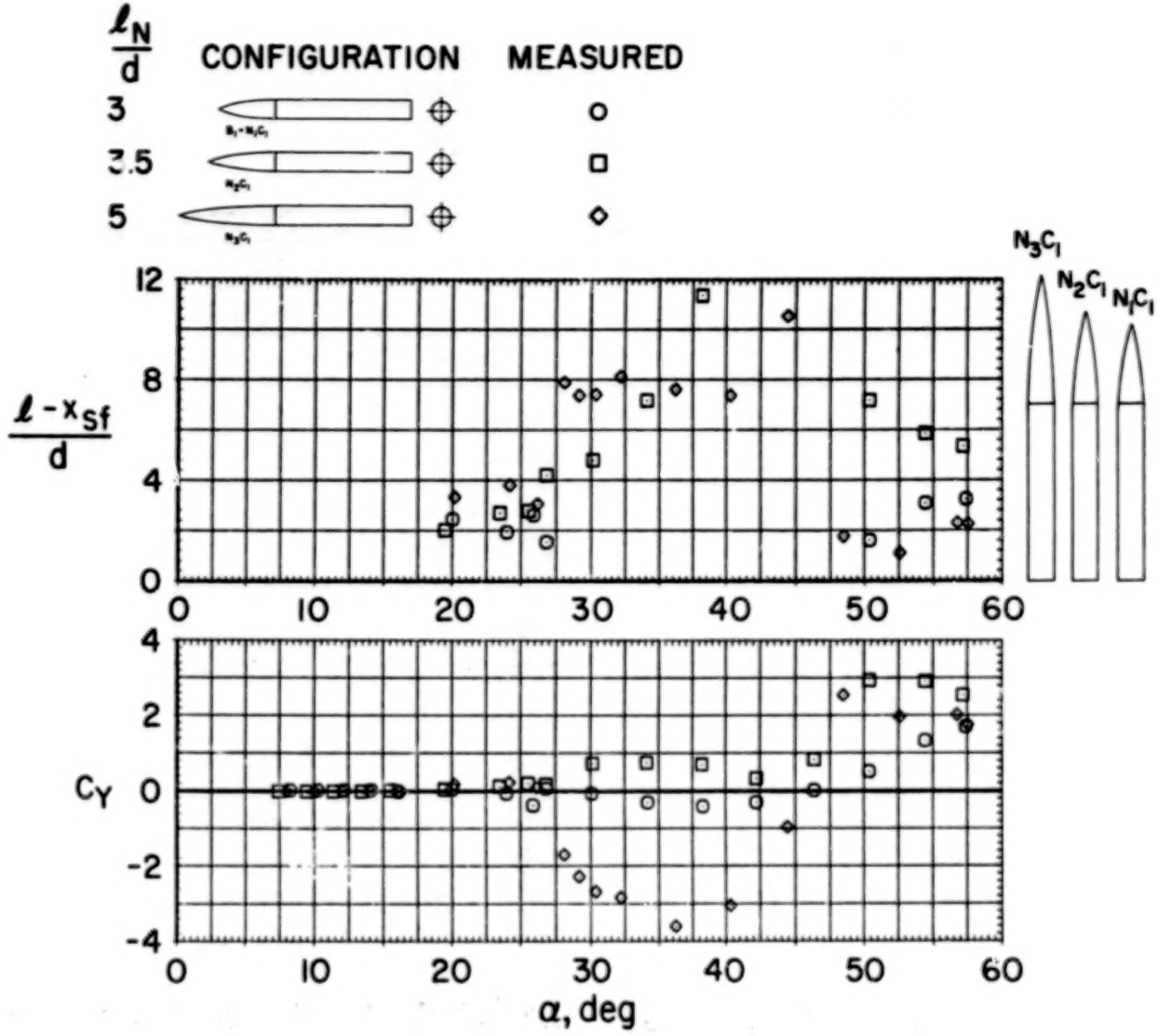

(a) $M_\infty = 0.6$, Re = 4.3×10^5.

Figure 66.– Effect of nose fineness ratio on side-force coefficient and side-force position for ogive-cylinder bodies of revolution.

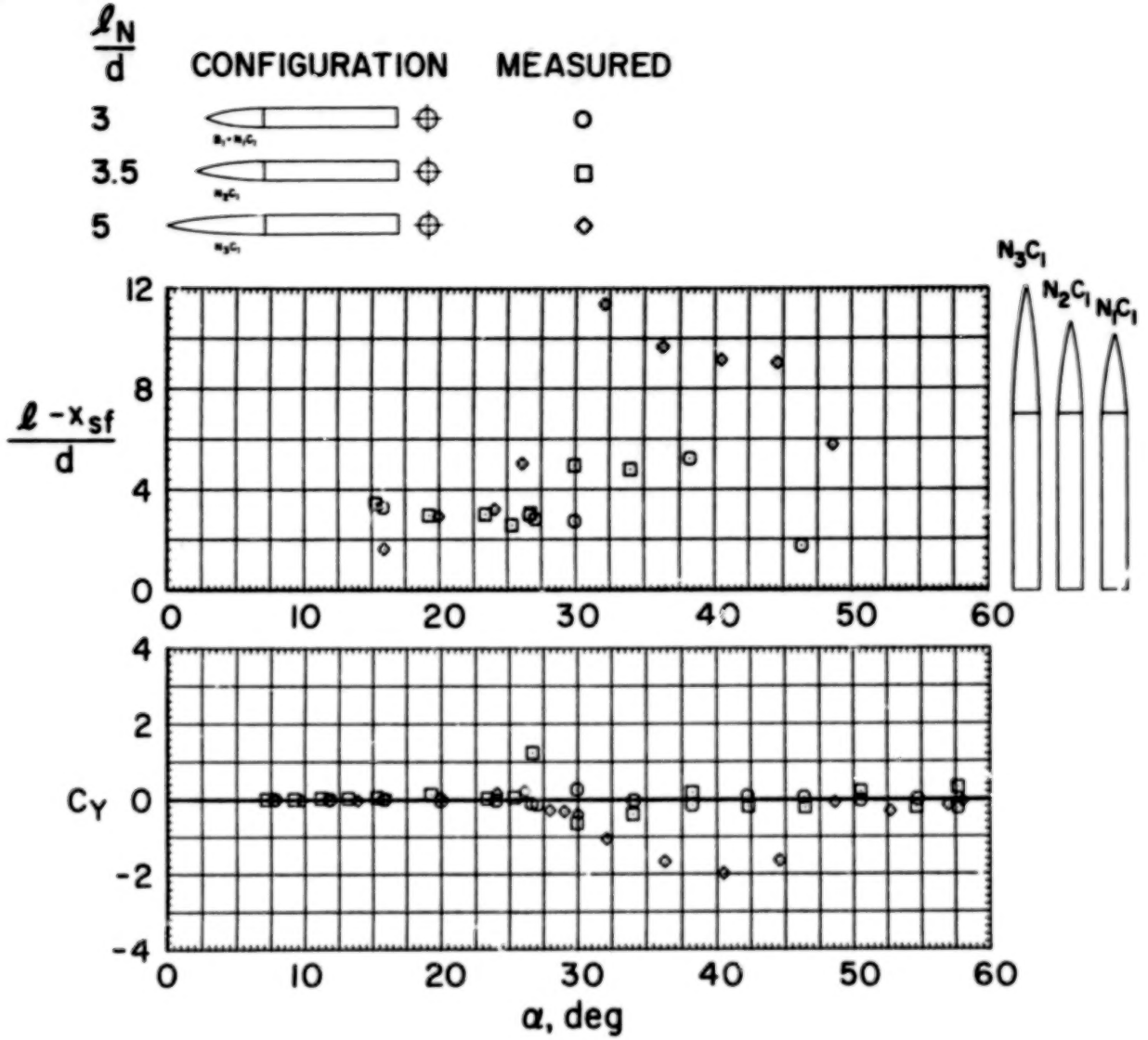

(b) $M_\infty = 0.9$, Re = 6.5×10^5.

Figure 66.– Continued.

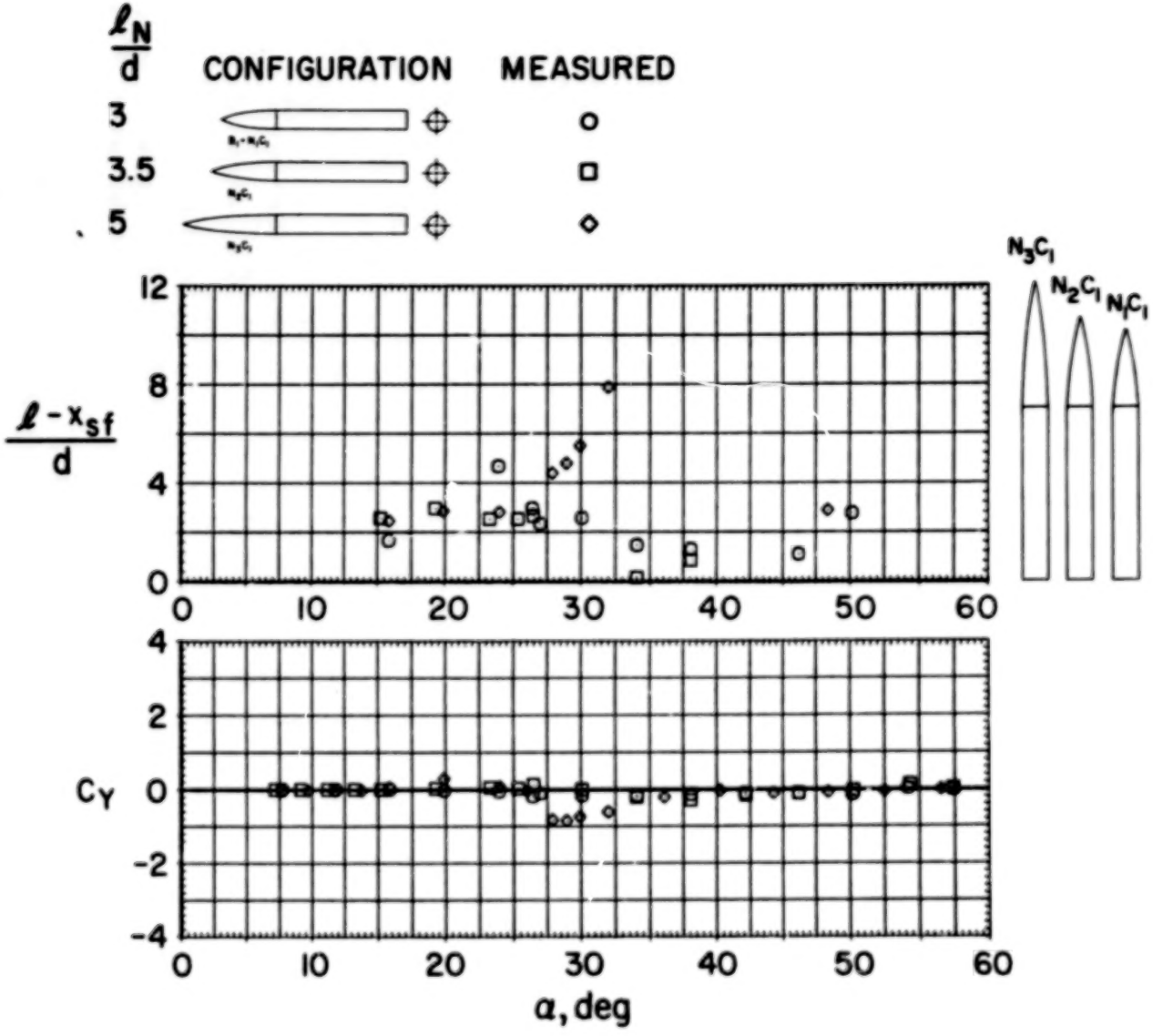

(c) $M_\infty = 1.2$, Re = 3.8×10^5.

Figure 66.– Concluded.

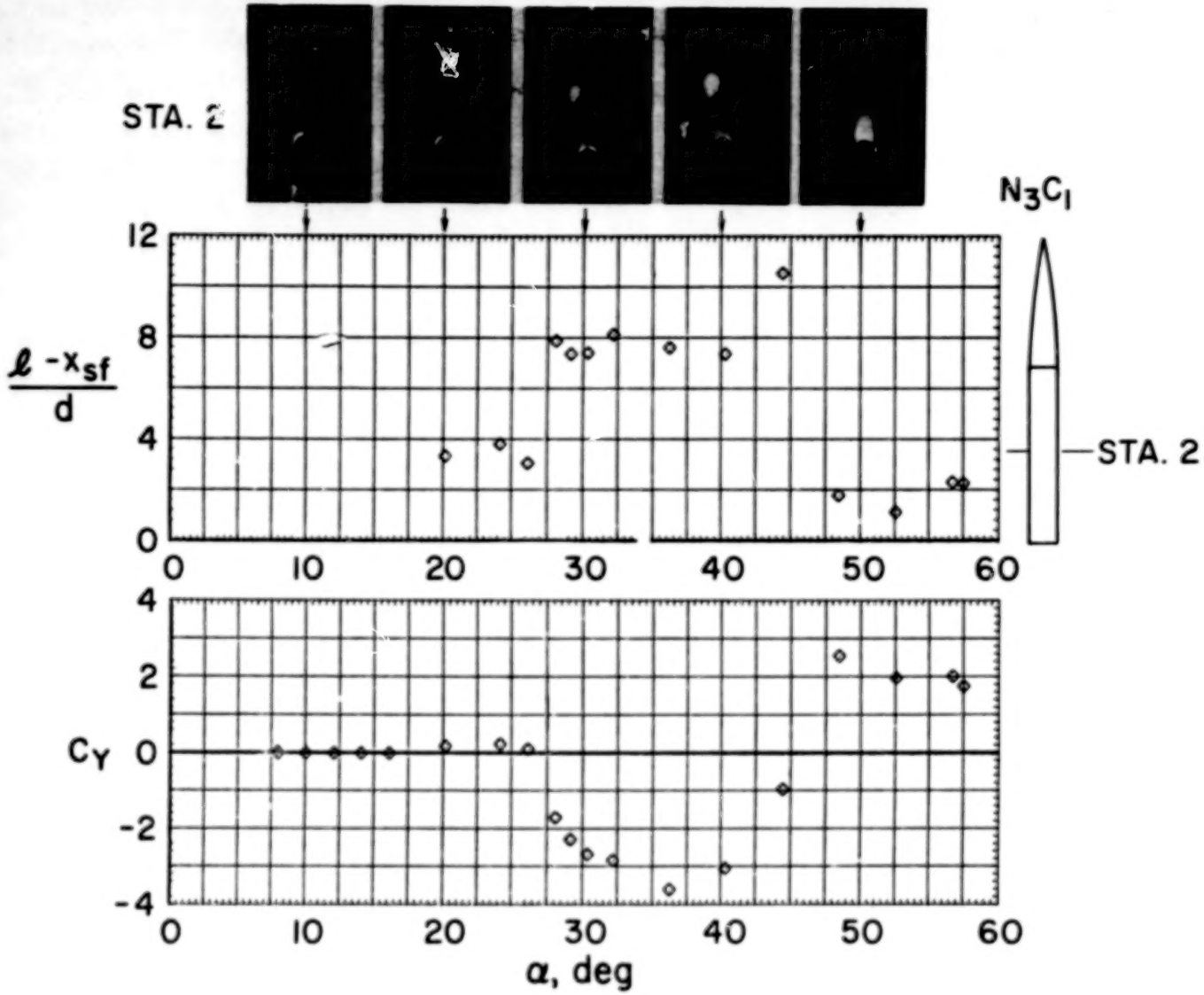

(a) $M_\infty = 0.6$, $Re = 4.3 \times 10^5$.

Figure 67.– Side-force coefficients, side-force positions, and vapor-screen photographs for ogive-cylinder body of revolution with fineness-ratio-5 nose.

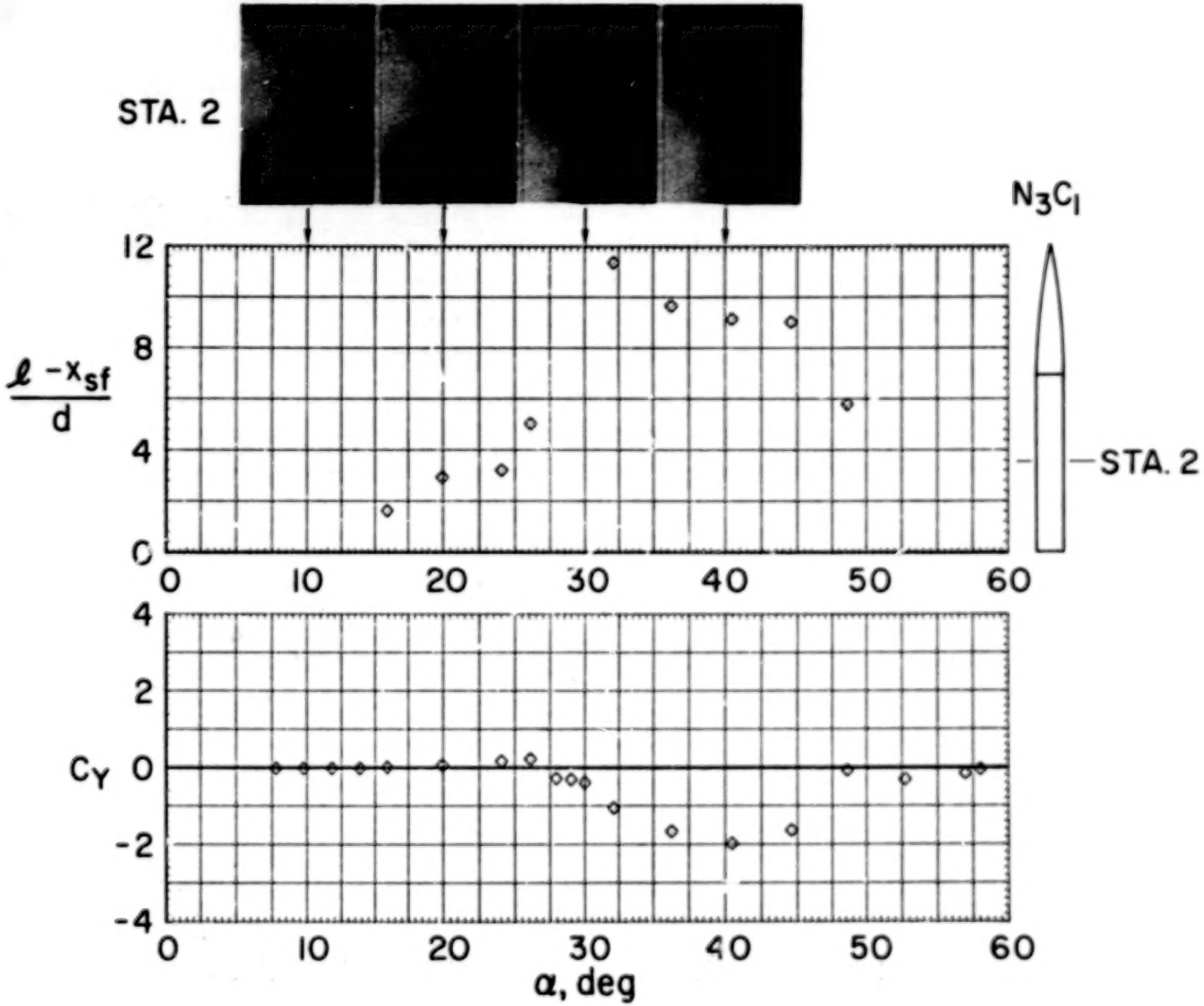

(b) $M_\infty = 0.9$, $Re = 6.5 \times 10^5$.

Figure 67.– Concluded.

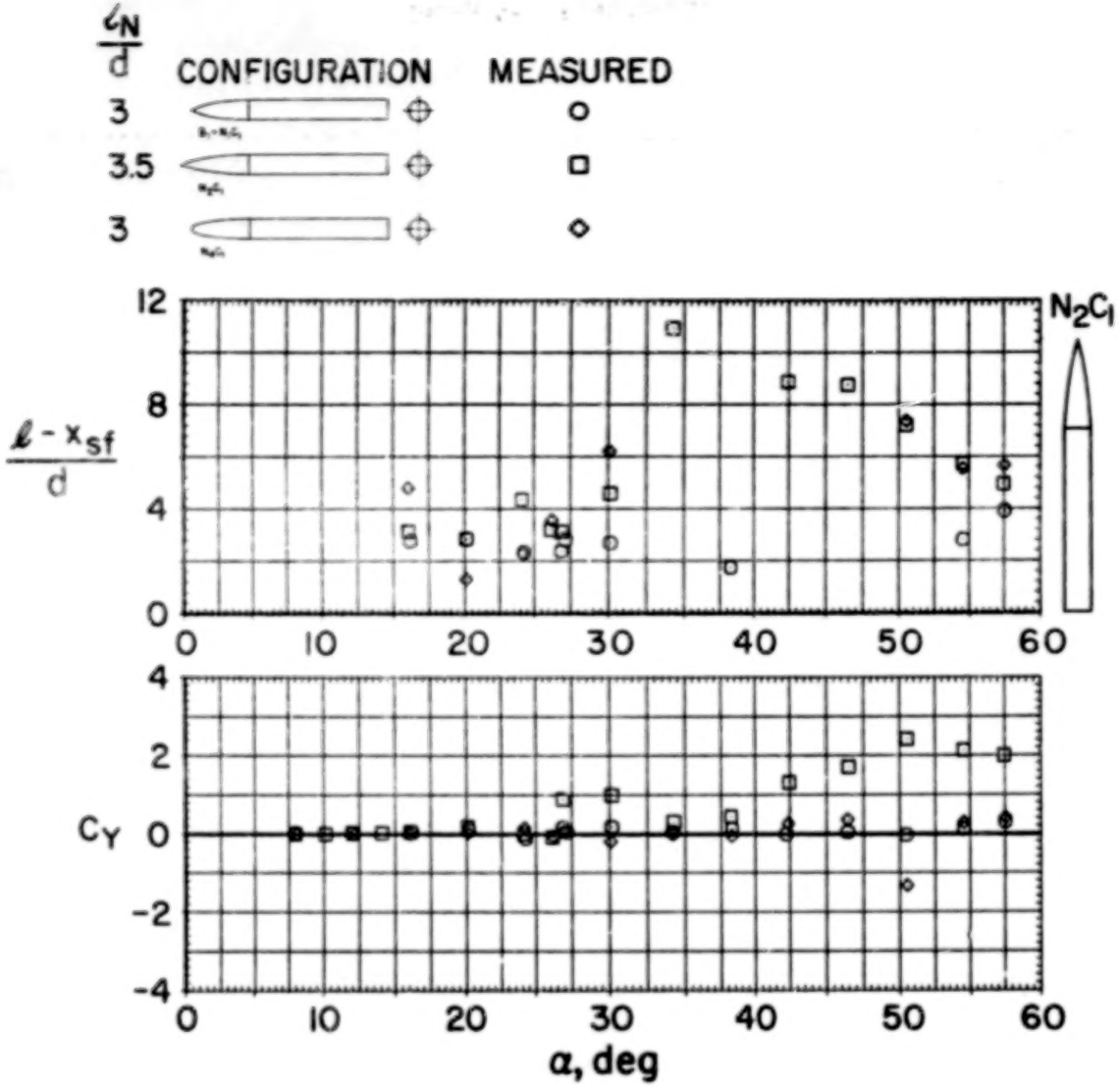

(a) $M_\infty = 0.6$, $Re = 6.5 \times 10^5$.

Figure 68.– Effect of nose-tip rounding on side-force coefficient and side force position for an ogive-cylinder body of revolution.

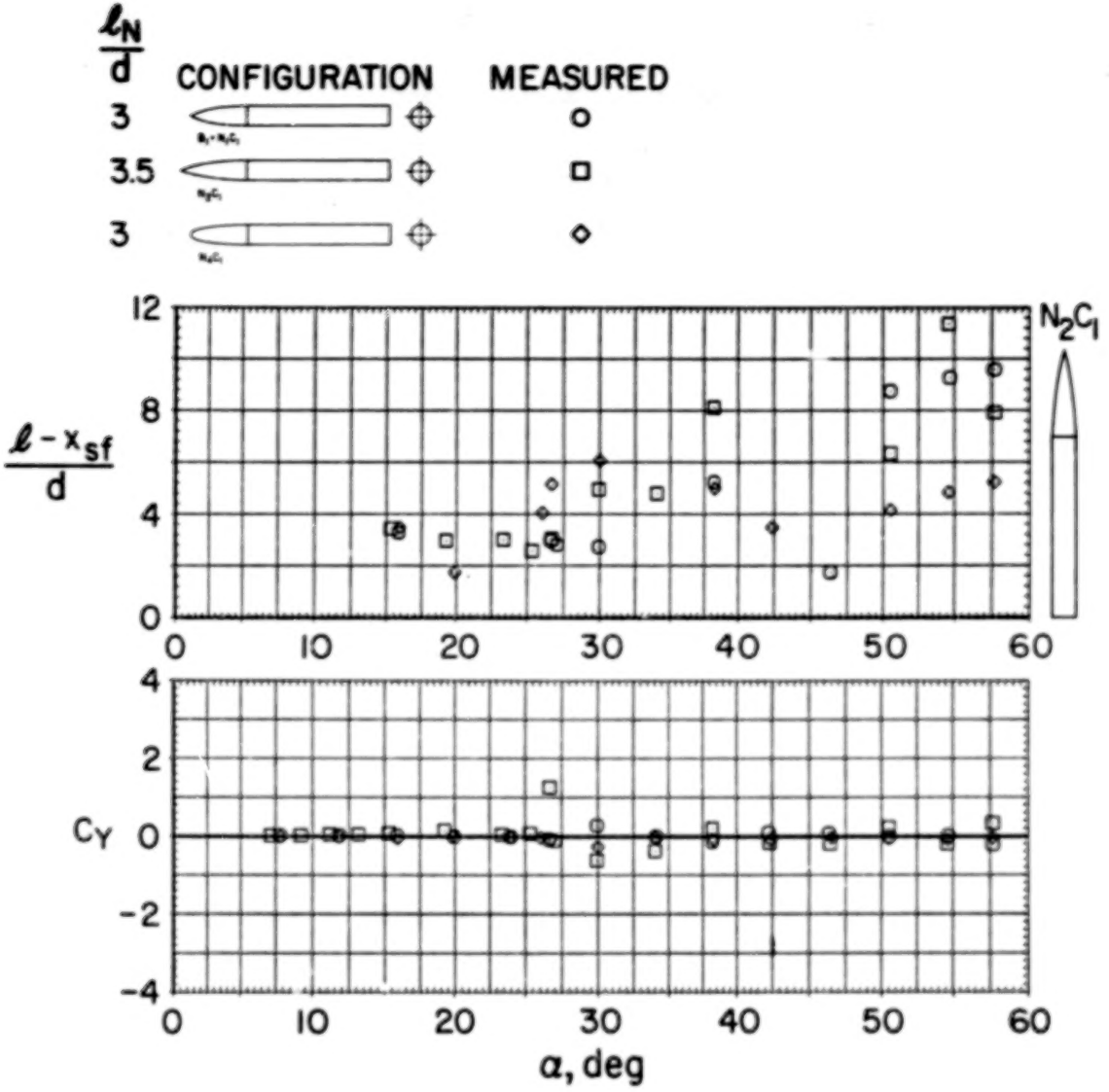

(b) $M_\infty = 0.9$, Re = 6.5×10^5.

Figure 68.– Concluded.

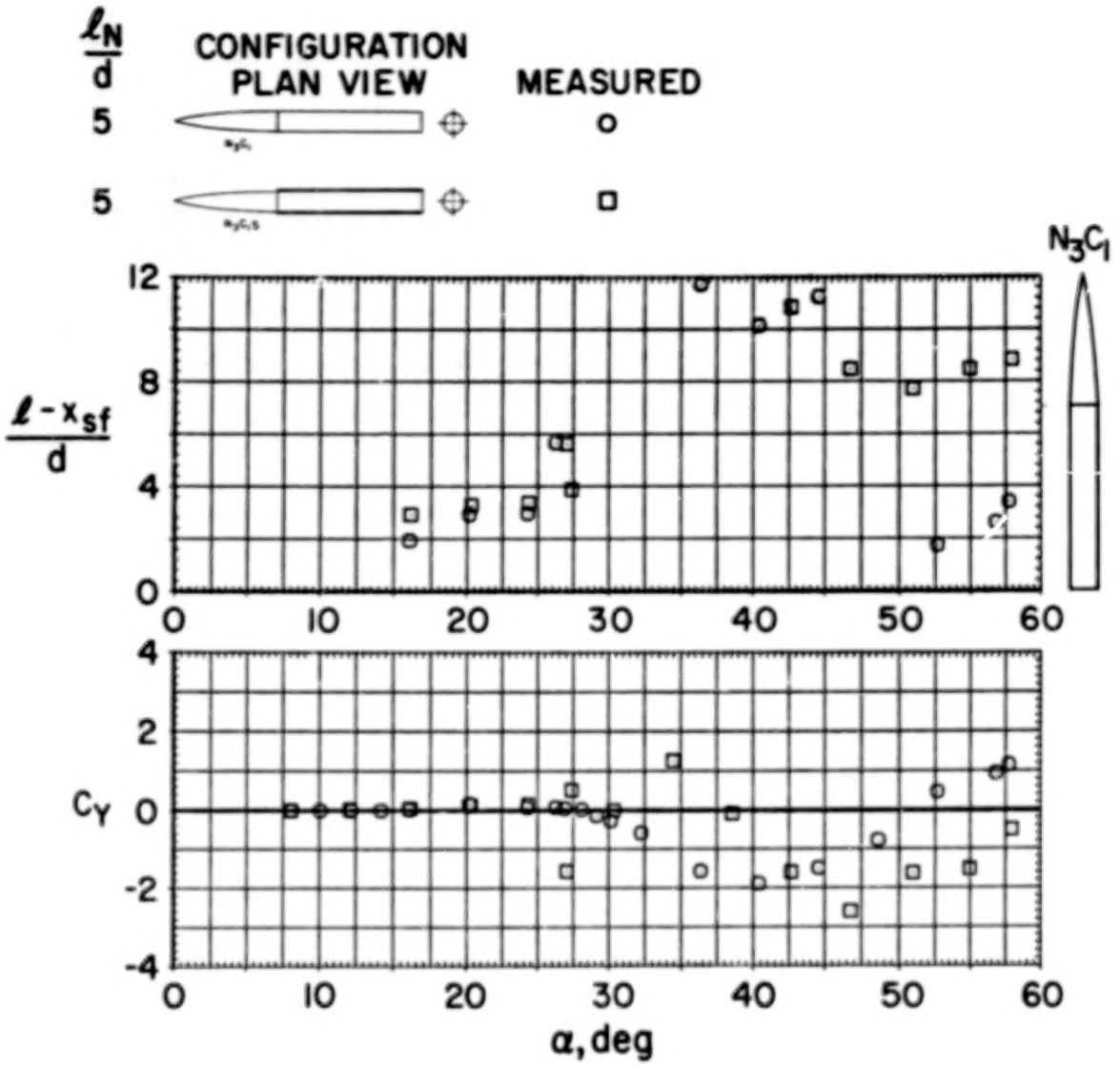

(a) $M_\infty = 0.6$, Re = 6.5×10^5.

Figure 69.– Effect of afterbody side strakes on side-force coefficient and side-force position for an ogive-cylinder body of revolution with a fineness-ratio-5 nose.

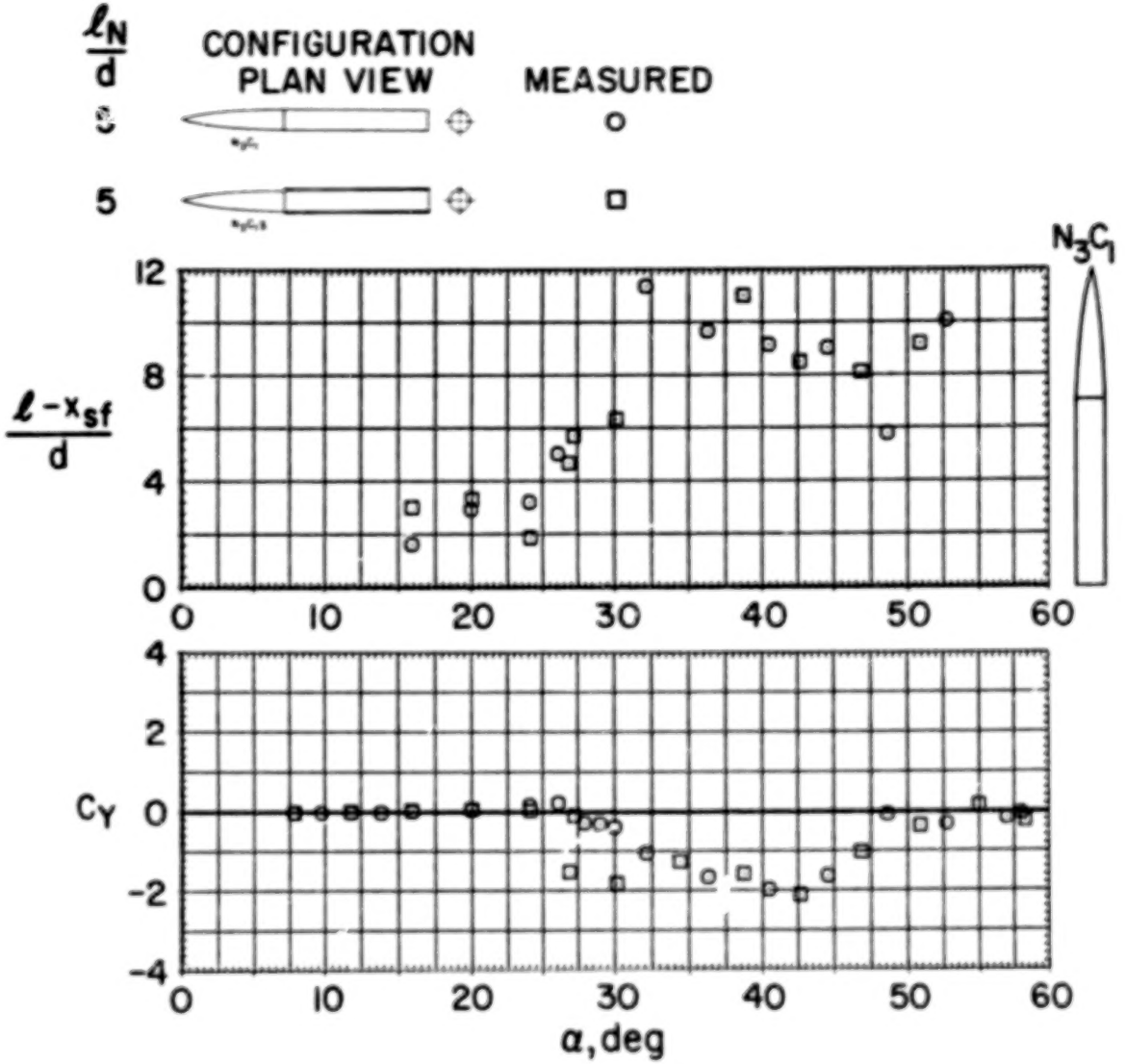

(b) $M_\infty = 0.9$, Re = 6.5×10^5.

Figure 69.– Concluded.

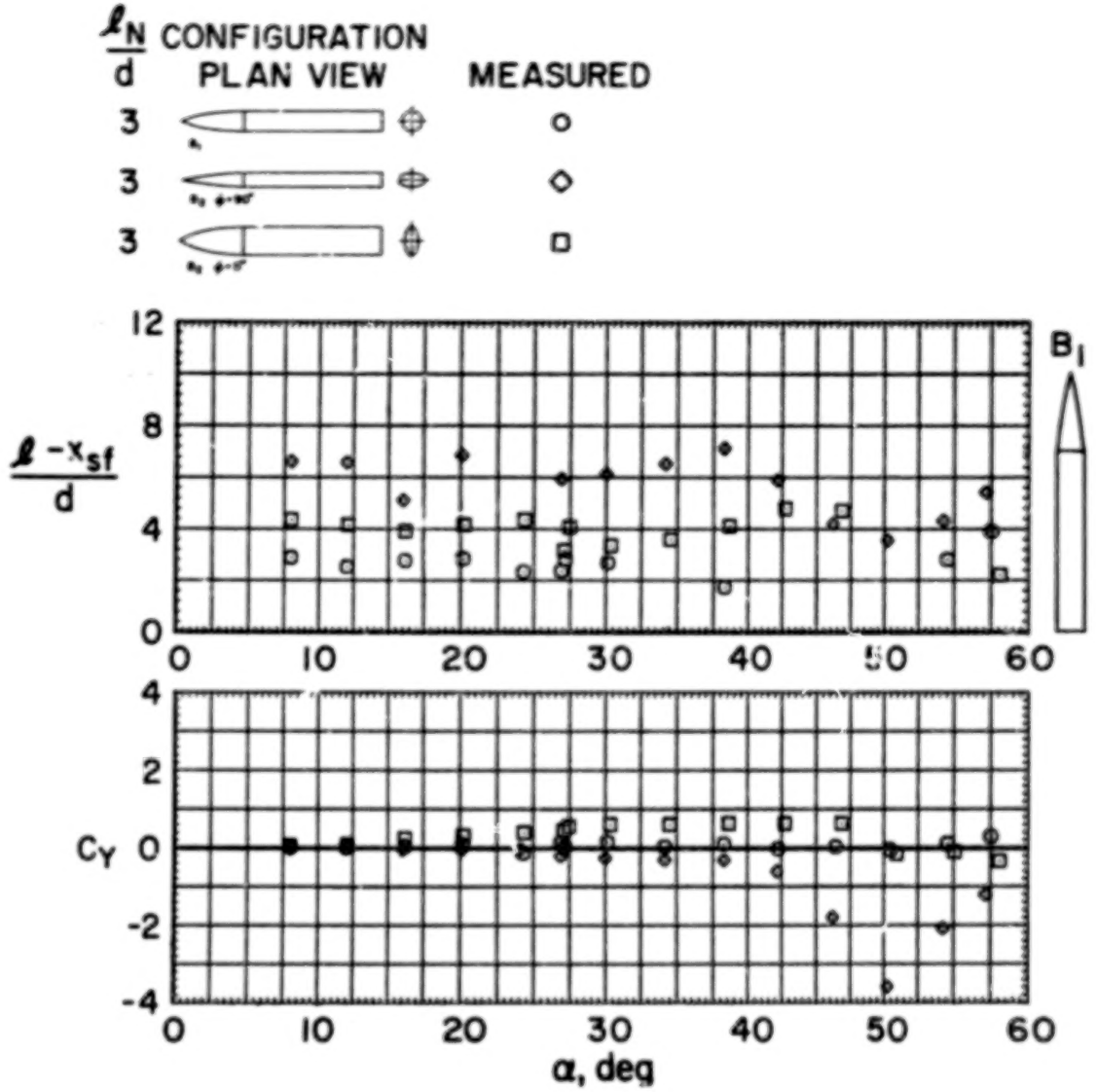

(a) $M_\infty = 0.6$, $Re = 6.5 \times 10^5$.

Figure 70.– Effect of elliptic cross section and roll angle on side-force coefficient and side-force position (elliptic body of constant a/b).

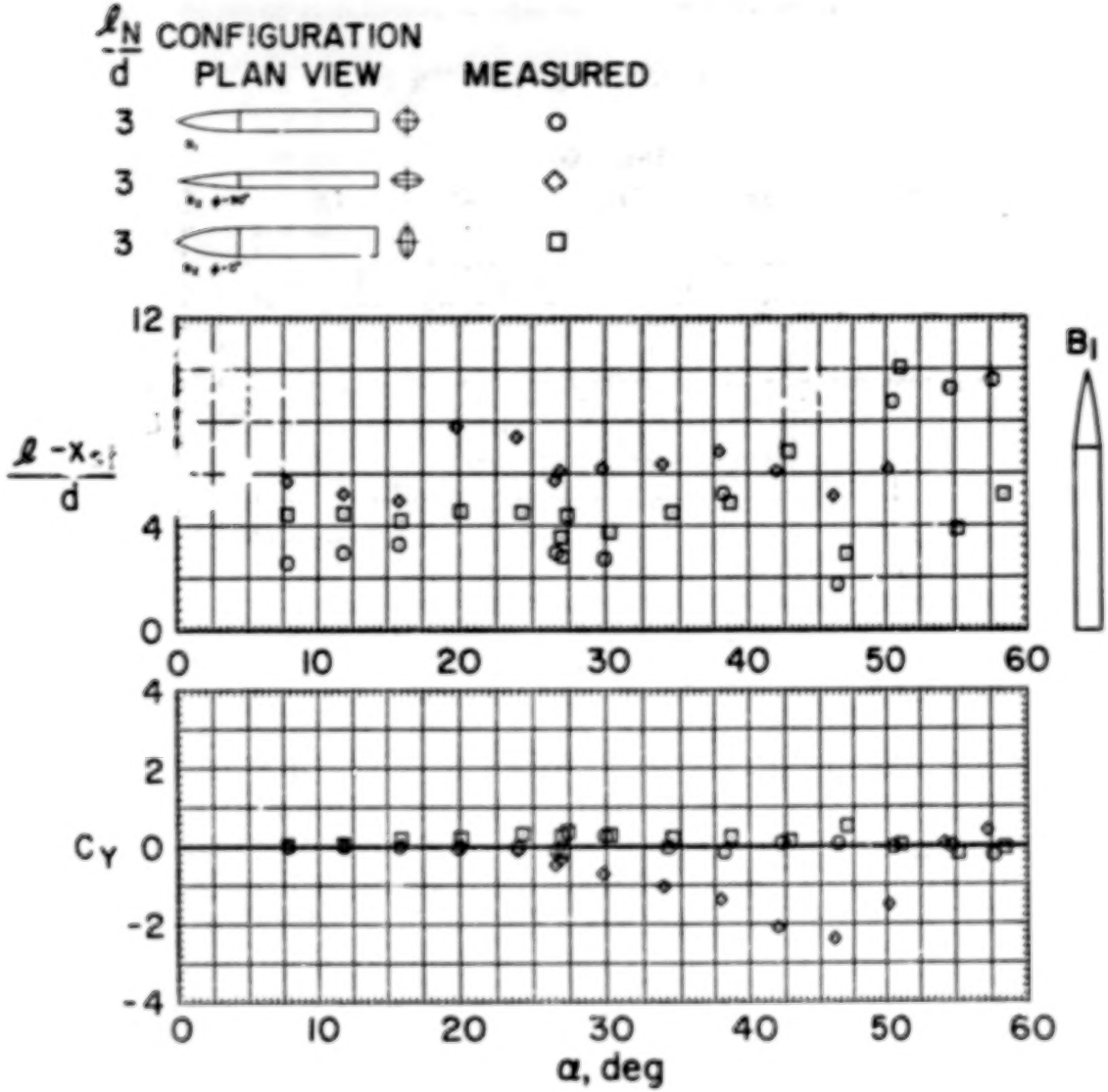

(b) $M_\infty = 0.9$, Re = 6.5×10^5.

Figure 70.– Concluded.

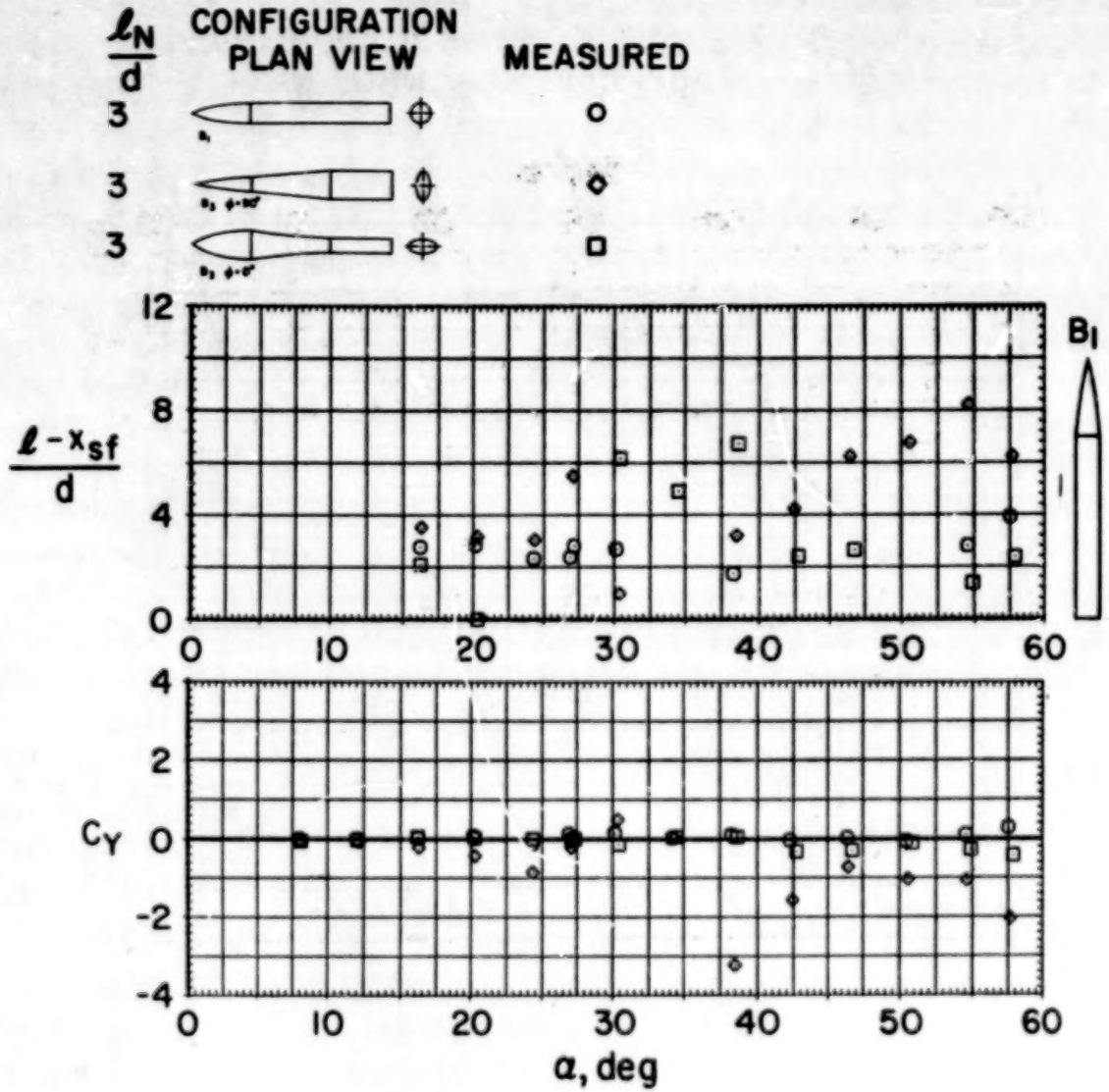

(a) $M_\infty = 0.6$, $Re = 6.5 \times 10^5$.

Figure 71.– Effect of elliptic cross section and roll angle on side-force coefficient and side-force position (elliptic body of variable a/b).

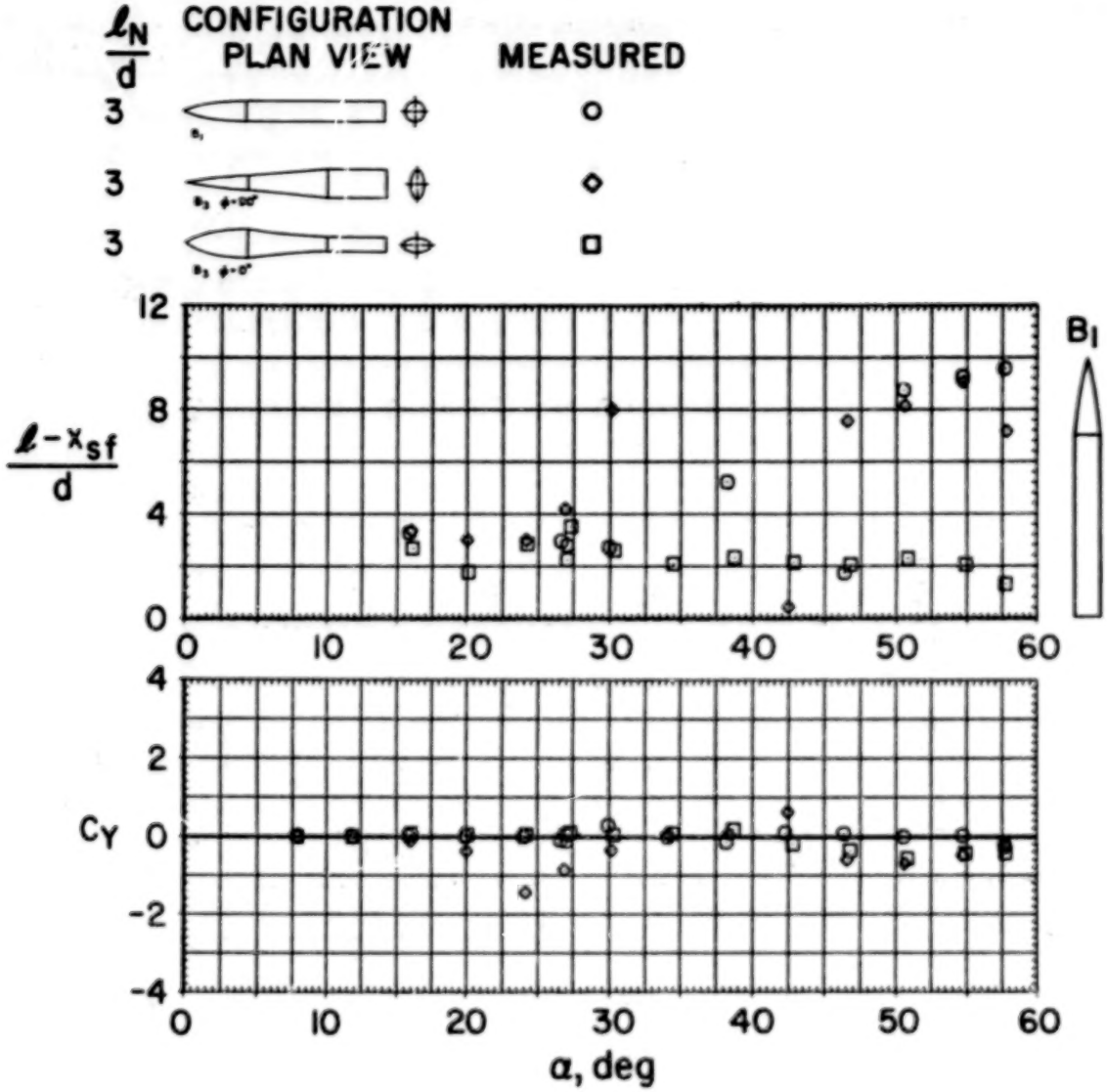

(b) $M_\infty = 0.9$, Re = 6.5×10^6.

Figure 71.– Concluded.

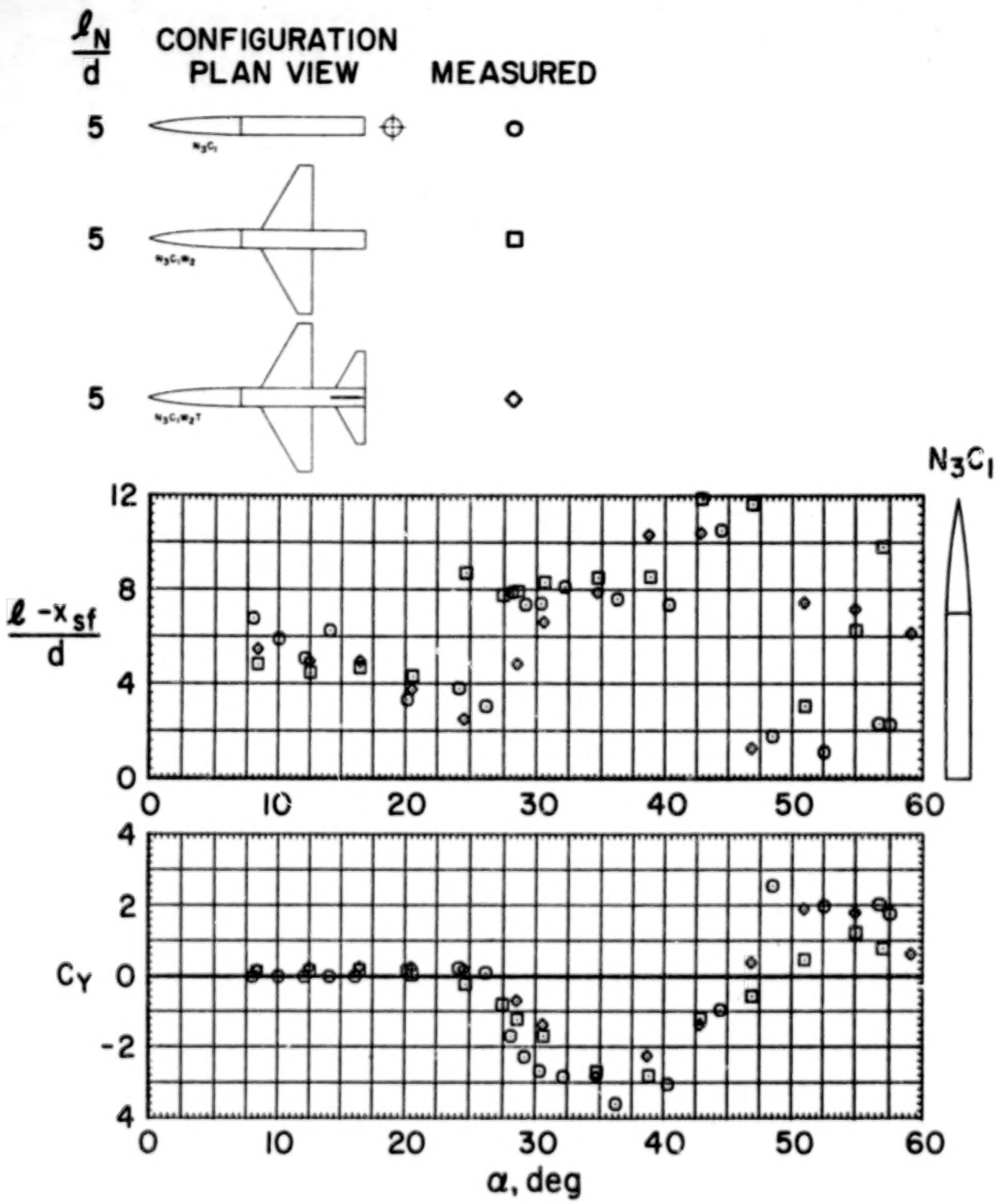

(a) $M_{c_\infty} = 0.6$, Re = 4.3×10^5.

Figure 72.– Effects on side-force coefficient and side-force position of adding a wing and a ···ing plus tail to a body.

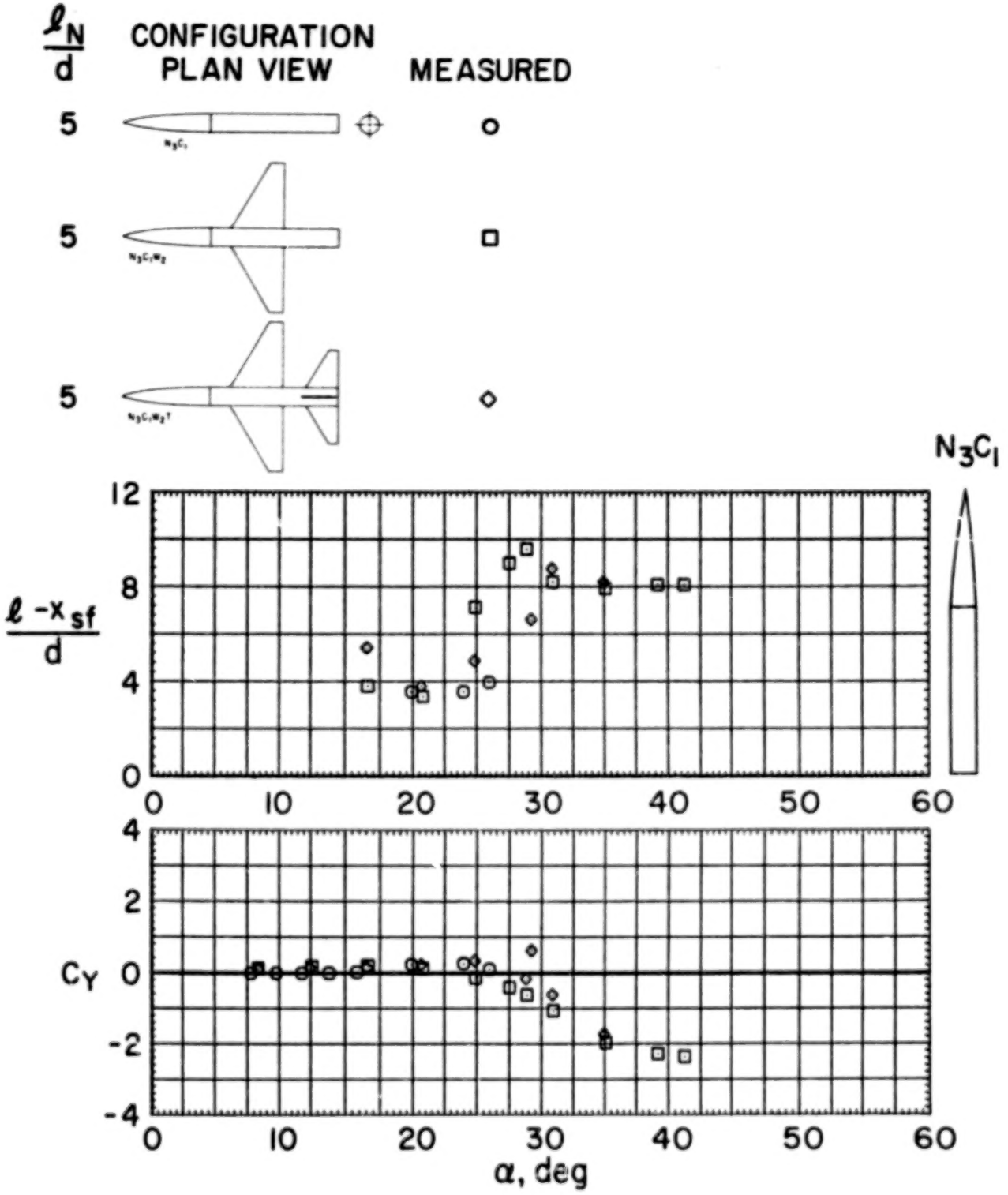

(b) $M_\infty = 0.9$, Re = 4.3×10^5.

Figure 72.– Concluded.

*U.S. GOVERNMENT PRINTING OFFICE: 1977 - 735-004/28

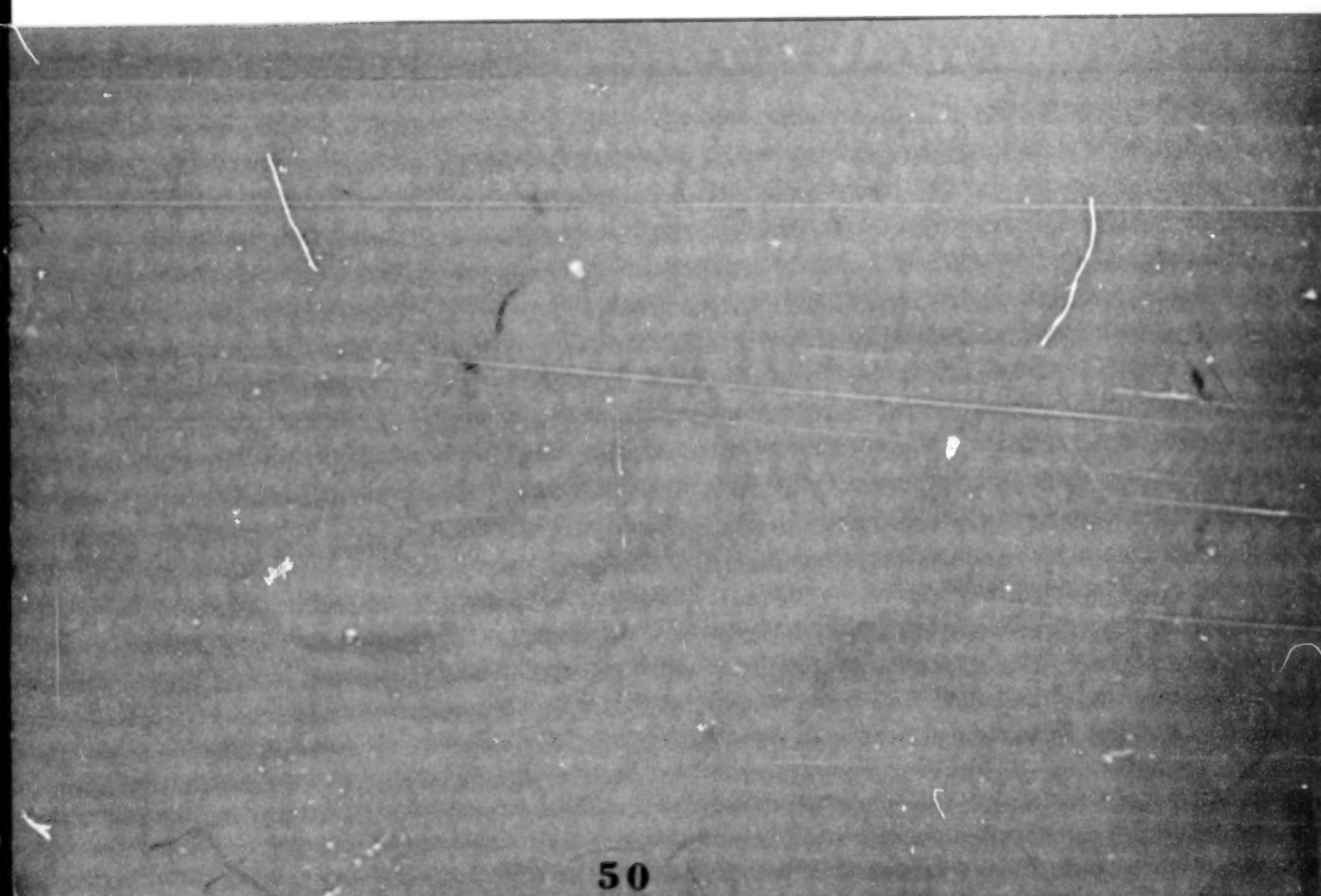

END

2.6.78